Conductive Polymers and Polymer Nanocomposites for Flexible Thermoelectrics

By Kening Wan

SUBMITTED IN PARTIAL FULFILLMENT OF THE REQUIREMENTS

OF THE DEGREE OF DOCTOR OF PHILOSOPHY

School of Engineering and Materials Science

Queen Mary University of London

Mile End Road, London, U.K. E1 4NS

October 2020

Declaration

I, Kening Wan, confirm that the research included within this thesis is my own work or that where it has been carried out in collaboration with, or supported by others, that this is duly acknowledged below and my contribution indicated. Previously published material is also acknowledged below.

I attest that I have exercised reasonable care to ensure that the work is original, and does not to the best of my knowledge break any UK law, infringe any third party's copyright or other Intellectual Property Right, or contain any confidential material.

I accept that the College has the right to use plagiarism detection software to check the electronic version of the thesis.

I confirm that this thesis has not been previously submitted for the award of a degree by this or any other university.

The copyright of this thesis rests with the author and no quotation from it or information derived from it may be published without the prior written consent of the author.

Signature:

Date: 07/Oct/2020

Acknowledgements

Looking back on the 4-year PhD journey, I feel it is both short and long. The short is because the time flies by and plenty of ideas are still waiting for me to implement. It is also long because I have savoured many memorable experiences both in research and in life.

I sincerely thank the China Scholarship Council and the Queen Mary University of London for awarding me the CSC-QMUL scholarship, letting me have such a fantastic experience of pursuing my PhD in QMUL.

I would like to express my heartfelt gratitude to my supervisor, Dr. Emiliano Bilotti, for his helpful guidance, inspiring encouragement, and generous sharing his knowledge. His patience and magnanimity to my immature ideas and enthusiasm about research supported and motivated me throughout the whole journey. I will always remember my first presentation during a Pasta, the valuable discussion during a Coffee, and our group celebration in the Pizza restaurant.

I would like to sincerely thank all the members in Nanoforce, where I spend most of my time. Especially, a huge thanks to Dr. Han Zhang for his supporting whenever I need help. He not only shares with me his knowledge in composite research but also gives me suggestions when I feel bewildered. Dr. Prospero J Taroni, who, I would say, led me into the world of organic thermoelectric. His humour brings me a lot of happiness and his experiences help me to start with experiments. Dr. Yi Liu, who initiatively shares her knowledge for pursuing PhD, and encourages me when I am depressed. And I gratefully thanks the technical support offered by Maurizio Leo, Dr. Giovanni Santagiuliana, Dr. Theo Saunders, Dr. Wei Tu; and special thanks to all my

lovely colleagues in Nanoforce, who help me in any shape of form, Dr. Nan Meng, Dr. Jiyue Wu, Dr. Jun Cao, Yunyin Lin, Xintong Ren, Arnaud Kernin, Leonardo Ventura, Rehan Bhatti, Yichen Wang, Xiangyan Yu, Claudia Bertei, Man Zhang, Wei Xiong, Dr. Kan Chen, Dr. Yinping Tao, Dr. Yaqiong Wang, Dr. Min Yu, Dr. Rui Mao and Dr. Yan Li.

And great thanks to all the members in our Organic Thermoelectric Lab, especially to Dr. Oliver Fenwick, Dr. Mark Baxendale and Dr. Bob C Schroeder for their generosity in sharing their professional knowledge and answering my questions. A lot of thanks to Dr. Manting Qiu, Dr. Christian Bech Nielsen, Dr. Vanira Trifiletti, Liu Zilu, Lewis Cowen, Tianjun Liu, Weidong Tang, Eugenio Galindez, Thibault Degousee and Sally Luong, with who I enjoyed to discuss and share knowledge in our group meeting.

I would also like to give my great thanks to Prof. Cees Bastiaansen, Prof. Ton Peijs, Dr. Dimitrios Papageorgiou, for their profound knowledge, comprehensive outlook, and great suggestions; Prof. Steffi Krause, who provided valuable knowledge on the understanding of impedance spectra, and Dr. Ying Tu, who shared me the experience in the set up for characterization of humidity sensor; Dr. Firat Guder and Giandrin Barandun, who offered me their technique and experience in wireless electronics; and Dr. Weibang who provided his knowledge of fabrication large scale CNT veils; Prof. Yang Hao and Ahsan Noor Khan who showed me the wireless signal transferring; Dr. Rebecca Stewart, Sophie Skach and An Liang who shared me the design of wearable sensors.

I greatly appreciate to Jun Ma for her kindness help on instruments set up and preparing LabVIEW programs; to Ken Scott and Geoff Gannaway, Jotham Selvarajah for giving technical support at the Physics laboratory; to Dr. Russell Bailey, Dr. Alice

Williams, Dr. Erica Di Federico, and Dr. Armando Lacerda, for professional supports in the lab of School of materials and engineering. I would like to thank Dr. Mouna Chetehouna and Dr. Jessica Henry who firstly provide me the opportunity to work as a laboratory demonstrator and teach assistant. I also want to mention all undergraduates and master students, Gioia Nchong Etchi Regoli, Bonnie Gar Bo Cheuk, Nigar Gul Malik, Sidney James Allen, Safiyyah Ammaarah Daar Mendez, I-Chuan Hsia, Pio Justin Malima, Amrit Preet Kainth, Tongrui Zhuang and Muhammad Arslan Badr, who worked with me, helped me and bring me new ideas.

Greatly acknowledgement to the European cooperation in science and technology, who support me to visit IMDEA, materials institute for a short-term scientific mission (Action CA15140). The great time I spend in IMDEA would not have been as fascinating without the warm people I met there. Dr. Juan José Vilatela and Dr. Anastasiia Mikhalchan host me and helped me to succeed in the application. The discussion with Dr. Juan José Vilatela taught me a lot; the patient and series altitude to researches of Dr. Anastasiia Mikhalchan really inspired me. Luis Arévalo who kindly demonstrated to me the whole process of the fabrication of CNT veils by FCCVD; Carlos González, and Dr. José Sánchez del Río Saez, who gave me technique support and provided me special access due to my short visiting time. Also, I would like to give my sincere thanks to all the hardworking PhD students there who gave me the fabulous memories, especially Yunfu Ou and Shuna Wen, who provided a lot of help with my accommodation and lives in Getafe.

I want to give my most special thanks to my parents for their unwavering love and support so that I can pursue whatever I want without any worries.

And finally, thanks to all my friends with who I spent a great time during these four years, and whom I may haven't mention but are as much deserving of an acknowledgement, for contributing directly or indirectly to my PhD researches.

Thank you!

Kening Wan

September 2020

Abstract

With the development of fields like soft (micro-) robotics, wearable devices and internet-of-things, there is a growing demand for new materials with combinations of functional properties, ranging from electrical conductivity, sensing and energy storage/harvesting, together with mechanical properties like large elastic deformations and toughness. Organic thermoelectric (OTE) materials and their composites are excellent candidates for self-powered sensors, due to their ability to harvest waste heat energy in a robust and reliable manner, combined with mechanical properties (*e.g.* high strain at break) and additional functionalities.

This thesis focuses on the application of OTE as multi-functional self-powered sensors. Three types of representative OTE materials have been mainly investigated to explore different characteristics and potential applications. Three different processing methods have been explored for achieving the different structures aiming at various functions and potential applications in fields like wearable electronics and self-powered sensors.

Poly nickel-ethenetetrathiolates ($Na_x(Ni\text{-}ett)_n$) has been selected as the n-type OTE material. Highly stretchable n-type composite films are obtained by blending with polyurethane. When subjected to a small temperature difference (< 20 ^oC), the films generated sufficient thermopower to be used for sensing strain and visible light, independently of humidity.

Poly (3,4-ethylenedioxythiophene) polystyrene sulfonate (PEDOT:PSS) has also been selected as the most widely investigated p-type OTE material. A novel self-powered ultrasensitive deformation sensor has been demonstrated based on PEDOT:PSS being

coated on Lycra® yarns. By controlling the crack induced patterns of the conductive PEDOT:PSS coating, the strain sensitivity could be tuned in a wide range.

Finally, carbon nanotube (CNT) has also been studied. A self-folding method has been used to create 3D structures by fixing CNT veils between patterned polycarbonate and biaxial stretched polystyrene films. The obtained honey-comb shaped OTE device has been utilised as a structural composite as a self-powered integrated sensor.

Table of contents

List of abbreviations and symbols

2D	2-dementional
3D	3-dementional
3ω	Three-omega
Ag	Silver
A_L	Cross sectional areas of Lycra®
A_P	Cross sectional areas of PEDOT
Bi_2Te_3	Bismuth telluride
BLE	Bluetooth® low energy module
b-PS	Biaxial stretched Polystyrene
CNTs	Carbon nanotubes
CPY	Cracked PEDOT:PSS coated yarn
DMSO	Dimethylsulfoxide
DOS	Density of states
DWCNT	Double wall carbon nanotube
e	Unitary charge
EA	Activation energy
EDOT	Ethylenedioxythiophene
E_F	Fermi energy
EG	Ethylene glycol
E_L	Young's modulus of Lycra®
E_P	Young's modulus of PEDOT
Fe	Ferrum
$FeCl_3$	Iron (III) chloride
GFRP	Glass fibre reinforced plastic
GO	Graphene oxide
HOMO	Highest Occupied Molecular Orbital
HI	Hydroiodic acid
I	Current
LBL	Layer-by-layer
LUMO	Lowest unoccupied molecular orbital
MWCNT	Multi-wall carbon nanotube
n	Carrier concentration
n(E)	Carrier concentration at energy E
n_e	Electrons' concentration
n_h	Holes' concentration, respectively
NL	$Na_x(Ni\text{-}ett)_n$/ PU composite
NNH	Nearest neighbour hopping
OTE	Organic thermoelectric
P3HT	Poly(3-hexyl thiophene)
PAA	Polyacrylic acid
PANi	Polyaniline
PEDOT	Poly(3,4-ethylenedioxythiophene)
PEDOT:PSS	Poly(3,4-ethylene-dioxythiophene): polystyrenesulfonic acid

PEDOT:ToS	Poly(3,4-ethylene-dioxythiophene): tosylate
PEI	Poly(ethyleneimine)
PEO	Polyethylene oxide
PET	Polyethylene terephthalate
PF	Power factor
PL	PEDOT:PSS/PU composite
P_{max}	Maximum output power
poly(M-ett)	Poly(metal-1,1,2,2-ethenetetrathiolate)
PPY	Polypyrrole
PY	PEDOT:PSS coated yarn
PSS	Polystyrenesulfonic
PSSH	Poly(4-stynesulfonic acid)
PU	Polyurethane
PVDF	Polyvinylidene fluoride
PVP	Poly(N-vinylpyrrolidone)
q	Heat flux density
R_1	Reference resistance
R_i	Internal resistance
R_L	Load resistance
ΔR_{sensor}	Sensor' resistance of the
Sb_2Te_3	Antimony telluride
SDBS	Sodium dodecylbenzenesulfonate
SEM	Scanning electron microscopy
SF	Sensitivity factor
SWCNT	Single wall carbon nanotube
T	Temperature
$\bar{T}$	Average of hot and cold side temperatures
T_0	Strat temperature
T_c	Cold side temperature
TE	Thermoelectric
Te	Tellurium
TEG	Thermoelectric generator
TGA	Thermogravimetric analysis
T_h	Hot side temperature
TTF-TCNQ	Tetrathiafulvalene-tetracyanoquinodimethane
UV-vis	Ultraviolet-Visible
V_{oc}	Open circuit voltage
V_t	Thermal voltage
VRH	Variable range hopping
WPU	Water-borne polyurethane
zT	Figure of merit (materials)
ZT	Figure of merit (devices)
$(zT)_{eng}$	Figure of merit (materials) with a large temperature difference
$(ZT)_{eng}$	Figure of merit (devices) with a large temperature difference
α	Seebeck coefficient
α_n	N-leg Seebeck coefficient
α_p	P-leg Seebeck coefficient
ΔT	Temperature difference
ΔV	Voltage between hot and cold ends

η_0	Carnot efficiency
η_{max}	Maximum power conversion efficiency
κ	Thermal conductivity
κ_c	Charge carrier thermal conductivity
κ_l	Lattice thermal conductivity
κ_n	N-type leg thermal conductivity
κ_p	P-type leg thermal conductivity
μ	Carrier mobility
$\mu\ (E)$	Carrier mobility at energy E
μ_e	Electrons' mobility
μ_h	Holes' mobility
σ	Electrical conductivity

List of figures

List of tables

Chapter 1 Introduction

1.1 Motivation and objective

Waste heat is everywhere. Nearly three-quarters of all the energy produced by humanity is squandered as waste heat and often released to the environment, according to the law of thermodynamics. The thermoelectric (TE) technology could provide a way to reduce the energy consumption, by reusing this waste heat and converting it directly into electricity.

Two hundred years after its discovery, the physical phenomenon of TE has been exploited to generate electricity from a temperature gradient. Only recently organic materials have attracted an interest as TE materials. Organic Thermoelectrics (OTE) are based on conducting polymers and polymer nanocomposites and could be suitable for low temperature (< 250 °C) waste heat harvesting. OTE are promising as they can overcome drawbacks of traditional inorganics TE materials like the utilisation of rare, expensive and/or toxic elements, the brittleness and difficult processing. OTE can be synthesized from abundant elements by using low cost fabrication techniques. Furthermore, their low thermal conductivity and flexible nature can favour new device architectures and applications. Nevertheless, the low energy conversion efficiency hindered their utilization as generators. Prime issues are the lack of good performing and stable n-type OTE materials, the impracticality of in-plane devices in addition to the low power outputs (pW to μW) under a small temperature difference (< 20^{o}C). Recently, not only p-type, n-type polymers and nanocomposites have made significant progress, but also new strategies and prototypes have been developed to improve the

OTE performance. Nevertheless, there is still a giant gap to fill before OTE generators could become commercially available.

On the other hand, the expected rapid development of intelligent devices and internet of things will increase the requirement of a robust and reliable power source, particularly in off-the-grid and maintenance-free applications. This will accelerate the demand of energy harvesting devices and the development of autonomous, self-powered devices. Given that only small power is required for operating these electronics, exploiting new OTE materials for energy harvesting modules, and integrating additional multi-functions and the unique mechanical properties, from flexible to rigid, within a single device, could become a reality.

The main objective of this doctoral research is to explore state-of-the-art OTE materials to be utilised as multi-functional self-powered sensors. One of the aims is to enhance the properties of OTE materials, including increasing TE property by doping or post-treatment, improving mechanical flexibility by compounding with another polymer matrix and boosting the sensitivity by crack engineering. The other aim is to develop new OTE device architectures, with excellent flexibility, capable of harvesting out-of-plate thermogradients while, ideally, eliminating metal electrodes connection between p-n legs to reduce the inner resistance. Their various applications such as a wireless movement sensor, a self-powered temperature/strain sensor and a self-powered composites health monitor, should be explored to demonstrate potential room temperature applications of OTE.

1.2 Scope of the thesis

This research project investigates three types of representative OTE materials to be used as self-powered multifunctional sensors, and processed by different methods.

The literature review presented in **Chapter 2** gives a broad overview of the TE technology, beginning with its basic knowledge and concepts, followed by a more focused review of OTE materials and devices. In particular, three types of OTE materials, PEDOT:PSS, Poly(M-ett), and Carbon nanotubes (CNTs), representing among the most promising classes of p-type conjugated polymer, n-type coordination materials, and carbon-based nanocomposites, respectively, have been reviewed. Different prototypes of OTE devices, especially flexible and stretchable designs, are then overviewed. Finally, two potential applications of the next-generation OTE devices are discussed: wearable sensor and self-powered sensors.

The materials, experimental procedures and characterisation techniques used in this research are summarized in **Chapter 3**. A highly stretchable n-type composite film, obtained by combining poly nickel-ethenetetrathiolates ($Na_x(Ni\text{-}ett)_n$) with a commercial polyurethane (Lycra®), is presented in **Chapter 4**, which can generate sufficient thermopower to be used for sensing strain and visible light when subjected to a small temperature difference (< 20 ^oC). The prototypes of a wearable self-powered sensor and a magic-ball shaped device, without employing any metal connections, have also been demonstrated. **Chapter 5** presents a stretchable TE yarn prepared by coating PEDOT:PSS on Lycra® yarns and cracks are introduced by pre-straining the yarns. Such TE yarn shows an ultrahigh and tuneable strain sensitivity together with a very high strain-at-break (~1000%). The same yarn can sense strain, temperature and can power itself thermoelectrically, eliminating the need for the use of an external power-supply to power the sensor. **Chapter 6** presents a honeycomb structural TE device based on CNT veils, by utilising a Kirigami inspired self-folding process. A self-powered health monitoring structural composite is demonstrated, utilising the electrical power generated from thermal gradient along the out-of-plane direction.

In **Chapter 7**, the results of this research are summarized and prospective for future research suggested. I sincerely hope this thesis could be followed up by further research so to be able to witness even a minimal contribution on reducing our global energy crises and/or improving our quality of life.

Chapter 2 Literature review

With the rapid development of intelligent devices and internet of things, much effort has been recently put in energy harvesting technologies that can harvest various forms of energy from the environment and convert it to electricity. Thermoelectric (TE) is one of such technologies that can harvest ubiquitous waste heat (gradients). Nearly two hundred years after its discovery, thermoelectricity is regaining recent momentum also thanks to the study of new organic thermoelectric (OTE) materials. OTE promises to tackle open issues, which limited the wider exploitation of traditional TE materials, including their brittleness and manufacturing challenges as well as the use of rare, expensive and/or toxic elements. Utilising the unique advantages of OTE, including ease of manufacturing, non-toxicity and wide availability of chemical elements as well as flexibility, new device designs can be developed and new applications can be explored, including wearable sensors and self-powered devices.

Conversely, the TE low energy conversion efficiency remains a largely unsolved hurdle, which is being addressed by the development of new materials.

In this chapter, the basic knowledge of thermoelectricity is first introduced. Then, the most promising organic thermoelectric materials are reviewed, divided as p-type, n-type and (nano)composite materials, with a particular emphasis on stretchable OTE materials. Finally, after reviewing TE device architectures, including flexible and stretchable device prototypes, examples of applications of new-generation OTE devices are also provided.

2.1 Basic knowledge of thermoelectricity

During the first half of 19th century, the physical phenomenon of 'thermoelectricity' was gradually developed with the Seebeck effect first reported by Thomas J. Seebeck in 1821, as well as the Peltier effect and Thomson effect, which were observed by Jean Charles Peltier in 1834 and Lord Kelvin in 1854. Thermoelectricity is a ubiquitous phenomenon present in all materials, resulting from the thermal diffusion of charge carriers along a temperature gradient. Specifically, when a material is subjected to a temperature gradient, the occupation of charge carriers in the density of state (DOS) is different from the hot side to the cold side, leading to the charge carriers (holes or electrons) diffusion and accumulation at the cold side, yielding a potential difference along the temperature difference. Depending on whether holes or electrons are the dominant charge carrier type, thermoelectric materials can be divided into p- and n-type. However, most materials present a very low thermoelectric effect which limits their practical use due to (i) the low electrical conductivity so that the thermodiffusion of charge carriers provides negligible electrical current and power; (ii) the instability of creating a sufficient electric potential for a considerable temperature gradient; and (iii) the high thermal conductivity which makes the temperature gradient difficult to be maintained.

2.1.1 Figure of merit

An ideal thermoelectric material will, therefore, not only have a large Seebeck effect, but also be a good electrical conductor, to transport charge carriers effectively while minimizing the Joule heating dissipation during the charge transport, as well as a good thermal insulator, to prevent heat flow through the material and maintain a large temperature difference. These are governed by the Seebeck coefficient, α (also commonly denoted by S), electrical conductivity, σ, and the thermal conductivity, κ,

respectively. The dimensionless thermoelectric figure of merit (zT), combining the above properties, is often used to evaluate the thermoelectric performance of a material, operated at the certain temperature, T:

$$zT = \frac{\sigma\alpha^2}{\kappa}T \qquad \textbf{Equation 2.1}$$

This dimensionless parameter is also used to assess the thermoelectric efficiency of devices, normally capitalize all letters as *'ZT'*. The maximum efficiency of a thermoelectric material depends only on zT, for a given temperature gradient. Enhancing the zT is hence one of the main aims in TE academic research, which can be achieved by increasing electrical conductivity and Seebeck coefficient, or by reducing the thermal conductivity. The numerator in the zT equation, $S^2\sigma$, is called power factor (PF), which is normally used for evaluating the TE properties of a class of materials whose κ is difficult to be determined or of secondary importance. Usually, α, κ and σ all vary with temperature. Hence, $(zT)_{eng}$ is also adopted to predict the material performance for accuracy[1]:

$$(zT)_{eng} = \frac{\int_{T_c}^{T_h}\sigma(T)dT\,(\int_{T_c}^{T_h}\alpha(T)dT)^2}{\int_{T_c}^{T_h}\kappa(T)dT}\Delta T \qquad \textbf{Equation 2.2}$$

where T_h and T_c refer to the hot and cold side temperature, resulting in the temperature difference ΔT. Ideally, zT should be ≥ 1 for commercial usage. ZT values above 2 have previously been reported [2], but only for very few (inorganic) compounds at temperatures higher than 600 K [3]. **Seebeck coefficient**

By measuring the voltage (ΔV) generated between hot and cold ends of a material, at a steady state, the Seebeck coefficient can be defined as

$$\alpha = -\frac{\Delta V}{\Delta T} \qquad \textbf{Equation 2.3}$$

The sign of α is positive for p-type materials, with holes accumulated at the cold end, and negative for n-type materials, when the majority charge carriers are electrons. The Seebeck coefficient, sometimes also called as thermopower, can be defined as the average entropy per charge carrier, weighted by the contribution of the carrier to conduction. Despite the Seebeck coefficient having a complex dependence on carrier concentration and microstructure, it can be determined by the asymmetric distribution of carriers around the Fermi level and energy dependence of the charge carrier mean free path. When the energy of the lowest unoccupied molecular orbital (LUMO) for the conductive band is close or lower than the Fermi level, the net charges by thermodiffusion in the semiconductor is negative (hence n-type material), and when the energy of highest occupied molecular orbital (HOMO) for valence band close or higher than Fermi level, it will be p-type materials with positive Seebeck coefficient. The greater asymmetric density of states (DOS) around Fermi level, *i.e.*, the higher slope of DOS at Fermi level, leads to a higher absolute Seebeck coefficient. Therefore, introducing some sharp features around the Fermi level and changing either the DOS or the Fermi level position can increase the Seebeck coefficient. Tuning of the doping level is the most common strategy to move the Fermi level or change the polaron/bi-polaron band to adjust the steepest slope located around Fermi level. The degree of order, such as crystallinity, will have a significant impact on the DOS. Ordered materials have sharp DOS features, resulting in a steep DOS at Fermi level and a high Seebeck coefficient. Except manipulating band structures, tuning carrier scattering mechanism also can improve the carrier mobility and enhance Seebeck coefficient.

Electrons, phonons, and electron-phonon interactions all can contribute to the Seebeck coefficient. In semimetals and metals systems, the migration of thermally excited electrons dominates the contribution to the Seebeck coefficient. Under the assumption

of the charge transport only occurs near the Fermi energy (E_F) and the transmission probability changes slowly in energy scale of k_BT, and $k_BT << \mu$, where μ is carrier mobility, the Seeebeck coeffiecient changes with temperature follows the Mott formula [4] as:

$$\alpha = \frac{\pi^2 k_B^2 T}{3q}\left(\frac{1}{n}\frac{dn(E)}{dE} + \frac{1}{\mu}\frac{d\mu(E)}{dE}\right)_{E=E_F} \qquad \textbf{Equation 2.4}$$

where k_B refers to the Boltzmann constant, $n(E)$ and $\mu(E)$ are the carrier concentration and mobility at energy E, and q is the electronic charge. In this case, the Seebeck coefficient is linearly proportional to the temperature.

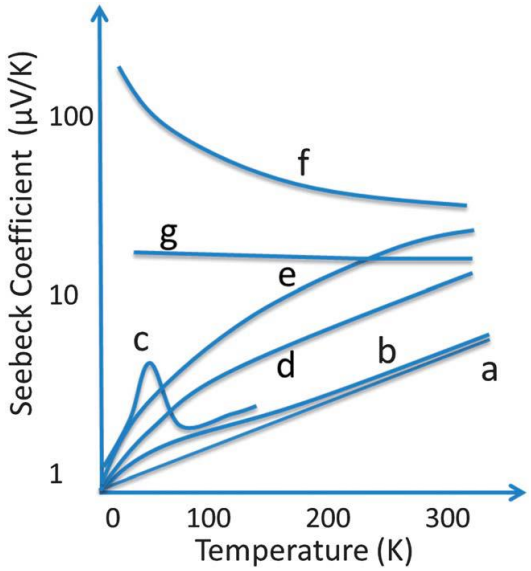

Figure 2.1 *Temperature dependence of the Seebeck coefficient for different types of conduction mechanisms in conducting polymers [5]. When the metallic band is narrow, Seebeck coefficient increases linearly with the temperature in a metallic manner (curve a). A strong electron-phonon interaction at very low temperatures leads to the deviation from linearity (curve b). The electron-phonon interaction manifests in a characteristic hump as curve c. For lightly doped polymers, the temperature dependence of the Seebeck coefficient is non-linear with either increase (curve d of $T^{1/2}$-dependence and curve e) or decrease (curve f of 1/T-dependence) with temperature. At higher doping levels, Seebeck coefficient becomes nearly independent of temperature (curve g).*

For conductive polymers, depending on the type of transport mechanism, the Seebeck coefficient shows very different temperature-dependent behaviours (Figure 2.1). For example, the Seebeck coefficient of lightly doped conductive polymers can either decrease or increase non-linearly with temperature but is mostly found independent of temperature. Whereas, for heavily doped conductive polymers, the Seebeck coefficient shows linear dependence with temperature, frequency increasing with temperature. However, at low temperatures (< 200 K), the Seebeck coefficient of highly conducting polymers, especially those with a good crystalline structure, decreases linearly with temperature. This is caused by electron-phonon scattering, known as 'phonon drag', which becomes significant when the phonons' mean free path increases at lower temperatures, until it becomes comparable to the electrons' mean free path. A combination of the above behaviours is usually found experimentally, because of the complexity of conductive polymer systems.

2.1.3 Electrical conductivity

Electrical conductivity, σ, is a fundamental property of a material that represents the ability to conduct electric current. It is related to the charge carrier concentration (n) and mobility (μ). For semiconductors, both holes and electrons can be transported in an electric field. Therefore, the electrical conductivity is given by

$$\sigma = e\mu n = e(\mu_e n_e + \mu_h n_h) \qquad \textbf{\textit{Equation 2.5}}$$

where μ_e, μ_h, n_e and n_h refer to the electrons' mobility, holes' mobility, electrons' concentration and holes' concentration, respectively; and e is the unitary charge with a unit of Coulomb (C). Therefore, the electrical conductivity of a material can be improved by increasing the charge carriers' density and/or mobility. For organic conductive materials, the structural order, from the molecular scale to the macroscale,

has the same critical influence on the electrical conductivity as the introduction of carriers. For instance, the charge transport within crystalline domains is highly anisotropic, because of the differences in the electronic coupling between molecules.

The order-disorder balance decides the transport mechanism, like band transport, hopping transport or mixed filamentary current pathway description, resulting in different dependencies of the electrical conductivity with temperature. Some highly ordered and highly doped organic materials behave like metals. The charge carrier density increases with temperature, while the mobility decreases, due to the enhanced lattice vibration, which increases the scattering and collisions between electrons and nucleus. Therefore, electrical conductivity decreases with temperature.

In semiconductors, electrons are only able to transport when excited into the conduction band. The density of these electrons increases exponentially with temperature; hence the conductivity is enhanced with temperature. When the material's band gap is large, typically for most intrinsic organic semiconductors, the charge density increase with the temperature is negligible, while the charge carrier mobility increases because the charge carrier hopping ability is activated by temperature. Hence, the electrical conductivity of disordered organic material often shows increasing trend with temperature.

2.1.4 Thermal conductivity

Thermal conductivity describes the material's ability to conduct heat. It is defined by the Fourier law

$$q = -\kappa \frac{dT}{dx} \qquad \textbf{\textit{Equation 2.6}}$$

where q is the heat flux density, in W cm^{-2}, meaning the heat flow rate per unit area, and $\frac{dT}{dx}$ is the temperature gradient, in K m^{-1}. Steady-state and transient-state measurements are the two basic types of methods to measure thermal conductivity. The former method can be used to measure in-plane thermal conductivity, but it is very time-consuming and seldom used in practice. Transient-state methods are much more well-developed for characterising thermal conduction properties of both bulk and film materials. Among the most widely adopted methods, three are mentioned herein: the laser flash, time domain thermal reflectance and differential three-omega (3ω) method [6].

Unlike inorganic materials, where electronic thermal conductivity is dominant and coupled with the electrical conductivity, in conductive polymers, thermal conductivity is contributed by both charge carriers and phonons (also called as lattice contribution). According to Wiedemann-Franz law, the thermal conductivity is the sum of the lattice thermal conductivity (κ_l) and the charge carrier thermal conductivity (κ_c):

$$\kappa = \kappa_l + \kappa_c = \kappa_l + L\sigma T \qquad \textbf{\textit{Equation 2.7}}$$

where L is the Lorenz constant ($\sim 2.45 \times 10^{-8}$ V^2 K^{-2} for metals and highly doped semiconductors, and $\sim 1.5 \times 10^{-8}$ V^2 K^{-2} for non-degenerate materials such as undoped semiconductors) [7]. For doped semiconductors, *i.e.* conducting polymers, ($\sigma \geq 100$ S cm^{-1}), κ_c and κ_l can be comparable in value, so it is important to consider both contributions. For materials with low electrical conductivity ($\sigma \leq 100$ S cm^{-1}), the lattice contribution (κ_l) can be the predominant one to thermal conductivity.

For lattice thermal conductivity, phonons can be scattered by other phonons, defects (*e.g.* impurities, dislocations), electrons, and boundaries, consequently, slow down the transport of phonons and reduce lattice thermal conductivity. Polymers generally have

low thermal conductivities (*i.e.* from 0.1 W m^{-1} K^{-1} to 2.0 W m^{-1} K^{-1}). Meanwhile, the anisotropy of polymer chains tends to form an anisotropic thermal conductivity, and it is more obvious when the chains are more ordered for a certain polymer, causing the highly anisotropic properties in-plane and out-of-plane. Therefore, it is vital to evaluate σ, α and κ in the same direction as the temperature gradient in order to ensure the accuracy of a material's thermoelectric performance.

2.1.5 Interrelated parameters

As mentioned above (Equation 2.4, 2.5, 2.7), the three thermoelectric parameters σ, α and κ are interrelated and all dependent for instance from the carrier concentration. Generally, the maximum electrical conductivity is achieved when the chemical potential lies in the conductive band (higher charge carrier concentrations), but Seebeck coefficient reaches a maximum when the chemical potential sits outside but close to the transport band. For thermal conductivity, the higher carrier concentration will lead to a higher thermal conductivity due to the heat being transferred by electrons. The strong interrelation of these three parameters imposes restrictions on maximizing *zT*. Precisely tuning the doping level to control the carrier concentration is one of the most efficient strategies to optimize power factor and *zT*, especially for traditional inorganic TE materials. Modelled from Bi_2Te_3, Figure 2.2 shows the compromise between large thermo-power and high electrical conductivity [8]. The *zT* value reaches a maximum at a carrier concentrations between 10^{19} and 10^{21} cm^{-3}, which is the concentrations found in heavily doped semiconductors [8].

Reducing κ, and in particular κ_l, is also a common method to achieve high *zT* values. Generally, hierarchical structures including atomic-scale defects, nanoscale precipitates, and grain boundaries make different wavelength phonons scatter and decrease the phonon mean free paths [9]. The ideal material can slow down phonon transport without

disrupting the crystallinity of the electron-transport region is named 'Phonon-glass electron-crystal'. It possesses electric properties of a good semiconductor single crystal but the thermal properties of an amorphous material [10].

It is notable that organic thermoelectrics have inherently low thermal conductivities (from 0.01 W m^{-1} K^{-1} to 2.0 W m^{-1} K^{-1}) compared to inorganic materials owing to their naturally weak van-der-Waals bonding and disordered microstructures. Therefore, the study of organic thermoelectrics only need to focus on achieving the trade-off between Seebeck coefficient and electrical conductivity. Unlike inorganic thermoelectric materials, electrical conductivity and Seebeck coefficient of organic counterparts are not always in strong correlation with each other due to their inhomogeneous and complex structural effects [8].

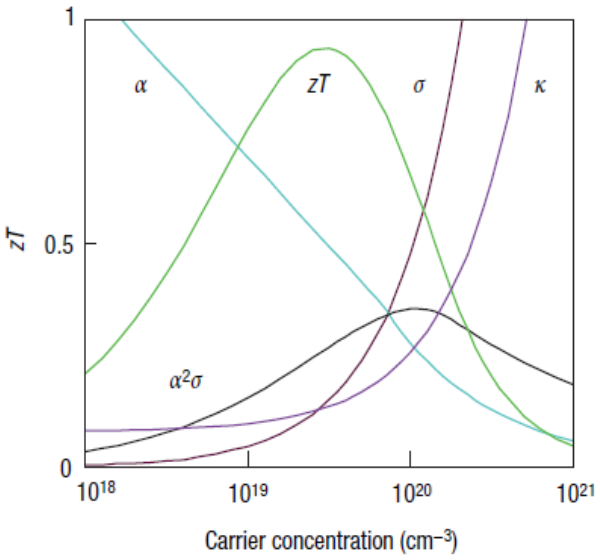

Figure 2.2 *Optimizing zT through carrier concentration tuning [8]. Maximizing the efficiency (ZT) of a TE involves a compromise of thermal conductivity (κ; plotted on the y axis from 0 to a top value of 10 W m^{-1} K^{-1}) and Seebeck coefficient (α; 0 to 500 μV K^{-1}) with electrical conductivity (σ; 0 to 5,000 $Ω^{-1}cm^{-1}$). Trends shown were modelled from Bi2Te3.*

2.2 Organic thermoelectric materials

Compared with inorganic thermoelectric materials, organic thermoelectric materials have attracted increased attention due to several intrinsic advantages. For example, organic thermoelectric materials are mainly based on earth-abundant elements, *i.e.*, carbon, hydrogen, and oxygen, ensuring the non-scarcity and non-toxicity of raw materials. Mature techniques for processing polymers exist, both via melting and solution, that are suitable for large scale and reduced costs production [5, 11]. Besides, the flexibility and light-weight properties of OTE materials are fit for new generation of flexible devices such as wearable electronics and soft-robotics [12-15]. Despite the relatively low *zT* values, at room temperature, state-of-the-art doped organic materials show TE properties approaching those of inorganic TE, as the benchmark of Bi_2Te_3 in Figure 2.3.

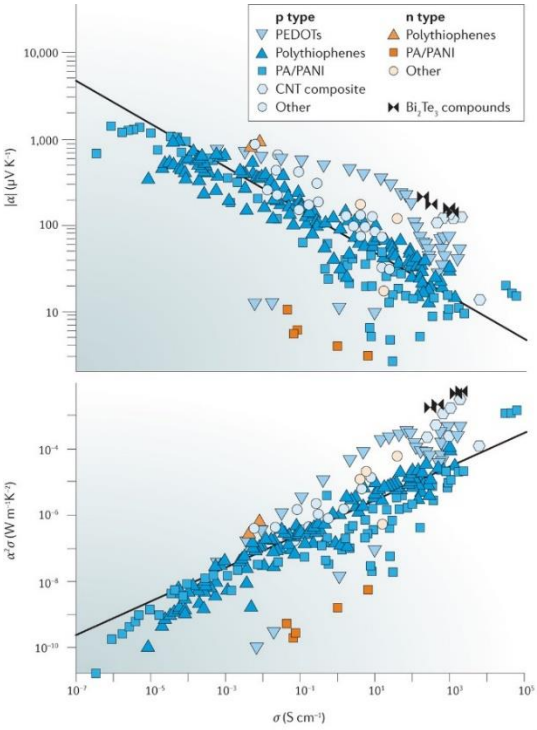

Figure 2.3 *The thermoelectric properties of OTE materials [16]. The thermoelectric properties of a wide range of OTE materials under room temperature follow the same empirical trend.*

2.2.1 Charge Transport in Organic Semiconductors

Different transport models have been developed to understand the thermoelectric properties of polymers. The earliest theory is based on the Boltzmann theory in organic crystal semiconductors proposed by L. Friedman [17], combining *ab initio* techniques (first-principles calculations [18, 19]). But most conducting polymers are heterogeneous systems, where crystalline domains, of various degree of perfections, coexist with amorphous domains, and charge carriers are localized by both energetic and spatial disorder. Therefore, hopping transport theories and Monte Carlo simulation were widely employed to describe the thermoelectric Seebeck effect of disordered organic semiconductors. Nearest neighbour hopping (NNH) is mostly used in lightly doped polymers, where the hopping rate is limited by spatial tunnelling distances due to carriers hopping to the nearest neighbour. Variable range hopping (VRH) is used in highly doped polymers, where the nearest available site has much high energy and the carrier has to hop to a distant site with a similar energy.

In lightly doped organic materials, charge carriers behave as NNH mechanism, the Seebeck coefficient will show a $1/T$ dependence with temperature, and electrical conductivity is proportional to e^{-E_A/k_BT}, where E_A is the activation energy. For conductive polymers with high carrier concentrations, the VRH performance of charge carriers emerges and the Seebeck coefficient will follow a $T^{1/2}$ dependence with temperature, and electrical conductivity will be proportional to $e^{-(T_0/T)^{\gamma}}$, where γ is 0.25 for 3-dimentional variable-range hopping and 0.5 for 1-dimentional variable-range hopping, and T_0 is the reference temperature [16, 20, 21]. The combination of the different transport models with various weighting in ordered and disordered regions are normally used to explain the electrical conductivity and Seebeck coefficient performance of the materials with heterogeneous phases.

2.2.2 Strategies to improve the performance of OTE

An α-σ coupling similar to inorganic thermoelectric materials, can also be prevalent in hopping transport of doped polymers. So, it is essential to control the charge carrier density of organic semiconductors by doping/dedoping techniques to maximise the power factor. Chemical or electrochemical methods are commonly used to fine tune the doping level in polymers. Besides, as mentioned above, there are strategies to decouple α and σ. For example, tuning the morphology of conductive polymers can reduce energy independent scattering so that electrical conductivity can increase without affecting the Seebeck coefficient. Addition of nanoparticles, like carbon nanoparticles (graphene, carbon nanotubes, etc.) or inorganic TE nanoparticles (Bi_2Te_3, SiGe, etc.) to form organic-inorganic hybrid materials is another approach that has been used (invoking the principle of energy filtering) to enhance Seebeck coefficient.

(1) Doping and dedoping

Doping is one of the most widely used methods for increasing the electrical conductivity of conductive polymers. Doping introduces electrons or holes into the polymer chains by a dopant, resulting in the formation of solitons, polarons and bi-polarons. Doping and dedoping can typically be obtained by either chemical or electrochemical methods.

The stability of electrically doped materials is vital and relies on the ionization energy for the addition of holes, and electron affinity for the addition of electrons. For introduction of holes, the ionization energy of the material, *i.e.*, HOMO, should be larger than ~ 5.0 eV [16] to form stable p-type TE materials. For example, the widely studied poly(3,4-ethylenedioxythiophene) (PEDOT) has an ionization energy of ~ 5.1

eV can be stably doped by a series of agents (*e.g.*, iodine, ferric trichloride, benzene sulfonic, camphor sulfonic acid, etc. [22]). For obtaining stable n-type TE materials, a great electron affinity (LUMO > 4 eV) is demanded to avoid oxidation reaction by the water or/and oxygen in environment [23]. However, the electron affinity of many organic materials is relatively small, which explains the difficulty in finding air-stable n-type OTE materials.

Besides, the size of the dopant can cause distortions of the polymer chains and affect the intermolecular charge transport between molecules. Moreover, large amounts of dopant can lead to phase segregation between the doped and the undoped part, reducing electrical conductivity [24, 25].

(2) Tuning molecular conformations

Conformation of polymer chains can heavily affect the semiconductor properties of conductive polymers. Various molecular-stacking structures, such as nanowires, nanorings, and nanosheets formed via the π–π interactions, can be beneficial to achieve a higher electrical conductivity, due to the highly oriented chain alignment, and a large Seebeck coefficient, due to the enhanced density of state near the conduction band edge [26, 27], while keeping a low thermal conductivity, due to the interface-phonon scattering.

(3) (Nano)composites

Addition of inorganic TE (nano)materials can combine the excellent TE performance of inorganic semiconductors with easy processability of polymers. For example, incorporating both n and p type Bi_2Te_3 ball milled powders into PEDOT:PSS, has been shown to hugely increase the power factor of the pure polymer [28]. In this organic-inorganic composite systems, only high-energy carriers can pass barriers, whilst low-

energy charge carriers will be filtered away by scattering (filtering effects). Although the charge carriers' concentration decreases the electrical conductivity, the asymmetry of mobile carriers around the Fermi energy increases, thus boosting the Seebeck coefficient, which can result in a significantly improved power factor.

Carbon nanotubes (CNTs) and graphene [29-32] are widely recognized as effective fillers to enhance the electrical conductivity of the polymer matrix due to their extremely high charge transport over long lengths. The addition of nanofillers can also modify the molecular conformations, with a beneficial effect on TE properties. Thus even the insulating graphene oxide can increase carrier mobility of conductive by inducing a more ordered structure, which leads to a higher electrical conductivity and higher Seebeck coefficient [33]. The layer-by-layer (LbL) assembling techniques to achieve highly ordered multilayer structures has shown very promising results [34-36]. LbL will be discussed in more details in **Section 2.2.5**.

(4) Others

Xavier Crispin's research group [37-40] investigated the role of ions on the thermoelectric effect and found large increases (up to several hundreds of $\mu V\ K^{-1}$) in the thermo-induced voltage at high humidity levels. The ionic effect increases the Seebeck and conductivity substantially, leading to a 2 to 4 orders of magnitude increase in PF (Figure 2.4). Although ionic Seebeck coefficient and conductivity is temporary [37], they are still useful. For example, combining ionic TE materials with supercapacitors, the ionic TE material can convert and store thousands of times higher energy than normal TE materials [39]. Utilising the ionic TE material for gating low-voltage organic transistors, the amplification is thousands of times higher than the traditional single leg TE [40].

Kar-Narayan's research group [41] reported a compositionally graded TE material in order to optimize the PF of various TE materials under different working temperature range. This compositionally graded film was connected by a 15 wt.% Bi_2Te_3/ Poly(3,4-ethylene dioxythiophene): polystyrenesulfonic acid (PEDOT:PSS) composite film and a PEDOT:PSS film in series, whose length was systematically tuned to optimize the PF along the applied temperature gradient. The optimized film exhibited a power output value (13 nW) higher than either the single 15 wt% Bi_2Te_3/PEDOT:PSS film (6.5 nW) or the PEDOT:PSS film (7.5 nW), under the same temperature gradient (70 °C) and external load resistance (50 Ω).

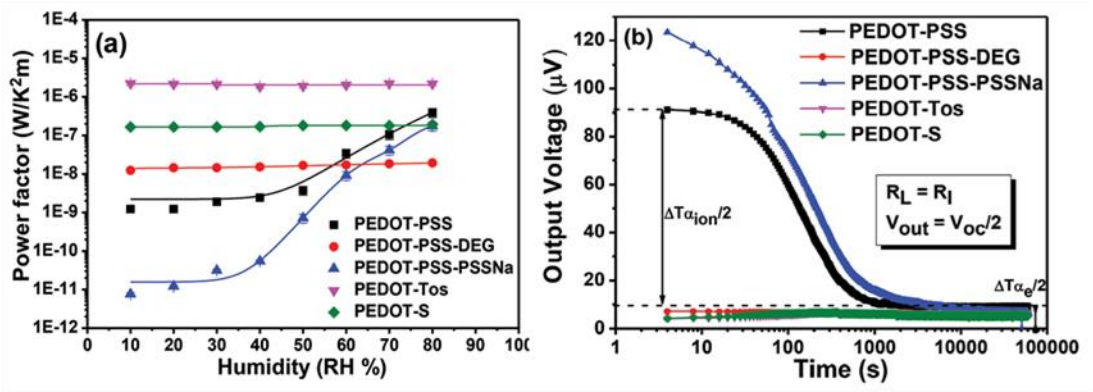

Figure 2.4 *The ionic-Seebeck effect of PEDOT derivatives [37]. (a) Power factor for PEDOT derivatives at different humidities and their (b) output voltage at 80% relative humidity. It shows the voltage generated by ionic-Seebeck effect fades with time.*

2.2.3 P-type conjugated polymers example: PEDOT:PSS

Among organic materials, the broad variety of p-conjugated polymers sparked interest as potential candidates for TE applications. The most studied conjugated polymers are polypyrrole (PPY), polyaniline (PANi), PEDOT, and their derivatives [42]. Amongst them, the derivatives of PEDOT and poly(3-hexylthiophene) (P3HT) exhibit remarkable TE performances for room temperature applications. PEDOT:PSS (Figure 2.5) is one of the most studied OTE materials and will be discussed in more detail below.

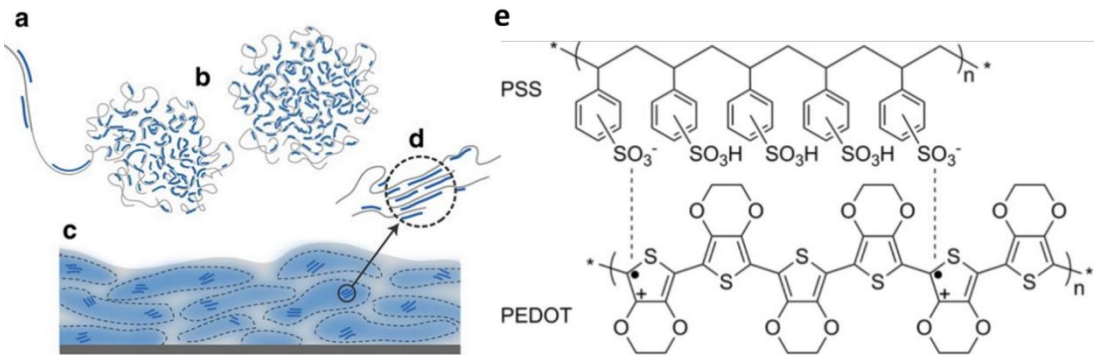

Figure 2.5 *Microstructure and chemical structure of PEDOT:PSS. Schematic microstructures of (a) PEDOT synthesised on PSS template, (b) colloidal gel particles in dispersion, (c) PEDOT:PSS-rich (blue) and PSS-rich (grey) phases in film, and (d) aggregates/crystallites parts in film [43]. (e) The chemical structure of PEDOT:PSS.*

PEDOT is normally (electro-) chemically polymerized from its monomer, ethylenedioxythiophene (EDOT), by oxidative polymerization. The counterion, polystyrenesulfonic (PSS), offers charge-balancing and colloidal dispersability in water to the hydrophobic PEDOT chains. Therefore PEDOT:PSS films can be easily formed via solution processing processed like coating, solution casting, spraying and printing. Commercialized PEDOT:PSS aqueous dispersions normally present excess of poly(4-stynesulfonic acid) (PSSH) to form stable water suspensions (*e.g.,* the weight ratio of PEDOT:PSS is 1:2.5 for Clevios® PH1000). The excess of insulating PSS-rich chains and the reduced chain alignments due to the hydrophilic mismatch between PEDOT and PSS, contribute to the inferior electrical conductivity in many commercial PEDOT:PSS grades. Tremendous efforts have been made to improve the electrical conductivity via removing the excess PSS and aligning the polymer chains to enhance the charge carrier transport.

Post-treatment has been proved as one of the most convenient and effective methods to increase electrical conductivity by several orders of magnitude, including organic polar solvent treatments, acids treatments, small molecules vapour treatments, and

electrochemical treatments. In the aqueous dispersion, phase segregated PEDOT phases are surrounded by a 'shell' of insulating PSS. In presence of organic polar solvents, PEDOT and PSS are separated by stronger electrostatic interactions, leading to a higher degree of π–π stacking of PEDOT [44], and, in turn, to a change in polymer chains conformant from coiled to linear. Solvent treatments can then improve the charge carrier transport mobility (from 0.045 to 1.7 $cm^2 V^{-1} s^{-1}$), the electrical conductivity and the Seebeck coefficient. For instance, the addition of dimethyl sulfoxide (DMSO) or ethylene glycol (EG) into PEDOT:PSS aqueous dispersion [45], increased the electrical conductivities of spin-coated PEDOT:PSS films from 0.2 to ~ 900 S cm^{-1}, without affecting the Seebeck coefficients constant at 13-15 μV K^{-1}. As a result, DMSO- and EG-doped PEDOT:PSS films achieved the PF of ~ 30 and ~ 25 μW $m^{-1} K^{-2}$, respectively. The highest *zT* value of 0.42 obtained in PEDOT:PSS has been reported by Kim *et al.* [46]. EG was again used to post-treat the PEDOT:PSS films to dissolve excess of insulating PSS from the films. And it is worth to mention that the remove of the PSS also accomplished with a better water-stability of the film.

Strong acid treatment of as-cast PEDOT:PSS films can increase the amount of PSSH combined by the H^+ from the acids and the PSS^-, facilitating the removal of insulating PSSH from films in aqueous solution. This resulted in a highly crystalline PEDOT:PSS structure, which increased the film conductivity by three orders of magnitude. For example, Kim *et al.* [47] reported a very high electrical conductivity of 4380 S cm^{-1} for PEDOT:PSS treated by H_2SO_4. However, the Seebeck coefficient slightly decreased after the acid treatment [48]. Fan *et al.* [49] utilized a sequential post-treatment with H_2SO_4, to improve electrical conductivity, and subsequent NaOH, to adjust the oxidation level of the PEDOT segments for Seebeck coefficient enhancement. The best properties reported for such sequential post-treatment of

PEDOT:PSS films are a Seebeck coefficient of 39.2 μV K^{-1}, an electrical conductivity of 2170 S cm^{-1} , and the corresponding power factor is 334 μW (m^{-1} K^{-2}), at room temperature.

Despite the huge progress in achieving very high electrical conductivity, the main bottleneck for further raising the power factor is now the Seebeck coefficient of pristine PEDOT:PSS (~15 μV K^{-1}). Electrochemical treatments have been reported that can boost the Seebeck coefficient by controlling the oxidation level of PEDOT:PSS [50, 51]. With the decrease of oxygen level, the electrical conductivity decreases gradually while the Seebeck coefficient increases significantly. Bubnova *et al.* [50] set up the PEDOT:PSS film as the gate electrode of an electrochemical transistor, and changed the electrode potential to control the oxidation level. The highest PF of 23.5 μW $m^{-1}K^{-2}$ was achieved at the oxidation level of PEDOT:PSS is 14.5 %. Park *et al.* [51] used a highly conductive solution casted PEDOT film with addition of a polymeric surfactant as the electrode for finely tune the oxidation level electrochemically. A maximum PF of 1,270 μW m^{-1} K^{-2} was obtained when the oxidation level was 24.1% (electrical conductivity: 1355 S cm^{-1}, Seebeck coefficient: ~100 μV K^{-1}).

It is worth to mention that the incorporation of inorganic or/and carbon nanomaterials into PEDOT:PSS has also shown potential in optimizing their power factors (refer to **Section 2.2.5**).

2.2.4 N-type coordination materials example: poly(M-ett)

The n-type OTE has fallen behind the considerable progress in p-type polymers and their composites owing to difficulties in n-type doping of organic semiconductors. N-type thermoelectricity has been studied in variety organic materials. The copolymers

of naphthalene diimide and bithiophene unit [52] or bithiazole unit [53], and benzodifurandione-phenylenevinylene [24] derivatives are the most studied n-type conjugated polymers. The biggest obstacle for these materials is their low electrical conductivities (normally 4×10^{-3} to 48 S cm^{-1} [54]). Tetrathiafulvalene–tetracyanoquinodimethane is the most reported crystalline organic OTE material, which possesses relatively high electrical conductivity (500 S cm^{-1}) [55], but it is hard to process. New generations of small molecular organic semiconductors, such as polydopamine, perylene diimides, dinaphtho[2,3-*b* :2′,3′-f]thieno[3,2-*b*]thiophene, thiophene-diketopyrrolopyrrole-based quinoidal molecules and C_{60} can show very large Seebeck coefficients (> 100 mV K^{-1}), although their electrical conductivity is still lower than 10^{-3} S cm^{-1}[56]. Besides, most of them require careful doping strategies but are easily dedoped in air over time.

Metal-organic polymers show a relatively high electrical conductivity, stability in ambient conditions and facility for syntheses. Poly(metal-1,1,2,2-ethenetetrathiolate), (poly(M-ett), consisting of the ethenetetrathiolate ligand coordinated to the metal centre with counter ions, were first investigated as OTE materials by Zhu's group in 2012 [57]. Poly(Ni-ett), with nickel as the coordination metal, exhibits exciting air-stable record-breaking n-type OTE performance. Its electrical conductivity and negative Seebeck coefficient reach 44 S cm^{-1} and -122 μV K^{-1} at room temperature, respectively, resulting in a peak power factor of 66 μW m^{-1} K^{-2}. It is worth noting that poly(M-ett) can show both p-type and n-type behaviour depending on the metal centre. Poly(Cu-ett), for instance, displays a positive Seebeck coefficient. Poly(Ni-ett) films prepared by electrochemical deposition [58] can present an improved structure ordering, resulting in a four to six times increases in electrical conductivity (400 S cm^{-}

[1]), compared with the amorphous powder samples, a similar Seebeck coefficient (-128 μV K^{-1}) and a maximum power factor of 453 μW m^{-1} K^{-2} at room temperature.

Additionally, the thermoelectrical property of Poly(M-ett) is tunable with the multiple oxidation state through changing the air exposure time during the synthesis. Menon *et al.* [59] reported poly(Ni-ett)-based composite film with the electrical conductivity decreasing from 43 to 5 S cm^{-1} and Seebeck coefficient improving from 27 to 33 μV K^{-1} by changing the air exposure time during the synthesis from 30 minutes to 24 hours. Sheng *et al.* [60] optimised the TE properties of Poly(Cu-ett) by using chemical oxidation and reduction, obtaining a highest power factor at room temperature of 4.17 μW m^{-1} K^{-2}, with the corresponding electrical conductivity and Seebeck coefficient of 10.7 S cm^{-1}, and 62.5 μV K^{-1} respectively.

The insoluble nature of the Poly(M-ett) limits traditional solution-based techniques. The addition of an insulating polymer matrix (*e.g.* polyvinylidene fluoride, PVDF) is normally used to allow solution processability. Jiao *et al.* [61] reported that both n- and p-type poly(M-ett) ball-milled with PVDF in DMSO are able to be inkjet-printed on PET substrate uniformly for a flexible TE device. However, the TE performance of these composite films are inferior due to the presence of insulating PVDF. The best power factors achieved for the n-type poly[K_x(Ni-ett)]/PVDF and p-type poly[Cu_x(Cu-ett)]/PVDF composite film are 0.15 μW m^{-1} K^{-2} and 0.12 μW m^{-1} K^{-2}, respectively, at 300 K. Later, Yee's group [62, 63] systematically studied the reaction conditions of Poly(M-ett) for optimizing the TE performance. The amount of nickel, varying from Poly($Ni_{0.5}$-ett), Poly($Ni_{0.75}$-ett), Poly($Ni_{1.0}$-ett) to Poly($Ni_{2.0}$-ett), affects both the electrical conductivity and Seebeck coefficient. Because the excess nickel not only acts as a counterion with alkali metals, but also as impurities in the final composites. With sub-stoichiometric nickel equivalents of 0.75, the produced Na($Ni_{0.75}$-ett)/PVDF

provides a high electrical conductivity of ~ 50 S cm^{-1} and thus a power factor enhancement of up to 23 μW $m^{-1}K^{-2}$ at room temperature [62]. They also reported that annealing at 160 ^{o}C can simultaneously enhance the electrical conductivity and Seebeck coefficient of Poly(M-ett)/PVDF composite films, resulting a highest power factor of 23.5 μW m^{-1} K^{-2} [63]. They believe that annealing can remove residual solvent and impurities (*i.e.*, water and carbonyl sulphide) from the films, and densify the film to improve chain packing.

2.2.5 TE polymer nanocomposites

Conductive polymer nanocomposites have been largely explored as thermoelectric materials. Combining (conductive) polymers with inorganic particles (*e.g.* p- and n-type Bi_2Te_3 [64]) or carbon nanomaterials [65, 66] are the two most common and efficient strategies. Among carbon nanomaterials, carbon nanotubes (CNTs) have attracted the most attention, being a 'one-dimensional material' [26]. Specifically, the power factor of CNTs can be dramatically increased by enhancing the mobility along the tube direction. Meanwhile the thermal conductivity can be decreased by lowering the diameters. Theoretically, the Seebeck coefficient of semiconducting single wall CNTs can reach a value larger than 2000 μV K^{-1} at room temperature as the tube diameter decreases to 0.6 nm [67] (Figure 2.6). When combined with a polymer matrix, their intrinsically high electrical conductivity can be retained, while reducing their high thermal conductivity due to the presence of the polymer. Besides, with the development of the new technique for fabricating self-standing CNT films in a large scale, CNT films and their derived CNT yarns can be directly utilised as TE materials.

In this section, we will focus specifically on CNTs and polymer nanocomposites based on CNT as thermoelectric materials.

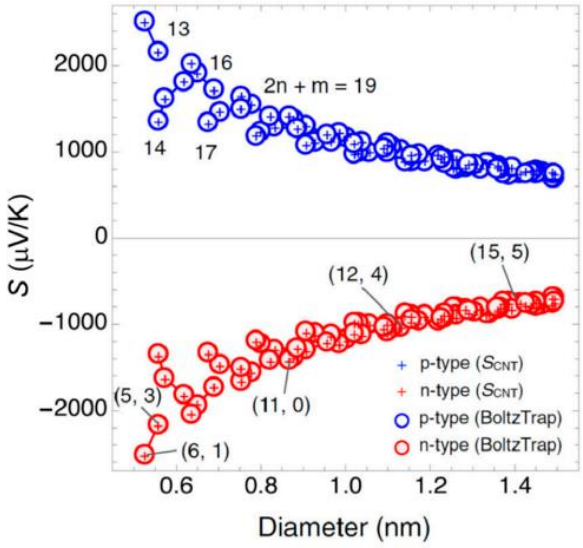

Figure 2.6 *Optimum Seebeck coefficient of the semiconducting single wall CNTs within the diameter range of 0.5-1.5 nm at 300 K [67].*

CNTs films can be seen as a typical p-type thermoelectric material in ambient conditions, with a positive Seebeck coefficient in the range of 20- 60 μV K^{-1}. CNTs are liable to be doped by oxidative dopants, such as oxygen, acids, and chemical oxidants. Annealing, acid wash and ultraviolet/ozone treatment [68] are widely used for enhancing the TE property. High doping level leads to an increase in electrical conductivity but a decrease in Seebeck coefficient. The highest reported positive Seebeck coefficient for CNT films was ~ 350 μV K^{-1} at 670 K after 20 s Ar-plasma treatment, which unfortunately decreased the electrical conductivity from 3500-4800 to 330-990 S m^{-1} [69].

CNTs films can also be converted into an n-type thermoelectric material by oxygen and water desorption. For example [70], semiconducting single-walled CNTs films show a Seebeck coefficient changing from 125 μV K^{-1}, at ambient conditions, to -133 μV K^{-1}, after gas desorption at room temperature. An ammonia plasma treatment at 110 °C also induce CNTs films to show a negative Seebeck coefficient (-80 μV K^{-1})

in air. Other typical n-dopants for CNTs are electron donating compounds such as $NaBH_4$, hydrazine, and poly(ethyleneimine) (PEI) [71]. For example, CNT can go from 22 μV K^{-1} to -24 μV K^{-1} after immersion in $NaBH_4$ solution for 48 h [72]. Although it is noted that the $NaBH_4$ reduction is not stable under air exposure. The amine-rich PEI, more air-stable, physically adsorbs onto CNTs and donates electrons to the nanotubes. After functionalisation with PEI, single wall carbon nanotube (SWCNT) shows a large and stable n-type Seebeck coefficient of -58 μV K^{-1} in air [73]. With the help of sodium dodecylbenzenesulfonate for a better CNT dispersion, PEI can more effective dope SWCNT, reaching a higher (in absolute value) Seebeck coefficient (-100 μV K^{-1}) [74]. By utilising vacuum filtrated CNT film, a compact-configuration flexible TE module has been fabricated by Zhou *et al.* [71]. As Figure 2.7 shows, PEI has been used to n-type dope the CNT film alternatively before folding. The so formed TE module can generate a remarkable thermopower of 410 μV K^{-1} and exhibits a maximum power output 2.51 μW at ΔT ~ 27.5 K.

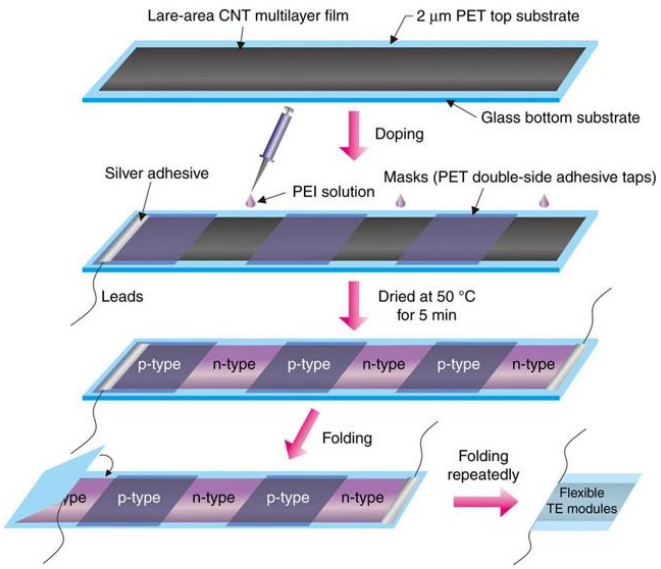

Figure 2.7 *Schematics of the fabrication process for a flexible CNT-based TE module [71]. The novel configuration, compact and efficient flexible TE module based on the large-area continuously synthesized CNT films and localized doping technology.*

Table 2.1 *The summary of the representative CNT- based nanocomposites and their thermoelectric properties.*

Composites	**κ (W m^{-1} K^{-1})**	**σ (S cm^{-1})**	**α (μV K^{-1})**	**PF (μW m^{-1} K^{-2})**	**Ref-erence**
PANI coated on a CNT network	~ 0.5	60	28	4.7	[31]
CNTs/PEDOT:PSS with vinyl acetate ethylene copolymer	~ 0.3	400	25	25	[65]
CNTs/PEDOT:PSS		4000	20	140	[75]
PEDOT:PSS and meso-tetra(4-carboxyphenyl) porphine stabilized MWCNT	~ 0.12	95	40	15	[76]
PEDOT:PSS and meso-tetra(4-carboxyphenyl) porphine stabilized DWNT	~ 0.12	960	70	470	[76]
SWCNTs/ P3HT doped by $FeCl_3$		1000	29	95	[77]
MWCNT/PPy composites		72	9	2.0	[78]
PANi/SWCNTs		125	40	20	[30]
In-situ polymerization PANi on SWCNT film		32	45	6.5	[79]
PANi/ SWCNTs		769	65	176	[81]
SWCNTs/PANI WITH m-cresol solvent		1440	40	217	[82]
PANI/graphene/PANI/DWCNT 40 quad-layered composite film		1080	130	1825	[84]
80-bilayer DWCNT-PEI/graphene-PVP composites		300	−80	-190	[35]
PEO/DWCNT-PAA 25 bi-layered composites		19.6	60	7.1	[85]

Conducting polymers such as PANi, PEDOT and their derivatives composites with CNTs have also been studied (Table 2.1). Polymer (nano)composites offer a new route to decouple the interrelated parameters. The most directly benefit is that the polymer matrix can reduce the thermal conductivity of CNTs. For example, Chuizhou *et al.* [31] reported an *in-situ* chemically polymerised PANI layer, uniformly coated on a freestanding CNT network containing randomly entangled individual CNTs and CNT

bundles. The thermal conductivity of the 20 wt. % PANI/ CNT composites dropped to ~ 0. 5 W m^{-1} K^{-1} close to that of PANI (~ 0.45 W m^{-1} K^{-1}) with the electrical conductivity of 60 S cm^{-1} and the Seebeck coefficient of 28 μV K^{-1}. Kim *et al.* [65] reported a segregated network composites of CNTs/PEDOT:PSS with vinyl acetate ethylene copolymer. The dissimilar bonding and vibrational spectra between CNT and PEDOT:PSS along with the segregation by vinyl acetate ethylene copolymer, reduced the thermal conductivity of the composites to 0.3 W m^{-1} K^{-1}. The interconnected network morphology (colloidal PEDOT:PSS particles bridging CNT-CNT junctions) guaranteed an electrical conductivity as high as 400 S cm^{-1} with 35 wt.% SWCNTs. Moriarty *et al.* [75] reported SWCNT/PEDOT:PSS nanocomposites, prepared by liquid-phase exfoliation, demonstrating an effective decouple between electrical conductivity and Seebeck coefficient. The formed barriers at the SWCNTs/PEDOT:PSS interface preferentially hindered the transport of low-energy charge carriers, and only allowed high-energy carriers to pass across the tube junctions, so to increase the mean carrier energy. This SWCNT/PEDOT:PSS showed an increase in electrical conductivity from 500 S cm^{-1} to 4000 S cm^{-1}, with the SWCNTs content increasing from 20 to 95 wt. %, while the Seebeck coefficient remained relatively unaltered at around 20 μV K^{-1}, resulting in a power factor as high as 140 μW m^{-1} K^{-2}. Similar works by using multi-wall carbon nanotube (MWCNT) and double wall carbon nanotube (DWCNT) [76], PEDOT:PSS and additional meso-tetra(4-carboxyphenyl) porphine also observed a decoupling between Seebeck coefficient, electrical conductivity and thermal conductivity. The electrical conductivity of these organic composites increased to approximately 95 S cm^{-1}, in the case of MWCNTs, and 960 S cm^{-1}, in the case of DWCNTs, as the concentrations of both the CNTs and PEDOT:PSS were increased. The Seebeck coefficient (~ 40 μV K^{-1} for MWCNTs and

70 μV K^{-1} for DWCNTs) and thermal conductivity (~ 0.12 W m^{-1} K^{-1}), however, remained relatively unaffected by the increase in concentration.

Furthermore, the π–π interactions between CNTs and polymers can affect the polymer structural morphology. For example, SWCNTs increased the crystallinity of P3HT resulting in an increase of electrical conductivity from 1.7×10^{-5} S cm^{-1} to 275 S cm^{-1} without doping. Doped by $FeCl_3$, the power factor of the composites reaches to 95 ± 12 μW m^{-1} K^{-2}, for filler content of 41-81 wt%[77]. Benefiting from the high electrical conductivity of CNTs and more ordered crystalline alignment of PPy, MWCNT/PPy composites reached an electrical conductivity of 72 S cm^{-1} at a MWCNT loading of 15 wt%, which is much higher than that of a pure PPy control sample (2.2 S cm^{-1}) [78] .

In-situ polymerization of polymers on CNTs template is an efficient method to grow polymers in an ordered manner on the surface of the CNTs. The π–π interaction between CNT and polymer can positively influence the alignment of polymers, wrapped on CNTs. This hybrid structure can increase the effective carrier delocalisation, and thus enhance the carrier mobility in conjugated polymers. By using SWCNTs as the polymerisation template, Qin *et al.* [30] reported that the electrical conductivity and Seebeck coefficient of PANi/SWCNTs composites reached 125 S cm^{-1} and 40 μV K^{-1}, respectively, and the maximum power factor was up to 20 μW m^{-1} K^{-2}, more than 2 orders of magnitude higher than pure polyaniline. A year later, Jilei *et al.* [79] used electrochemical method for *in-situ* polymerization PANi on SWCNT film, reporting electrical conductivity, Seebeck coefficient and maximum power factor of 32 S cm^{-1}, 45 μV K^{-1} and 6.5 μW m^{-1} K^{-2}, respectively. In addition to the π–π interactions between SWCNTs and PANI, Qin *et al.* [80, 81] found that tuning the molecular chain arrangement of PANI from a compacted coil to an

expanded coil, by using *m*-cresol (Figure 2.8), can further increase its power factor. The electrical conductivity of PANi/ SWCNTs has been highly increased to 769 S cm^{-1} thus obtaining a maximum power factor of 176 μW m^{-1} K^{-2}. Combining both *in-situ* polymerization with the m-cresol solvent processing, the power factor of the SWCNTs/PANI composite films reached a power factor of 217 μW m^{-1} K^{-2} at room temperature [82].

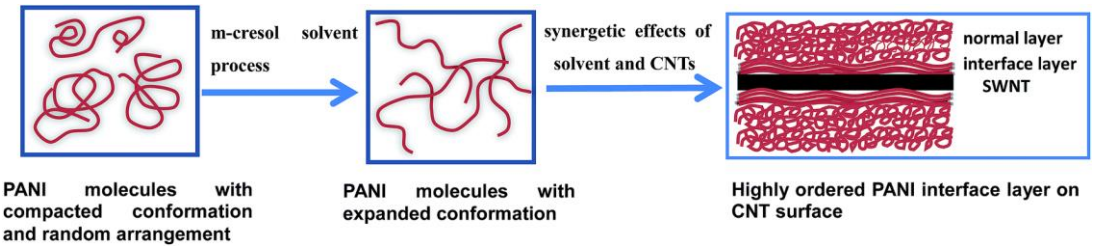

Figure 2.8 *Schematic representations of the formation of an ordered PANI interface layer. It is induced by the synergistic effects of the solvent process and the π–π conjugation between PANI and CNTs [81].*

Novel researches on layer-by-layer deposition polymer on CNTs have recently shown the ability to easily adjust nanotube distance, density, and film thickness [83], which alters the Seebeck coefficient. Besides, the layered structure seemed to improve carrier mobility, increasing both electrical conductivity and Seebeck coefficient. Cho *et al.* [84] reported a 40 PANI/graphene/PANI/DWCNT quad-layered composite film prepared by LbL assembly (Figure 2.9), exhibiting an electrical conductivity of 1080 S cm^{-1} and a Seebeck coefficient of 130 μV K^{-1}, resulting in a remarkable power factor of 1825 μW m^{-1} K^{-2}. The authors pointed to the continuous 3D PANI-wrapped DWCNTs and connected graphene network as the reason for the exceptional performance. By alternately LbL depositing DWCNTs, stabilized by PEI, and graphene stabilized by polyvinylpyrrolidone (PVP), they also reported a high power factor n-type 80-bilayer DWCNT-PEI/graphene-PVP composites film. [35] In

addition to its remarkable power factor of -190 μW m^{-1} K^{-2} at room temperature, the highly ordered graphene layers also offered barrier the gas diffusion, resulting in a relatively air-stable n-type composite film.

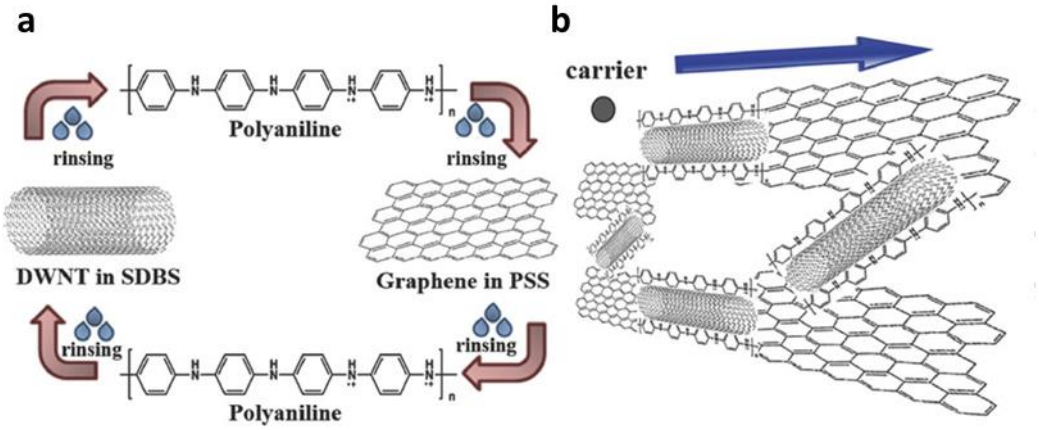

Figure 2.9 *Schematic representations of the layer-by-layer assembly of PANI/graphene/PANI/DWCNT multilayers. (a) The fabrication procedure and (b) carrier transport in the multilayers [84].*

Besides, the mixture of CNTs with polymers can bring some stretchablity to the as-fabricated composites. For example, Cho and Son [85] fabricated a stretchable OTE multilayer film by alternately depositing 0.1 wt% polyethylene oxide (PEO) and 0.03 wt% DWCNT, dispersed with 0.1 wt% polyacrylic acid (PAA). Because of the weak bond strength and high chain mobility between PEO and PAA layers, the PEO/DWCNT-PAA multi-layered composites exhibit a crack-free surface up to 30% strain and retain their thermoelectric performance 90% of unstretched sample. The resultant 25 bi-layered composite film (~ 500 nm thick) displayed an electrical conductivity of 19.6 S cm^{-1}, a Seebeck coefficient of 60 μV K^{-1} and attributed to the three-dimensional conjugated network of DWCNT.

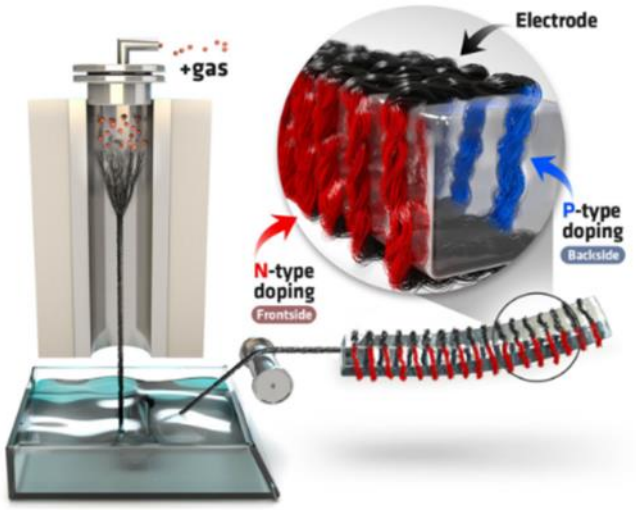

Figure 2.10 *Schematic illustration of flexible thermoelectric generator based on CNT yarn [86].*

Interestingly, the random and unsorted CNT veils produced by floating catalyst chemical vapour deposition (FCCVD) can obtain Seebeck coefficients greater than 60 μV K^{-1}, reaching even 100 μV K^{-1} or higher [87]. The same can be easily tuned to n-type, with Seebeck coefficient of around -80 μV K^{-1} [32], by chemical doping methods previously mentioned. Owing to an electrical conductivity normally exceeding 1000 S cm^{-1} [71], an ultrahigh power factor of 2482 μW m^{-1} K^{-2} and 1570 μW m^{-1} K^{-2} at room temperature has been observed for both single-wall and multi-wall CNT tapes by Weibin *et al*. [71, 88] and An *et al.* [89, 90]. The significantly longer CNTs produced by FCCVD, compared with the typical solution-processed (*e.g.* sonication) CNTs, can explain the excellent TE performance. These CNT veils open the possibility of fabricating flexible TE devices with high TE performance, comparable to inorganic TE devices. For example, Choi *et al.* [86] presented an all flexible thermoelectric generator (TEG) based on CNT yarns prepared by FCCVD technique as Figure 2.10 shown. A TE generator formed by 60 pairs of n- and p-doped

CNT yarns exhibited the maximum power density of 10.85 and 697 μW g^{-1} at temperature difference of 5 and 40 K, respectively.

2.2.6 Stretchable OTE materials

In addition to improving the TE performance, the mechanical property (*i.e.* large deformation to break) of the new generation OTE materials has attracted particular attention. Especially for the wearable device application, stretchability is important, for instance, to conform different shapes (like the human skin) and endure various human motions. Although stretchable OTE films have been claimed in a lot of papers (Table 2.2), most of their stretchabilities are still relatively small. For example, Liang *et al.* [91] reported a 'stretchable' polypyrrole (PPy) /SWCNT composite film that can maintain a power factor of ~19 μW m^{-1} K^{-2} under a strain level of 2.6%, produced by *in-situ* polymerization of the PPy on SWCNTs. Its small stretchability (strain at break is 3.2%) was ascribed to strong interfacial interactions between PPy and SWCNT, their surface wrapping morphology, and the effective stress transferring in films. Xiao *et al.* [92] fabricated a structural composites which is a 'lychee-like' hydroxyl-functionalized polystyrene (PS) core (Figure 2.11) wrapped by SWCNTs and water-dispersible polyurethane segregated networks. The composite film could withstand the mechanical stress of 6 MPa up to 3.8% strain.

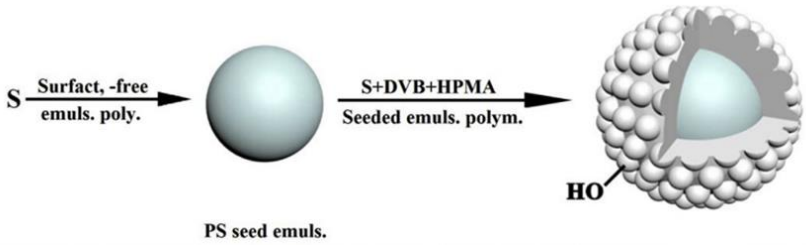

Figure 2.11 *The preparation procedure of the lychee-like hydroxyl-functionalized PS core [92].*

Here, stretchable TE material is defined as: a material can withstand a strain higher than 30% strain with a stable TE properties. Under this definition, the stretchable OTE materials can be divided into the following 3 categories by the fabrication method.

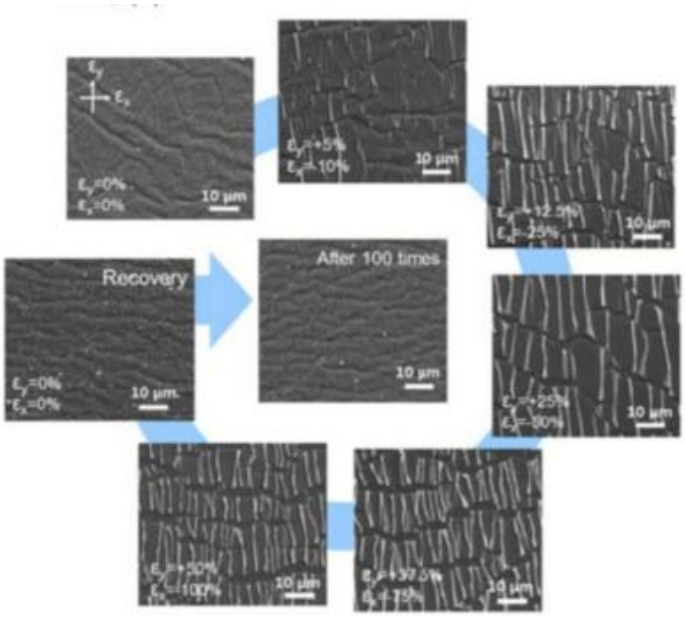

Figure 2.12 *SEM images of WS_2 film under various elongations and after 100 cycles [93].*

Coating the OTE materials on a stretchable substrate is an efficient technique to achieve stretchability. For example, Oh *et al.* [93] transferred a chemically exfoliated transition metal dichalcogenide nanosheet filtered film on a PDMS substrate. The sample showed a stable TE performance after 100 stretching cycles, at 50% strain, owing to the wrinkles on the nanocomposite film (Figure 2.12) and the nanosheets acting as a lubricant to release the strain by slippage. But it worth to note that during the strain, the electrical resistance increased with strain, leading to the power output reduction of 2 orders of magnitude, at 50% strain. Coating into periodic wrinkles/buckles or patterning into wavy lines, such as depositing a thin film of OTE materials on a pre-strained elastomeric substrate, can extend the TE performance to larger strains. As shown in Figure 2.13, samples of metal dichalcogenide

nanosheet/SWCNT nanocomposites film on a 0-30% pre-strained PDMS, exhibited stable thermoelectric properties up to the pre-strained value (0-30%), but decreased rapidly for strains exceeding the pre-strain range [94].

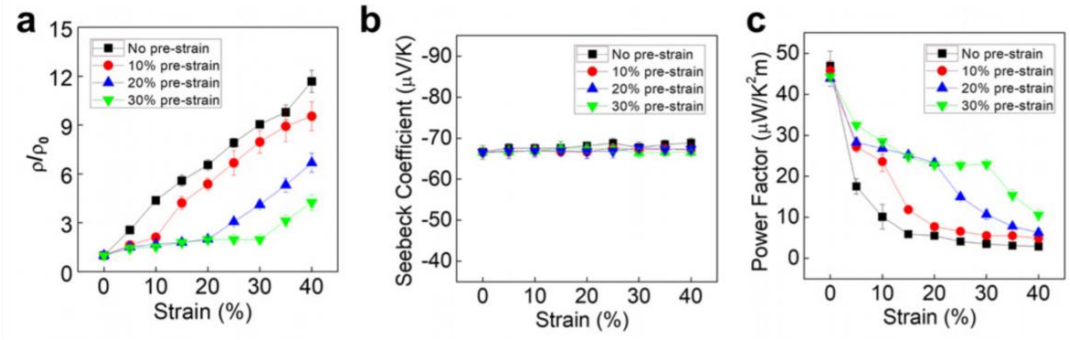

Figure 2.13 *Thermoelectrical properties of the wrinkled nanocomposite films under tensile strain [94]. (a) Resistivity, (b) Seebeck coefficient, and (c) power factor of the wrinkled nanocomposite films as a function of the tensile strain.*

Table 2.2 *The summary of recent reported stretchable thermoelectric materials.*

Materials	**Stretch-ability**	**σ (S cm^{-1})**	**α (μV K^{-1})**	**PF (μW m^{-1} K^{-2})**	**Ref-erence**
PPy/SWCNT composite	2.60%	400	24	~19	[91]
PS core wrapped by SWCNTs	3.80%	110	24	6.28	[92]
WS_2 nanofilm on PDMS	50%	12	-70	5~7	[93]
$NbSe_2$ nanofilm on PDMS	50%	160	13	26~34	[93]
WS_2/SWCNT on pre-strained PDMS	30%	105	-67	471	[94]
PEDOT:PSS/ WPU with ionic liquids	600%	140	22	6.7	[97]
PEDOT:PSS/ionic liquids	70%	538	35	66	[98]
PEDOT:PSS/Zonyl	50%	393	18	1.2	[99]
PEDOT:PSS/PU	250%	79	16	2	[144]

There are few studies of embedding conductive fillers into elastomers to achieve high stretchability combined with TE properties, such as PEDOT:PSS mixture with PDMS [95] or polyurethane (PU) [96]. One example is blending a water-borne PU (WPU)

with PEDOT:PSS with the introduction of ionic liquid. The as-casted free-standing elastomeric composite showed a strain at break of 600% [97]. The excellent stretchability was not only induced by the WPU, but also the ionic liquids, showing a 46-times larger elongation at break and a 35-times lower elastic modulus, compared with PEDOT:PSS. At 60% strain, the electrical conductivity reduced to half of the original conductivity (140 S cm^{-1}), but the Seebeck coefficient remained at around 22 μV K^{-1} until 100%.

The effect of ionic liquids on mechanical and TE properties of PEDOT:PSS has been reported earlier by Kee *et al.* [98]. They found the ionic liquids (1-Ethyl-3-methylimidazolium 4,5-dicyanoimidazolate) induced PEDOT:PSS morphological transition from the amorphous structure into crystalline nanofibers surrounded with ionic liquids-assisted soft domains. This results in an outstanding mechanical deformability and fatigue resistance. Samples of PEDOT:PSS/ionic liquids coated on PDMS could go up to 70% quasi-static tensile strain or cycling strains of up to 30%, without a severe degradation in TE performance. An additional benefit of using the ionic liquids is to simultaneously enhance the Seebeck coefficient (from 15 to 35 μV K^{-1}) and electrical conductivity (from 3 to 538 S cm^{-1}) of PEDOT:PSS by controlling its oxidation level and nanostructure. This effect has also been reported with different surfactants. The fluorosurfactant, Zonyl, changed PEDOT:PSS morphology into an elongated lamellar structure so to enhance electron mobility, and increases the stretchability of the PEDOT:PSS as well. Spin-coating the treated PEDOT:PSS films onto 5% pre-stretched PDMS substrates, the sample retained TE performance ($\sigma \sim$ 393S cm^{-1}, $\alpha \sim 18$ μV K^{-1}) enduring up to a 60% static strain and over several hundred cycles of 50% max strain [99]. Owning to the polymeric surfactant (Triton X-100), a ternary composite film based on PEDOT:PSS was fabricated by Kee *et al.* [100],

which exhibited a viscoelastic behaviour up to 35% tensile strain, without degradation in electrical conductivity or Seebeck coefficient. Moreover, Triton X-100 also acts as a healing agent so that after being cut completely, the composite films autonomously recover their thermoelectric properties in around one second.

2.3 Organic thermoelectric device

Thermoelectric generators convert a thermal gradient across the generator into electricity. Vice versa, electricity is passed through thermoelectric coolers to generate temperature gradient by using the cold side.

Despite the great activity in the development of OTE materials, OTE devices are still at a proof-of-principle stage, even though the device geometry and the interface property have an equally vital influence on the final energy conversion efficiency. The flexible and lightweight nature of OTEs offers new opportunities, compared to the traditional rigid inorganic counterparts. Moreover, large scale processing techniques, like roll-to-roll and ink-jet printing, are promising for large-area, affordable and wearable applications.

In this section, the design principle is briefly discussed, followed by a survey of recent progress on OTE devices.

2.3.1 Basic architectures

A prototypical thermoelectric device consists of many TE couples, each consisting of an n-type and a p-type TE element (also called ‘leg’) forming a π-shape p-n junction, electrically in series and thermally in parallel. When the junctions at top are heated, the electrons in n-type legs and holes in p-type legs diffuse to the cold side, generating a potential difference, and a resulting current flow when connected into a circuit. The opposite is true for TE coolers.

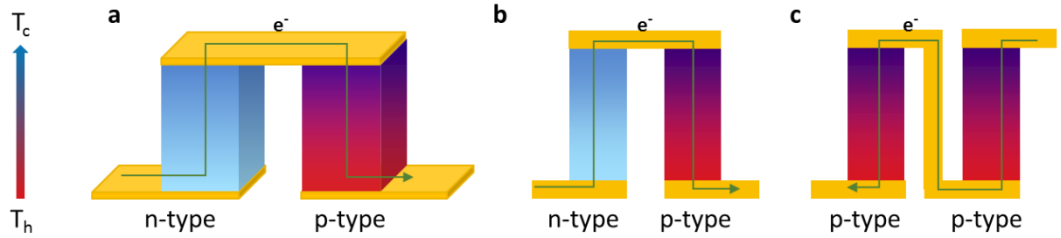

Figure 2.14 *Schematic of three types TE modules. An element of p-n couple of (a) conventional inorganic TE modules and (b) film-shaped OTE modules, (c) A p-p element of film-shaped OTE modules without n-type leg. The arrows indicated the directions of electrons flow under the temperature gradient.*

Conventional inorganic thermoelectric devices consist of bulk legs tiled over a ceramic substrate with patterned electrical contacts, as shown in Figure 2.14a. The temperature gradient required for operating this TE device geometry is perpendicular to the substrate. However, most of OTE materials are thin films, with best TE properties along the plane; a characteristic more difficult to exploit in practical scenarios (with the temperature gradient along the film) (Figure 2.14b). This necessitates the development of alternative device geometries to accommodate the temperature gradient direction. An additional problem in OTE is the scarcity of air stabile n-type materials. OTE device designs based only a single p-type leg has been considered (Figure 2.14c).

2.3.2 Power conversion efficiency

The *ZT* for a TE device can be described by the combination of properties of both n- and p- type legs, when two materials have different TE performance and assumed that the volumes of these two components is equal to

$$ZT = \frac{(\alpha_p - \alpha_n)^2}{\left(\sqrt{\frac{\kappa_p}{\sigma_p}} + \sqrt{\frac{\kappa_n}{\sigma_n}}\right)^2} \qquad \textbf{Equation 2.8}$$

where α_p, κ_p and α_n, κ_n are the p-type leg Seebeck coefficient and thermal conductivity, n-type leg Seebeck coefficient and thermal conductivity, respectively. The maximum power conversion efficiency, (η_{max}), of a TE device, both generator and cooler, is related to the ZT and the Carnot efficiency limit $\eta_c = \Delta T/T_h$ and can be given by [101]

$$\eta_{max} = \frac{\Delta T}{T_h} \frac{\sqrt{1+Z\bar{T}}-1}{\sqrt{1+Z\bar{T}}+\frac{T_c}{T_h}} \qquad \textbf{\textit{Equation 2.9}}$$

where T_h and T_c denote to the hot-end and cold-end temperatures, respectively. ΔT is the difference of T_c and T_h and $\bar{T}$ is the average of the two temperatures. It is clear that the maximum power conversion efficiency can be optimised by a higher value of ZT and a large temperature difference across the materials or devices [101]. The effects of ZT on efficiency with varying T_h are plotted in Figure 2.15, with the cold end fixed at room temperature. The conversion efficiency is only 5-10% for ZT ~ 0.7 when the heat source temperature is ≥ 400 K, which is rather low compared with alternative established technologies. The energy-harvesting potential of TE generator is still promising for low power (micro- to milliwatts) applications. Considering the human body releases about 100 W of thermal energy (estimated from the 2000 calories energy requirement per day per person) under basal metabolic conditions (~ 37 °C), electricity at ~ 0.6% efficiency would be generated from the TE generator with ZT ~ 1, under an ambient temperature of 20 °C and optimal harvesting conditions. Therefore, it is possible to harvest ~ 600 mW of the total power from the entire body. And assuming the body surface area of ~ 1.5 m^2, the flexible OTE which can conformably contact with the body and realise the appreciable power density of ~ 30 μW cm^{-2}.

For TE generators, only when the load resistance R_L is equal to the device internal resistance, R_i, η_{max} can be achieved. And in terms of coolers, the maximum coefficient-of-performance is obtained when the optimum current (I) is given as [101]

$$I = \frac{(\alpha_p - \alpha_n)(T_h - T_c)}{2R_i(\sqrt{1+Z\bar{T}}-1)} \qquad \textbf{Equation 2.10}$$

As the device ZT (α, κ, σ) is not constant with temperature change, the η_{eng} should be introduced to predict reliably and accurately the practical conversion efficiency [1]

$$\eta_{eng} = \frac{\Delta T}{T_h} \frac{\sqrt{1+(Z\bar{T})_{eng}\left(\frac{\hat{a}}{\Delta T/T_h}-\frac{1}{2}\right)}-1}{\hat{a}\left(\sqrt{1+(Z\bar{T})_{eng}\left(\frac{\hat{a}}{\Delta T/T_h}-\frac{1}{2}\right)}\right)+\frac{T_c}{T_h}} \qquad \textbf{Equation 2.11}$$

where the â is a dimensionless factor and defined as $\sigma(T_h)\Delta T / \int_{T_c}^{T_h} \alpha(T)dT$ [1].

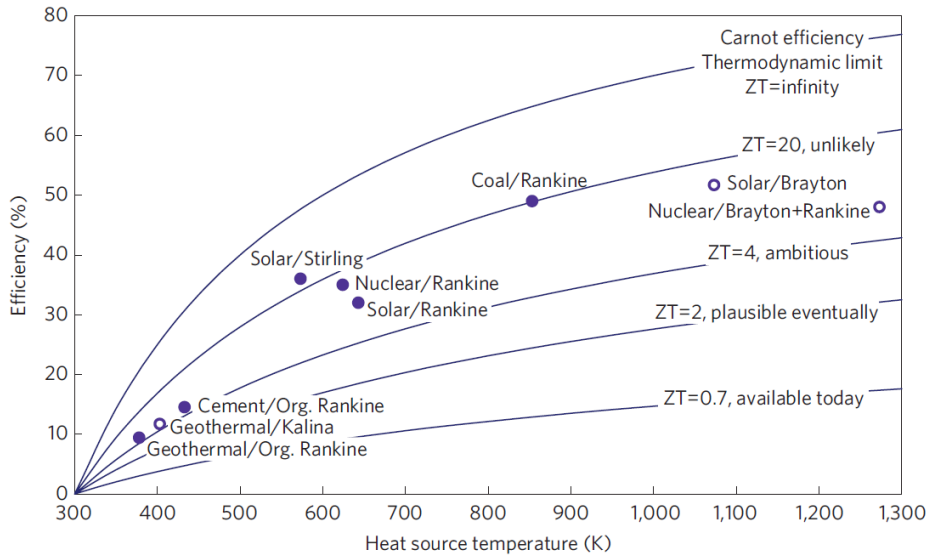

Figure 2.15 *Estimate of the energy conversion efficiency [102]. Ideal relationships between the heat to electrical conversion efficiency by TE with different zT and the heat source temperature. Compared with the efficiency of 'best practice' mechanical heat engines.*

2.3.3 Optimization of power efficiency

Maintaining the highest sustainable ΔT is one of the most important factors, which needs to be considered for designing TE generator. But there are a number of other interconnected parameters, such as the device internal resistance and the amount of legs connected in series. For example, increasing the leg length or decreasing the leg cross-section contributes positively to maintaining a larger ΔT across the TE generator, but also increases legs' resistance and intensify the Joule heating, which is generated by the thermoelectric current, I, and proportional to I^2R_i. A smaller legs density (*i.e.* fill factor) in the TE generator allows a higher ΔT, but at the same time, reduces the total number of thermoelectric elements to build up power generation in the same area (Figure 2.16). Therefore, a certain geometry of the thermoelectric legs and the density of legs can be found to optimise these contrasting effects and gain the highest power coefficient.

As mentioned earlier, the maximum power output power in a TE generator, P_{max}, is achieved only when the load resistance, R_L, is equal to its internal resistance, R_i. Experimentally, P_{max} is obtained from the product of voltage and current by adjusting $R_L = R_i$. For prediction, P_{max} can be estimated by the expression

$$P_{max} = \frac{V_t^2}{4R_L} \qquad \textbf{Equation 2.12}$$

where V_t refers to the voltage produced within the TE device due to the temperature gradient and is called the thermal voltage of the TE generator. V_t is based on not only the thermoelectrical properties of the TE materials (*i.e.* Seebeck coefficient) but also the numbers of legs, and ΔT across the TE generator. Meanwhile, R is determined by both the electrical conductivity of the TE materials, the number of legs, the dimensions of an individual elements and contact resistance both between legs and electrodes.

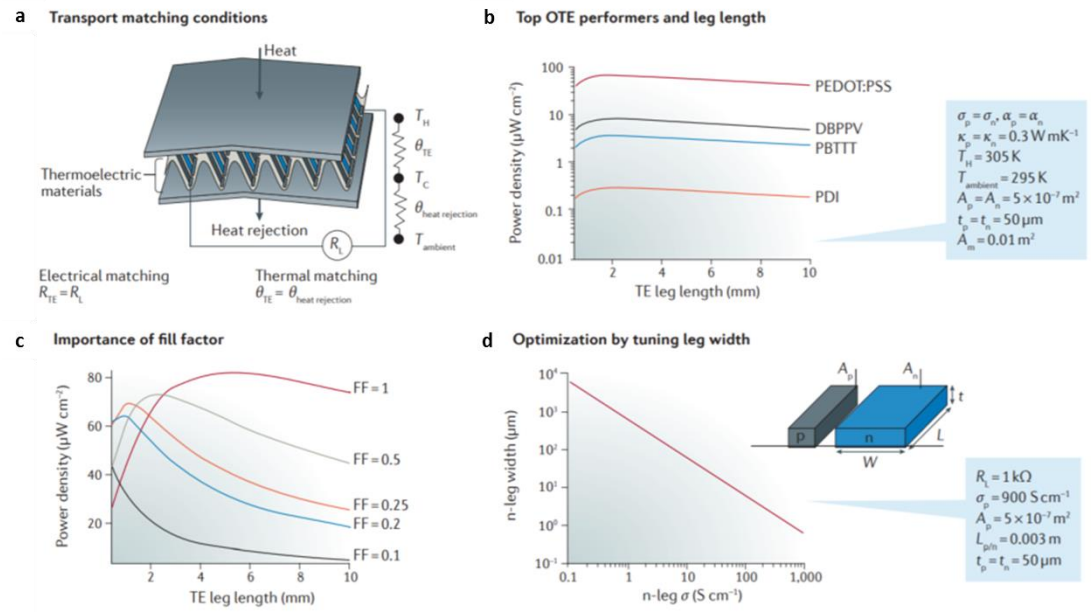

Figure 2.16 *Various parameters for optimization of OTE performance[16]. (a) The thermal and electrical transport trade-offs; (b) length of the p-type and n-type legs; (c) the fill factor and (d) the widths (cross-section area) affect the power density of thermoelectric devices.*

In practise, there are a lot of issues that can affect the power coefficient of a fabricated TE device. For rigid TE devices, the interface between the TE legs and the substrate may degrade or even break down in long-term high-temperature operations mainly because of the mismatch of the thermal expansion. Flexible TE devices might circumvent this problem. But thermal and electrical contact between the metal contacts and the organic materials remain a fundamental issue, aggravated by the great difference, for instance, in stiffness and DOS structure. Moreover, as mentioned in the OTE materials section, there is a lack of air-stable n-type OTE materials available. Therefore, more promising single (p-type) leg devices should be designed to reduce the heat transfer through the metallic interconnect, in order to maintain the temperature difference across the device. Also, high heat transfer efficiency from away from the cold side (usually obtained with rigid and bulky heat exchanger) is crucial and non-trivial in case of wearable flexible devices.

2.3.4 Prototypes of organic thermoelectric devices

The device architecture is one of the challenges encountered in developing organic thermoelectric devices. The traditional π-shape design (as Figure 2.17a shows), would require (OTE) legs with a thickness of millimetres to centimetres, to maintain sufficient temperature gradients. Different device prototypes have been reported inspired from the traditional cross-plane geometries (Table 2.3).

The first organic power generator in a vertical architecture consisting of 54 legs with ~ 40 μm length has been reported by Crispin *et al.* [103]. Precursor solutions of poly(3,4-ethylenedioxythiophene):tosylate (PEDOT:Tos) and organic conducting salt tetrathiafulvalene-tetracyanoquinodimethane (TTF-TCNQ) were filled into epoxy-based polymer cavities (each 1 × 1.5 mm) as p and n legs, respectively, connected by gold electrodes. The fabricating OTE generator (Figure 2.17b) exhibited a maximum power output of 0.128 μW at ΔT ~ 10 ^{o}C. Further improvement of the power was limited, among other things, by the low efficiency and stability of the n-type polymer and small ΔT caused by the limited thickness. More studies have appeared reporting increasing number of legs and single (p-type) devices with legs connected in-series with a metal like Ag. Roar *et al.* [104] provided an efficient way of serially connecting a total of 18,000 PEDOT:PSS elements by means of large-area roll-to-roll thin-film printing as Figure 2.17c shown. 1.2 μm thick rotary screen printing PEDOT:PSS films as p-type legs were interconnected serially with Ag on a polyethylene terephthalate foil. By considered the influence of the substrate thickness on the thermal gradient over a device, this demonstration emphasized the high-throughput potential for organic thermoelectric modules.

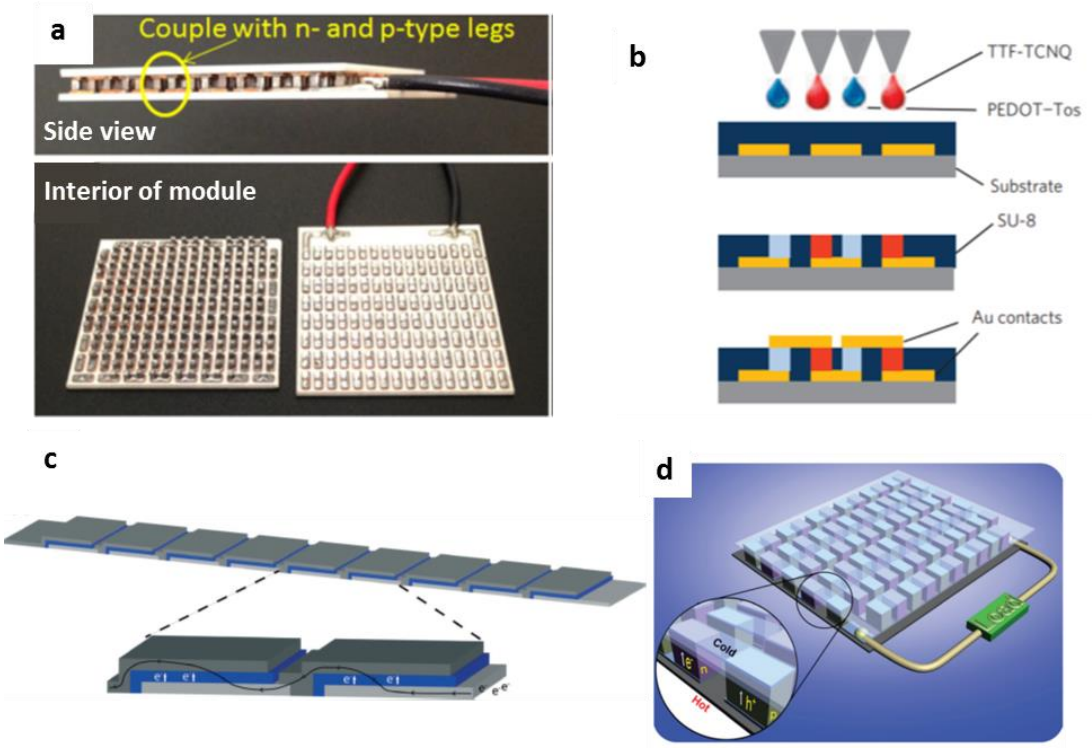

Figure 2.17 *Prototypes of vertical architecture organic thermoelectric devices. (a) Pictures of an off-the-shelf TE module [105]. (b) A vertical architecture organic thermoelectric power generator via casting in cavities contacts [103]. (c) Schematic illustrations of thin-film-based design employing only one TE material for series connection [104]. (d) And the thermoelectric module consisting of 35 thermocouples. [57]*

Zhu's group [57] fabricated 0.9 mm thick pellets by pressing poly(M-ett) powder as both n-type and p-type legs. Benefiting from the increased thickness of the legs, a thermoelectric module consisting of 35 thermocouples generated a maximum power of 750 μW at ΔT ~ 82 °C, with a power output density of 1.2 μW cm^{-2} at 30 °C temperature differential (Figure 2.17d). Later, a highly integrated flexible 440 legs module were fabricated by Poly[K_x(Ni-ett)] as n-type and Cu(I)-ethylenetetrathiolate as p-type material filled in a separated cavities (1 mm × 2 mm in the cross section) by a 5 mm thick polydimethylsiloxane membrane [106]. The maximum power output exceeded 1 mW at ΔT ~ 82 °C.

Solution processing techniques are compatible with a future industrial and practical implementation. For example, Kar-Narayan's research group reported utilization of the aerosol-jet printing technique for direct-write deposition of scalable TE devices. A variety of TE inks has been used, including Bi_2Te_3/PEDOT:PSS, Sb_2Te_3/PEDOT:PSS [107] and Sb_2Te_3/MWCNTs/PEDOT:PSS [108]. The 85 wt % Sb_2Te_3 with PEDOT:PSS nanocomposites on a polyimide substrate exhibited the PF of 28.3 μW $m^{-1}K^{-2}$ (α ~ 33.8 μVK^{-1}, σ ~ 247.3 S cm^{-1}) [107] as well as good flexibility (80% resistance increase and 93% Seebeck coefficient remained at bend curvature of 190 m^{-1}). Benefiting from the high-precision controlled deposition process, more complex structures can be designed, *e.g.*, piling up more layers of the TE legs for enhancing the TE properties, printing TE inks on flexible or stretchable substrates for improve mechanical properties. Typically, solution processing techniques only produce thin films or coatings on a substrate. Optimising the device architecture based on thin OTE films is very demanding. Design architectures for which the heat transfer is in the plane direction of these elements is more appropriate for organic module than the traditional vertical architecture. A screen printed OTE module on paper by using conducting PEDOT:PSS and Ag paste has been reported by in 2014 [109] (Figure 2.18a). In such design, the thermal gradient is along the length of the PEDOT:PSS leg and power added up by the connections resulting in about 50 μW at a ΔT of 100 ºC. The thermal gradient can also develop along the width direction of PEDOT:PSS leg, as in the laminated architecture shown in Figure 2.18b. The printed PEDOT:PSS are then piled up and connected by Ni foil. The final device exhibited a power output of 37 μW at a ΔT of 50 ºC [110].

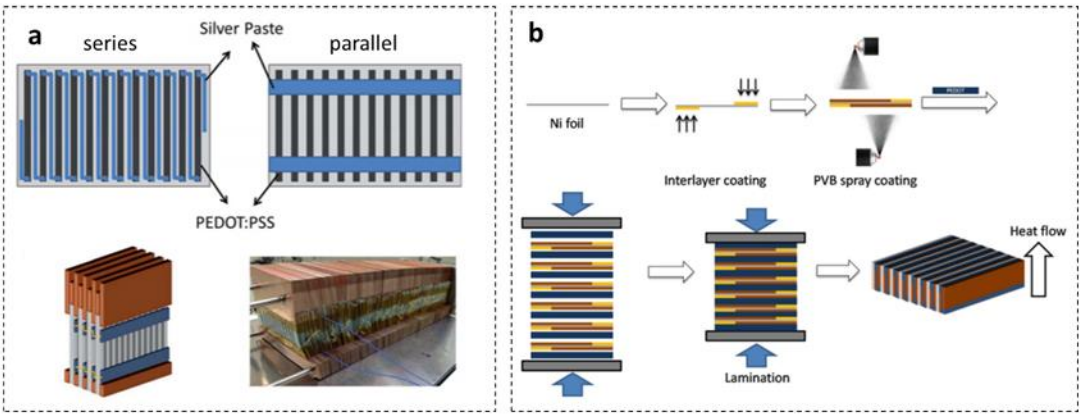

Figure 2.18 *Prototypes of in-plane architecture organic thermoelectric devices. Schematic representation of the (a) series and parallel PEDOT:PSS array, and the assembled PEDOT:PSS modules sandwiched between copper plates [109]. (b) Schematic of the fabrication of OTE devices using thermal lamination [110].*

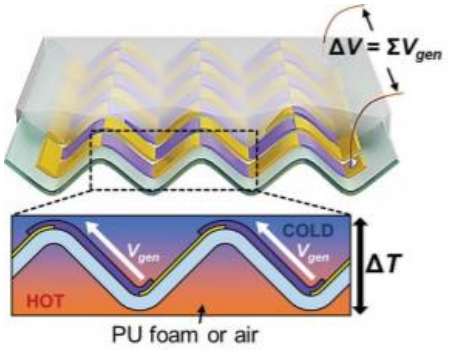

Figure 2.19 *The chevron-structured OTE device [111].*

Daegun *et al.* [111] designed a chevron-structured OTE device, tactfully integrating the in-plane PEDOT:PSS patterned PET film into a 24-single-thermocouple OTE generator for harvesting a vertical heat flow, as shown in Figure 2.19. Under the temperature difference of 17.5 ^{o}C, the generator can output a power of ~ 1 μW. It worth mentioning that the generator has been encapsulated by PU foam to reduce the internal thermal conductivity through the device (down to 0.03 W m^{-1} K^{-1}). This enabled a temperature difference which was twice that of the bare TEG when the generator was attached to a heating surface of 35 °C and exposed to air at 25 °C without any heat sink.

Table 2.3 *Different prototypes of organic thermoelectric devices with a large number of legs for harvesting the cross-plane thermal gradient.*

Materials	**Prototypes**	**Leg Numbers**	**Power Output**	**Reference**
PEDOT:Tos/TTF-TCNQ	Filled into polymer cavities	54 p-type legs	0.128 μW at ΔT ~ 10 °C	[103]
PEDOT:PSS	Large-area roll-to-roll printing	18,000 p-type legs		[104]
poly(M-ett)	Thick pellets by pressing	35 couples	750 μW at ΔT ~ 82 °C	[57]
poly(M-ett)	Filled in cavities	220 couples	1 mW at ΔT ~ 82 °C.	[106]
Sb_2Te_3/PEDOT:PSS	Aerosol-jet printing	50 p-type legs	~24 μW at ΔT ~ 20 °C	[107]
PEDOT:PSS and Ag paste	Screen printed OTE module on paper	35 couples	50 μW at ΔT ~ 100 °C	[109]
PEDOT:PSS and Ni foil layers		35 couples	37 μW at ΔT ~ 50 °C	[110]
PEDOT:PSS patterned PET film	Chevron-structured	24 p-type legs	1 μW at ΔT ~17.5 °C	[111]

The in-plane architecture can also have the additional benefit of being more easily compatible with surfaces of different shape and suitable for the 'in-plane' heat gradient. In particular, a TE device fabricated by directly brush-painting onto a curved surface (Figure 2.20a) enabled a power production of 205 μW cm^{-2} at a ΔT ~ 20 °C, much higher than the 8.6 μW to 76.9 μW obtained by a traditional module, with thicknesses varying form 0.1 mm to 1 mm, respectively [112]. A radial OTE device architecture was proposed by Menon *et al.* [113, 114]. This OTE device consists of Poly(Ni-ett) blended with poly(vinylidene fluoride)/dimethyl sulfoxide as the n-type and PEDOT:PSS with tellurium (Te) nanowires as the p-type materials on paper substrates (Figure 2.20b). The polymer-based radial TEG was accommodated on a hot pipe as a heat source without any active cooling and managed to produce an open-circuit voltage of 85 mV and a power density of 15 nW cm^{-2} when ΔT ~ 45°C. Apart from

that, the advantage of the flexibility of the OTE provides the possibility to fabricate a flexible or even stretchable OTE device. The following sections will discuss in more details recent progress on flexible (Table 2.4) and stretchable (Table 2.5) OTE devices.

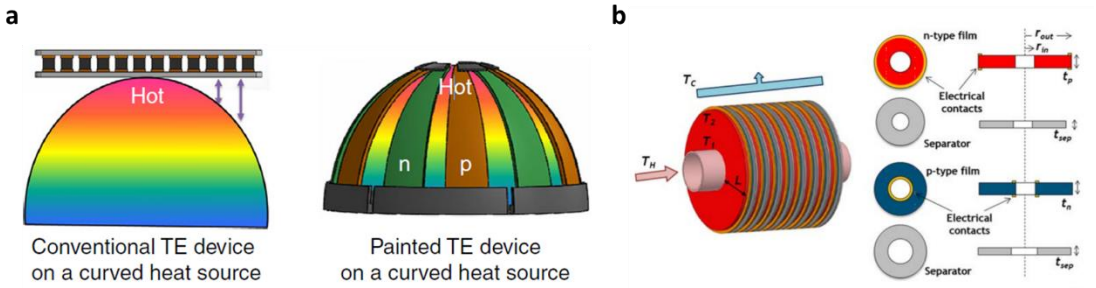

Figure 2.20 *In-plane TE devices conform to different shapes of surface. (a) Schematic of power generator of the conventional TEG and the painted TE generator on a curved heat source. [112] (b) Schematic of a radial TEG in which n-type polymers (red) and p-type polymers (blue) coat circular disks. Metal contacts (orange) are used for series connections, whereas separators (grey) electrically isolate adjacent disks [113, 114].*

2.3.5 Flexible OTE device

Construction of flexible thermoelectric devices is important for practical applications of organic thermoelectric materials. Flexible devices could be simply fabricated by depositing the OTE materials on a flexible substrate. For example, composites of ball-milled poly(Ni-ett) in PVDF as both n and p type materials have been inkjet-printed on PET substrate by Zhu's group [61]. The obtained flexible TE module, consisting of six thermocouples (Figure 2.21a), could output a power of about 45 nW under a 25°C temperature gradient. Electrochemical deposition on a patterned substrate can produce more legs simultaneously. The TEG, consisting of 108 n-type poly[K_x(Ni-ett)] legs (Figure 2.21b) was fabricated by depositing materials on PET at a time [115]. Each row (eighteen legs connected in series) can output 0.468 μW power under a temperature difference of 12 °C. Solution casting polymerisation technique can be applied to large area film processing without the size limitation of the chamber or the

substrate. Teahoon *et al.* [51] reported a flexible OTE device based on PEDOT has been fabricated by solution casting polymerization techniques on PET. After a precise control of the oxidation level of the polymer, this one leg device can generate an open circuit voltage of 10 μV by the touch of fingertips (ΔT ~ 0.1 ºC) at room temperature (Figure 2.21c).

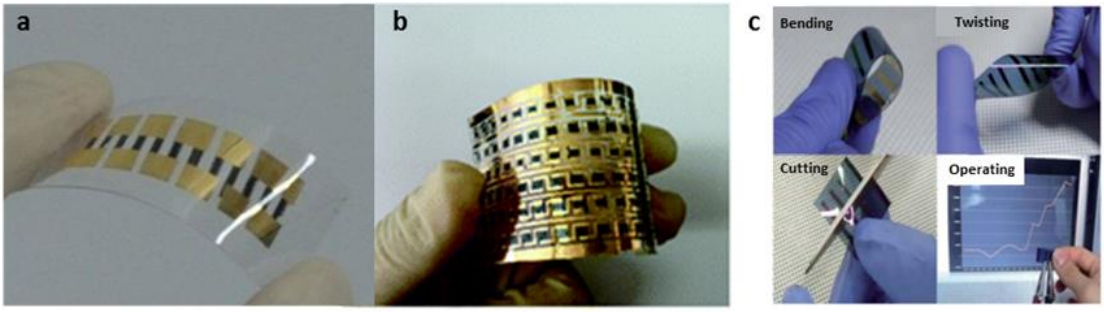

Figure 2.21 *Prototypes of flexible organic thermoelectric devices on substrates. (a) Image of a six-leg inkjet-printed composite TE device on a flexible PET substrate [61]. (b) Image of a 108 poly[K_x(Ni-ett)$_n$] legs on a flexible PET substrate [115] and (c) images of the flexible PP-PEDOT thermoelectric film under bending, twisting, cutting, and the electricity generation by the touch of fingertips [51].*

Instead of plastic flexible substrate, fabric could be a better choice for supporting the yarn-based TE legs, especially for e-textile applications. PEDOT:PSS dyed silk yarns were sewed onto a felted wool fabric to fabricate an in-plane thermoelectric module with 26 p-type legs, as in Figure 2.22a. The inherent flexibility of the module could be twisted repeatedly without changing the total resistance and yielding ~ 12.3 nW maximum power for an in-plane temperature difference of ΔT ~ 66 °C [116]. By using the same TE device architecture, the connecting metal wires were replaced by a nanocomposite of MWCNTs and poly(N-vinylpyrrolidone) (PVP) coated on commercial PET sewing threads. Combining the n-type yarns with PEDOT:PSS dyed silk yarns as p-type leg, the device was capable of producing a maximum power output of 0.3 nW (for 4-thermocouple as Figure 2.22b) and 7.1 nW (for 38-thermocouple) at

a temperature gradient of 80 °C [117]. With a simpler approach than embroidering with a coated yarn, Yong *et al.* [118] directly coated PEDOT:PSS on a commercial fabric strip (Figure 2.22d), then attached these strips on the uncoated fabric as flexible substrate and connected with metal wires, for a flexible thermoelectric power generator (Figure 2.22c). This fabric device can generate a TE voltage output of 4.3 mV at a temperature difference (ΔT) of 75.2 °C.

Not all OTE devices would necessarily require a substrate. Ya *et al.* [119] fabricated a flexible TEG with a self-standing Te-nanowire/P3HT polymer composite, with a positive Seebeck coefficient of 285 μV K^{-1}. A temperature difference of 55 °C could provide an output voltage of 19 mV. Zaifang *et al.* [120] reported a highly conductive (~ 2500 S cm^{-1}) structurally ordered PEDOT:PSS film (with a peak power factor of 107 μW K^{-2} m^{-1} at room temperature) directly used as a flexible thermoelectric module, which can give out a maximum output power density of 99 ± 18.7 μW cm^{-2} under a small temperature gradient of 29 °C.

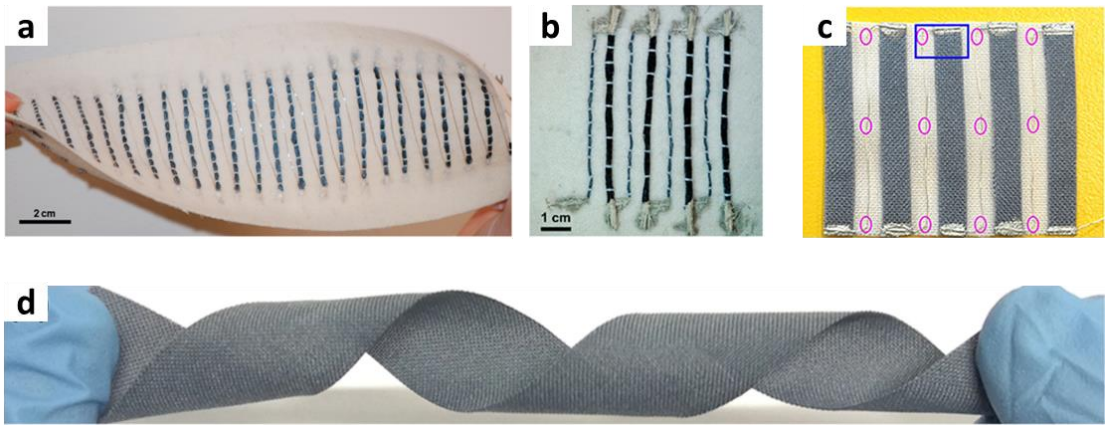

Figure 2.22 *Prototypes of the in-plane textile thermoelectric device. The textile thermoelectric device with (a) 26 p-type legs [116] and (b) with 4 thermocouples comprised of n-type coated PET yarns (11 yarns per leg), p-type dyed silk yarns (2 yarns per leg) and silver paste for contacts [117]. And image of (c) the positive face of the TEG device assemble by (d) coating PEDOT on polyester fabric [118].*

Connecting more free-standing films to form a multi-leg thermoelectric device and hence increase the power output is demanding. However, the technique normally used is still to fix free-standing films, connected with metal wires or conductive paste, back onto a flexible substrate. For example, a PEDOT:PSS/Te composite, fabricated via filtration process, was positioned onto a polyimide substrate and connected by silver (Ag) paste to assemble a 8 single-leg power generator [121] (Figure 2.23a). The requirements of the substrate pose a limit to the flexibility of the device. New architectures for substrate-free whole free-standing TE modules would be desirable. Hewitt *et al.* [122], designed a Z-shape (Figure 2.23b) device by using SWCNT for the p-type layers and polyethylenimine doped single walled carbon nanotubes for the n-type layers. A single thermocouple had a Seebeck coefficient of 96 ± 4 μVK^{-1}, producing a total power output of 14.7 μW per thermocouple at the maximum temperature difference of 50 ^{o}C.

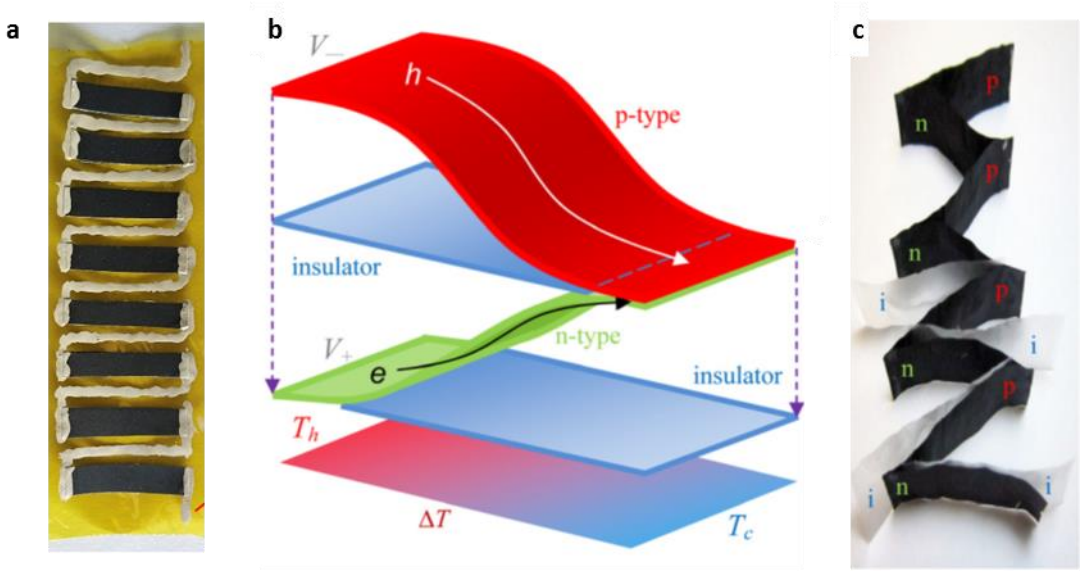

Figure 2.23 *Prototypes of the flexible thermoelectric device based on free-standing films. (a) Image of a flexible device consisting of eight (PEDOT:PSS/Te)-Ag thermocouples on a polyimide substrate [121]. (b) Schematic for the multi-layered*

TE composite, and (c) The final heat pressed multi-layered structure resulting in a single flexible module [122].

Table 2.4 *The summary of representative flexible organic thermoelectric devices.*

Materials	**Prototypes**	**Leg numbers**	**Voltage/Power output**	**Ref-erence**
Poly(Ni-ett)/PVDF	Deposition on PET	6 couples	45 nW at ΔT ~ 25°C	[61]
poly[K_x(Ni-ett)]	Electrochemical deposition on PET	108 n-type legs	468 nW at ΔT ~ 12 °C	[115]
Oxidation level controlled PEDOT	Polymerisation on PET	1 p-type leg	10 μV at ΔT ~ 0.1 °C	[51]
PEDOT:PSS dyed silk yarns	Sewed on a felted wool fabric	26 p-type legs	12.3 nW at ΔT~ 66 °C	[116]
P-type: PEDOT:PSS dyed silk yarns N-type: MWCNT/ PVP coated PET threads	Sewed on a felted wool fabric	4 couples	0.3 nW at ΔT ~ 80 °C	[117]
		38 couples	7.1 nW at ΔT ~ 80 °C	[117]
PEDOT:PSS	Coated on fabric strips on a fabric	5 p-type legs	4.3 mV at ΔT ~ 75 °C	[118]
Te-nanowire /P3HT	Self-standing films	1 p-type leg	19 mV at ΔT ~ 55 °C	[119]
PEDOT:PSS	Structurally ordered films	1 p-type leg	59 μW at ΔT ~ 29 °C	[120]
PEDOT:PSS/Te composite	Filtrated films on a polyimide	8 p-type legs	2.5 mV at ΔT ~ 13 °C	[121]
P-type: SWCNT N-type: PEI doped SWCNT	Free-standing Z-shape device	1 couple	14.7 μW at ΔT ~ 50 °C	[122]
P-type: PEDOT:PSS/ Sb_2Te_3 N-type: PEDOT:PSS/ Bi_2Te_3	Thick films on a polyimide	15 couples	12.1 mV at ΔT ~ 5 °C 19.1 mV at ΔT ~ 10 °C	[139]

2.3.6 Stretchable OTE devices

The stretchability of TE devices not only enables engineering to widen the application fields, but also to optimise the distance between the hot and cold end of the TEG in

order to increase power generation. For example, an origami foldable thermoelectric nanogenerator (Figure 2.24a) [123] and a helical architecture (Figure 2.24b) [124] based on papers as the substrate hosting thermopiles (Bi_2Te_3-Sb_2Te_3 pairs) presented more than double power generation when stretched to the maximum position than it is at zero strain.

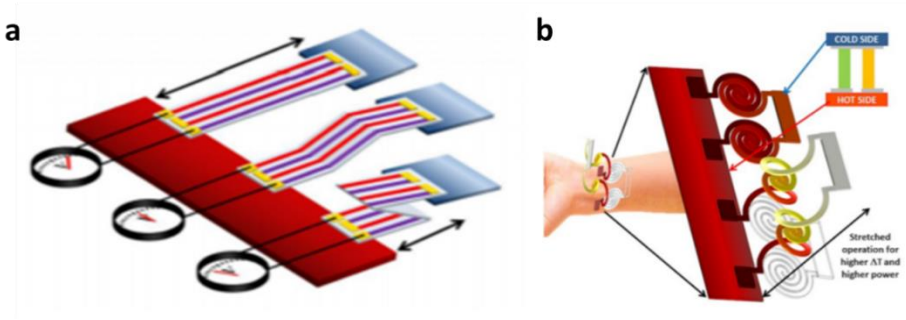

Figure 2.24 *Stretchable TE devices optimized the power output. Stretchable TEGs developed (a) on paper substrates [123] and heretical structures [125] illustrate the advantage of adaptively increasing the distance between cold and hot sides to increase power generation.*

As mentioned in **Section 2.3.6**, stretchable thermoelectric materials are great candidates for fabricating stretchable TE devices. It is also important to find out creative strategies and designs for fabrication of a robust devices based stretchable and perhaps un-stretchable materials. Hereafter, three main strategies are discussed.

(a) Geometrical effect

Engineering the structure of devices can introduce or enhance their stretchability. For instance, by using geometries inspired by origami and Kirigami. Origami comes from the Japanese word ‘ori’, which directly translates to the word ‘folding’. Kirigami is similar to origami but it also allows ‘cutting’. Both origami and Kirigami methods have been used in studies of topography, geometry, as well as engineering, with a combination of arts and science. Focusing on stretchable thermoelectric materials,

Origami/Kirigami can not only convert 2-dimensional (2D) printed arrays of thin-film legs into 3-dimensional (3D) architectures (in order, for instance, to gain the thermal gradient parallel to the substrate), but also introduce stretchability into the designed system, even for original brittle materials. For example, the eight pairs BiTe-based TEG manufactured by the Origami method can withstand a stretching deformation of 20% without power output change (**Figure 2.25**a) [126, 127].

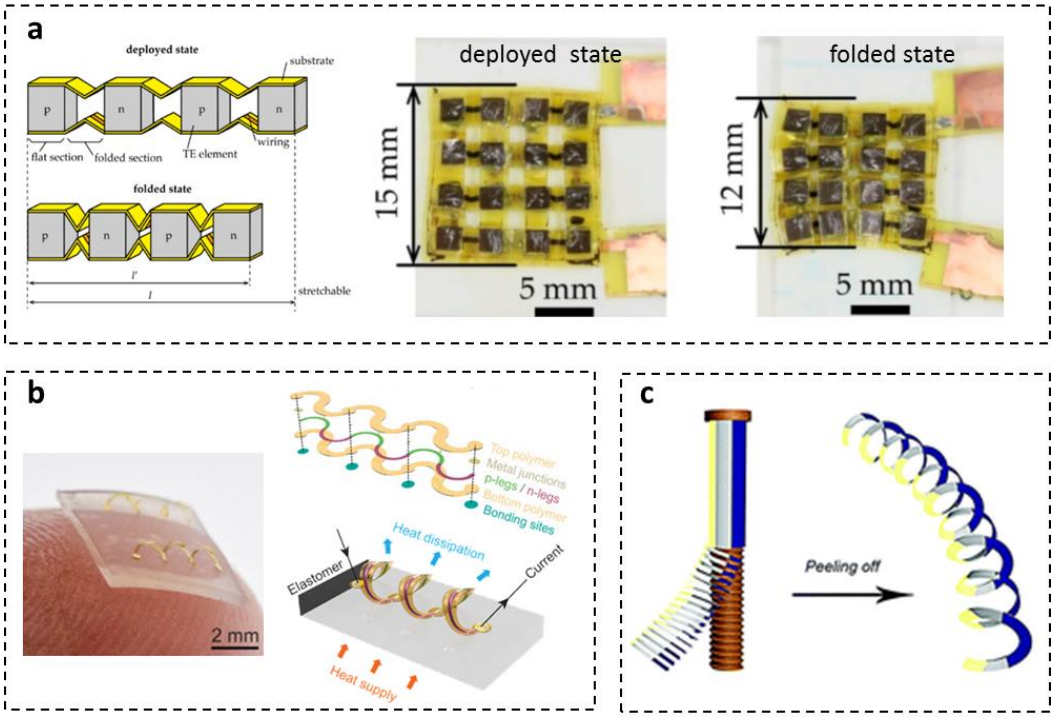

Figure 2.25 *Stretchable TE devices based on geometry. (a) Eight-pair stretchable TE device based on origami-like folding deformation, and its deployed state and folded state [126]. (b) A stretchable TE device for energy harvesting based on 3D thermoelectric coils. The 2D precursor structures assembly and chemically bonding into a 60% uniaxially pre-stretched PDMS, transform to final 3D architectures by release [128]. (c) The helical, highly stretchable, breathable and wearable TE devices based on the template of a simple screw [129].*

Spiral and helical shape have been used to transform 2D TE materials into 3D (stretchable) devices. For example, Kewang *et al.* [128] fabricated a 3D helical

structured TE device from 2D serpentines via compressive buckling, induced via relaxation of a pre-stretched elastomer substrate, to which the serpentines are bonded at selected locations (**Figure 2.25Error! Reference source not found.**b). Although the heavily doped p- and n-type silicon ribbons legs are brittle, the 3D helical structure could be stretched 60% in the in-plane direction and compressed 30% vertically for hundreds of cycles, with only minimal degradation in the electric properties (*e.g.*, the resistance of an 8 × 8 array increased 22% for 200 cycles of 60% biaxial stretching). Xiaojie *et al.* [129] reported another design of the 3D helical inorganic TEG by mixing polyvinylidene fluoride with Bi_2Te_3 or bismuth selenide (Bi_2Se_3) as p and n legs coated on the opposite sides of a polyurethane substrate over a screw (**Figure 2.25**c). The peeled-off helical structured TE device had a power output invariable after stretching for 1000 cycles up to 60% strain. Utilising the intrinsic flexibility of some OTE materials, more stretchable TE devices can be fabricated. A Kirigami-engineered PEDOT:PSS free-sanding film could be stretched up to 200% strain (Figure 2.26), with an optimized power factor of 95 $\mu W\ m^{-1}\ K^{-2}$ [130].

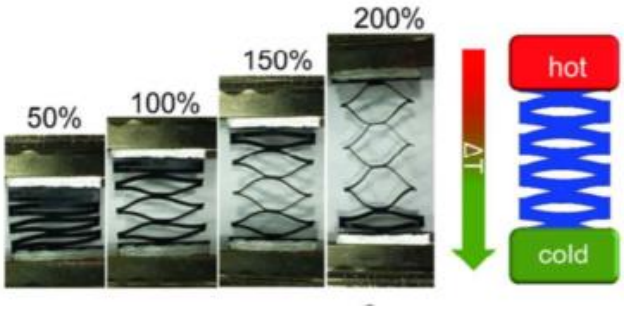

Figure 2.26 *Kirigami patterned freestanding PEDOT:PSS-based OTE device [130].*

(b) Stretchable electrodes

Stretchability of the system can also be provided or enhanced by stretchable interconnects and electrodes. Flexible modules were fabricated using commercial Bi_2Te_3 p-type and n-type legs connected with a gallium-based liquid alloy [131, 132].

The TEG generated 40.6 μW cm^{-2} in power density with 20 °C temperature difference across the entire device at an average temperature of 25 °C. More notably, an excellent reliability and robustness under repeated mechanical strains of 20% was demonstrated [131]. A similar TEG presented no change in electrical resistance after 1000 bending cycles to a radius of 5 mm [132].

(c) Towards textiles of OTEs

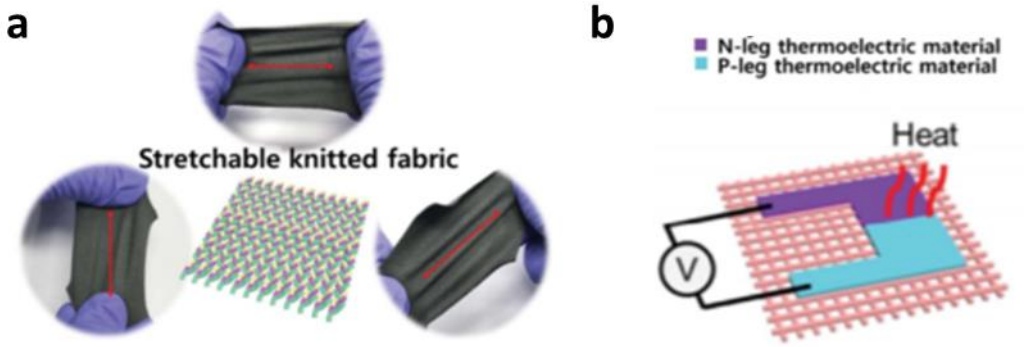

Figure 2.27 *Stretchable fabric based OTE device [94]. (a) Images of the multi-axis stretchable knitted fabric. (b) Schematic illustration of the p and n-leg printed onto the textile substrate as a TEG.*

Textile thermoelectric devices have recently attracted a lot of interest due to their easy integration in fabrics and their (three-dimensional) deformability. A fabric based TE material could harvest low-grade heat generated from the human body and could be suitable for wearable electronic devices. Among different types of textiles, the knitted structures show excellent stretchability due to the number of interdependent loops (Figure 2.27a). The space in each loop allows such fabrics to be elongated, widened, or distorted by external or internal forces [133], and has therefore potential to be integrated into a stretchable thermoelectric device. Minhyun *et al.* [134] reported a stretchable thermoelectric device via coating Ag nanoparticles as n-leg and

PEDOT:PSS as p-leg on a knitted fabric (Figure 2.27b). It exhibited excellent durability over 800 cyclic tensile tests with only a decrease of 7% of the initial voltage at 20% max strain. However, it is worth to noting that, although the fabric-based thermoelectric can be stretched up to 100% in both directions in plane, the output voltage will decrease to 50% after 100% strain. This was partially due to the non-homogenous coating. The thicker coating, within the small gaps of the fibre bundle, was more prone to crack under stretching, resulting in permanent damage to the conductive paths of the printed materials.

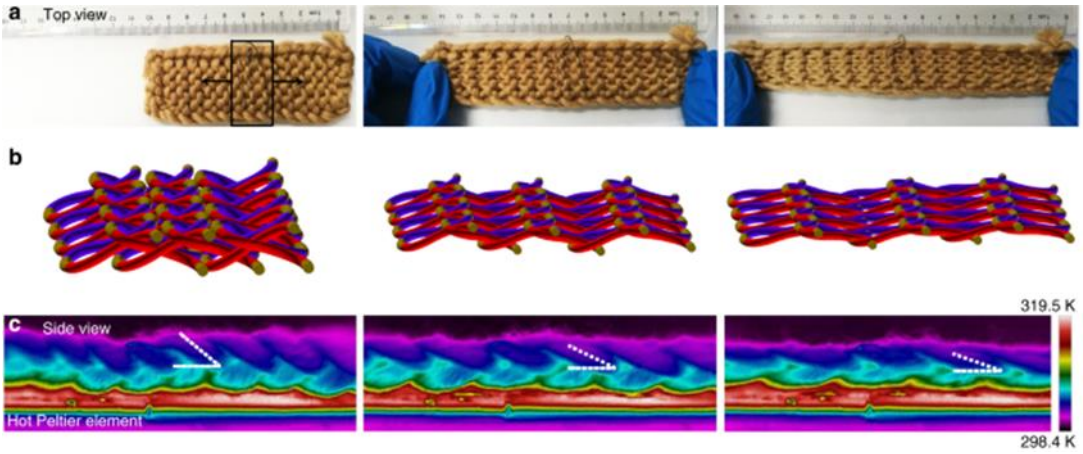

Figure 2.28 *Stretchable OTE textile [135]. Photographs of (a) the top view, (b) schematic, and (c) side view Infrared thermal images after longitudinal stretching by 0%, 40%, and 80%. The dashed line in (c) marks the standing angle of the TE loops.*

Very recently, a promising stretchable thermoelectric textile has been reported [135]. Instead of coating on the stretchable fabric substrate, the reported TE fabric was produced by weaving the alternately doped carbon nanotube fibres wrapped with acrylic fibres (Figure 2.28). Therefore, it can be woven into various fabric architectures for different applications, such as sensing, energy harvesting, or thermal management. And utilising the elasticity originated from interlocked thermoelectric

modules, stretchable substrate-free TE devices could be fabricated, showing an excellent stretchability (~ 80% strain) with no power output degradation; under an out-of-plane temperature difference of 44 °C by attaching to a heater, the device generated a peak power density of 70 m Wm^{-2}.

Table 2.5 *The summary of representative stretchable thermoelectric devices*

Materials	Methods	Stretchability	Applications	Reference
Bi_2Te_3	Stretchable electrodes	20% strain	Wearable generators	[131]
Commercial TE legs		5 mm radius (bending)	Wearable generators	[132]
P-type: PEDOT:PSS N-type: Ag	Coating on a knitted fabric	20% strain	Temperature sensors	[134]
Doped CNT fibres wrapped with acrylic fibres	Woven into fabrics	80% strain	Fabric generators	[135]
PEDOT:PSS/PU	Solution casting film	700% strain	Self-powered strain sensors	[146]
Graphene/ecoflex	Solution casting film	100% strain	Self-powered strain sensors	[147]
PEDOT:PSS and Triton X-100	3D-Printed	35% strain	Self-healing generators	[100]
PEDOT:PSS, nanofibrillated cellulose, glycidoxypropyl trimethoxysilane.	Aerogel		Pressure-temperature sensors	[143]
PEDOT:PSS	LBL coated on a foam	80% strain (compression)	Wearable generators and pressure sensors	[144]
PEDOT:PSS	Coated on a melamine foam	80% strain (compression)	Self-powered pressure sensors	[145]

2.4 Applications of OTE device

Apart from the growing interest in improving the power factor of OTE materials and in new designs for flexible TE devices, increasing effort has been dedicated on exploring

potential applications, taking advantage of positive features like mechanical flexibility while offsetting drawbacks like low efficiency. The basic potential applications of a TE device are as a generator, a cooler, an electrical temperature controller and a temperature sensor. For application as generator, researchers usually tend to increase the number of legs to increase the voltage output, while optimising the dimensions of legs and architecture of devices for gaining a high-power output and high-power density. For example, a 220-thermocouples device based on poly(M-ett) in 1 mm × 2 mm cavities of a 5 mm thick PDMS can generate in excess of 1 mW under a temperature difference of 60 ^{o}C and able to power a liquid crystal display calculator [106]. A generator formed by 300 pieces of PEDOT:PSS patterned printed papers connected in parallel, produced a power output of over 50 mW at a ΔT of 100 ^{o}C, able to illuminate light-emitting diodes [109].

Finding the right application for OTE devices should make better use of the unique properties of OTE materials. In the following sections, two more promising applications will be reviewed.

2.4.1 Application example: wearable electronic device

The human body is effectively a heat engine which, as a consequence of the continuous metabolism, emanates more than 100 W of heat, during regular day-time activities [136]. Converting such heat into electrical power, for instance via a wearable thermoelectric device, might allow to operate more and more common wireless and portable personal electrical systems [137, 138].

A 2D shaped OTE device would have one side in contact to skin and the other side away from the skin, to gain a temperature gradient. For example, the 8 single-leg generator based on PEDOT:PSS/Te composite [121], already mentioned in Section

2.4.5, has been utilised by contacting one side to a forearm skin and the other side raised up in the air (Figure 2.29a). When the ambient temperature is 19 ^{o}C, and the temperature difference approximately 13.4 ^{o}C, 2.5 mV open circuit voltage and 3 mW maximum power output could be harvested (the maximum power output has been estimated by the composites electrical conductivity, ignoring contact resistance and Ag connections, which have not been reported in the paper). Different thermal insulators can be utilized between the human body and the cold side of the OTE device. Ju *et al.* [139] designed a flexible 15-thermocouples device on a fabric, with one side staked on the fabric and another side directly in contact with the skin (Figure 2.29b,c). This device, made by the incorporation of PEDOT:PSS into a screen-printed inorganic TE thick film, can produced 12.1 mV voltage at a 5 ^{o}C temperature difference, and 19.1 mV open circuit voltage with 60 nW cm^{-2} power density at $\Delta T \sim 10$ ^{o}C. In another approach, inspired by origami, Eun *et al.* [140] demonstrated a flexible thermoelectric generator by folding into a bridge shape, as shown in Figure 2.29d,e. A device formed by 32 legs of printed Te-PEDOT:PSS composite showed a stable thermoelectric voltage of over 12 mV in response to human body heat, with a maximum power output of 10.59 nW at $\Delta T \sim 10$ ^{o}C.

There are several limiting factors for a wearable thermoelectric device. One is the small temperature difference between the human skin and surroundings. Although several prototypes to utilise low-power systems (~ 1.5 mW) have recently been shown [141], such as active radio-frequency identification locators, pulse oximeters, pedometers and heart rate monitors, the milli-watt power range is still very restrictive. Besides, the wearability and heat transfer from human body to device also needs to be improved. New architectures that can conform to different 3D shapes (*i.e.* skin), that are flexible and even stretchable are necessary for future applications.

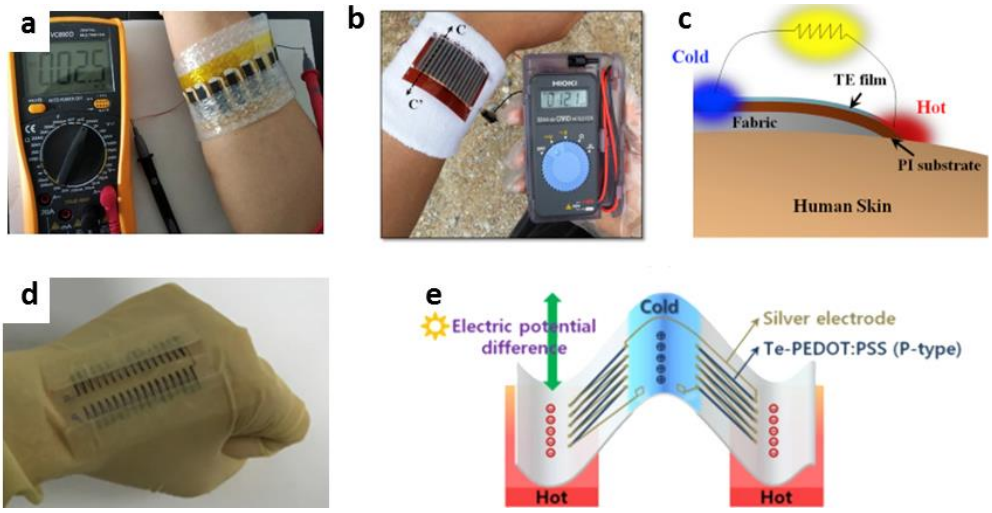

Figure 2.29 *Prototypes of wearable generators. (a) The wearable generator based on the 8 single-leg TE device [121]. (b) A 15-thermocouple wearable generator at a temperature difference of about 5 ^{o}C and (c) its cross section [139]. (e) The thermoelectric generator embedded in a glove with 32 legs arranged in two rows and (e) its schematic diagram of the thermoelectric generator and working principle [140].*

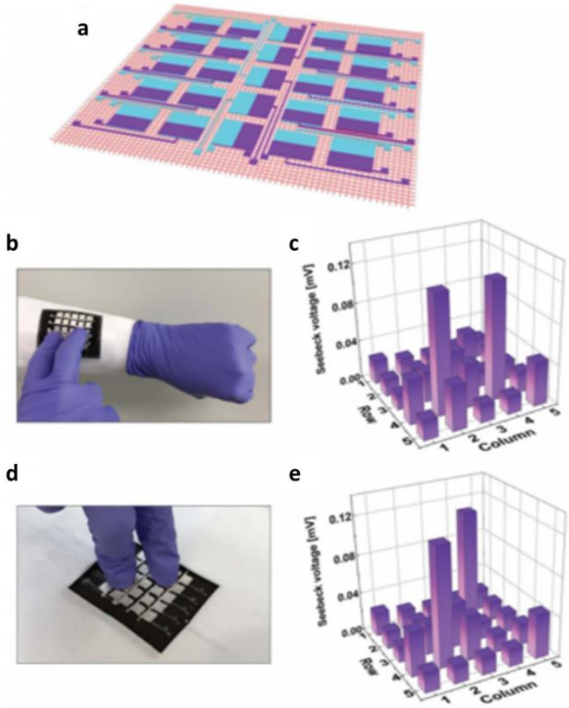

Figure 2.30 *Prototypes of wearable temperature sensor [94]. (a) Schematic layout and (b,d) the optical images of the wearable temperature sensor array. (c,e) Voltage output mapping corresponding to the temperature distribution induced by the fingers touch on the specific areas.*

Instead of harvesting body heat for generator, wearable OTE devices could also be applied as temperature sensors. Normally, one end of the sensor is in contact with a surface at a constant temperature (*e.g.* room temperature), helped by a heat sink module for instance. The other end is used for sensing. The voltage output performance of the device is correlated to the temperature difference across the ends, which depends on the temperature on the sensing side. A flexible thermoelectric composite film of Te-nanowire/P3HT was used as a temperature sensor with a response time of 17 s and a reset time of 9 s [119], which is dependent on the contact thermal conductivity between the hot surface and the active TE materials. It worth mentioning that the detection sensitivity of the sensor is a function of the voltage measurement instrument resolution and the Seebeck coefficient of the materials. In this work [119], the composites film had a positive Seebeck coefficient of 285 $\mu V\ K^{-1}$, so a temperature variation of 0.15 ^{o}C in ambient atmosphere can be detected as 0.08 mV output voltage change. Minhyun *et al.* [94] designed a 5 by 5 sensor arrays printed on the knitted fabric (Figure 2.30 a) as already mentioned in the **Section 2.4.6**. This 25 mm^2 stretchable device responded to the temperature changes on each pixel (< $1mm^2$). Therefore, a gentle finger touch to the sensor array introduced a local stimulus, and demonstrated in a real-time mapping (Figure 2.30 b-e).

Because the thermoelectric temperature sensor measures the temperature difference with self-generated voltage, so no additional power source is required. Recently, the application as a self-powered sensor is emerged, combining with response to additional stimuli.

2.4.2 Application example: self-powered sensors

Self-powered devices are those operated by harvesting ambient energy present within the environment of the system [142]. They can be powered by harvesting sources like

vibration, pressure, heat, temperature difference, magnetic fields, radiation, and so on. Among them, piezoelectric effect has been extensively studied in self-powered devices. But vibration is not always a continuous and reliable source of energy. TE devices, on the other hand, can be very reliable as long as operating across a regular temperature difference. Applied as self-powered sensors, TE devices also show the potential to be a dual-parameter sensor, with the ability to decouple the response to different stimuli like chemical, mechanical, or biological stimuli. It is worth noting that the power for measurement circuits are not considered for the concept of 'self-power' sensors.

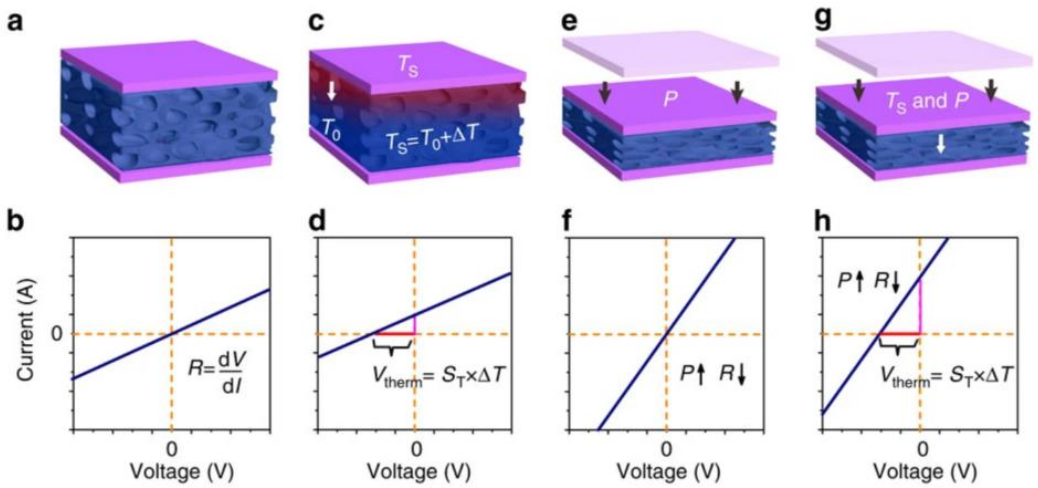

Figure 2.31 *Schematic illustration of the temperature-pressure sensor [119]. (a,b) Pristine device with the (c,d) a temperature gradient (ΔT), (e,f) a pressure, and (g,h) a coupled temperature and pressure stimuli and the corresponding I-V curve.*

Recently Zhang *et al.* [119] developed flexible dual-parameter temperature-pressure sensors by coating PEDOT:PSS onto the surface of microstructured PU frames for self-powered e-skin applications. Based on the thermoelectric property, the temperature difference between the device and an object was detected by the voltage output. The pressure was instead detected by piezoresistivity, probing by the change in device resistance. The effective transduction of temperature and pressure stimuli

into two independent electrical signals permitted the simultaneous detection of temperature and pressure stimuli with an accurate temperature resolution of 0.1 ^{o}C and a high-pressure-sensing sensitivity of up to 28.9 kPa^{-1}. Due to the thermoelectric effect, this device self-supply power for the detection of the pressure once a small temperature gradient is available.

Later, several similar dual-parameter sensors based on OTE materials have been reported based on thermoelectric effect and piezoresistive properties. For example, a temperature-pressure dual-parameter sensor was reported a year later by Shaobo *et al.* [143]. They fabricated an aerogel via freeze drying water dispersions of three organic materials: PEDOT:PSS, nanofibrillated cellulose, and glycidoxypropyl trimethoxysilane. The following DMSO vapour treatment boosted the pressure sensitivity by two orders of magnitude and eliminated the effect of the resistance of the aerogel change with temperature, to further decouple the two signals. Another report of wearable self-powered pressure sensor was layer-by-layer coated PEDOT:PSS on a foam [144]. The foam was synthesised by CNF-PEI-PEDOT:PSS and exhibited piezoresistive response to pressure. At an ambient temperature of 18 ^{o}C, and when in contact with a forearm skin (34 ^{o}C), the device could generate a voltage of 0.3 mV. A coaxial microstructured melamine foam was also fabricated as a self-power pressure sensor [145]. The melamine foam core provided a compressible and elastic framework, while the coated intermediate PEDOT:PSS acted as a conductor and a thermoelectric material. A styrene-ethylene-butylene-styrene shell coated outside the foam ensured mechanical stability and resilience to stabilize the brittle PEDOT:PSS layer under high loading conditions. The assembled wearable TE device, containing 21 single-thermocouples of the coaxial foam, was able to generate more

than 100 nW at ΔT ~ 10 °C, and demonstrated a high sensitivity to pressure without external power supply.

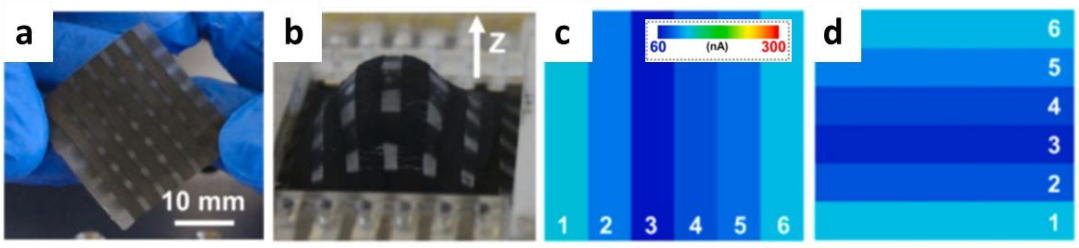

Figure 2.32 *Self-powered multi-channel strain sensor [146]. (a) Photographs of a multi-channel 3D strain sensor and (b) it under deformation, and the corresponding current mapping figures of orthogonal (c) x and (d) y directions from the two groups of graphene electrodes on top and bottom surfaces.*

Self-powered strain sensors or temperature-strain dual-parameter sensors have also been reported. The first self-powered TE strain sensor was reported by our group [147]. A blend of PEDOT:PSS with commercial elastomeric polyurethane showed a great stretchability, with a strain-at-break of ~ 700% for blends with 90 wt.% PU, and a Seebeck coefficient of ~ 15 μV K^{-1}. Under a temperature difference, the self-standing film could supply voltage for powering itself to sense strains. A year later, a graphene-ecoflex nanocomposite film has also been reported as a self-powered strain sensor [146]. A multi-channel 3D strain sensor system (Figure 2.32) manufactured based on the composites stripes showed the function of strain detection along various directions. Besides, by combining different advanced materials, more functional self-powered TE sensors have been developed. For example, Crispin's group [100] fabricated a novel organic mixed ion-electron conducting aerogel with PEDOT:PSS and nanofibrillated cellulose, to form the mechanical structure of the aerogel, and crosslinked by glycidoxypropyl trimethoxysilane, to introduce elasticity. Except the response to pressure, temperature, the ionic Seebeck effect of the PEDOT:PSS was utilised to sense humidity. The Seebeck coefficient peak value at high humidity (> 60%) is the

sum of the electronic and the ionic Seebeck. Because the ionic Seebeck coefficient is time dependent, the electronic and ionic Seebeck coefficient could be decoupled and, in turn, also the temperature gradient and humidity could be distinguished. Therefore, as shown in Figure 2.33, three individual parameters - pressure, temperature, humidity - were detected in a single device configuration.

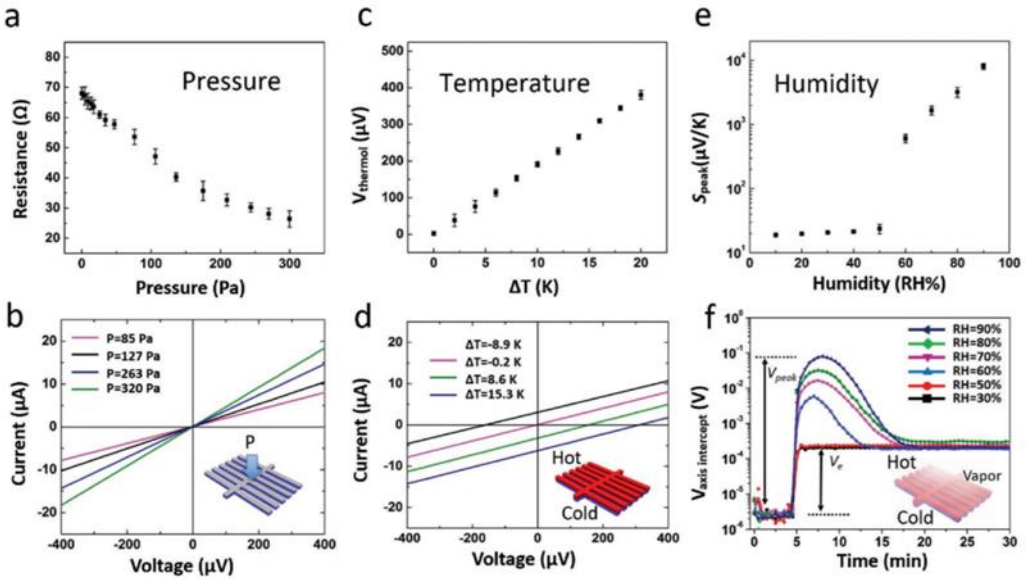

Figure 2.33 *Self-powered strain, temperature and humidity sensor [100]. The aerogel TE device applied as (a,b) pressure and (c,d) temperature sensor under relative humidity of 30%. And its application of (e,f) humidity sensor under* $\Delta T \sim 10\,^{o}C$.

2.5 Summary and challenges

OTE have seen a remarkable progress in the field of high *zT* value materials. Novel OTE device architectures, flexible and multi-functional applications have been explored in the past few years. OTE are becoming interesting alternatives to traditional inorganic thermoelectrics.

It must be admitted that organic thermoelectrics are still in the initial development stage and still face a number of challenges. Since 2008, the values of the power factors of organic thermoelectric materials have increased by 4 orders of magnitude. *zT* values

greater than 0.2 in both p-type (PEDOT:PSS) and n-type (Poly(M-ett)) achieved at room temperature are comparable to those of many inorganic counterparts. But we have to notice that: i) the number of high TE performance OTE materials is still scarce; ii) after processing, especially blending with insulating polymers for high flexibility, both α and σ dramatically reduced. For the development of state-of-the-art organic thermoelectric materials, further understanding the fundamental mechanism of heterogonous systems are demanded, which is more complicated that in the case of inorganic homogeneous systems. The molecular structure of the conductive polymers and the morphology of their composites are also important. For example, a systematic investigation of the critical roles of a conjugated backbone, side chains, and polymer molecular weight relationship with the TE performance can guide future materials selection as well as processing.

From technical side, precise measurement of key thermoelectric parameters for organic thermoelectric materials are different from inorganic bulk materials. Seebeck coefficient and in-plane thermal conductivity reported by different groups are measured by different home-made systems, some of which are affected by environment conditions, sample size and shape and substrate. Thus, the result accuracy and comparability need to be considered. A standard for measuring OTE device performance does not exist, due their various types and structures.

Beyond the challenges in OTE materials and the measurement techniques, several issues also limit OTE devices. Most polymers have a limited thermal stability (<400K). The resulting small temperature operating window makes the temperature gradient across the device very limited. One could compensate by utilising OTE generators on larger surfaces. This is possible considering that large-scale and cost-effective producing techniques could be employed with organic materials. Research should also

focus on improving the power density, for example, by condensing the device structure and optimise the interfaces between materials and electrodes. An alternative way to go beyond current limitations is to explore new applications with low energy requirements. Wearable electronics for harvesting body heat and self-powering sensors are good examples but have not been well developed yet.

Chapter 3 Experimental section

This chapter describes the materials and experimental techniques that were used to prepare and characterize the OTE materials and devices.

3.1 Materials

The $Na_x(Ni\text{-}ett)_n$ nanoparticles used in **Chapter 4** were synthesised in collaboration with the group led by Dr. Bob C. Schroeder at University College of London. Firstly, 1,3,4,6-tetrathiapentalene-2,5-dione (TPD, 1 g, 4.8 mmol, Sigma Aldrich) was reacted with excess sodium methoxide (1.2 g, 22.2 mmol, Sigma Aldrich) in a refluxing methanol solution at 75 ^oC for 24 hours. Subsequently, nickel (II) chloride hexahydrate was prepared from nickel (II) chloride (0.63 g, 4.8 mmol, Sigma Aldrich) and water (300 mL, deionized) were added. After refluxing for another 24 hours, the resulting solution was immediately exposed to air for 30 minutes. A black polymer precipitate was obtained by filtering and washed with water, methanol, and diethyl ether, sequentially, dried under vacuum for 24 hours and ground to a fine powder.

CNT veils were kindly provided by Dr. Weibang Lu at Chinese Academy of Sciences and Dr. Juan Jose Vilatela at IMDEA Materials Institute. Briefly, CNT veils were made by floating catalyst chemical vapor deposition (FCCVD). The feedstock, which contained about 96.5 wt% ethanol (carbon source), 1.9 wt% ferrocene (catalyst precursor) and 1.6 wt% thiophene (promoter), was injected (0.15 ml/min) into a hot CVD furnace (~ 1150 ^oC) along with the carrier gas (600 ml min^{-1}) consisting of hydrogen and argon (~ 1:1 volume ratio). CNTs were formed and entangled into sock-like aerogel in the furnace, then was pulled out and collected by a rotating roller continuously. Finally, the high porosity CNT sponge on the roller was densified by mechanical compression.

PEDOT:PSS (Clevios PH1000) was purchased from Heraeus GmbH. The PU films and fibres in this thesis were obtained from 940 dtex Lycra® yarn from Invista. DMSO (> 99.9 %) and EG (99.8%) were purchased from Sigma Aldrich. Multi-Walled Carbon Nanotubes (NC7000) were purchased from Nanocyl S.A. The commercial available bi-axially oriented Polystyrene film (Grafix shrink film) was obtained from a craft retailer, Polycarbonate (PC) films (Lexan 8010MC) with a thickness of 250 micron were provided by Sabic.

3.2 Preparation of thermoelectric materials

Preparation of PU /DMSO dispersions (Chapter 4):

Lycra® Invista yarns were washed with soap, acetone and isopropanol in sequence, in order to remove surface dust, oil and spinfinish. Afterwards, the Lycra® yarn was cut into small pieces and dispersed in anhydrous DMSO (1 wt. %) by magnetically stirring at 80 ^{o}C in an oil bath for 12 hours to afford dispersions with 1 wt. % solid content.

Preparation of $Na_x(Ni\text{-}ett)_n$/ Lycra composite films (Chapter 4):

5 wt. % $Na_x(Ni\text{-}ett)_n$ was dispersed in anhydrous DMSO by bath sonication (ultrasonic cleaner, VWR) for 30 minutes and, subsequently, stirring for 2 hours. It was mixed with 1 wt. % PU /DMSO dispersion at different ratios. The content of $Na_x(Ni\text{-}ett)_n$ in final composite films were 10 wt.%, 30 wt.%, 50 wt.%, and 70 wt.% (Figure 3.2). Composite films were prepared by drop casting approximately 2 ml of the mixture on pre-cleaned glass sides (75 mm × 25mm) and were dried at 80 ℃ in oven in an ambient atmosphere. Different casting temperatures were explored ranging from 40 °C to 140 °C (Figure 3.1). Based on the electrical conductivity of the casted film, 80 °C was chosen as the casting temperature. The drop-casting procedure was repeated 5-8 times until the weight of solid was approximately 0.1g. Self-standing $Na_x(Ni\text{-}ett)_n$/ Lycra

(NL) films of approximately 50 μm thickness were obtained after drying at 80 °C in a vacuum oven for 12 hours and peeling off (as Figure 3.3).

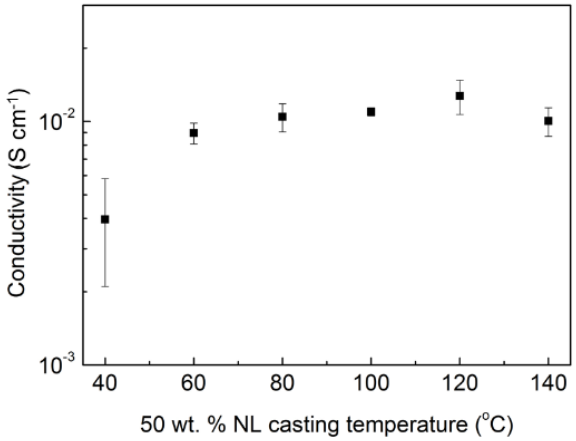

Figure 3.1 *Electrical conductivity of the 50 wt% NL film corresponding to the casting temperature. The error bars represent to the standard diviations calculated from 5 specimens for each casting temperature with 5 times repeated measurements on each specimen.*

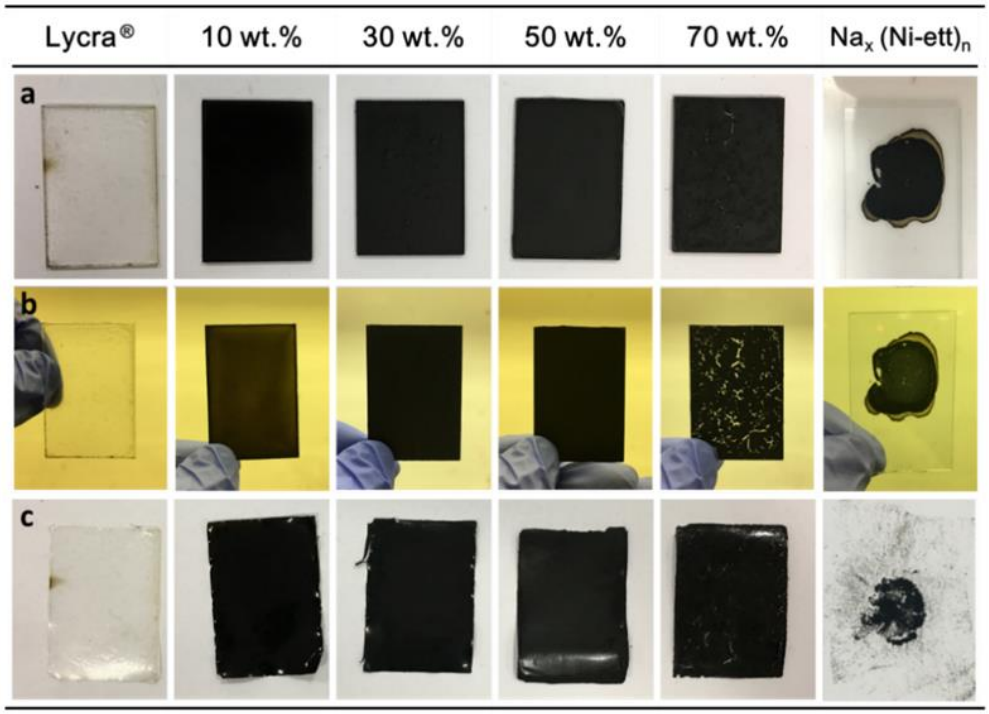

Figure 3.2 *Digital pictures of the pure Lycra® film, 10 wt. %, 30 wt. %, 50 wt. %, and 70 wt. % NL films, respectively. a) On desk, b) hold towards to the lights and c) peeled off from the glass slides.*

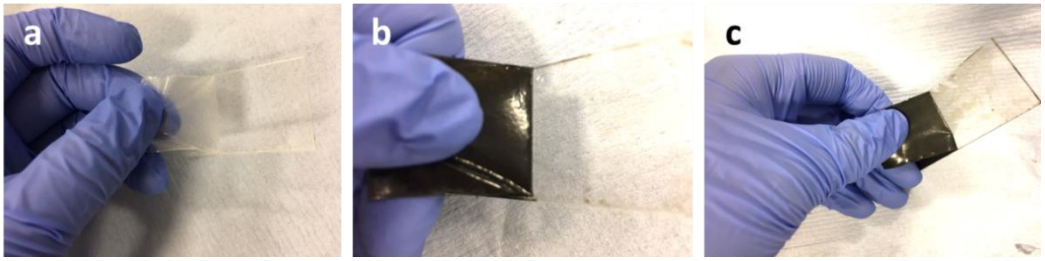

Figure 3.3 *Optical pictures of (a) pure Lycra® film, (b) 30 wt. % NL film, and (c) 50 wt.% NL film are easily separated from the substrate glass slides by peeling off.*

Preparation of PEDOT/ Lycra composite films (Chapter 4):

A similar procedure was used for preparing PEDOT:PSS/Lycra® (PL) films. Cryogenically dried PEDDOT:PSS solids were dispersed in anhydrous DMSO (1 wt %) by a homogenisation (Heidolph SilentCrusher M set at 500 rpm for 5 minutes) and probe ultrasonication (Sonics VibraCellTM, amplitude 35 %, 1 sec. on, 1 sec. off, for 20 min) in sequence. The obtained PEDOT:PSS/DMSO dispersion was then mixed with 1 wt.% Lycra®/DMSO dispersion in a volume ratio of 1:9. Afterwards, the same drop-casting method and drying procedures as for NL films were used which resulted in films with a similar thickness and dimensions as the NL counterpart.

Preparation of PEDOT coated yarns (Chapter 5):

The washed Lycra® yarns were dipped into DMSO at 50 °C for 10 minutes, followed by dipping into a PEDOT:PSS solution in DMSO (10 wt %) for 5 minutes (Figure 3.4). The swelling level is controlled by the dipping time in DMSO. Optimized conditions were selected to infiltrate DMSO into the surface of the single filaments of the whole yarns by detecting the transparency change of the yarns. After the coating procedure, the yarns were fully dried at 120 °C in the oven for 5 hours not only to evaporate all the solvent, but also to anneal the yarns. The PEDOT:PSS coated yarns, named PY, was obtained after the as-mentioned procedures and cut into specimens with 20 mm length for the measurements. Cracked PEDOT:PSS coated yarn (CPY) was fabricated

by stretching PY to 5%, 10%, 20%, 30%, 40%, 50%, 80%, 100%, 300%, 1000% and named as CPY-5, CPY-10, CPY-20, CPY-30, CPY-40, CPY-50, CPY-80, CPY-100, CPY-300, CPY-1000, respectively.

Figure 3.4 *Schematic illustration of the 2-step swelling/coating fabrication procedure for the PEDOT:PSS coated Lycra® yarn (PY).*

Preparation of p&n doped CNT veils (Chapter 6):

The 'as-grown' CNT veils were anealed at 450 °C for an hour and then emmersed in hydrochloric acid (36%-38%) for 12 hours. Afterwards, the CNT veils were washed in deionized water for seveal times until a pH of 6-7 is reached, and then dried in the 100°C oven for 2 hours for testing and doping.

Poly(ethyleneimine) (PEI) and $FeCl_3$ dissolved in ethanol were used for n- and p-type doping, respectively. Different concentrations of the dopant solutions were used ranging from 2 mM to 20 mM. For comparison, the amount of the dopant solutions was all kept at 50 µl and dropp-casted onto a 15mm × 15 mm squared CNT veils on glass slides as substrates.

3.3 Fabrication of TE devices

Fabrication of a stretchable OTE device (Chapter 4):

PL and NL films were used as p-type and n-type legs, respectively. First, p-n junctions were prepared by pressing at 120 °C, 30 bar for 1 minutes. The p-n junctions were

folded along the out-of-plane direction and were insulated by polyurethane films. Subsequently, the device was pressed at 30 bars, 160 ℃ for 5 minutes within a mould. A device was fabricated by coupling 8 p-n junctions and was used for wearable self-powered sensor demonstration at a temperature difference of 20 ^{o}C. Silver paste was used to adhere copper tapes on the ends of the TE device as electrodes.

Fabrication of a 'magic ball'-shaped generator (Chapter 4):

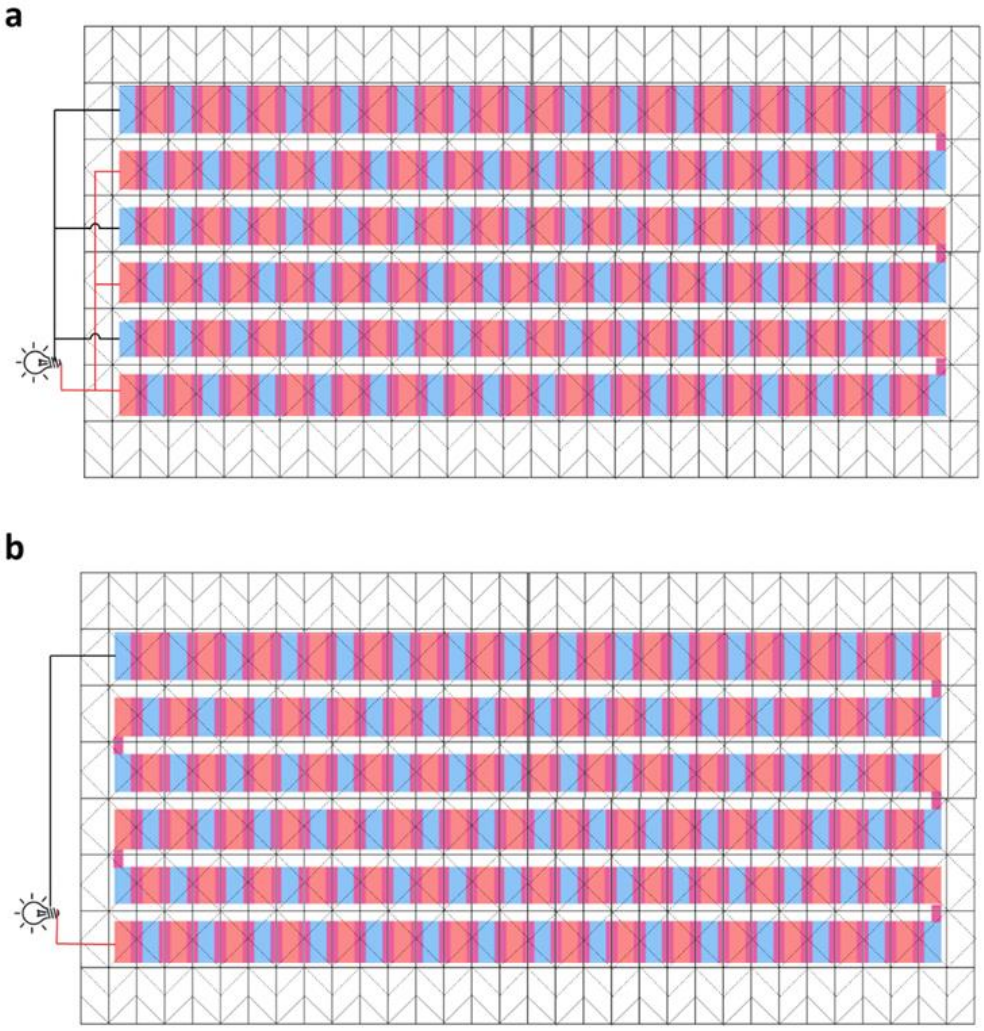

Figure 3.5 *The design of the 90-couple (a) in series (b) and parallel "magic ball" TE device. The pink, blue and purple colour indicate the p type, n type and the overlap parts of p and n type TE materials, respectively. The solid and dash lines indicated the peak and valley folding of origami. The red, black thick lines and lamp illustrate the electrical circuit the magic ball device exposed to a temperature difference.*

A $Na_x(Ni\text{-}ett)_n$/DMSO solution and a PEDOT:PSS aqueous solution as n and p legs were painted on the paper. A 100 ^oC hot plate was underneath the paper for drying. After complete drying, the painted paper was folded into a 'magic ball' shape (Figure 4.13a). The painting patterns and the folding designs are shown in Figure 3.5. Silver paste was used to adhere copper wires on the ends of the TE device as electrodes.

Fabrication of a wearable OTE device (Chapter 5):

The fabric device was made by sewing 10 PYs and constantan wires as p- and n-type legs, respectively. PYs and constantan wires were connected in series via knitting the constantan wire at the PY's ends. Carbon grease was used to increase the contact between PYs and constantan wires.

The smart glove was fabricated by sewing PY through the thickness and fixed both sides by thread. Electrodes were embedded by tying thin copper wire knots at the ends. The connection between the yarn and electrodes was enhanced by carbon grease and ethyl cyanoacrylate (Loctite®, Henkel).

Fabrication of self-folding honeycomb structured TE devices (Chapter 6):

Three types of the PC patches: small (8mm×1.5mm), medium (8mm × 8.5mm) and large (8mm ×10mm) were cut using by a Silhouette cameo. CNT veils and biaxial stretched Polystyrene (b-PS) were cut into the designed patterns as shown in Figure 3.6. Subsequently, the CNT veils are densified in the presence of a few drops of ethanol to adhere them onto both sides of the b-PS film. Afterwards, the CNT veils were doped into p and n type alternatively and dried at ~ 40 ^oC. Cyanoacrylate glue (Loctite®, Henkel Ltd.) was used to adhere the CNT veils to the b-PS and PC patches. Afterwards, the as-assembled sample was dried at room temperature overnight, before putting into the 130^oC oven for the self-folding procedure.

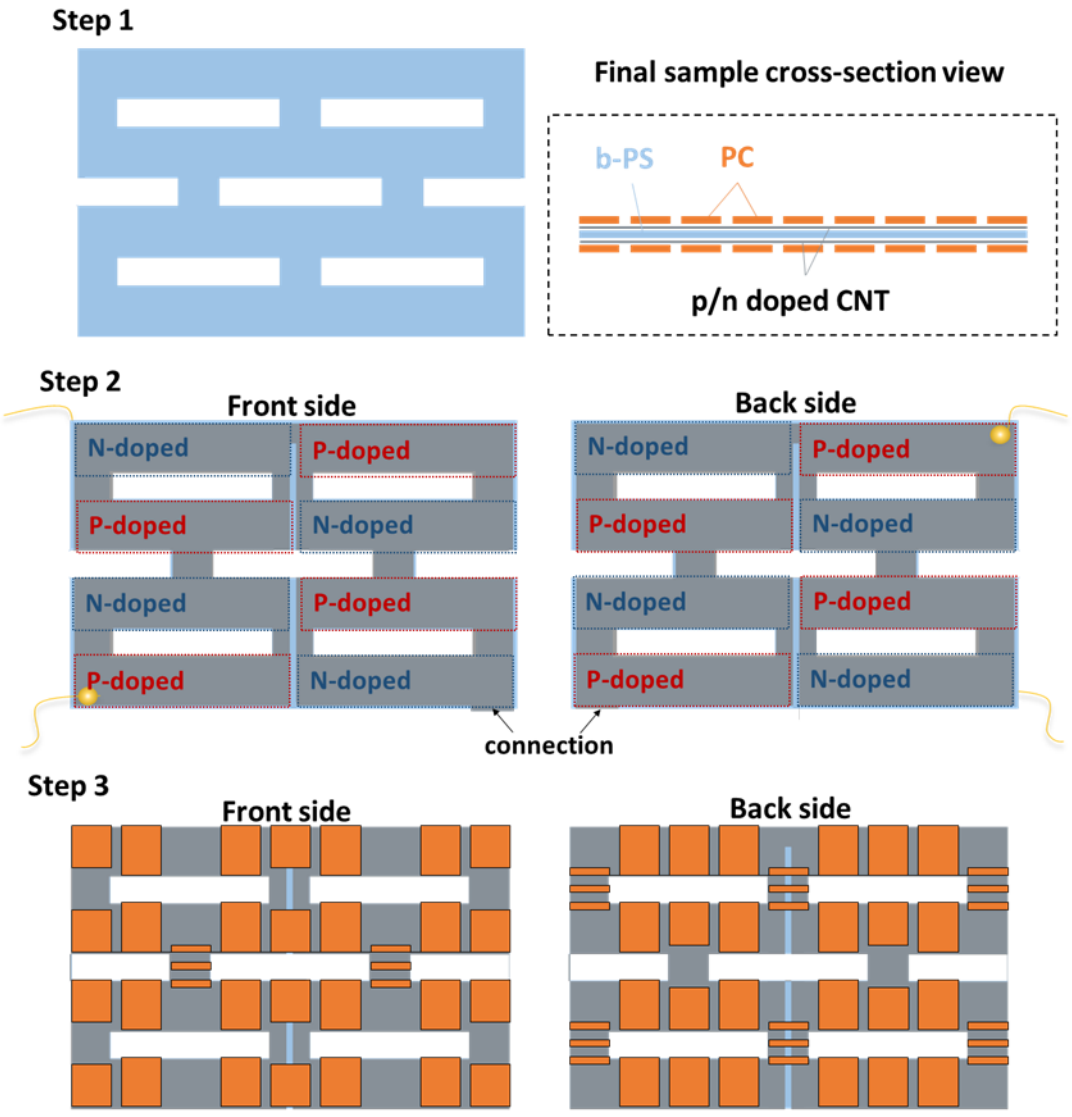

Figure 3.6 *Schematic illustrations of the design of a 4-cell honeycomb structure TE module. The p & n doped CNT veils (grey) connected and attached on both sides of b-PS, followed by the patterns of PC patches (orange) adhesion on. After self-folded in to the 4-cell honeycomb structure TE module, 8 couples of p-n legs are existing in the modules connected by 2 electrodes (yellow).*

Multi-Walled Carbon Nanotubes (MWCNTs) were dispersed in acetone and sonicated by probe sonication for 10 minutes and 5000 J energy at 20% of the maximum amplitude level. An airbrush (H4001 HP-CPLUS, Iwata Performance) with an air compressor (Iwata studio series) was used for spraying MWCNTs/acetone solution on one side of the 10 × 10 cm glass fibre prepreg (MTC510) with epoxy volume fraction

of 42%. 30 psi (2.07 bar) air pressure and a 10 cm distance between spraying nozzle and prepreg were used. Approximately 60 mg MWCNTs were sprayed resulting ~ 7 wt.% MWCNTs contained in the epoxy of the coated prepreg (Figure 3.7a).

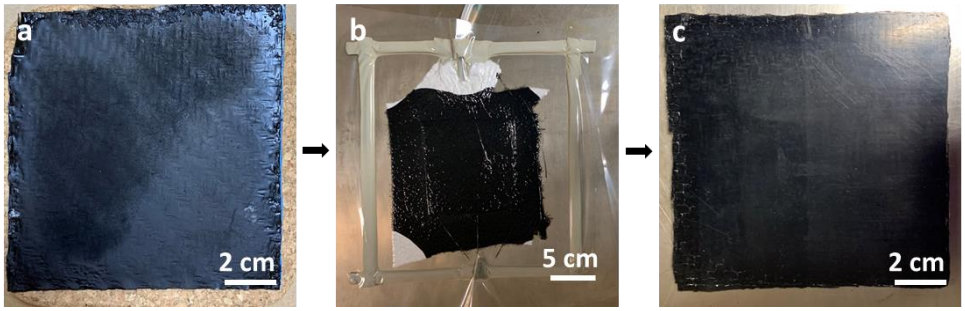

Figure 3.7 *The fabrication of MWCNTs sprayed composites laminates. Images of (a) the sprayed MWCNTs on glass fibre prepreg, (b) with 4 piles of uncoated prepregs in a vacuum bag and (c) after curing.*

As Figure 3.7 shows, after drying under vacuum at room temperature for 12 hours, the coated prepreg was placed on top of 4 piles of uncoated prepregs, with the coated side face on top. After vacuum for 30 minutes to avoid trapped bubbles, a typical curing cycle (3 °C min^{-1} from room temperature to 120 °C for 2 h) was applied using a programmable oven under vacuum. After cutting and polishing, the glass fibre reinforced composite panels were adhered to both sides of the self-folded honey-comb structured TE module. Copper wires as electrodes were connected to both the TE module and the MWCNTs coated side of the composite panels with silver paste as the adhesion.

3.4 Characterization of TE materials

3.4.1 Seebeck coefficient

An MMR Technology Seebeck Effect Measurement System was used throughout this research. The system consists of a programmable refrigerator chamber controller

(K20), and programmable stage heater controller (SB100) as shown in Figure 3.8a, and a variable temperature Dewar as Figure 3.8b shown. The Dewar contains an amplifier circuit board and a Joule-Thomson refrigerator (Figure 3.8c) and is connected to a vacuum pump and a nitrogen flow via a filter-dryer in order to regulate the temperature of the chamber during operation. The whole system is operated using Seebeck Effect Software.

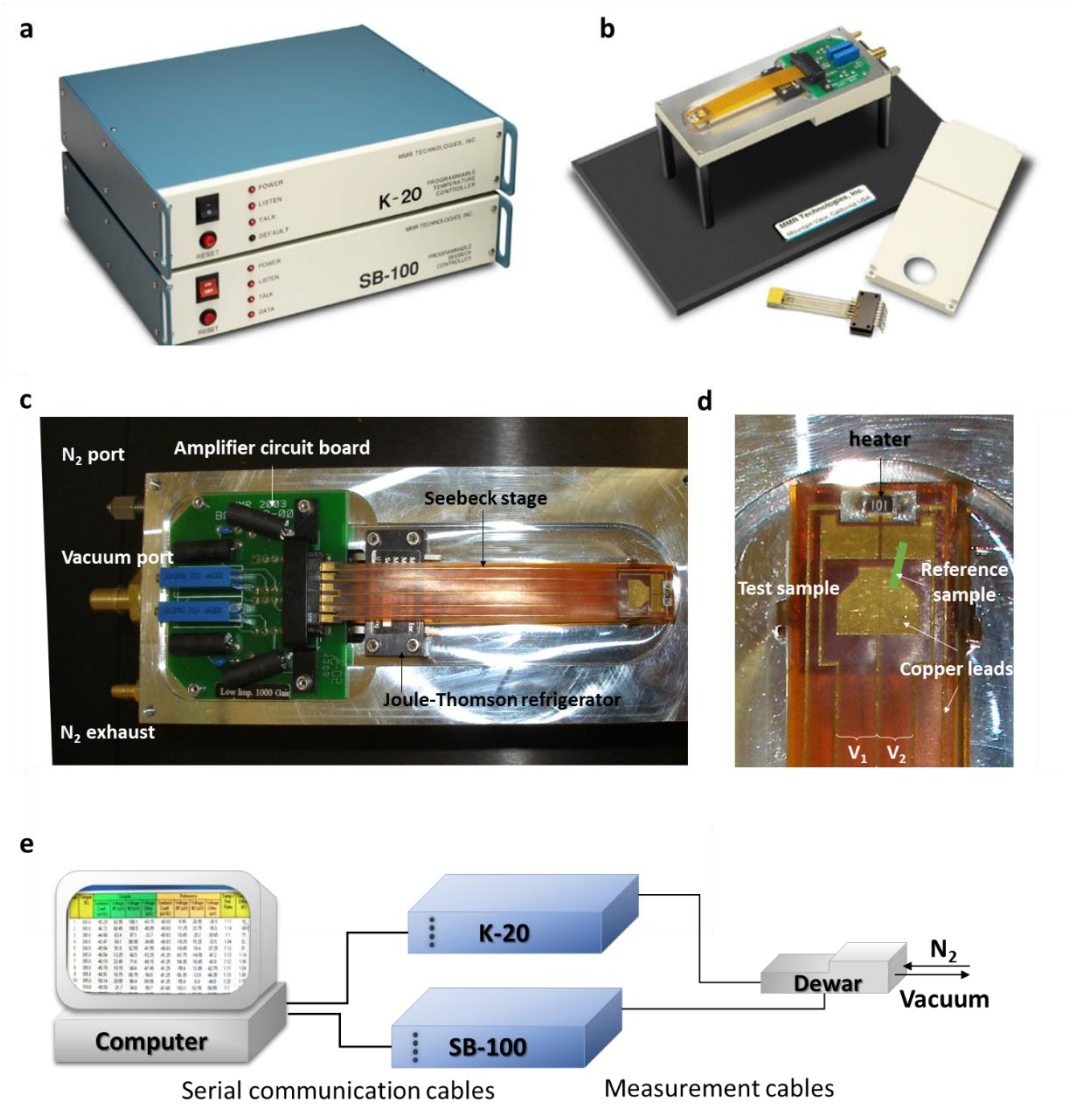

Figure 3.8 *Pictures of the MMR system. A picture of (a) the programmable refrigerator chamber controller (K20), (b) the programmable stage heater controller (SB100), (c) the variable temperature Seebeck system (Dewar) and (d) the Seebeck stage. (e) Schematic of the set-up for Seebeck coefficient measurements.*

Sample dimension of smaller than 1 mm width and 5 mm length are mounted on the Seebeck stage for testing. As Figure 3.8c shows, the Seebeck stage has 2 pairs of thermocouples including one pair for a reference sample and the other pair for the test sample. Each pair outputs voltages namely V_1 and V_2 are monitored by SB100. The heater is controlled by SB100 for heating one side of all samples, while the whole Seebeck stage are attached to the refrigerator that provides a given stable temperature for measurement. Therefore, when the power applied to the heater, a temperature difference between two ends of samples is applied. As a result, a voltage will be generated where $V_1 = a_1\,\Delta T(P)$ and $V_2 = a_2\,\Delta T(P)$,where $\Delta T(P)$ is the temperature difference created by the power (P) to the heater, which is same at both sides. Thus the Seebeck for test sample (a_1) can be calculated from the reference sample (a_2) using $a_1 = a_2 V_1 / V_2$. A small ΔT (~ 1 ^{o}C) are used in order to maintain the temperature in the chamber, so that the measurement results are not accurate due to the undesired substantial offset voltages. Therefore, two measurements on different power setting are used to eliminate the voltage offsets, and Seebeck coefficients for test sample will be $a_1 = a_2(V_1(P_1) - V_1(P_2)/\,(V_2(P_1) - V_2(P_2))$ where $V_1(P_1)$ and $V_1(P_2)$ indicate the V_1 value when the power applied to the heater the first time (P1) and the second time (P_2), and $V_2(P_1)$ and $V_2(P_2)$ is V_2 value when applied P_1 and P_2, respectively.

In this research, all samples were cut into 1mm × 4mm size film. The self-standing films were cut directly, others were cut with the flexible substrate, normally 125 μm thick polyethylene terephthalate (PET) films. Constantan wires are used as reference sample and they are mounted on the test sample side with the Ag paste for connection. It is worth to mention that ~ 0.1mm diameter Constantan wires were chosen due to requirement of equal heat flow through the reference sample and test sample. As a

reference and for easy daily application, 27 ^{o}C was set for the chamber for all the Seebeck coefficient measurement. Photo-Seebeck effect, i.e., the Seebeck effect to which the photo-induced carriers contribute, was measured by controlling light irradiation through a transparent window. A white fibre light source with wavelength range of 400-900 nm was used.

For Seecbeck coefficient measurements in this thesis without specific description, the Seecbeck coefficient is an average of 5 specimens for 20 measurements on each at room temperature. The Seecbeck coefficient change with time measurement is an average of 5 measurements results on a same specimen.

3.4.2 Electrical conductivity

Both 4-probe and 2-probe methods were used in this research. 4-probe method were used for determining the electrical conductivity of all 2D samples, which can eliminate the contact resistances and thus give a more accurate electrical conductivity result. 2-probe method was chosen for 1D samples and measurement in some chambers where 4-probe equipment cannot access.

Therefore, 2-probe method has been used to measure the electrical resistance change with humidity in **Chapter 4**, the resistance of coated yarns in **Chapter 5** and to compare resistance before and after folding in **Chapter 6**. A step voltage was applied by *Agilent 6614* DC power supply with the current measured by a *Keithley 6485* picoammeter simultaneously. The unit resistance of 1 cm length yarn was calculated by the slope of the of *I-V* curve using least squares linear fitting. Average values were taken from 30 specimens. The resistivity change in a temperature sweep was also obtained by the 2-point probe method. A tabletop probe station (*PS-100, Lakeshore*) equipped with a semiconducting parameter analyser (*Keithley, 4200SCS*) were used to

apply a step voltage and to measure the current. The temperature of the chamber was controlled by *Model 336, Lakeshore* controller under vacuum. The resistance of the sample at each temperature were calculated from the slope of each *I*-*V* curves.

4-probe method were used to measure all film-shaped samples in **Chapter 4** and **Chapter 6**. A bespoke four-point probe (0.25 mm probe space) made of an *Agilent 6614 System DC power supply* with *Keithley 6485 picoammete*r and *Keithley 2000 multimeter* were used for electrical conductivity measurements. In this system, 4 probes are linearly and equally spaced on the sample. With the voltage supplier and picoameter connected in the circuit with the 2 outer probes, a known current *I* is passed between the outer points of sample. Due to the sample size is much bigger than the probe space, the same current *I* can be considered to flow between the middle points. The voltage *V* between these two points is measured by the voltammeter. The sheet resistance can be determined from the slope of *V* and *I* directly, while the resistivity (ρ) should consider the electron distribution though the thickness of the sample which is defined as:

$$\rho = \frac{\pi t}{ln(2)} * \frac{V}{I} \qquad \textbf{\textit{Equation 3.1}}$$

where the *t* is thickness of the film which was test by a Bruker Dektak Vision 64 profilometer. The electrical conductivity is the inverse of the resistivity. In this research, 37.5 mm×25mm films on rigid and flat substrate glass slides, were used for testing, and results are averaged of at least 5 specimens with 20 measurements.

3.4.3 Mechanical test

Mechanical tests were performed by a tensile tester (*Instron 5566*). The tensile tests are performed according to the ASTM D882-02 standard. The strain rate was 100% min^{-1} if not specified. Films (**Chapter 4**) were cut by a D882-02 standard die, 40 mm

× 5 mm strips, and their thickness were measured by a calliper, while yarns (**Chapter 5**) are used as it is. The cross-sectional area of the Lycra yarns was calculated via the linear density, as detailed in **Section 5.2.1**.

The stress and strain are defined as the force per unit cross-sectional area of a material and the extension per unit length, respectively. The representative curves for tensile stress against strain were plotted. The Young's modulus was calculated from the slopes of linear stress-strain curve in the near-zero range and averaged out of 6 to 10 individual specimens. And strain-at-break also obtained from the plots as it is the ratio between elongation and initial length when sample breaks.

Three point bending test were used for composite plates in **Chapter 6** are following the ATSM D790 standard. The samples with thickness of ~ 3 mm were cut into 12.7mm width and the distance between two holding points was 48mm. A speed of 1mm min^{-1} was used.

3.4.4 Thermogravimetric analysis

The thermal stability was characterized through thermogravimetric analysis (TGA) by TA Instruments Q500 Thermogravimetric Analyzer using a programmed procedure to raise temperature from 20 ^{o}C to 900^{o}C by 10 ^{o}C min^{-1}. Isothermal measurements were performed for 10-15 min at both the start and end temperature.

3.4.5 Ultraviolet-Visible spectroscopy

Ultraviolet-Visible (UV-vis) spectra of the NL solutions with different concentrations were obtained using a *Perkin Elmer Lambda 35* at a wavelength between 300 nm and 900 nm. The absorption spectra were used to detect electronic transitions at the ground state and the excited state. This technique was used in **Chapter 4** to confirm the homogeneity of the $Na_x(Ni\text{-}ett)_n$/Lycra solutions using Beer-Lambert law (*i.e.*,

absorptivity is in proportion to concentration of the sample) and to estimate the band gap of the pure $Na_x(Ni\text{-}ett)_n$ using the Tauc plot method [148]. DMSO as background spectrum was eliminated from the sample's spectrums. All concentration solutions have been diluted by DMSO for 100 times to be detectable.

3.4.6 Scanning electron microscopy

Scanning electron microscopy (SEM, *FEI Inspect F*) was used to image the morphology of samples. 10 kV accelerating voltage was used for composite films and 3 kV for yarns. For the evaluation of the cross-section, samples were cryo-fractured in liquid nitrogen.

3.4.7 Raman spectroscopy

The Raman spectra were collected from an inVia Qontor confocal Raman microscope with a 633 nm laser source for 5% 10% power at 50X magnification.

3.4.8 Optical microscopy

Optical microscopy images were obtained by an Olympus BX60 microscope equipped with an Olympus SC100 digital camera, in reflection mode without polarizers.

3.4.9 Infrared camera

Thermographic images were produced using an infrared camera (*FLIR E40*) for monitoring the temperature gradient and temperature change in time. The sample's temperature change in time was measured and analysed using the FLIR software.

3.4.10 Impedance spectroscopy

Impedance spectra were measured using an Autolab Frequency Response Analyser FRA2 with a potential stat PGSTAT10 (*Windsor Scientific, U.K.*) for understanding the composite films' electrical conductivity change with humidity in **Chapter 4**. It is

operated under an AC amplitude of 100 mV peak to peak, DC off-set potential 0 V, and 10 Hz to 10 MHz frequency range. A *Keysight E4980A* in a four-terminal pair configuration in the frequency range of 20 Hz to 10 MHz was used for measuring coated yarns in **Chapter 5** to understand the mechanism of the tuneable and ultrahigh sensitivity to deformation. Two ends of the yarn are fixed on a frame at the start distance of 10 mm and connected to the copper wire electrodes with carbon grease paste. Impedance measurements were operated at different strains of the yarn, which was stepped stretched up to 300% strain by the frame.

3.5 Characterization of TE devices

3.5.1 Thermal voltage and power output

The thermal voltage and power output were measured by connecting the ends of the materials or fabricated generator at a given temperature difference. The thermal voltage output was measured directly by a *Keithley 2000* Multimeter. For power output measurements, a variable resistor (range from 0 Ω to 999 MΩ) was connected in the circuit. Voltage and current were recorded simultaneously with the resistor change from 0 Ω to 999 MΩ. The power output is the product of voltage and current, and maximum power output was obtained when the external resistance equals to the resistance of the test materials/devices.

3.5.2 Sensor demonstration

External strain sensor:

For external sensor demonstration, the resistance change during stretching (**Chapter 4&5**) and bending (**Chapter 6**) was recorded by an *Agilent 34401A 6½* digital multimeter in 2-point resistance measurement model. The extension values were acquired from the tensile tester and synchronized with the resistance data.

Wireless strain sensor:

For the wireless strain sensor demonstration of the coated yarns presented in **Chapter 5**, the sensor is attached to the joint of index finger and the finger movements were detected by the resistance change of the yarn. A Bluetooth® low energy module (BLE, *Adafruit Feather nRF52 Bluefruit LE*) based on a Nordic chip (*nRF52832*) was used to read the voltage of the sensor on an analog-to-digital converter. The electrical resistance of the sensor (ΔR_{sensor}) was calculated based on the reference resistor (R_1) in BLE as Figure 3.9 by $R_{sensor} = (3.3/U)*R_1 - R_1$. Where U is the voltage measured across R_1. The data were sent to a smartphone via BLE and was plotted in real-time.

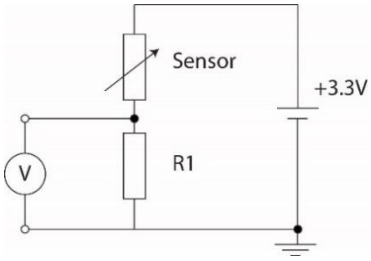

Figure 3.9 *The equivalent circuit of the wireless strain sensor system.*

Self-powered sensor:

For self-powered sensor demonstration, heater mats (*RS, 12 V dc, 7.5 W, item 245-556 and RS, 12 V dc, 1.25 W, item 245-499*) were applied on one side of the sensor, and the other end was maintained at room temperature to obtain a constant temperature difference at extremities.

For the self-powered strain sensor in **Chapter 4**, a load resistor (100MΩ) and a picoammeter (*Keithley 6485*) was connected to the sensor in series, and a voltmeter (*Keithley 2000 Multimeter*) was connected to the load resistor in parallel to record the both current and voltage output change with different stimuli. For the high sensitivity yarn in **Chapter 5** and structural composites in **Chapter 6** a picoammeter (*Keithley*

6485) was connected to the sensor. Without the external load, the 'short-circuit' current only corresponds to the sample's inner resistance change, thus, the current signal is more sensitive to deformation than that of the connection for **Chapter 4**.

Apart from the mechanical stimulation, fibre optical light source (*Coherent, model 1-150*) was used for visible light sensitivity tests, with irradiation intensity measured using a monocrystalline silicon reference cell (*SRC-1000-TC-QZ, VLSI Standards, Inc.*). For the self-powered temperature (gradient) sensor, a controllable temperature was applied at one side using a commercial thermoelectric module. The actual temperature was measured using a thermal couple. The voltage signal was collected using a multimeter (*Keithley 2000*) in real time.

Sensitivity to humidity (Chapter 4):

A bespoken humidity controller for testing the samples' humidity sensitivity. 0.6 L min^{-1} of nitrogen gas with a different humidity was flown into a ~ 700 cm^3 chamber which takes ~ 600 s for stabilization. A commercial humidity sensor (*Fisher brand*) was used for calibration (Figure 3.10). Impedance, resistance and voltage output were measured using electrodes connected out of the chamber.

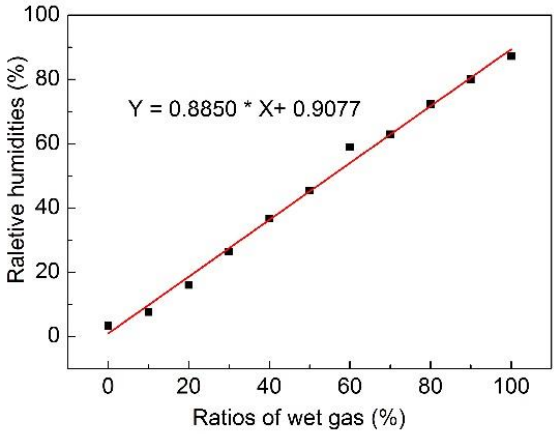

Figure 3.10 *Calibration the bespoken relative humidity chamber controlled by the percentage of the dry air and wet air at 20 °C.*

Chapter 4 $Na_x(Ni\text{-}ett)_n$/polyurethane composites as self-powered sensors

4.1 Introduction

As mentioned in **Chapter 2**, thermoelectricity is recognised as a very reliable and durable potential energy harvesting phenomenon for self-powered sensors [149-151], exploiting temperature gradients. The first work for applications of organic thermoelectricity (OTE) as flexible self-powered sensors is the PEDOT:PSS coated foam for sensing both pressure and temperature [152]. A self-powered vapour sensor, based on CNTs, was also reported [153]. Recently, our group has developed new stretchable and tough composites made of a commercial PU and PEDOT:PSS, which could autonomously sense strain [147]. However, reports are very limited and only p-type OTE materials have been studied so far. In order to generate higher power outputs, it is essential to have an n-type OTE counterpart, so that series connected p-n junctions can be designed.

The organometallic coordination polymer, $Na_x(Ni\text{-}ett)_n$, has been reported to possess excellent n-type TE properties [58, 154, 155], including a Seebeck coefficient of -80 $\mu V\ K^{-1}$ and an electrical conductivity of ~ 42 $S\ cm^{-1}$, combined which a relatively good air-stability and simple synthesis [154]. More recently, values of room temperature Seebeck coefficient of -128 $\mu V\ K^{-1}$ and $ZT \sim 0.3$ have been reported for Poly(Ni-ett) prepared by electrochemical deposition [58]. A number of challenges still restrict its commercial exploitation, including low toughness and tear resistance, in addition to poor solubility and processability. Besides, another challenge is related to OTE devices. The typical in-plane π-shape architecture obtained by an assembly process of p- and n-type legs, connected in series by, typically, metal contacts. This assembly

process is time consuming, hardly scalable and the resulting structure, with metal contacts, is rigid and brittle.

Therefore, in this chapter, a highly stretchable n-type TE composite based on PU (Lycra®) and $Na_x(Ni\text{-}ett)_n$) is presented to overcome all these limitations. For instance, a 50/50 composite has a high elongation to break of 500% (more than 5 times its initial length) combined with a relatively high absolute Seebeck coefficient (-40 μV K^{-1}). The composites are able to harvest sufficient power, even from small temperature differences (< 20 ºC), to autonomously sense a number of stimuli, such as strain, visible light and temperature. Moreover, by exploiting the enhanced processability of TE polymer compounds, we propose new manufacturing strategies and designs to overcome the shortfalls. The composites could simply be joined by hot pressing into a series-connected multi-leg TE flexible and stretchable devices. Origami-inspired TE devices with different configurations are also presented.

4.2 Results and discussion

4.2.1 Morphological and mechanical properties

Pure $Na_x(Ni\text{-}ett)_n$, synthesized according to a procedure described by Menon *et al.* [155] does not dissolve in common solvents and does not form coherent films. However, Lycra®, a commercial PU-based synthetic fibre commonly used for elastic skin-tight garments and sports attires and was used as an elastomeric matrix for coherent, flexible, and stretchable films containing $Na_x(Ni\text{-}ett)_n$. Thus, a series of $Na_x(Ni\text{-}ett)_n$/PU self-standing composite films (called "NL films" from here on), with $Na_x(Ni\text{-}ett)_n$ contents ranging from 10 to 70 wt.%, has been prepared by solution mixing and drop-casting.

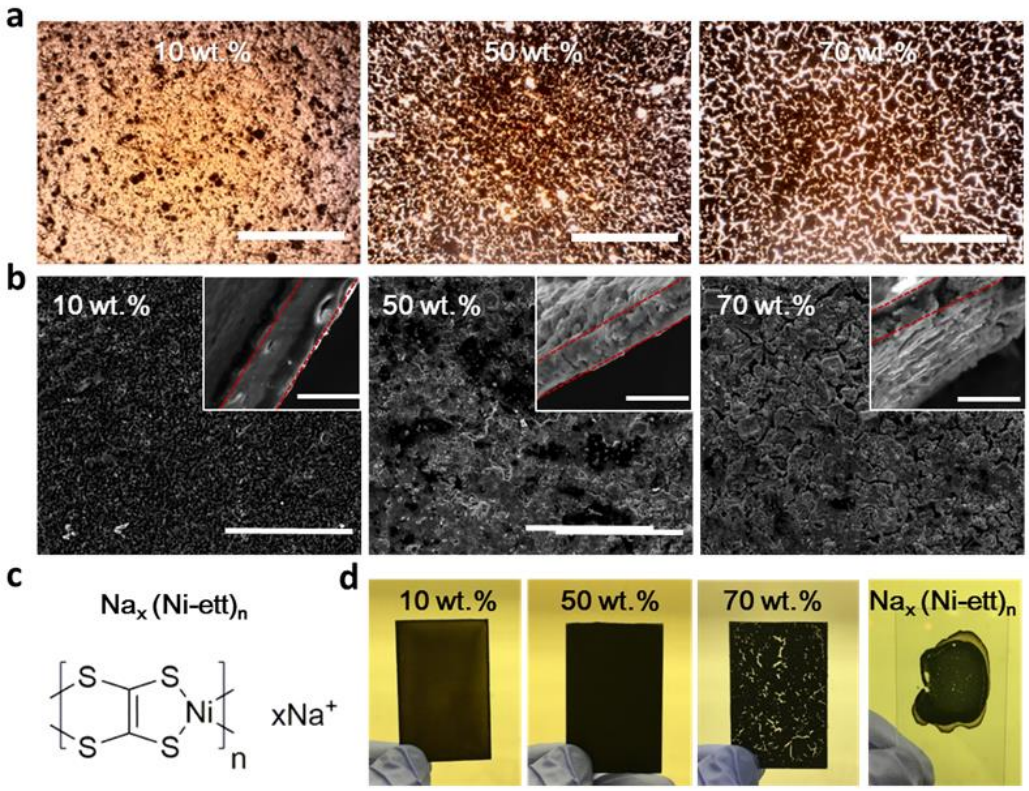

Figure 4.1 *Morphological studies of NL films containing different $Na_x(Ni\text{-}ett)_n$ concentrations. (a) Optical microscopy pictures (scale bars are 500 μm), (b) scanning electron microscopy of top surface (scale bars are 100 μm) and cross sections (inset; scale bars are 10 μm) of one layer 10, 50 and 70 wt.% NL films; broken red lines identify the borders of the cross sections; (c) $Na_x(Ni\text{-}ett)_n$ chemical structure; (d) digital optical pictures of multi-layer NL films on glass slides.*

A systematic study of the NL film morphology is presented for various $Na_x(Ni\text{-}ett)_n$ loadings. Optical transmission microscopy (Figure 4.1a) of relatively thin drop-casted films (typical thickness of 5-8 μm) reveals that a $Na_x(Ni\text{-}ett)_n$ loading higher than 50 wt.% generates inhomogeneous and incoherent films, as a result of an extended agglomeration of $Na_x(Ni\text{-}ett)_n$ particles. Scanning electron microscope (SEM) is used to further investigate the external surface morphology (Figure 4.1b) and cross-sectional areas (insets of Figure 4.1b) of 10, 50 and 70 wt.% NL films. For low $Na_x(Ni\text{-}ett)_n$ contents (*e.g.* 10 wt.%), a relatively good dispersion can be observed. For loading above 50 wt.%, the agglomeration of $Na_x(Ni\text{-}ett)_n$ particles, appearing as dark dots, is

evident. NL films, containing $Na_x(Ni\text{-}ett)_n$ concentration higher than 70 wt.%, present cracks and defects throughout the whole volume of the sample, confirming the inability of both $Na_x(Ni\text{-}ett)_n$ and PU to form a coherent matrix. SEM images of the cross-sectional areas show that a porous structure emerges with increasing $Na_x(Ni\text{-}ett)_n$ content. To improve the coherence of NL films at high $Na_x(Ni\text{-}ett)_n$ content, the film thickness (typical thickness of 5-8 µm) is increased by depositing multiple drop casted layers. This allows even NL films with more than 70 wt.% of $Na_x(Ni\text{-}ett)_n$ to be peeled off from the glass substrates and to be tested for their mechanical properties.

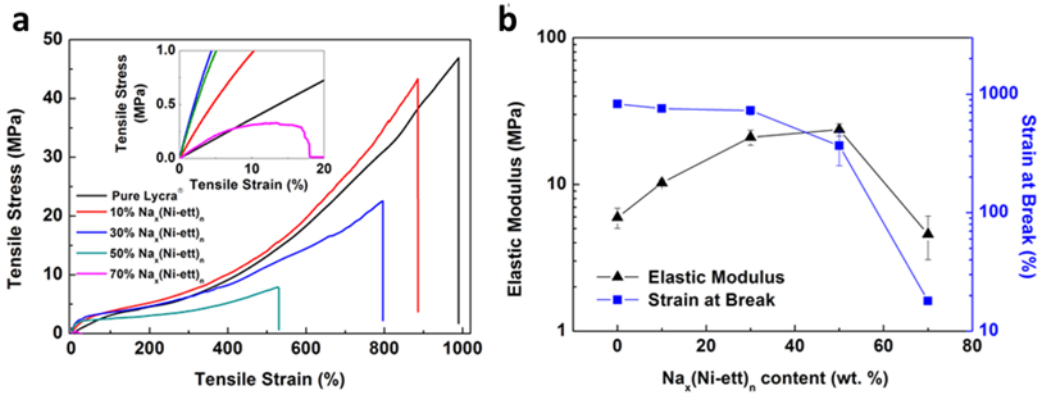

Figure 4.2 *Mechanical studies of NL films containing different $Na_x(Ni\text{-}ett)_n$ concentrations. (a) Typical stress-strain curves and (b) elastic modulus and strain-at-break of self-standing NL films. Error bars represent the standard deviation.*

Typical stress-strain curves of NL films are shown in Figure 4.2a. The strain-at-break monotonically decreases with increasing $Na_x(Ni\text{-}ett)_n$ content (from ~ 1000% of pure PU films down to (18.0 ± 0.2)% for the 70 wt.% NL film) while the elastic modulus increases (from (6.0 ± 0.9) MPa for pure Lycra® to (23.6 ± 2.3) MPa for the 50 wt.% NL film) (Figure 4.2b). This is the typical behaviour of polymer composites containing rigid brittle particles, described by many micromechanical models [156]. $Na_x(Ni\text{-}ett)_n$ concentrations higher than 50 wt.% results in inhomogeneous, brittle films and a decrease of both elastic modulus and strain-at-break. NL films with a $Na_x(Ni\text{-}ett)_n$

content lower than 50 wt.% are potentially excellent candidates for stretchable strain sensors, provided that they retain the thermoelectric properties of $Na_x(Ni\text{-}ett)_n$.

4.2.2 Thermoelectrical properties

In order to evaluate the thermoelectric properties of the NL films and their potential use in self-powered sensors, both Seebeck coefficient (α, μV K^{-1}) and electrical conductivity (σ, S cm^{-1}) have been measured. The corresponding power factor (PF, μW m^{-1} K^{-2}) have been calculated according to: $PF = \alpha^2 \times \sigma$. The usual inverse relationship between α and σ, requiring trade-off in traditional inorganic TE materials, is not observed here. Figure 4.3a shows a monotonic trend for α and σ, both increasing with the $Na_x(Ni\text{-}ett)_n$ content. The behaviour of σ with the $Na_x(Ni\text{-}ett)_n$ amount is expected from percolation theory [157]: the conductivity increases due to a densifying conductive network until it reaches a plateau determined by the conductivity of $Na_x(Ni\text{-}ett)_n$. The trend of the Seebeck coefficient is less intuitive but not unusual for heterogeneous composite systems [158, 159]. This phenomenon has been explained by enhancement of carrier mobility as the percolated network becomes more robust upon densification [160].

The PF of the NL composite films reaches 0.9×10^{-3} μW m^{-1} K^{-2} and 1.3×10^{-3} μW m^{-1} K^{-2} for films with $Na_x(Ni\text{-}ett)_n$ concentration of 50 wt. % and 70 wt. %, respectively (b). An accurate *ZT* value cannot be reported as the thermal conductivity (κ) of the films is difficult to measure in the in-plane direction. However, an upper limit of thermal conductivity can be predicted from the values relative to the individual phases: ~ 0.15 W m^{-1} K^{-1} for polyurethane [161] (a polymer similar to Lycra) and ~ 0.2 W m^{-1} K^{-1} for $Na_x(Ni\text{-}ett)_n$ (at 27 °C) [154] by a simple series-model and parallel model. For parallel model [1], each phase is assumed to contribute independently to the overall

heat transfer. So the totally thermal conductivity of the NL films (κ_t) is proportionally to its volume fraction:

$$\kappa_t = \kappa_n \Phi_n + \kappa_l \Phi_l \qquad \textbf{Equation 4.1}$$

where κ_n, κ_l are the thermal conductivity of $Na_x(Ni\text{-}ett)_n$, and Lycra® respectively, and Φ_n and $\Phi_l$are the volume fractions of them. The weight fractions (m) of them are known, the density (ρ) of pure $Na_x(Ni\text{-}ett)_n$ is 1.62 g cm^{-3} by calculating from the gravimetric measurements of NL films, and the density of Lycra® is 1.06 g cm^{-3}. Therefore, $\Phi_n$and $\Phi_l$can be calculated as:

$$\Phi_n = \frac{m_n/\rho_n}{\frac{m_n}{\rho_n}+\frac{m_l}{\rho_l}} \qquad \textbf{Equation 4.2}$$

$$\Phi_l = 1 - \Phi_n \qquad \textbf{Equation 4.3}$$

Therefore, $\kappa_t(50) \approx 0.17$ W $m^{-1}K^{-1}$ and $\kappa_t(70) \approx 0.18$ W $m^{-1}K^{-1}$.

If assume no contact is confined to the $Na_x(Ni\text{-}ett)_n$, then the thermal conductivity can be predicted by a series model [1]:

$$\kappa_t = \frac{1}{\Phi_n/\kappa_n + \Phi_l/\kappa_l} \qquad \textbf{Equation 4.4}$$

Then, $\kappa_t(50) \approx 0.17$ W $m^{-1}K^{-1}$ and $\kappa_t(70) \approx 0.18$ W $m^{-1}K^{-1}$.

Therefore, the thermal conductivity of 50 wt. % NL film estimated is ~ 0.18 W m^{-1} K^{-1}, as a result, a *ZT* in the region of 3×10^{-7} can be expected. Compared to the results of the other poly(Ni-ett) materials [58, 154, 162], this is relative low, but it is comparable to polymer composites containing poly(Ni-ett) [62, 63, 163]. The low PF value is probably related to the low electrical conductivity. On the other hand, a low electrical conductivity combined with a filler content close to percolation threshold, can be beneficial to generate a highly sensitive resistive sensor. It is also worth to

mentioning that the temperature behaviour (Figure 4.3c,d) of the thermoelectric properties follows to the neat poly(Ni-ett) temperature behaviours.[16-17]

Due to its high extensibility (strain at break of ~ 500%) and thermoelectric properties, the 50 wt.% NL composite film is selected to further study its self-powered sensing ability, as presented in the following sections.

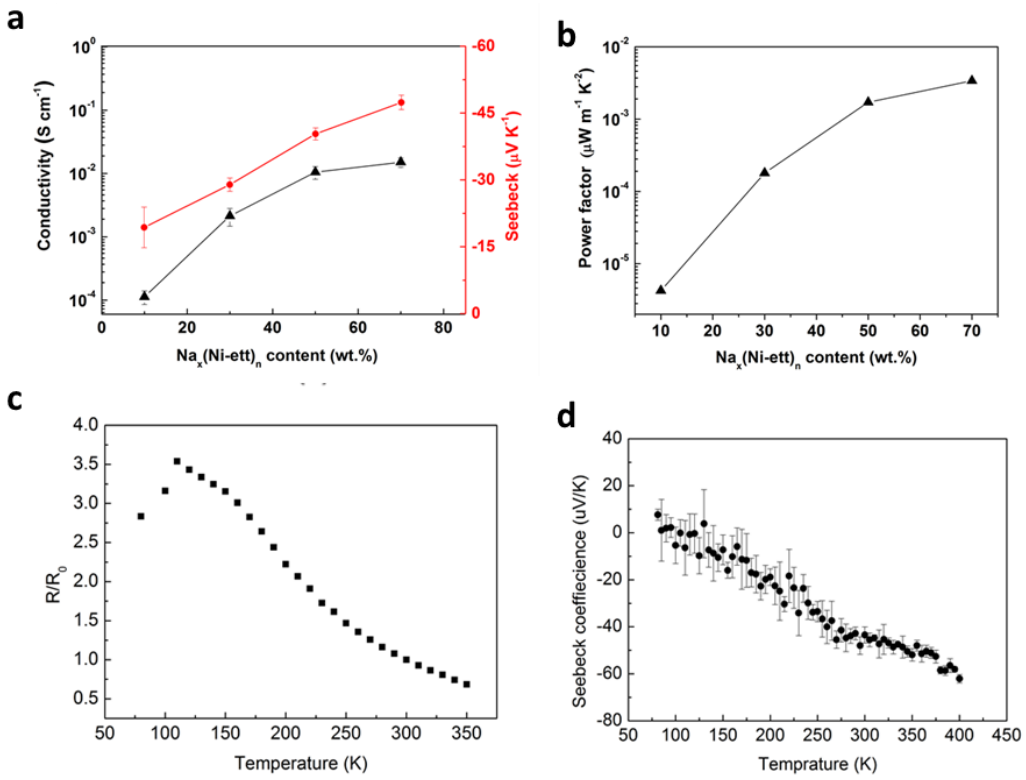

Figure 4.3 *Thermoelectric properties of NL films. (a) Electrical conductivity, Seebeck coefficient and (b) Power factor with different $Na_x(Ni\text{-}ett)_n$ content at room temperature. The (c) resistance and (d) Seebeck coefficient performance with temperature sweep of 50 wt% NL film. Error bars represent to the standard diviations calculated from 5 measuements at each temperture on the same sample.*

4.2.3 Self-powered strain sensing

To examine the capabilities of utilising the fabricated NL films as self-powered strain sensors, the electrical resistance and Seebeck voltage have been monitored *in-situ* at different strains.

In order to evaluate the strain sensitivity of the 50 wt. % NL film, a constant external power has been supplied to its extremities (Figure 4.5a). The electrical resistance has been measured while deforming the film uniaxially, at a constant extension rate, until break. The resistance variation ($\Delta R/R_0$, with $\Delta R = R - R_0$, where R is the electrical resistance at a given extension, and R_0 is the initial resistance) increases linearly with the extension (Figure 4.4). The strain sensitivity of a sensor is usually represented by its gauge factor, *GF*, defined as $GF = (\Delta R/R_0)/\varepsilon$ [164], where ε is the strain. Figure 4.4 shows that the *GF* exceeds 20, in the range of deformation between 5% and 50%, which is very high compared to the values of traditional metal-based strain gauges (~ 2) [165]. Notably, the gauge factor is also high (~ 13) at even larger strains between 50 and 300%. To the best of our knowledge this is the highest *GF* value reported at such high strains [166, 167].

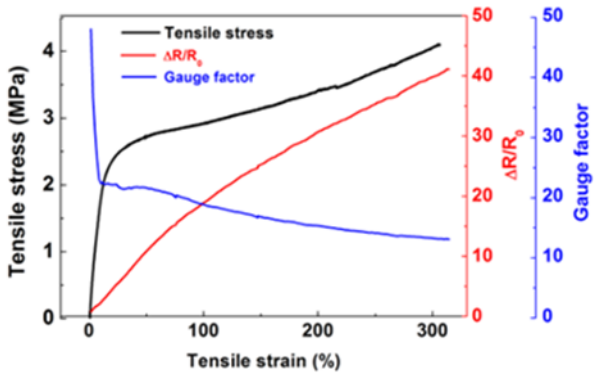

Figure 4.4 *Strain sensitivity of 50 wt.% NL films. Typical stress-strain curves with its resistance variation ($\Delta R/R_0$) and corresponding gauge factor, as a function of applied strain.*

The change in electrical resistance in our sample upon uniaxial deformation probably originates from two concurrent factors: the dimensional changes of the sample, and the changes in the conductive network (*i.e.* changes in the composite electrical resistivity). The geometrical contribution, $\frac{\Delta R_g}{R_0} = \varepsilon(2 + \varepsilon)$ [168] (assuming that the

volume of the material remains constant), is not sufficient to explain the experimental resistance variation (Figure 4.5b). The percolated network formed by the conductive $Na_x(Ni\text{-}ett)_n$ domains must be affected by the uniaxial deformation, *i.e.*, the intrinsic conductivity of the NL films must change with strain.

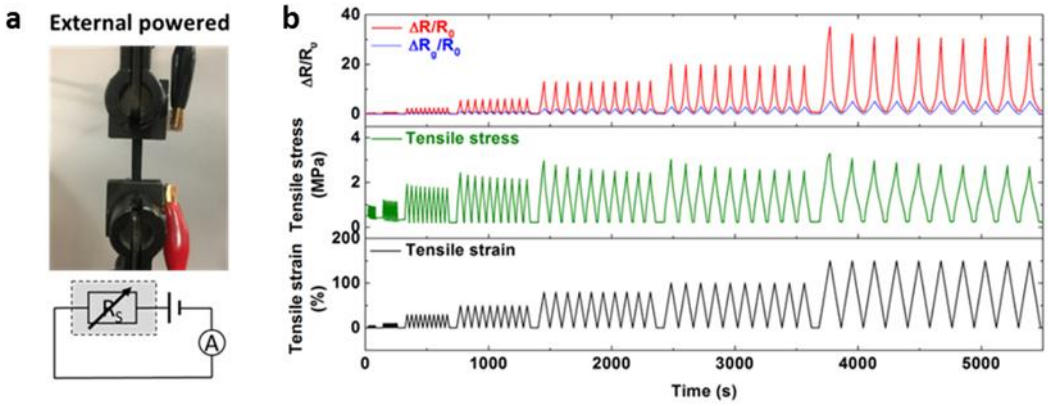

Figure 4.5 *Demonstration of externally powered strain sensor. (a) The set-up and schematic circuits of the externally powered strain sensor. The grey rectangles refer to the equivalent elements of the film during measurements; R_s is the NL film's internal resistance. (b) Actual and geometrical resistance change under cyclic tensile strains applied.*

To demonstrate the concept of self-powered (strain) sensing based on the TE effect, a constant temperature difference (ΔT ~ 50 ^{o}C) is applied to the 50 wt.% NL film, by fastening a heat pad to one end of the film, via the lower clamp of the tensile testing set-up (Figure 4.6a, c). A thermal voltage developed along the film, in proportion to the temperature difference. When the sample is connected in series to a resistor, R_L, a thermal current can also be generated. Figure 4.6b shows that both current and voltage change as a function of the imposed strain (applied in a sequence of different cycles with max strains of 5, 10, 30, 50, 80 and 100%), demonstrating the ability to sense and generate thermoelectric power simultaneously. The simultaneous change in voltage and current with strain can be explained in the equivalent circuit of Figure 4.6a. The

constant temperature difference along the film generates a voltage *(U)*, which is assumed to be independent of the strain. However, the increase in sample resistance (R_s) with the strain lowers the current generated: $I(\varepsilon) = \frac{U}{Rs(\varepsilon)+RL}$. Consequently, the voltage measured across the resistor is smaller ($V(\varepsilon) = I(\varepsilon)RL$), in agreement with the signal of voltage and current as shown in Figure 4.6b. Therefore, based on the specific application, either signal can be chosen for sensing.

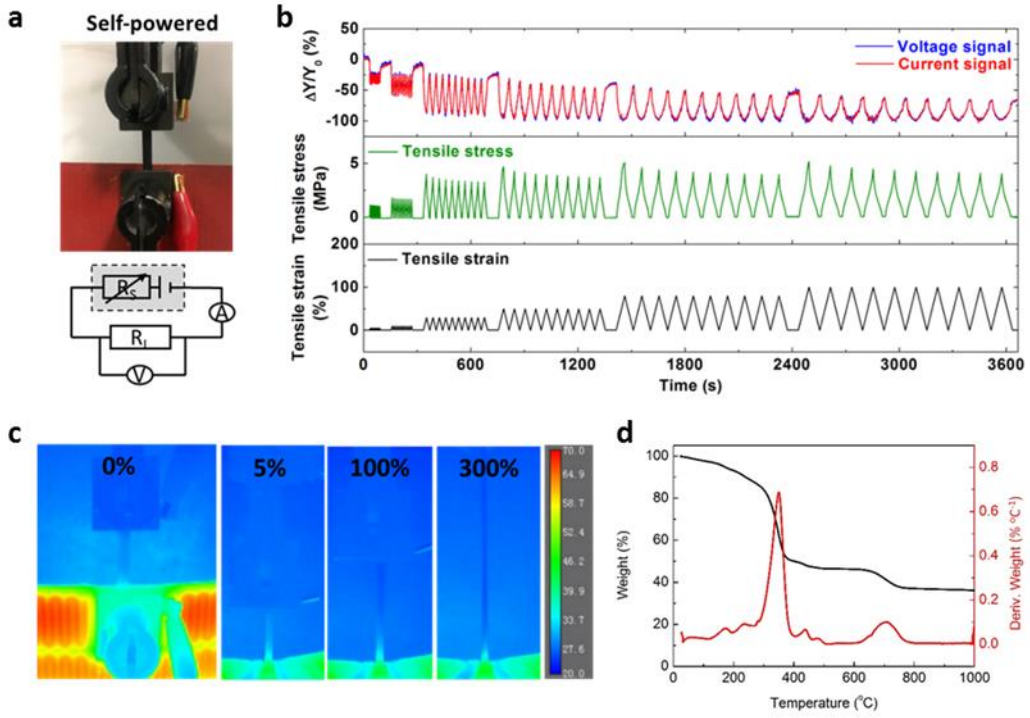

Figure 4.6 *Demonstration of self-powered strain sensor. (a) The set-up and schematic circuits of the self-powered strain sensor. The grey rectangles refer to the equivalent elements of the film during measurements; R_s is the NL film's internal resistance and R_L is the external load. (b) Real-time signals change ($\Delta Y/Y_0$ refers to the change percentage of voltage or current) with cyclic tensile strains. (c) Infrared pictures of the temperature difference along the film by contacting one end with a heating pad (T ~ 70 °C), and deformed at different strains. (d) Graph of Thermo Gravimetric Analysis (TGA) for $Na_x(Ni\text{-}ett)_n$ under 40 ml min^{-1} air atmosphere, from room temperature to 1000 °C at 10 °C min^{-1} heating rate.*

It should be noted that there is a limit to the maximum temperature difference that can be effectively employed. The lower bound of the cold side temperature is related to the glass transition temperature of Lycra (below -60 ^oC) [169]. The hot side temperature is limited by the softening temperature of Lycra (~180 ^oC [170]), well before reaching the degradation temperature of $Na_x(Ni\text{-}ett)_n$ (~ 340 ^oC, Figure 4.6d). Even at lower temperatures, there might be some non-recoverable deformations and viscoelastic stress relaxation effects, as shown in Figure 4.6b (hot side: 75 ^oC). In the specific case of the NL films, the maximum temperature difference can be estimated to be approximately 70 ^oC , and the maximum voltage generated is ~ 3 mV (for a single film).

4.2.4 Self-powered visible light sensor

The same NL films can simultaneously sense other stimuli, like visible light. A 50 wt.% NL film was irradiated with visible light fibre source (wavelength ranging from 400 to 900 nm), at different radiation intensities, while maintaining a ΔT_0 ~ 50 ^oC. Considering that the charge carrier density could be affected by the light, it is important to characterise the Seebeck coefficient and the electrical conductivity before and during irradiation. Figure 4.7a demonstrates that the Seebeck coefficient and conductivity do not change significantly at an irradiation intensity of 2 kW m^{-2}, when the surrounding temperature is controlled, which excludes any photo-Seebeck effect or photoelectric effect. In fact, it can be seen that the main effect of light irradiation is a change of the sample temperature (Figure 4.7b). The experimental linear relationship between light intensity and sample equilibrated temperature can be used to design a visible light sensor. In analogy to the aforementioned strain sensing case, the sensitivity to visible light irradiation is first characterised using an external electrical power source. As shown in Figure 4.7c, the electrical resistance linearly decreases

with light intensity. This is related to the increase in sample temperature and corresponds to the typical response of organic and polymeric semiconductors. Higher temperatures increase the electrons' kinetic energy and the likelihood of electrons to transit from the valance band to the conductive band (Figure 4.8), *i.e.*, thermal excitation of carriers into the conduction band.

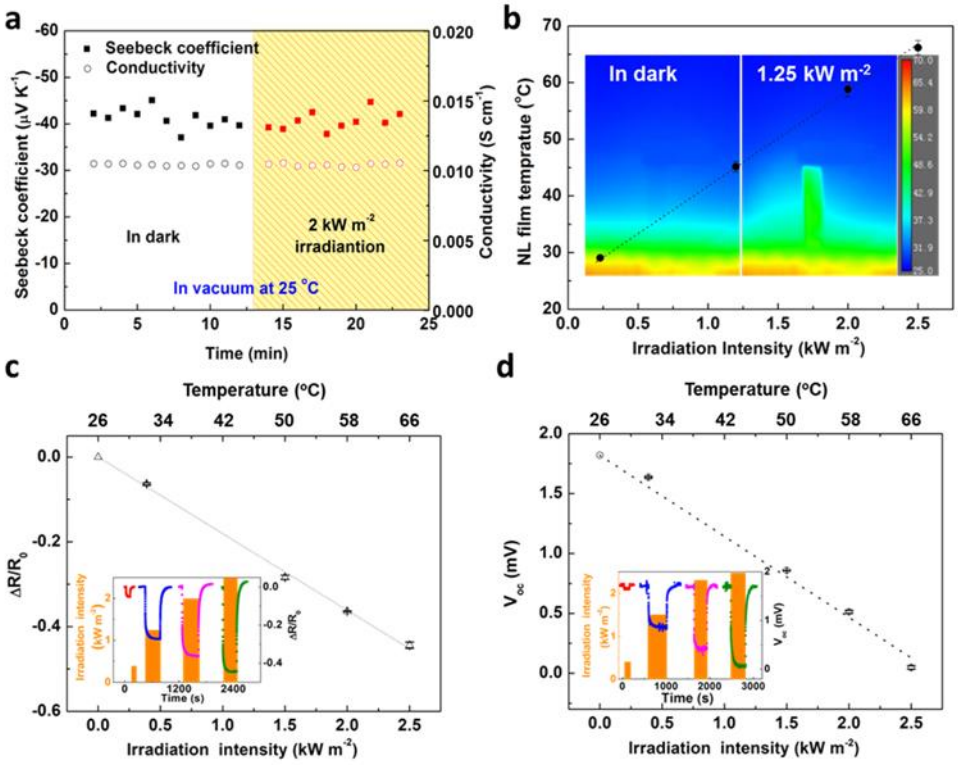

Figure 4.7 *Sensitivity to visible light irradiation of 50 wt.% NL film. (a) Seebeck coefficient and electrical conductivity of 50 wt.% NL film, measured in vacuum and under controlled temperature, with/without irradiation. (b) The sample temperature changes with 30 s interval of light at different intensity irradiations, and a representative infrared camera image. (c) Electrical resistance variation and (d) open circuit voltage (V_{oc}) change with different irradiation intensities, averaged over 5 cyclic tests (representative signal curves of these cyclic tests are shown in the insets). Error bars in (c, d) represent the standard deviations.*

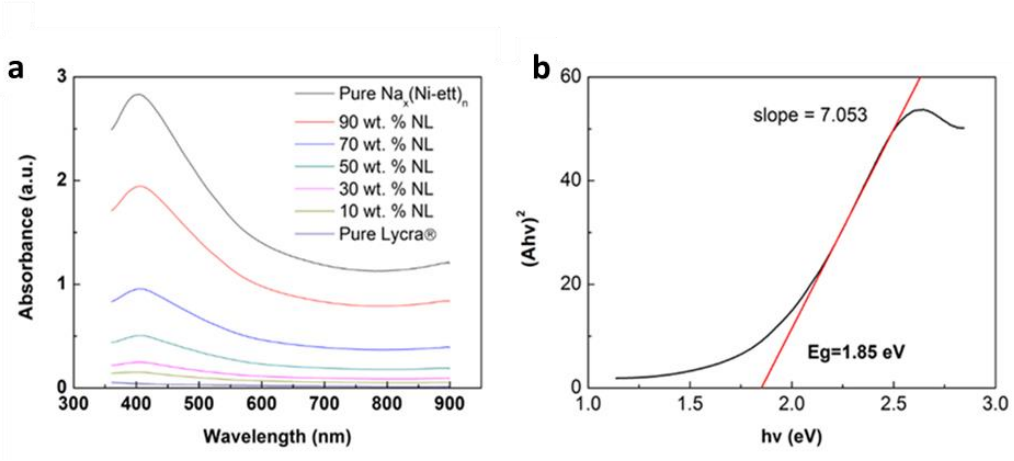

Figure 4.8 *Ultraviolet–visible (UV-vis) spectrum of (a) NL DMSO solutions mixed by different ratios of 1 wt. % Lycra® and 5wt. % $Na_x(Ni\text{-}ett)_n$ solutions. All the solutions have been diluted by 100 times. (b) Band gap of the pure $Na_x(Ni\text{-}ett)_n$ is ~1.85 eV, calculated by Tauc plot method as direct semiconductor.*

For the evaluation of self-powered sensor, the power output as a function of the temperature change (ΔT) was measured. The sample was irradiated whilst simultaneously applying a temperature difference using the same set-up as in the self-powered strain sensing experiments. In this case, the open-circuit voltage, U suddenly decreases upon irradiation (insets of Figure 4.7d). Figure 4.7d shows that a linear correlation exists between U and the irradiation intensity, linked to the Seebeck effect: $U = \alpha \Delta T$, where the light irradiation heats the whole film including the cold side, thus the temperature difference (ΔT) between the ends of the film decreases and the generated thermal voltage U becomes smaller. We can use the measured open-circuit voltage to calculate the temperature difference across the film ($\Delta T = \frac{U}{\alpha}$) and sample temperature (and irradiation intensity using the linear relationship in Figure 4.7b) by $T = \Delta T_r - \frac{U}{\alpha}$, where the ΔT_r is the referenced constant temperature difference which in this case is 70 ^{o}C. Cyclic tests also have been performed at different light intensities over a time interval of 30 s, followed by 30 s of light off (Figure 4.9c). Even under the

cyclic irradation with 2 kW m^{-2} intensity and 300s on and off applied, the film still shows a good reproducibility, stability and reversibility (Figure 4.9a,b).

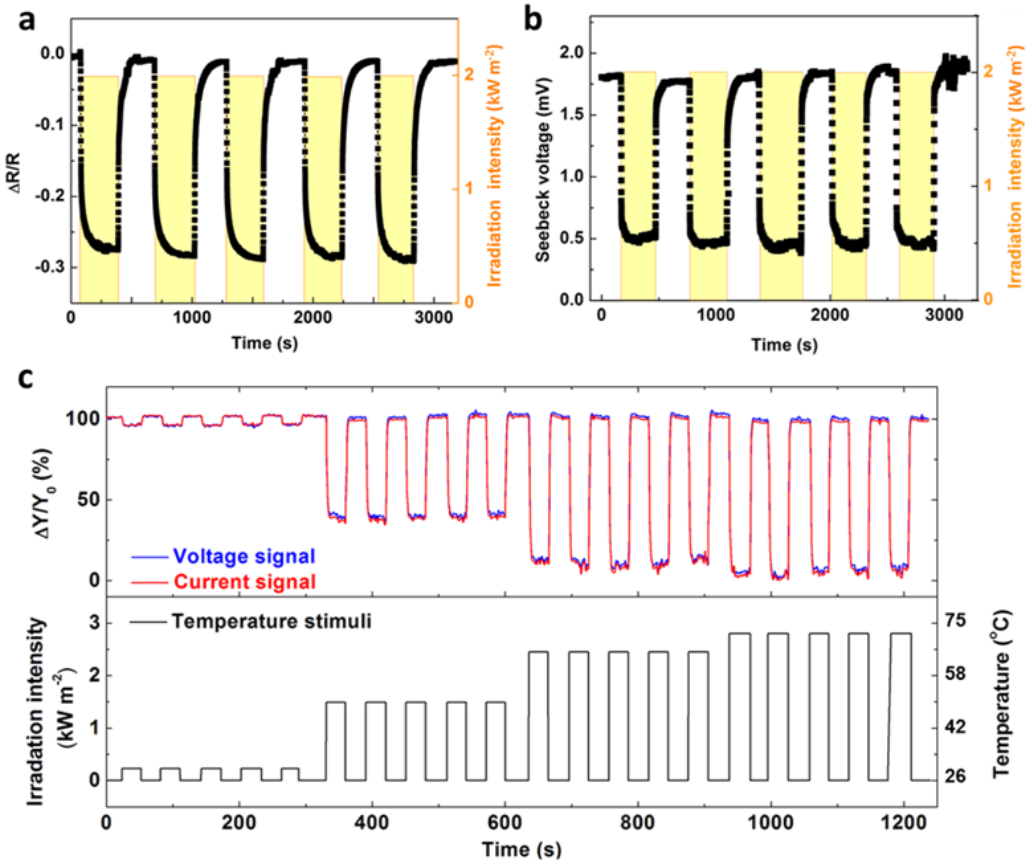

Figure 4.9 *Demonstration of self-powered visible light sensor. (a) The normalized resistance and (b) Seebeck voltage change with a cyclic test under intensity of 2 kW m^{-2}. (c) Signals change ($\Delta Y/Y_0$ is change percentage of voltage across or current through the 10 kΩ load resistor), recorded while irradiated cyclically over time.*

Using the same measurement circuit as in the case of strain sensing, the normalised current and voltage can be recorded. We define a sensitivity factor (SF), analogous to strain gauge-factor, as:

$$SF \equiv \left|\frac{\Delta Y/Y_0}{\Delta X}\right| \qquad \textbf{Equation 4.5}$$

where ΔX, ΔY refers to the change in environment stimuli and NL films response signals, respectively. Y_0 is the initial value of the NL films response signal. Here, the

resistance signal to irradiation SF is ~ 18% $(kW\ m^{-2})^{-1}$ and the open circuit voltage SF is ~ 36% $(kW\ m^{-2})^{-1}$. It is also worth to underline that it is possible to discriminate the signals caused by light irradiation from those caused by a mechanical strain [143]. By recording the *I-V* curve of the materials, the I-intercept changes can be used to measure the irradiation intensity and/or temperature (difference) change. The slope of the *I-V* curve changes (*R*) can be used to record the strain.

4.2.5 Sensitivity to humidity

In an attempt to explore sensitivity to other stimuli and, equally importantly, exclude problems of cross-sensitivities, the effect of relative humidity (RH) on the thermoelectric properties of the 50 wt. % NL film was studied. The resistance variation of the externally-powered sensor placed in a controlled humidity chamber is barely affected by the humidity, both in the case of a quasi-static (Figure 4.10a,b) and cyclically increasing (Figure 4.10c,d) values of humidity. A lower than 12% can be detected when RH increases from 5% to 90% (Figure 4.10a), which gives a SF as small as ~ 0.1 % $(\%RH)^{-1}$ (according to Equation 4.5). This small resistance variation can be explained by the presence of a polar solvent [171] (water), which can reduce the Coulombic interactions between the Na^+ ions in Ni-ett and increases their mobility. This hypothesis is compatible with the very weak ionic behaviour that can be observed in our sample: Figure 4.10b shows the perfect semi-circuits. Although, electrical and ionic conductivity [171] are jointly present , the weak humidity dependence of the resistance (Figure 4.10c) indicates that electronic conductivity is dominant. At a ΔT ~ 25 ^oC, the open-circuit voltage *U* is essentially independent from RH (Figure 4.10d), with very small fluctuations induced by air flow.

The simultaneous self-powered sensitivity to strain and temperature and insensitivity to humidity of our NL films might be particularly desirable in certain applications like in smart packaging and wearable technologies.

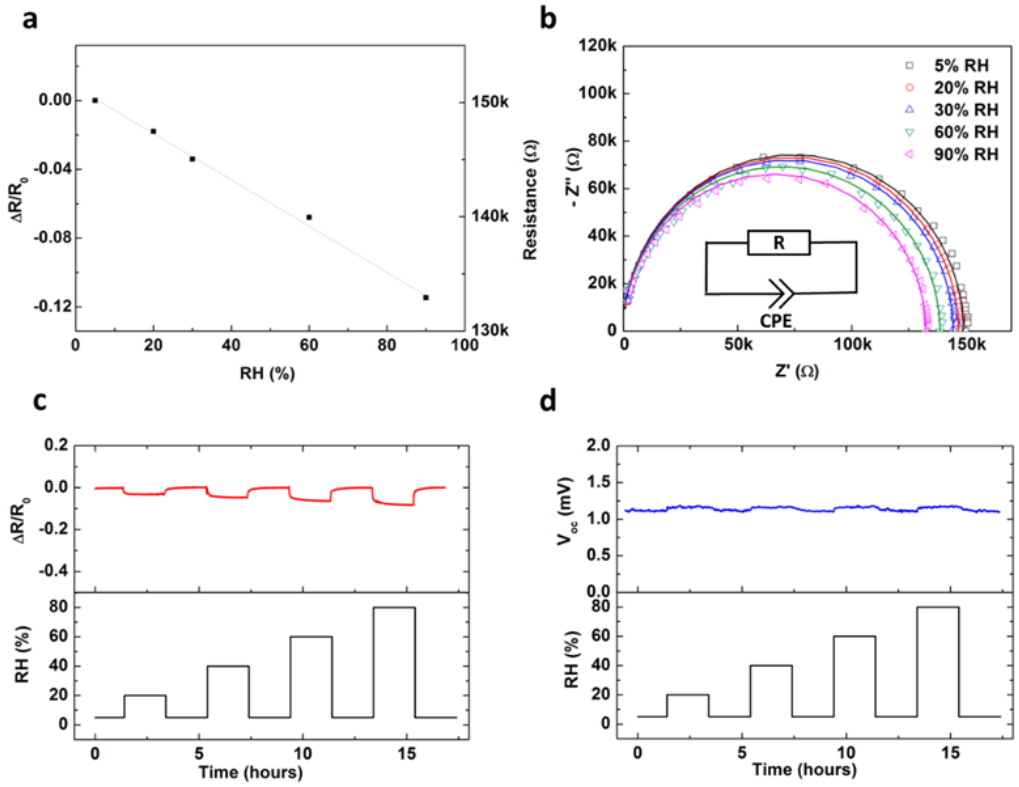

Figure 4.10 *Sensitivity of the 50 wt.% NL film in externally- and self-powered configurations to relative humidity (RH). (a) The AC (fitted results) resistance variation with RH (data collected after 1 hour at the applied RH level to allow the sensor to stabilise). (b) Nyquist plots and equivalent circuit fitting curves of NL film at different humidities. Resistance (R) contribution in parallel to the constant phase element (CPE). (c) Resistance variation ($\Delta R/R_0$) and (d) open-circuit voltage (V_{oc}) response to RH cycles.*

4.2.6 Multi-leg device assembly

The power harvested with a single NL film, at a ΔT of 30 °C, is in the order of few pW. To satisfy the power demand of an integrated self-powered system, a power output of at least 3-100 μW [172-174] is required. This could be achieved by (i) increasing the temperature difference; (ii) connecting our n-type NL material with a

p-type TE counterpart in series to form a p–n junction; and connecting many p-n junctions in series, (iii) optimise the size and shape of each leg. If the first strategy is constrained by the maximum temperature range, as discussed before (**Section 4.2.3**), the latter two are more flexible and viable to increase power output. Our group has recently developed a p-type organic TE compound, based on blends of Lycra® and PEDOT:PSS [147], which is an ideal candidate for such a (multi-leg) all-organic stretchable TE device.

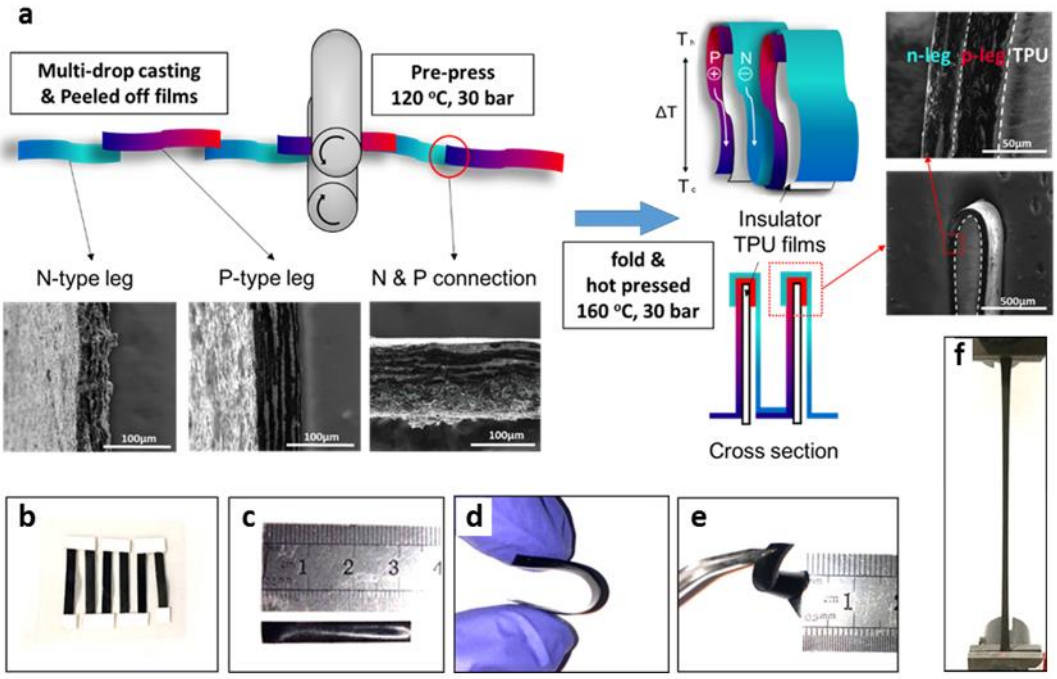

Figure 4.11 *Fabrication of flexible OTE devices based on NL and PL films. (a) Illustrative sketch of the continuous assembly line, with cross-sections of p, n-legs, connections, a p-n junction, and a digital picture of a folded 1-couple TE device. Comparison with (b) traditional in plate π-shape achitecture, the assembled (c) 2-leg device shows flexibility to be (d) bended, (e) twisted, and (f) stretched.*

In deciding how to best connect p- and n-type legs instead of the in-plane connection (Figure 4.11b), one could look at the current state-of-the-art. As schematically illustrated in Figure 4.11a, series connections of p-n junctions have simply been created by hot pressing at 160 °C of the p-type (Lycra®/PEDOT:PSS [147]) and n-type

(Lycra®/$Na_x(Ni\text{-}ett)_n$) legs with an interposed flexible electrical insulation layer (polyurethane film). This process is potentially continuous, fast and scalable, which is critical for any future large scale industrial applications. The junction between p- and n-type legs created by hot pressing is robust (see SEM micrographs of the cross-sectional area in Figure 6a), and the TE device remains flexible (Figure 4.11c-f) even in the case of a relatively large thickness.

The power outputs of different TE devices, with an increasing number of p-n junctions, have been measured for different external load resistances (Figure 4.12a,b). As expected, both the thermal voltage *U* and the maximum power output P_{max} increase with the number (*n*) of p-n junctions (Figure 4.12a), in accordance with the following equations:

$$U = n(\alpha_p + \alpha_n)\Delta T \qquad \textbf{Equation 4.6}$$

$$P_{max} = \frac{U^2}{4(n(R_p+R_n)+(2n-1)R_{p-n})} \qquad \textbf{Equation 4.7}$$

where α_p, R_p, α_n and R_n are respectively the absolute values of Seebeck coefficient and resistance of the p and n legs. $R_{p\text{-}n}$ refers to the contact resistance between p-type and n-type materials which could hinder carrier transport. These equations show that $U \propto \Delta T$ and when $R_{p\text{-}n}$ is much smaller than $R_p + R_n$, it can been simplified into $P_{max} \propto \Delta T^2$, which is in agreement with experimental data of Figure 4.12b. Based on the film low thermal conductivity, it is probably also possible to increase the cross section area and decrease length in order to decrease the resistance (R_L). Figure 4.12c,d shows, on a single n-type leg, that this kind of geometric optimisation can boost power output by at least an order of magnitude.

Extrapolating these results, it can be estimated that 111 k couples, with dimensions of 1 mm × 3 mm× 3 mm, are required to reach a power output of 10 μW, for a ΔT of 10 ^{o}C . This is calculated based on Equation 4.6 and 4.7. The resistance of each n-leg is:

$$R_n = \frac{L}{\sigma \times A} = \frac{3mm}{0.01S\ cm^{-1} \times 1mm \times 3mm} \approx 1000\Omega$$

The resistance of each p-leg (the following data of P-leg are referenced from previous work [2] and repeated in this work) is:

$$R_p = \frac{L}{\sigma \times A} = \frac{3mm}{60S\ cm^{-1} \times 1mm \times 3mm} \approx 0.17\Omega$$

The voltage output of per p-n junction couple at ΔT ~ 10 ^{o}C is

$$U_{p+n} = \Delta T \times S = 10\ \mathrm{K} \times (20 + 40)\mu\mathrm{V\ K^{-1}} = 6 \times 10^{-4}\ \mathrm{V}$$

Assuming that the contact resistance is 0.01 Ω, the number of the n & p couples (n) needed for 10 μW is:

$$P_{max} = \frac{(\mathrm{n} \times U_{p+n})^2}{4(n(R_p + R_n) + (2n-1)R_{p-n})}$$

$$\mathrm{n} \approx 111\mathrm{k}$$

The main limitation is the poor conductivity, but recent reports have presented improvements in both conductivity and Seebeck. Taking the best conductivity results (50 S cm^{-1}) [3] of $Na_x(Ni\text{-}ett)_n$ with insulating composites as example, the resistance of n-leg will decrease by:

$$R_n = \frac{3mm}{50S/cm \times 1mm \times 3mm} \approx 0.2\ \Omega$$

Therefore, only 44 n&p couples (n) would be needed for 10 μW when ΔT = 10 °C. And the total device would only be 0.4 cm^3 in volume, provided by the separator is 0.01mm thickness.

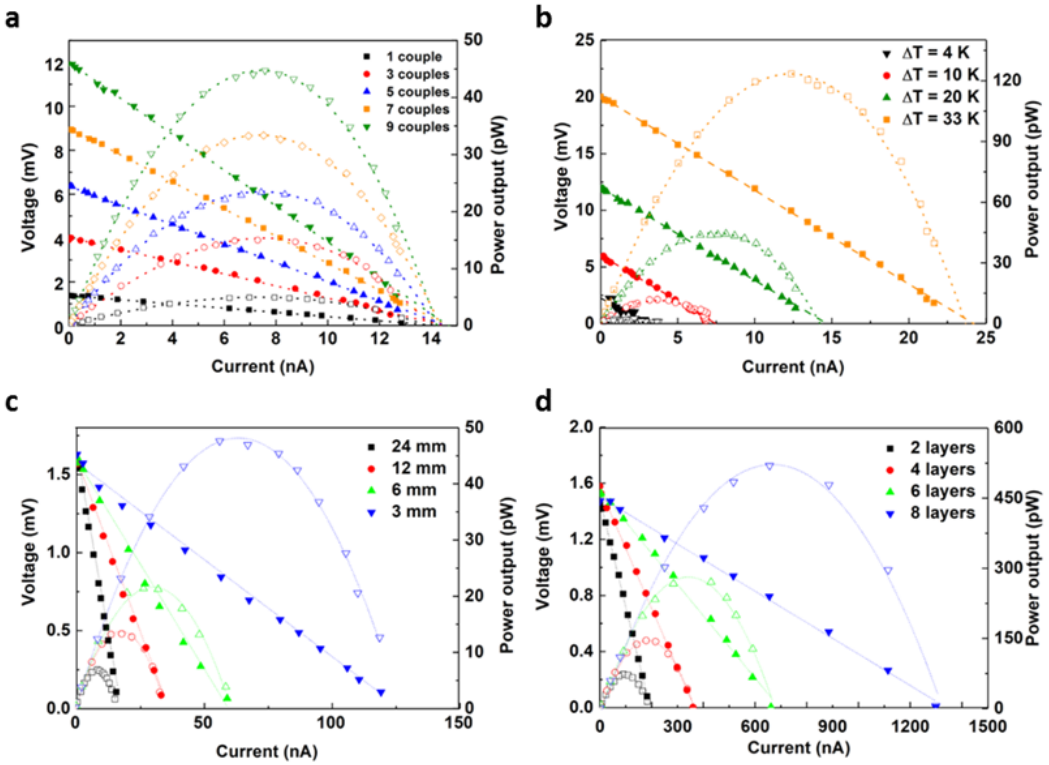

Figure 4.12 *Characterisation of flexible OTE devices based on NL and PL films. Open-circuit voltage and power output generated by (a) different couples of the OTE device at ΔT ~ 25 °C and (b) a 9-couples TE at different temperature differences. Dimension effects to open-circuit voltage and power output generated by single NL film, with (c) different length and (d) thickness (stacking layers of 20 mm length NL films) at ΔT ~ 27 °C. Empty and full symbols in all figures indicate power and voltage, respectively.*

4.2.7 Demonstrations of device applications

In order to demonstrate the application of these materials as wearable sensors, an 8-couples TE 'bracelet' device has been used to power a single NL stripe sensor, connected to the index finger, to detect its movements (Figure 4.13a). The electrical connections and signal acquisition system are represented by the equivalent circuit in

Figure 4.13a. When the index finger bends to different angles, both current and voltage show clear signal changes (Figure 4.13b). This shows the potential of these materials as self-powered sensors.

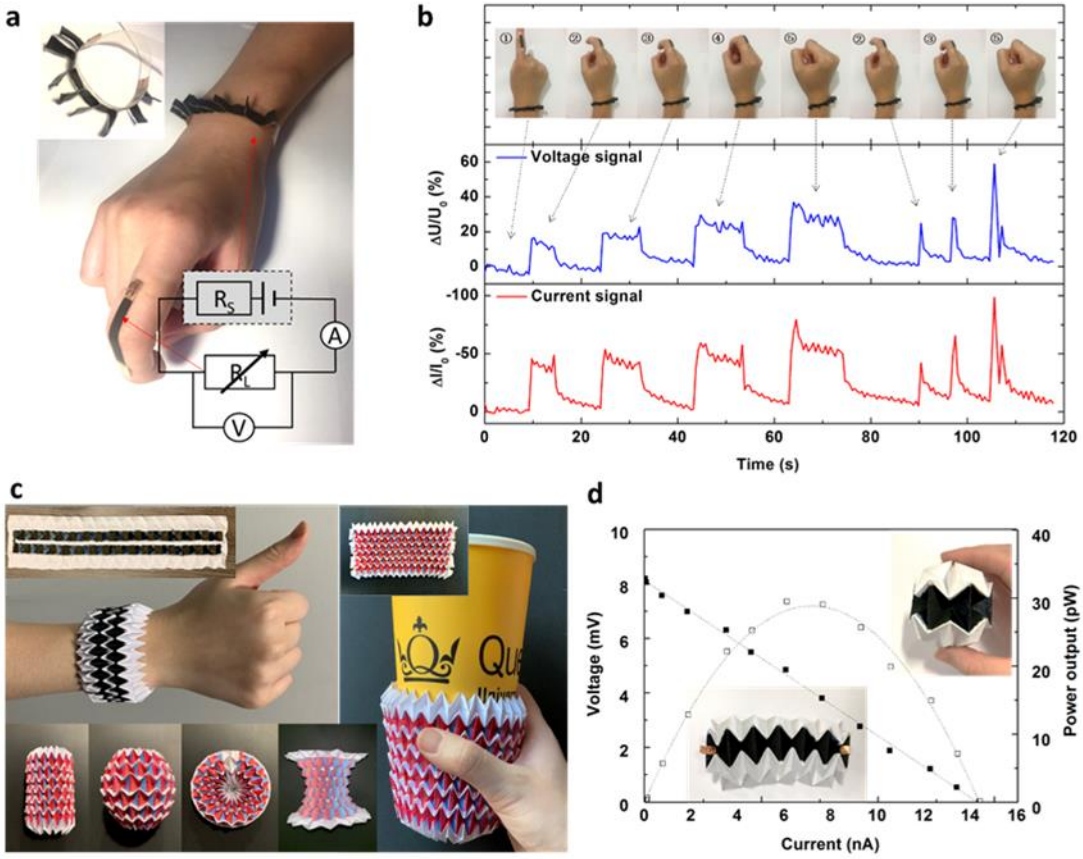

Figure 4.13 *Examples of applications and proof-of-concepts of flexible TE sensing devices. (a) Digital optical pictures, demonstrating a self-powered 'bracelet' TE device. The 'bracelet' is made by the 8-couples and powers a strain sensing NL stripe, working as an index finger motion detector. (b) The response to different positions of the index finger, self-powered by a ΔT of ~ 20 °C. (c) The multi-couples TE devices, inspired by the origami "magic ball". (d) The power output of 6-couples TE device under ΔT ~ 20 °C.*

Examples of more complicated device architectures have been attempted. For instance an origami-inspired "magic ball" [175-177] is used here as a method to transform 2D in-plane structures to 3D out-of-plane shapes, constituted by p-n TE legs, connected in series or in parallel in order to increasing power output and reliability. A simple 6-

couples TE device (Figure 4.13c) has been fabricated by coating $Na_x(Ni\text{-}ett)_n$ and PEDOT:PSS on paper as the n and p leg respectively. The power output reaches 30 pW when a temperature difference of 20 ^oC is applied. Larger TE devices can be fabricated in the same way. Following the design of 'magic-ball', a 90-couples TE device can simply be manufactured (Figure 4.13d), showing the ability to adapt to different shapes, geometries and applications. Among these, one could envisage exploitations as inflating and 3D conformable surfaces, for instance in soft robotic, smart packaging, wearable, automotive and Internet-of-Things applications.

4.3 Conclusion

This chapter demonstrates a facile strategy to develop stretchable and multifunctional self-powered sensors based on the thermoelectric effect in organic conductors. Greatly improved mechanical properties have been achieved by compounding brittle n-type $Na_x(Ni\text{-}ett)_n$ within a flexible Lycra® matrix, while preserving the thermoelectric properties. For an optimised ratio, with 50 wt % $Na_x(Ni\text{-}ett)_n$, an outstanding strain-at-break of 217 ± 37 % is achieved, in conjunction with the Seebeck coefficient of -40 $\mu V\ K^{-1}$ and electrical conductivity of 0.01 $S\ cm^{-1}$.

This novel compound has shown sensitivity to different stimuli, like strain and light irradiation. When exposed even to 10-20 ^oC temperature difference, the device is also able to generate enough power to enable autonomous sensing.

By exploiting the enhanced processability of our polymer TE compounds, a new manufacturing strategy has been proposed to overcome the typical shortfalls of π-shaped TE devices: brittleness and complex, time-consuming, and hardly scalable manufacturing processes. Series of p-n junctions could simply be created by hot pressing an n-type leg ($Na_x(Ni\text{-}ett)_n$ /Lycra®) with a previously developed p-type leg

(PEDOT:PSS/ Lycra®), and an intermediate flexible electrical insulation layer, with a process which is potentially continuous, fast and scalable. The concept of the self-powered sensors is demonstrated in the detection of an index finger motion. Projecting into the future, an origami inspired inflatable and 3D conformable "magic ball" TE device has also been demonstrated, which might be exploited for instance in soft robotic, smart packaging, wearable electronics, and Internet-of-Things.

Chapter 5 PEDOT:PSS coated Lycra yarns for highly sensitive self-powered sensors

5.1 Introduction

Flexibility and sensitivity are among the most important properties for stretchable and wearable sensors. Great research efforts have recently been dedicated to the selection of smart materials as well as the design of structures to achieve a high flexibility and stretchability (large deformations). Although a high flexibility [178-180] and sensing capability to different stimuli [181-185] was demonstrated, a number of critical constraints still limit the practical use of flexible sensors. One of the key challenges is how to retain functions (*e.g.* sensing ability, energy storage/harvesting, electrical/thermal conductivity) at large deformations. For example, strain sensors with either a high GF (up to 1000-16000) and a low strain at break (2%-7%) [186, 187] or, vice versa, with a wide working strain range (up to 280%-300%) but a low GF (0.06-13.1), have been reported [188-190]. Very recently, this challenge has been partially addressed by incorporating auxetic mechanical metamaterials in PDMS (GF ~ 800 and a strain-at-break of 160%) [191] or by patterning Ag nanowires on polydimethylsiloxane films (GF ~ 150000 and a strain-at-break of 60%) [192] Therefore, the need still exits to develop an easy processing method to generate a high sensitivity and high deformability at the same time.

Apart from the sensitivity and deformation issue described above, energy storage devices are typically rigid which is another critical constraint limiting the practical use of flexible and highly deformable sensors. Autonomous systems that are able to generate enough power *in-situ* during usage are usually based on, for instance, the photovoltaic [193-195], piezoelectric [196], triboelectric [197, 198], and

thermoelectric (TE) effect [146, 179, 199]. Thermoelectricity is intriguing as it allows to harvest energy from ubiquitous temperature differences, such as body temperature to ambient temperature, in a reliable and consistent manner. Smart textiles with TE properties are intriguing as they could harvest energy from ubiquitous temperature differences, such as body temperature to ambient temperature, in a reliable and consistent manner. In fact, smart yarns have already shown great capability to sense various stimuli including deformations [200-202], temperature [181], gas [182, 203], humidity [183-185] and are even utilized for energy generation or storage [204, 205]. However, limited research has been conducted on highly deformable and self-powered strain sensors using the TE effect.

Therefore, in this chapter, an ultrasensitive self-powered smart yarn, based on the thermoelectric properties of PEDOT:PSS coated on commercial Lycra® yarn is presented for the first time. A unique combination of large deformations and ultrahigh sensitivity is achieved by imposing and tuning pre-cracks in the PEDOT:PSS coating layer. Moreover, the sensor could be autonomously powered by the thermoelectric response of the PEDOT:PSS coating, when subjected to a temperature gradient (*e.g.* 20 ^{o}C), and detect, for instance, cyclic strains and temperature (difference). At the end of this chapter, some applications such as a smart glove are demonstrated which harvest body heat and transfer it into electricity. Moreover, autonomous sensors that record environmental and object temperatures are demonstrated which illustrates the applications as multi-functional, self-powered and high sensitivity sensors.

5.2 Results and Discussions

5.2.1 Fabrication and characterization of PEDOT:PSS coating

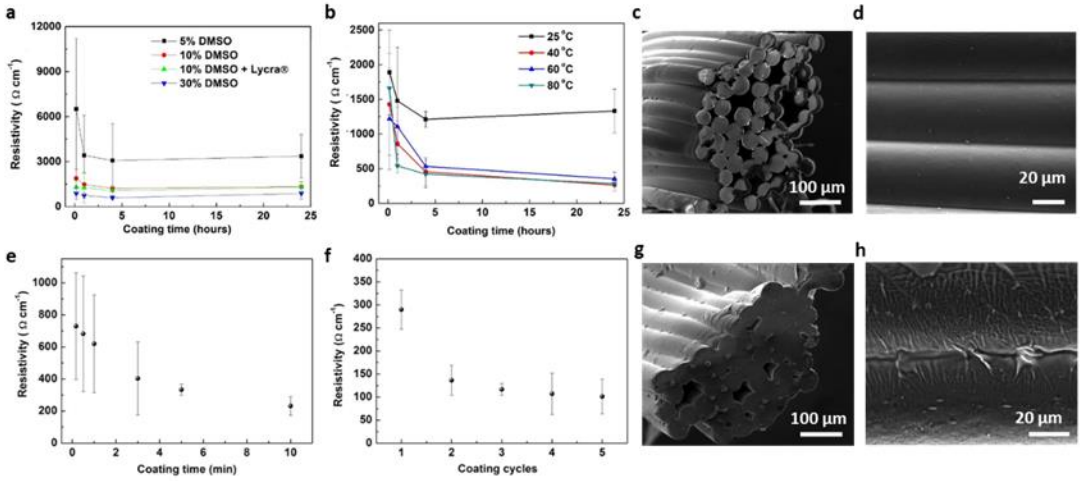

Figure 5.1 *Comparison of PEDOT:PSS coated Lycra® yarns by two methods. The effect of (a) coating solution content with solution temperature of 40 °C and (b) coating temperature with 10wt% DMSO to resistivity with coating time for the simple dip-coating method, i.e., without swelling procedure. (c) Cross-section and (d) surface view SEM figures of the simple dip-coated yarn with coating condition of 1.6 wt.% PEDOT:PSS mixed with 10wt% DMSO in water solution, under 40 °C, coated for 1 hour. Effect of (e) coating time and (f) coating cycle to resistivity for the PY coated by swell-coating method. (g) Cross-section and (h) surface view SEM figures of swell-coated yarns, which coated for 5 minutes in 1.6 wt.% PEDOT:PSS and 1 cycle. Error bars in (a, b, e, f) represent the standard deviations.*

The ultra-sensitive smart yarn was fabricated by a swell-coating method, which involves application of a PEDOT:PSS layer over the surface of multifilament Lycra® yarn. Due to crosslinking of the polyurethane chains, the yarns swelled when immersed in DMSO solution, allowing some free volume between crosslinked networks of the yarn at the first step, hereafter called ‘swelling’. This swelling leads to an increase of the surface area of the Lycra® yarns, allowing more area to be coated by the PEDOT:PSS in the subsequent coating step. Consequently, it is expected to

have a larger amount of PEDOT:PSS coated onto the Lycra® yarn than through a simple dip coating process. 1.6 wt.% PEDOT:PSS mixed with different ratios of DMSO 5wt% to 20wt% (Figure 5.1a) and with different solution temperature (Figure 5.1b) haven been investigated for the simple dip coating process. The electrical resistance decreases with immersion time, DMSO content and solution temperature, while the swell-coating method shows a significantly increased electrical conductivity even within a short coating time (in 5 minutes).

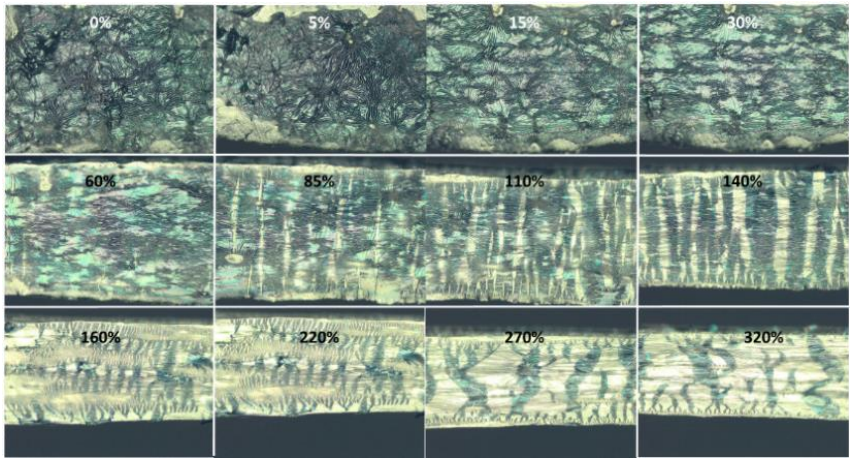

Figure 5.2 *The microscope pictures of swell-shrink coated Lycra® film. Hot pressed Lycra® film were cut into strip and coated by PEDOT:PSS in the same method as PLY. The images show the circle-shaped wrinkles induced by shrinkage and cracks induced at the different strains.*

A unique surface feature with wrinkled PEDOT:PSS coating layer was obtained during the drying process, due to the difference in volumetric shrinkage and the large mismatch in their stiffness values between PEDOT:PSS and Lycra® yarns. It was expected that shrinkage should take place in both longitudinal and lateral directions of the yarn as evidenced by the circular wrinkles on flat Lycra® films after the same swell-coating process (Figure 5.2). However, lateral wrinkles, perpendicular to the yarn's axial direction, are much more evident than the other direction (Figure 5.1h), which is believed to be due to the larger axial deformation taking place during the

drying and shrinkage processes as a result of yarn geometry. This is further supported by the smooth surface of simple coated yarns, where no shrinkage happened. The well-connected coating layer (Figure 5.1g) is attributed to the good interfacial adhesion between the PEDOT:PSS layer and the polyurethane substrate.

The interfacial shear stress can be calculated by both critical length or by Agrawal and Raj model. The critical length (l_c) is defined as the minimum length of the PEDOT patches for a given thickness (t) which will allow the tensile failure of the PEDOT layer rather than shear failure at interface, *i.e.*, the minimum length the patches are able to crack by reaching the fracture stress. As PEDOT:PSS is much stiffer than the Lycra® yarn, the Kelly-Tyson model can be applied, in which the matrix is simplified as an ideally elastic material. Also, it can be considered as an iso-strain situation, where the direction factor of the patches will be equal to 1. Under the given loading, the shear effect builds up from the patches ends where a plastic displacement zone exists. The stress carried increases until it reaches a constant σ_P in the middle part of the patches. With the increase of the applied load, the strains of PEDOT coated Lycra® yarn increases resulting in a higher stress in the PEDOT layer and which will reach the fracture stress at the maximum stress $\hat{\sigma}_p$. PEDOT film breaks where it reaches the ultimate strength at X_c. If the length of any fragment is less than $2X_c$, the tensile stress in this fragment cannot reach the ultimate strength and it does not break anymore. The equilibrium equation of tensile force in patches and shear force at interface is

$$wt(\sigma(x+dx)-\sigma(x)) = \tau(x)\, wl_c dx \qquad \textbf{\textit{Equation 5.1}}$$

where the w is the patches width, τ is the shear strength. And t is the thickness of the coated PEDOT:PSS layer. Therefore,

$$\tau(x) = t(\frac{d\sigma}{dx}) \qquad \textbf{\textit{Equation 5.2}}$$

the critical length $l_c = 2X_c$ is termed and can be calculated as

$$l_c = 2\,\hat{\sigma}_p\,t/\,\tau \qquad \textbf{\textit{Equation 5.3}}$$

The fragment size is convergent to 22 μm as read in Figure 5.9b. The critical length l_c of coated PEDOT:PSS layer can be given by $l_c = L_p/K$ [206]. The well-accepted value K = 0.75 [207] was used. So $l_c \approx 29\ \mu m$. The $\hat{\sigma}_p$ for PEDOT:PSS is 30 MPa under RH 40%, at the maximum strain at break ~ 3% [208]. The thickness of PEDOT layer is 500 nm as measured from SEM picture.

Therefore, based on the relationship between critical length and the interfacial shear stress (Equation 5.3), the shear stress between the PEDOT layer and Lycra® yarn can be calculated as 1.4 MPa.

As the brittle PEDOT:PSS coating on ductile Lycra substrate can be applied to Agrawal and Raj model [209], the maximum interfacial shear stress can be further estimated from:

$$\tau = \frac{\pi t \hat{\sigma}_p}{1.5 \times W_c} \qquad \textbf{\textit{Equation 5.4}}$$

where the W_c is the crack width which is ~ 23 μm as can be derived from Figure 5.9f. And by using the same value of t and $\hat{\sigma}_p$ as calculating by critical length, the value of τ is also 1.4 MPa. This good interfacial shear stress between the coating and the substrate is attributed to the formation of hydrogen bonds between the oxygen-containing groups in the PEDOT:PSS and the N−H groups of polyurethane yarns.

The presence of DMSO in the PEDOT:PSS water suspension is important as it increases the conductivity [210], and improves the water-stability of the coated yarns. The stability in water has been verified by the constant electrical resistance of the coated yarn after 42 hours submersion in water (Figure 5.3) due to the PEDOT:PSS microstructural changes induced by the polar solvent, DMSO. Specifically, with PSS extracted by DMSO, hydrophobic nature of PEDOT-rich domains has been

accentuated. This finding indicates the potential of utilizing current coated yarn in humid environments.

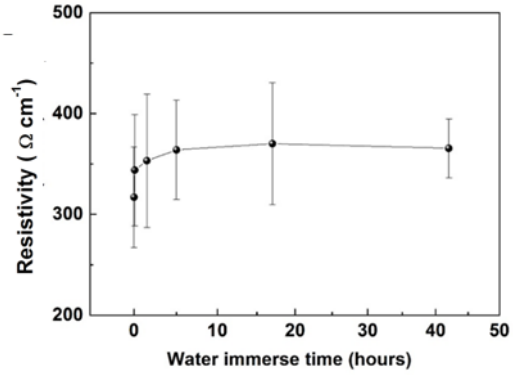

Figure 5.3 *The water stability of PLY. Unit length resistance change with water immersing duration of pure PEDOT:PSS and DMSO treated PEDOT:PSS films immersed in water. Error bars represent the standard deviations.*

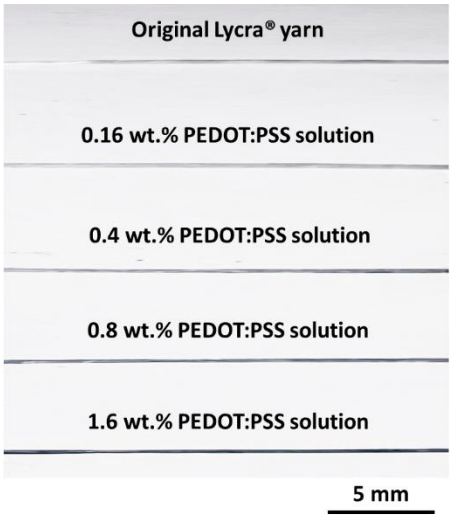

Figure 5.4 *The influence of the PEDOT:PSS concentration on the coating. The digital pictures of Lycra® yarns coated within the different concentrations PEDOT:PSS in water solution. The concentration is calculated by diluted the as-purchased 1.6wt% PEDOT:PSS solution with de-ionized water into different ratio. The higher concentration of PEDOT:PSS solution the darker the blue yarns indicates the more PEDOT:PSS is attached on the yarn.*

In order to optimize the coating process, particularly in relation to the electrical properties, a number of processing parameters have been investigated, ranging from PEDOT:PSS concentration, to coating times and number of coating layers. The 1.6 wt.% PEDOT:PSS solution, 5 minutes coating duration and 1-cycle coating is found to be the most suitable combination for current conductive yarn strain sensors. Coating solutions with 0.2 wt.% to 1.6 wt.% concentration have been investigated (Figure 5.4). Only above 0.8 wt.%, the coated yarn achieves a low enough electrical unit length resistance (3.2 ± 0.5 MΩ for 0.8 wt.% to 330 ± 35 Ω for 1.6 wt.%) to be measurable by a 2-probe test station (as described in **Chapter 3**) over a specimen length of 1 cm. Figure 5.1e presents the effect of coating time on the electrical resistivity, showing an decreasing trend with longer period of immersion, which is stabilized to a plateau above 5 minutes. This is assumed to be related to the saturation of solvent exchange between PEDOT:PSS/water suspension and DMSO in Lycra® yarn. When more cycles of coating are applied, the electrical resistivity of the yarn is further reduced, and is no longer limited by the solvent exchange saturation (Figure 5.1f).

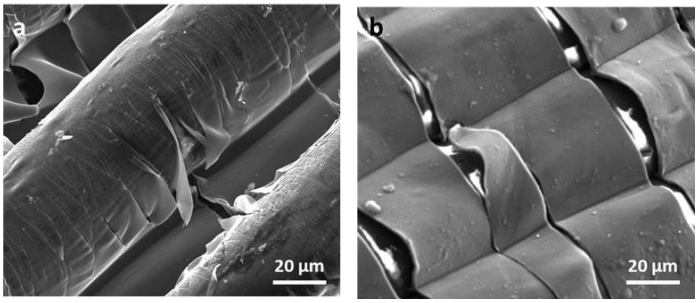

Figure 5.5 *Morphology of different coating cycles yarns. SEM figures of the stretched (a) 1-coating and (b) 3-coating cycles yarns. Thickness is obtained by measuring the cross section of PEDOT:PSS layer on cracked parts in SEM pictures.*

It is worth noting that there is a trade-off between the electrical properties and adhesion between PEDOT:PSS coating and substrate due to the large mismatch in their stiffness

values, affecting subsequent crack patterning and electrical sensing properties. For example, after 3 coating cycles the yarn has a thicker PEDOT:PSS coating (~ 1.5 μm) compared to the 1-cycle coating yarn (approximately 300-500 nm) based on their SEM images (Figure 5.5a). This has also been verified by the calculation from Young's modulus (as mentioned later). As expected, an improved electrical conductivity was found with the thicker yarn coating (115 Ω resistance per unit length). However, electrical resistance is out of the measurable range when the yarn returns from 300% to 0% strain, due to the permanent cracks between conductive coating patches propagated around the whole yarn (Figure 5.5b), disconnecting the electrical pathway. This throughout propagation is attributed to the progressive increase in PEDOT:PSS stiffness with coating thickness boosting by the number of coating cycles rising. As a result, the stiffness mismatch between the PEDOT layer and the ductile Lycra® yarn is amplified, and the cracks developed on the PEDOT:PSS layer are increasing until they totally extend around the yarn, rendering them electrical insulating even when unloaded and hence, unsuitable for use as a strain sensor. Therefore, the 1-cycle coated yarn with 5 minutes immersion time, named PEDOT:PSS coated Lycra® yarn (PY), has been employed for the following investigations.

The mechanical properties of treated Lycra® yarns have also been investigated (Figure 5.6**)**. After coating with PEDOT:PSS at optimized conditions, the Young's modulus was doubled compared to the pure Lycra® (Table 5.1). The cross section of the yarns are calculated from the 940 dtex (*i.e.* gram per 10 km) of the as purchased Lycra® yarn. The density of the Lycra® yarn is between 1.15 g cm^{-3} to 1.32 g cm^{-3}, where 1.2 g cm^{-3} is used to simplify calculations. The cross section has been simplified as a circle shape, therefore, the cross section is $\frac{940\ dtex}{1.2\ g\ cm^{-3}\times 10\ km} = 0.078\dot{3}\ mm^2$.

Table 5.1 *Young's modulus of Lycra yarns, PY and CPY.*

Sample	Lycra®	Swollen Lycra®	PY	CPY-300
Young's Modulus	7.5 ± 0.1 MPa	8.3 ± 0.5 MPa	16.6 ± 1.3 MPa	7.8 ± 0.6 MPa

Based on the Young's modulus difference before and after coating, the thickness of PEDOT:PSS layer can be estimated. The total force (F_T) on the coated yarn is the sum of the force on Lycra® (F_L) and PEDOT (F_P). The total length change is same as the length change of Lycra® and PEDOT at low strains within the elastic region (ε < 3%). Therefore, the PY system is equivalent to a two-component parallel system. The PY's Young's modulus (E_{PY}) is related to the Young's modulus of Lycra® (E_L) and PEDOT (E_P) along with the respective cross-sectional areas (A_L and A_P) based on

$$E_{PY} = \frac{E_L A_L + E_P A_P}{A_L + A_P} \qquad \textbf{Equation 5.5}$$

Here, the A_P is given by

$$A_P = 2\pi h \sqrt{\frac{A_L}{\pi}} = 2h\sqrt{A_L \pi} \qquad \textbf{Equation 5.6}$$

If we combine the Equation 5.5&5.6 the coated PEDOT thickness (h) can be calculated as

$$h = \frac{\sqrt{A_L}(E_{PY} - E_L)}{2\sqrt{\pi}(E_P - E_{PY})} \qquad \textbf{Equation 5.7}$$

The values of E_{PY} and E_L are 16.6 MPa and 7.5 MPa as Table 5.1 shows, and the E_P of 1.9 GPa [211] has been used as reported at 40% RH. Therefore, the thickness of the PEDOT layer is 380 nm and is close to the results obtained from SEM measurements and observations. As the moduli of the 2-5 times coated PYs are 27.8, 40.7, 24.5 and 25.6 MPa respectively, by using the same method, the thickness of the

2 and 3 times coated yarns can be calculated and are found to be increasing to 850nm and 1400 nm, respectively. However, for the 4 and 5 times coated layers the thickness decreases to 710 nm and 630 nm, while the conductivity results in Figure 5.1f verified the coated PEDOT amount should higher than the 3 times coating. This means when coatings accumulate and stack into thick layers the PY does not fit to the parallel model anymore.

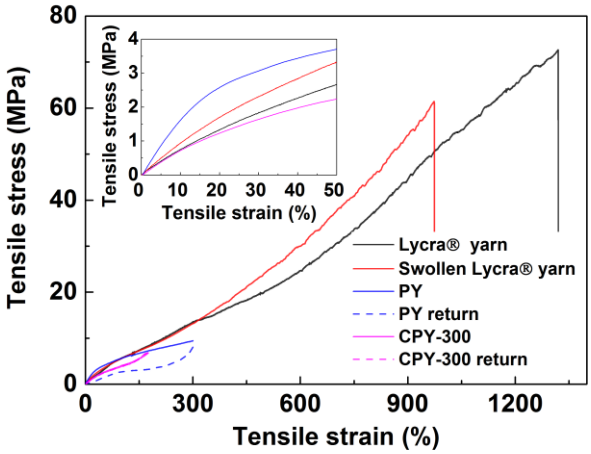

Figure 5.6 *Mechanical property of Lycra yarn, PY and CPY. Representative stress-strain curves for as-received Lycra® yarn, DMSO swollen Lycra® yarn dried in 120 ^{o}C oven for 2 hours, PY and CPY-300 and (insert) their performance at low strain. The stress is calculated by estimating the cross section. The swollen Lycra® yarn shows a slightly higher Youngs' modulus compared to pure Lycra®, as the swollen cross section area is slightly larger, while the same area value has been used for tensile stress calculation of both yarns.*

Based on the geometry, the amount of PEDOT:PSS coated on the yarns can be estimated *i.e.*, the volume fractions can be calculated. The volume ratios of the PEDOT:PSS in whole coated yarn is $\frac{A_P}{A_P+A_L}$ = 0.5 vol. % by assuming that the PEDOT:PSS on lycra is a double-wall cylinder and a the density of ~ 1 g cm^{-3} [212] for PEDOT:PSS (ρ_P) and 1.2 g cm^{-3} for Lycra® (ρ_L). Therefore, the weight ratios for

the PEDOT:PSS in whole 1-timed coated yarn is $\frac{A_P \rho_P}{A_P \rho_P + A_L \rho_L} = 0.4$ wt. %. After relaxation from the first cycle of 300% strain, the PEDOT:PSS coating layer was cracked and its Young's modulus then was the same as for pure Lycra® yarns. This indicates that the PEDOT:PSS layers have cracked patches smaller than the critical length for reinforcement and cannot transfer the tensile stress from the yarn substrate, *i.e.*, the load is mainly carried by the polyurethane after 300% strain treatment.

5.2.2 Electrical strain sensing

The electrical properties of flexible sensors are pivotal for their performance as strain gauges. Upon stretching of the PY, an exponential increase in electrical resistance is shown in Figure 5.7a, with a large variation in their GF values as defined by $(\frac{d(\frac{\Delta R}{R_0})}{d(\varepsilon)})$ at different parts of the curve. Starting with a GF value of less than 3.0×10^2 in the strain range of 80-100%, an ultrahigh GF value up to 1.8×10^5 was reached at strains between 260% and 300% in the same loading cycle. This is due to the fragmentation of the conductive coating layer upon tensile loading. Considering the rigid nature and low strain-to-break of PEDOT:PSS coating, it is expected that this conductive coating layer will start to crack at very low strain (*i.e.* 5% or even below), as evidenced by the irreversible resistance change upon unloading.

This PY yarn after relaxation from 300% strain is termed CPY-300 (crack-induced PY subject to a maximum 300% strain). To better understand the sensitivity of CPY-300, subsequent loading cycles with up to 200% strain were applied. Interestingly, it is found that the strain sensitivity of CPY-300 is much higher than that of PY, even in the low strain range, reaching GF of 2.1×10^4 between 30-40% (Figure 5.7b) compared to only 82 during initial stretching of the PY. This is because of the occurrence of PEDOT:PSS cracks upon first tensile loading, leading to a pre-defined pattern of a

pre-cracked conductive coating layer with a much easier disconnecting process upon subsequent loadings, especially at small strain range. In the strain range of 50% to 200%, the GF of CPY-300 reaches 4.9×10^4, 166-fold higher compared to the original PY. It is worth noting that a slightly increasing trend of GF was observed from second to fourth tensile loadings, approaching to a stable level after the fourth cycle. This is attributed to subsequent crack formation and propagation upon deformation. As the subsequent loading is much lower than the pre-strain (300%), a saturation of new cracks is reached within few cycles, while the crack morphology becomes invariant and the resistance change with strain becomes stable and reversible (Figure 5.8a).

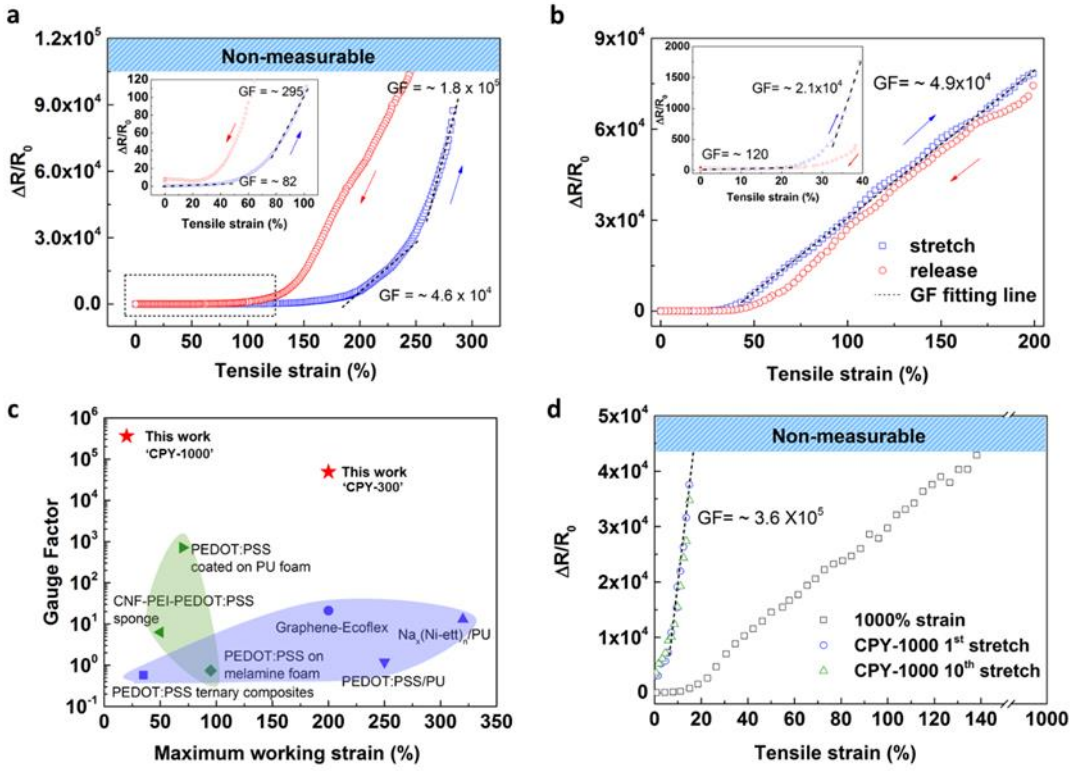

Figure 5.7 *Sensitivity to strain for PY, CPY-300 and CPY-1000. Resistance change and gauge factor (obtained from the linear fittings) of (a) the 1st time strain PY to 300% strain and (b) the 6th cyclic strain CPY-300 to 200%, with low strain figures inserted. (c) The summary of the maximum working strain (purple region for stretching and green part for compression) and GF of self-powered strain sensors in literature [100, 144-147, 213, 214] compared with this work's results. (d) Resistance change of 1000%*

strain and the presentative 1st and 10th time resistance change with strain of CPY-1000.

The obtained CPY shows an unprecedented property combination for advanced deformation sensors, possessing an outstanding sensitivity to the deformation together with a very wide strain sensing window. CPY-300 fulfils the long existing gap in strain sensors possessing high sensitivity and high deformation range simultaneously (Figure 5.8b). Compared to the sensitivity values from literature, current CPYs have shown the highest GF values ever reported for self-powered strain sensors (Figure 5.7c) together with an excellent stretchability.

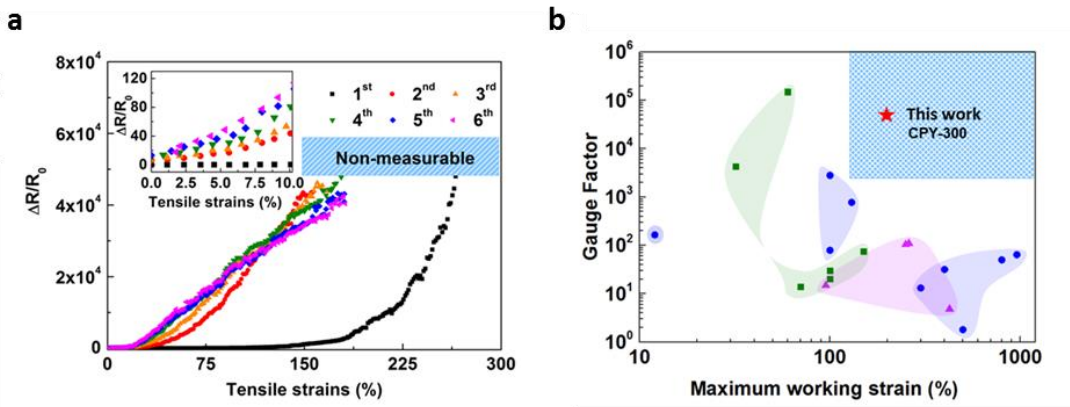

Figure 5.8 *Ultrahigh sensitivity to strain. (a) Resistance change and gauge factor (linear fittings) under different strains of all 6 times repetitions. PY is the first time stretch until 300% strain (after relaxation, it is called CPY-300) and the following stretch is cyclic stain to 200%. And the zoom in figure at low strain is inserted. (b) Comparable with the main performance (maximum strain range and maximum GF) of recently reported strain sensors, our work, especially CPY-300 shows the extremely high stretchability and sensitivity in the challenge region (highlighted region) [166-168, 215-226]. The green, blue and purple shadows instead of the sensors based on graphene, carbon nanotube and conductive polymer, respectively.*

Furthermore, CPY can be stretched up to 1000% strain due to the high stretchability of Lycra® with a great strain sensitivity (Figure 5.8d). And it is worth mentioning that

after this higher strain value of 1000% (CPY-1000), a corresponding sensitivity of GF ~ 3.6×10^5 is achieved with up to 20% strain and good reversibility. This GF is 3000-fold higher than the CPY-300 in the same strain range, while the measurable range of the resistance for CPY-1000 is limited to 20% strain due to the huge resistance which is above the limit of the current measurement equipment. This superior sensitivity is attributed to the less connected conductive PEDOT:PSS patches in CPY-1000, with more secondary cracks induced by this very large strain comparing to CPY-300. Clearly, with the different pre-strains (*i.e.* 300% or 1000%), the sensitivity and measurable deformation range can be tuned for different applications.

5.2.3 Understanding the tuneable and ultrahigh strain sensitivity based on pre-strain induced crack patterns

The ultrahigh sensitivity of this smart yarn is associated with the crack patterns of the conductive PEDOT:PSS coating layer during the pre-straining step. Upon deformation, the pre-formed cracks are easily expanded so the conductive patches are separated from each other even at small deformations, leading to a sudden and large increase in electrical resistance. Additionally, the smart yarn can be easily tuned into the most sensitive state with an optimum range of pre-strain for applications as a strain sensor.

To better understand the mechanism of crack patterns effects on the sensitivity of CPYs, a series of crack patterns have been created on the PEDOT:PSS coating by imposing different pre-strains onto the PY, ranging from 5% to 100% with abbreviations of CPY-5 to CPY-100, respectively (Figure 5.9a). By increasing the pre-strain levels, the coating patches' length (L_p) decreases while the crack width (W_c) increases. As summarized in Figure 5.9b, the W_c between coating layers increases with

pre-strain values, and the L_p decreases until it reaches the minimum length of ~ 22 μm, which is relevant to its critical length.

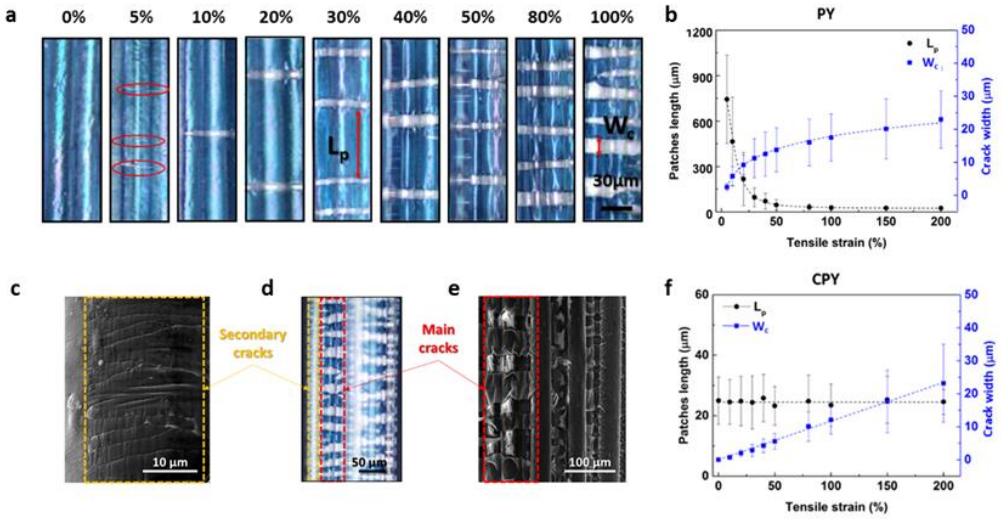

Figure 5.9 *The PY's and CPY's cracking distribution under different strains. (a) Optical microscopy images of the PYs under different pre-strains, showing the crack development with pre-strain. (b) PY's crack width (W_c) and patches length (L_p) distribution under different pre-strains. SEM pictures show the (c) secondary cracks after relaxing from 300% strain and (e) main cracks under 300% strain. And (d) the secondary and main cracks distribution on the yarn as a presentative (strain ~ 150%) microscope images. (f) CPY's W_c and L_p distribution under different strains. Error bars in (b, f) represent the standard deviations.*

The electrical properties under cyclic testing strain of 3% and various pre-strained CPYs are summarized in Figure 5.10, aiming to explore the relationship between crack patterns induced by pre-strains and subsequent electrical sensing properties. With an increased pre-strain value from 10% to 50%, both the resistance and the GF are significantly increased (from 8 to 302). This is likely due to the increased W_c and decrease in L_p from CPY-5 to CPY-50, with a much larger gap between conductive coatings. When further increasing the pre-strain to 100%, the GF slightly decreases to plateau at around 250. This is the result of the initial resistance (R'_0), which refers to the CYPs' resistance at 0% strain, monotonically increasing with pre-strain, and

surpassing the resistance variation with strain(ΔR). It is worth noting that the increase of crack density is less pronounced when pre-strains are larger than 50%.

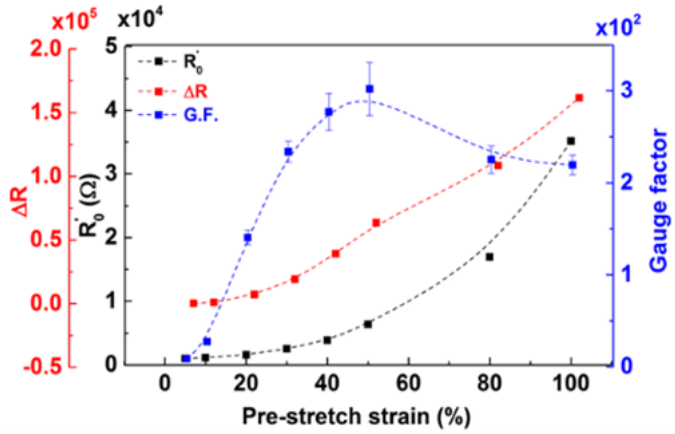

Figure 5.10 *The tuneable strain sensitivity. The effect of the pre-strain to CPY-5 to CPY-100's initial resistance (R'0), resistance variation with strain (ΔR) and gauge factor under cyclic 3% strain with error bars representing the standard deviations.*

The electrical impedance response to a relatively wide range of frequencies can help to explain this mechanism. Impedance spectra of PY and CPY at different strains were fitted with appropriate equivalent circuits. When PY is stretched for the first time (Figure 5.11a&b), pure resistive behaviour is dominating at low strains (≤ 20%). Initially, increasing strain causes an increase in the resistance, which is composed of contact resistance R_c and film resistance R_1 (Figure 5.11c). As cracks are developing at higher strains (≥ 30%), the impedance becomes dependent on frequency. With further increased strain level, the cracks partially disconnect the conductive from each other acting as capacitors. The combination of cracks and conducting paths are best described with a resistor R_1 and a non-ideal capacitor or constant phase element (CPE1 in the equivalent circuit, with $Z_{CPE} = 1/(T\omega^P)$) in parallel with the resistance of the contacts R_c in series (Figure 5.11c). The fitted results are presented in Table 5.2, the CPE with its P value close to 1 indicates a narrow distribution of the L_p and W_c values.

The R_1 resistance increases exponentially and the capacitance decreases exponentially with increasing strain due to the L_p decreasing and W_c increasing.

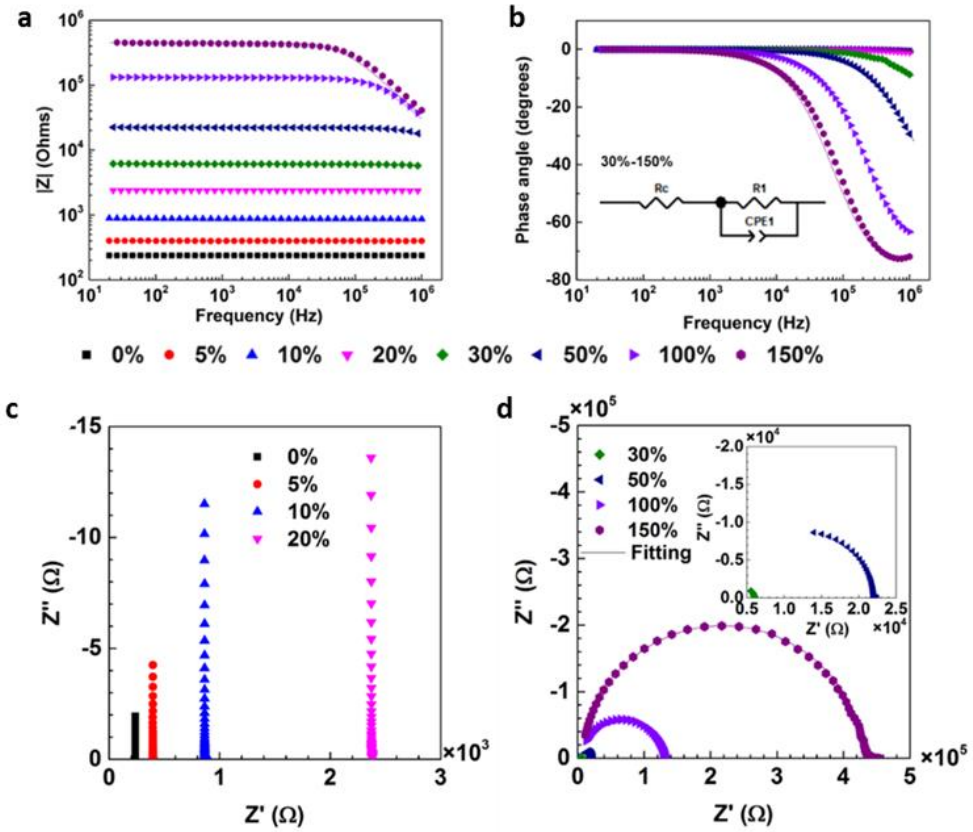

Figure 5.11 *Impedance spectroscopy of PY. The frequency dependencies of the (a) moduli of the complex impedance (Z) and (b) phase angle (θ), Nyquist plots at (c) low strain and (d) high strain, with fitted results (lines) based on a pure resistor (R_c+R_1) model for lower than 20% strain and inserted equivalent circuit model for strain of 30% and above.*

Table 5.2 *Impedance parameters of PY as a function of different strains.*

PY Strain	R_c (W)	R_1 (W)	CPE_1-T (pF)	CPE_1-P	Chi-squared	Error
0%		237				0.015%
5%		397				0.029%
10%		870				0.066%
20%		2375				0.041%
30%	2574	3478	66.6	0.95	4.06×10^{-4}	
50%	3520	1.86×10^{4}	14.0	0.96	8.69×10^{-5}	
100%	4768	1.25×10^{5}	11.6	0.95	7.28×10^{-5}	
150%	6764	4.24×10^{5}	9.1	0.96	1.41×10^{-4}	

After relaxing from 300% pre-strain, CPY-300 shows a constant L_p with subsequent increasing testing strain, while W_c increases linearly with strain (Figure 5.9f). At lower strain (5%), the yarn still behaves as a pure resistor (Figure 5.12a-c) as the W_c are small enough to remain electrically connected. However, the impedance becomes dependent on frequency at the much lower testing strain value of 10% compare to PY which starts at 30% strain, as the pre-cracked patterns are much easier to separate. At 10% strain, a high capacitance of 1030 pF is observed for CPY because the number of cracks of CPY at 10% strain is greater but its W_c is smaller than that of PY at the same strain. With increasing strain, the cracks become wider, a similar increase in resistance and decrease in capacitance as for PY are observed. It is interesting that after 50% strains, the behaviour of CPY is quite different from before as it is equivalent to two resistor and capacitor parallel combinations connected in series (Figure 5.12c). Looking into the cracks morphology formed upon pre-strain (Figure 5.9c-e), some secondary cracks (L_p and W_c smaller than 5 μm) exist between major cracks along the yarns, which is also valid in the case of a differently shaped substrate: a solution casted Lycra® film as shown in Figure 5.2. These secondary cracks develop as a result of the main cracks propagating into one another, particularly in thinner parts of the coating, as well as film edges. They act as a resistor connected in series or parallel to the main PEDOT:PSS cracked patches, allowing these electrically conductive pathways to remain connected, leading to PY and CPY remaining conductive even at high strains. However, above 50% strain during the second stretch, these secondary cracks are much easier to separate and the distance between parts of the small PEDOT:PSS patches are large enough to act as capacitors. Therefore, a secondary resistance-capacitor parallel combination is added to the equivalent circuit model. With the strain

increasing, the secondary capacitance is increasing linearly due to the total length of small cracks also increasing (Table 5.3).

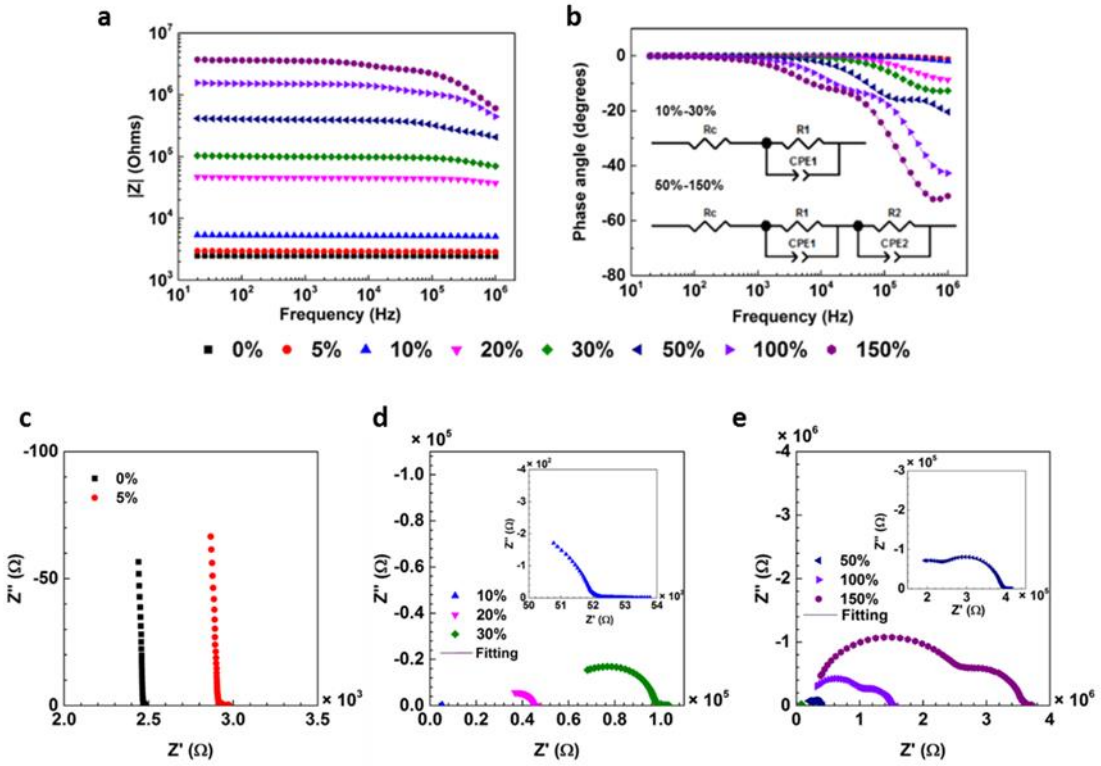

Figure 5.12 *Impedance spectroscopy of CPY-300. The frequency dependencies of the (a) moduli of the complex impedance (Z) and (b) phase angle (θ), Nyquist plots at (c) low strain, (d) medium strain and (e) high strain, with fitted results (lines) based on a pure resistor (R_c+R_1) model for lower than 5% strain, and inserted equivalent circuit models for 10-30% strains and higher than 50% strains, respectively.*

Table 5.3 *Impedance parameters of CPY as a function of different strains.*

CPY strain	R_c (W)	R_1 (W)	CPE_1-T (pF)	CPE_1-P	R_2 (W)	CPE_2-T (pF)	CPE_2-P	Chi-squared	Error
0%	2467								0.05%
5%	2922								0.08%
10%	456	4739	1030	0.89				2.44×10^{-5}	
20%	1.36×10^{4}	3.12×10^{4}	103	0.87				1.62×10^{-4}	
30%	4.12×10^{4}	5.68×10^{4}	44.7	0.88				1.44×10^{-4}	
50%	1.29×10^{5}	1.08×10^{5}	1.28	1.00	1.52×10^{5}	18.3	0.96	2.65×10^{-4}	
100%	1.92×10^{5}	8.29×10^{5}	0.78	0.97	4.76×10^{5}	36.2	0.93	1.16×10^{-4}	
150%	2.35×10^{5}	2.27×10^{6}	0.86	0.94	1.09×10^{6}	55.0	0.89	2.47×10^{-4}	

5.2.4 Thermoelectric properties and power output

Thermoelectric properties provide a robust and reliable energy source for self-powered sensors by harvesting thermal energy from the environment. As expected from the presence of PEDOT:PSS coating, the yarns show typical p-type thermoelectric properties. Within the temperature range from 210 to 360 K (Figure 5.13a), the Seebeck coefficient (α) shows a small increase from 11 μV K^{-1} to 15 μV K^{-1} and the resistivity decreases by half, which is in line with the properties of PEDOT:PSS films treated by DMSO. The Seebeck coefficient of CPY remains invariant compared to PY. However, the induced cracks in the coating increase the resistivity 2500-folds after 300% pre-strain.

When the PY is connected to a variable external load resistance, the voltage and power output can be measured at various temperature differences (ΔT). The open-circuit voltage U_{open} ($U_{open} = \alpha \Delta T$) is expected to increase linearly with the temperature difference between the ends of the sample **(**Figure 5.13b). The maximum power output P_{max} ($= U^2/2R = \Delta T^2 \alpha^2/2R$, where R is the internal resistance of the yarn) should instead increase with the square of ΔT. It can be observed that a single yarn with a length of ~ 1.5 cm, at a temperature difference of 35 °C, can generate a power of 60 pW. With the temperature difference increasing to 95 °C, 1.3 mV can be generated, together with a maximum power output of 480 pW. The current power output level is promising but only if a multi-'leg' fabric-like device can be produced with both p- and n-type yarns and low enough internal resistance. Therefore, a basic device design is shown in Figure 5.13c, with PY as p-type legs and constantan wires acting as both n-type legs and electrical connections. Such a thermoelectric device, with 10 pairs of legs can generate a maximum power of 105 pW, and 18 mV under a temperature gradient of 35 °C (Figure 5.13d).

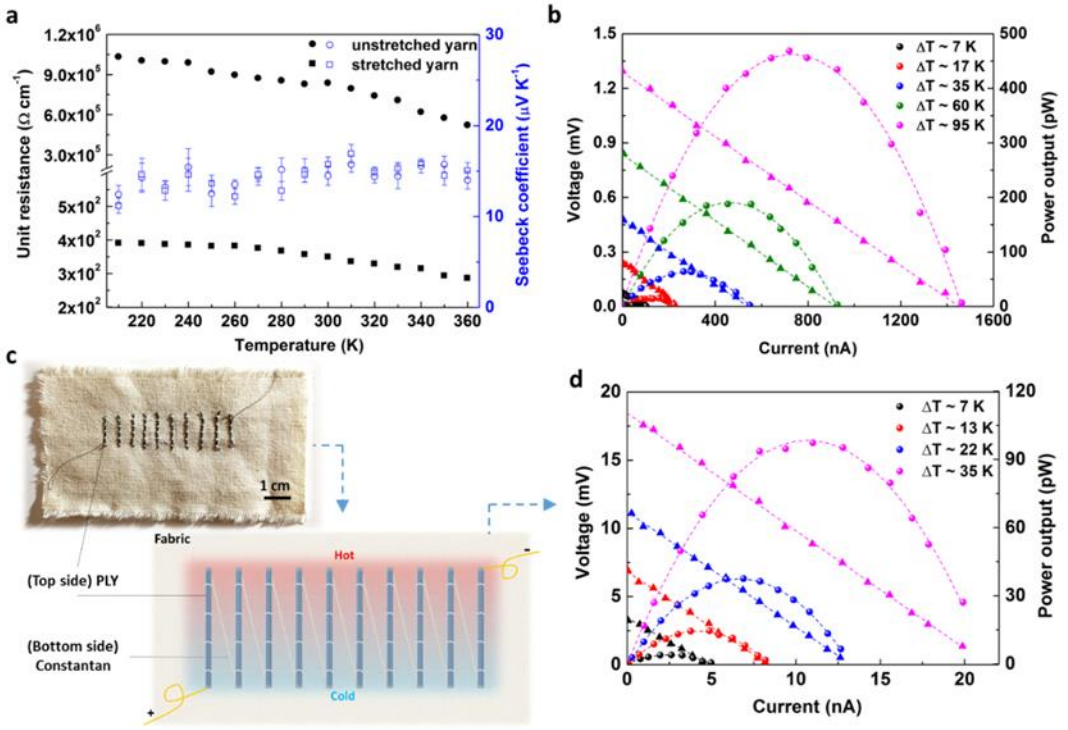

Figure 5.13 *Thermoelectric properties of the PY. (a) Unit length (1 cm) resistance and Seebeck coefficient of stretched and unstretched PY under temperature sweep from 200 K to 360 K. Error bars represent the standard deviation of 5 times Seebeck coefficient measurement on the same specimen at each temperature. (b) power output (circle) and voltage output (triangle) of 2 cm PY under different temperature difference when various external loads are applied. (c) The photograph and the illustration of the 10 pair legs fabric-based thermoelectric device, and its (d) power output (circle) and voltage output (triangle) under different temperature gradients.*

5.2.5 Towards multi-functional self-powered sensor application

The ultra-sensitive CPY smart yarns with tuneable sensitivity and strain range could be used in various multi-functional applications such as wireless strain sensors as well as self-powered strain sensors. When connected with external power, the CPY-300 works as a strain sensor with wide sensing range of strain and ultrahigh sensitivity. A very clear resistance change can be observed both at large strains, *i.e.* 200%, tested 100% min^{-1} strain rate (Figure 5.15a.i) and low strain strains, *i.e.* 1%, tested at 10% min^{-1} strain rate (Figure 5.15a.ii). The effect of tensile strain rate increases from 5%

min^{-1} to 150% min^{-1} and the sensitivity is slightly increasing from GF ~ 120 to 165, which is compatible with the viscoelastic response of Lycra® (Figure 5.14). The lowest strain, 3%, gave a 2-fold resistance changes, which corresponds to a GF of 200 as shown in the insert of Figure 5.15a.ii. Based on the wide sensing range, this strain sensor could be used in wearable devices for body motion monitoring, as demonstrated in Figure 5.15b for example. The sensing signal ($\Delta R/R_0$), which increases synchronously to the bending of the index finger, can be transmitted wirelessly and in real-time to a mobile phone.

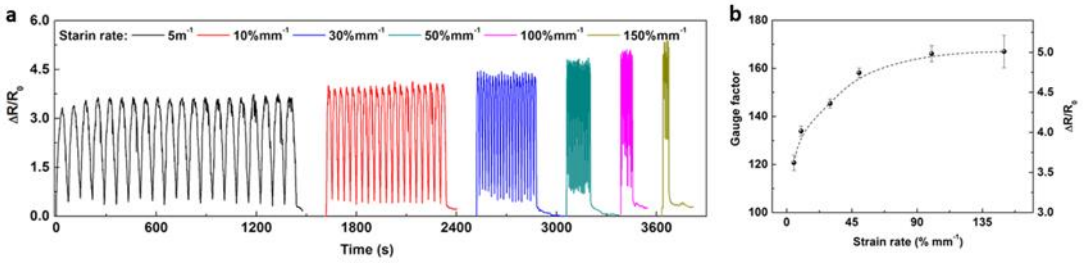

Figure 5.14 *The strain rate effect to sensitivity. (a) The resistance change of CPY with the cyclic 3% strain under different strain rates and (b) their corresponding GF value. Error bars represent the standard deviations of 20 cyclic tests at each strain rate.*

In absence of the external power supply, current CPY sensors can also function as a self-powered sensor upon an ambient temperature gradient. As the CPY is connected in short circuit, the current output will change with the strain, as a consequence of the CPY's resistance change. A thermal current is developed in the circuit at a temperature gradient of 20 K. This constant temperature difference along the film generates a thermal voltage (U), which is independent of the strain. Therefore, the current $I(\varepsilon)=U/R(\varepsilon)$ is inversely proportional to its resistance (R). Figure 5.15c shows the output current signal change as a function of the imposed strain, demonstrating the ability to sense and generate thermoelectric power concurrently.

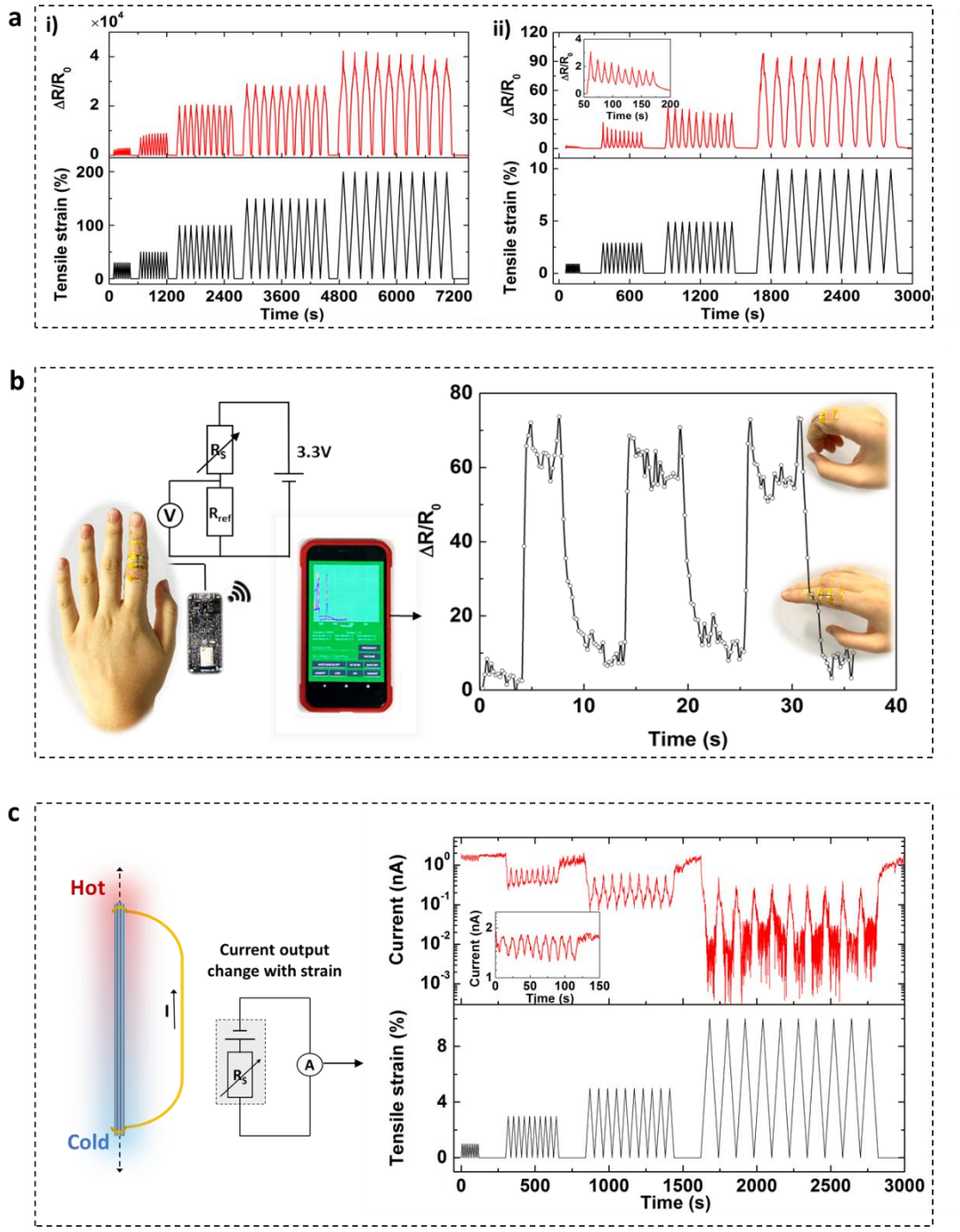

Figure 5.15 *Demonstration of CPY working as strain sensors. As externally powered strain sensor (a) under i) high and ii) low strain & strain rate, showing ultrahigh sensitivity with a wide operation window. Demonstration of CPY working as (b) wireless strain sensor, and (c) self-powered strain sensor: the short circuit current output under small strains (with 10% mm^{-1} strain rate) and under constant temperature difference ($\Delta T \sim 20$ K).*

Based on the intrinsic thermoelectric properties of the CPY, it can also be used as a temperature (gradient) sensor. A variable temperature on one end of the CPY can be detected by a change in voltage (Figure 5.16a) with a constant reference temperature (*e.g.* room temperature) at the other end of the yarn, so the CPY could supply the voltage different accordingly. Although for multi-sensorial applications in general, it is important to be able to discriminate the signals induced by different stimuli, thus, the current system can be easily accommodated to avoid multi-stimuli intervention. It can be decoupled easily by testing short circuit current for the strain signals and open circuit voltage for voltage signals. Meanwhile, strains have no effect on the thermal voltage output, which is also an essential requirement for multi-functional and self-powered strain sensors. The thermal voltage output has been measured under different strains (Figure 5.16b). This voltage is constant, for the same temperature difference, for any strain between 0% and 30%. This demonstrates that, for this strain range, the CPY thermoelectric voltage output signal only depends on the temperature difference. Hence, CPY can been considered as a self-powered temperature (gradient) sensor, with the voltage output as the data acquired. For the proof of concept, a 'smart' glove has been fabricated by stitching the CPY half on the outer surface and the other half inside the thermally insulated glove (Figure 5.16c). In such configuration, the hand temperature is kept constant by the glove, and can then be considered as the reference temperature of the CPY sensor. Therefore, it can sense the ambient temperature or the temperature of the objects in contact with the glove. In a different embodiment, a CPY can harvest body heat and power a second CPY strain sensor.

These results demonstrate that CPY could be used as multi-functional self-powered sensors, with both strain and temperature detection, energy harvesting, and desirable physical properties such as high deformability and water resistance properties.

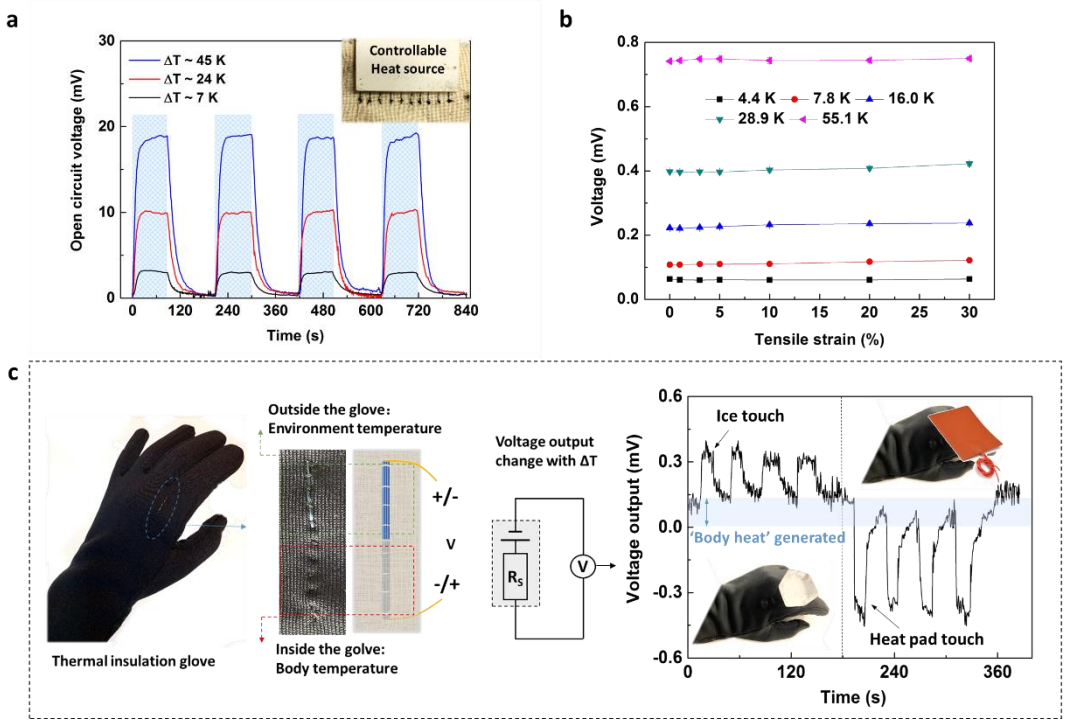

Figure 5.16 *Demonstration of CPY working as temperature sensors. (a) Demonstration of CPY working as self-powered temperature (gradient) sensor: the open circuit voltage output at different temperature differences with different strains. And (b) the influence of the different strains to thermal power output. (c) The demonstration of a smart glove with CPY applied as energy generator by body heat and self-powered temperature sensor, with the temperature of heat pad is 60 °C.*

5.3 Conclusion

In this chapter, a novel self-powered, ultra-sensitive strain and temperature sensor is reported based on PEDOT:PSS coated Lycra® yarns which are prepared by a simple swell-coating method. The ultrahigh sensitivity to strain (GF ~ 49000 at 50 % to 200%) and large stretchability (up to 1000%) provide a unique combination of properties fulfilling the long existing challenge in strain sensors, with the highest value achieved in both sensitivity and stretchability simultaneously. By controlling the pre-strain value to induce cracks patterns of the conductive PEDOT:PSS layer on Lycra®, the sensitivity can be adjusted for satisfying various requirements on sensitivity. The Seebeck coefficient of the PEDOT:PSS was preserved at 15 μV K^{-1} after stretching,

providing temperature sensing ability regardless of deformation and/or energy harvesting for self-powered sensing.

The open circuit voltage signal can be used to detect temperature variations, while the short circuit current can be used to sense mechanical deformations. The sensing yarns have great potential in various applications especially wearable electronics. A wireless movements' detector and a proof-of-concept glove, which can harvest body energy and sense the environment and object temperature in a self-powered mode.

Looking into further developments for the future, one challenge to further broaden the practical applicability will be to increase the power output. The power harvested by thermoelectricity (~ 60 pW under ΔT ~ 35 ^{o}C for 1 yarn) is, for instance, still insufficient to operate commercial data transfer systems (1-10 μW typically required). The development of more efficient organic thermoelectric materials, particularly n-type, is a potential strategy for reaching high TE powers. Alternative energy harvesting mechanisms, like piezoelectricity and triboelectricity, perhaps in combination with flexible energy storage solutions, could also yield very promising results.

Chapter 6 Self-folded CNT veils into honeycomb structured TE device

6.1 Introduction

In **Chapter 2** it was shown that carbon nanotubes (CNTs) and their composites are a special category of TE materials that is receiving an exponentially growing interest owning to their outstanding tuneable TE properties, high electrical conductivity, high mechanical properties and good environmental stability. Among others advantages, large, continuous, and self-standing ensembles of CNTs such as fibres, yarns, veils, and fabrics [227, 228] are at the forefront of advanced materials development. Their structural integrity and possibility of direct integration into composites avoid technical limitations (e.g. short tubes) of using conventional CNT powders (e.g. dispersion via ultrasonication). CNTs can show high Seebeck coefficients, both in p-type (> 60 μV K^{-1}[229]) and n-type (normally larger than -58 μV K^{-1}[73]), high electrical conductivity (> 1000 S cm^{-1}[71]), and thus an ultrahigh power factor of 2482 μW m^{-1} K^{-2} [71, 88] and 1570 μW m^{-1} K^{-2}[89, 90] at room temperature for, respectively, SWCNT and MWCNT continuous films.

To achieve a high-power output from a TE device, a normally overlooked factor is how to connect p-type and n-type alternating legs. Zhou *et al.* [71] reported a compact-configuration flexible TE module based on the vacuum filtrated CNT film, with a thermopower of 410 μV K^{-1} and maximum 2.51 μW power output achieved at $\Delta T \sim 27.5$ K in the in-plane direction. Choi *et al.* fabricated a flexible thermoelectric generator to harvest the thermal energy in the out-of-plane direction. By doping a continuous CNT yarn with alternating p-type and n-type sections, around a polydimethylsiloxane (PDMS) block [86], they achieved a maximum power density

of 697 μW g^{-1} at ΔT~40 °C with 90 p-n pairs. Choi *et al.* also demonstrated that with 9 pairs of p-n connections, the CNT films can generate 3.4 mV by converting body heat directly (ΔT ~ 7 °C) [230].

Very limited effort has been dedicated to utilising integrated TE modules in high performance lightweight structural applications. The only reported work from literature is by George *et al.* in 2019 [231], where a series of p-type and n-type doped commercial carbon fibre tows was fabricated as bottom ply of a structural TE composite, with 5 pairs of p-n legs generating 19.56 mV voltage output at the ΔT ~ 75 °C from an in-plane thermal gradient. Although the feasibility of integrating TE modules into structural composites has been successfully demonstrated, it is worth noting that most of the thermal gradients in fibre reinforced composites might be found at out-of-plane (through thickness) direction rather than the in-plane direction.

Clearly, to utilise the TE effect in nano-engineered high performance composites, two obvious and practical challenges remain: (i) how to best utilise the out-of-plane thermal gradient; (ii) how to increase the power output from TE modules, or in other words, how to effectively connect many alternating p-g legs; (iii) how to achieve the above, without compromising the original high in-plane mechanical properties.

This chapter presents an innovative strategy to achieve high power output TE in structural composites, addressing all three challenges simultaneously by utilising a Kirigami inspired self-folding process. This process has been initially developed by Arnaud Kernin, a colleague in the same research group at QMUL, and adapted to the field of thermoelectricity and (structural) self-powered sensing, by the introduction of CNT veils. Arnaud's PhD thesis, to be shortly submitted, will include more details, particularly on the underlying mechanism of self-folding. The well-acknowledged

mechanically strong (i.e. bending rigidity) honeycomb structure can enable not only the utilisation of thermal gradient in the out-of-plane direction, but has also the capability of accommodating alternating p-n legs series connected for energy harvesting. The electrical power output obtained from this integrated TE honeycomb in hierarchical composites is sufficient to perform the *in-situ* deformation and damage sensing, providing added multi-functionalities such as self-powered structural health monitoring. This new method to integrate TE module into hierarchical composites via self-folding to form honeycomb structure could be used in various high performance composite applications in the fields of aerospace, automotive and renewable (solar) energy sectors, especially in remote and hard to access locations.

6.2 Results and Discussions

6.2.1 Thermoelectric performance of CNT films

The thermoelectric and electrical properties of CNT films have been systematically characterised, with annealing and purification processes employed to improve their performance. The effect of subsequent folding steps on the electrical properties has also been examined. A large scale CNT veil (1.5 m^2) manufactured by floating catalyst based chemical vapor deposition (FCCVD) method [232, 233]. Since the thermoelectric properties of CNT veils can be affected by residual impurities like metal catalysts and amorphous carbon from the manufacturing processes. An annealing process followed by a further acid washing step has also been employed to remove impurities. This purification procedure (particularly the acid wash) can introduce some defects in CNTs, which have been herein evaluated by Raman spectroscopy. Figure 6.1a shows characteristic peaks of D band and G band at ~ 1,330 cm^{-1} and ~ 1,582 cm^{-1}, respectively. Because the D-band refers to the disordered crystalline structure or defects in carbon materials, and the G-band refers

to the regular sp^2 carbon atoms in the graphitic area [234, 235], the intensity ratios of D and G band (I_D/I_G) indicates the disordered carbon content in the materials. The I_D/I_G ratios increased slightly from 0.19 to 0.33 after the first annealing, attributed to the removal of amorphous carbon, particularly on the CNT surface. The ratio slightly decreased to 0.30 after the acid treatment 'purified CNTs'), evidence of some induced defect introduced onto the graphitic structure, but necessary to eliminate the catalyst.

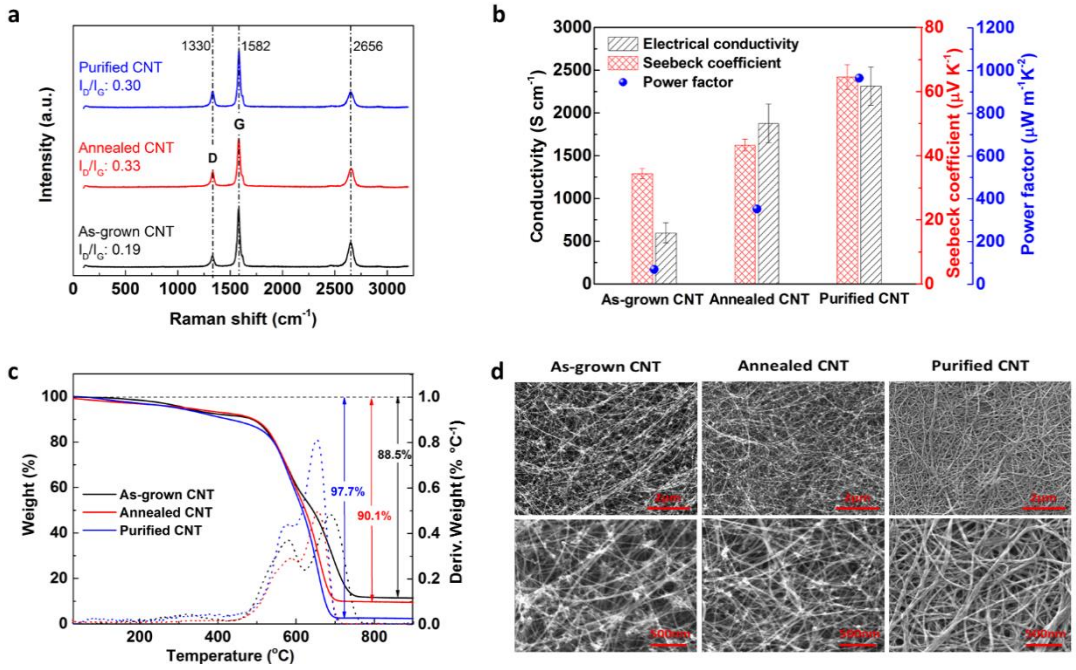

Figure 6.1 *Comparison of as-grown, annealed and purified CNT veils. (a) The normalized Raman spectra excited with a 633 nm laser. (b) Thermoelectric properties (electrical conductivities, Seebeck coefficients and power factor). Error bars represent the standard deviations. (c) Mass loss, and its derivative, as a function of temperature. (d) SEM morphological micrographs.*

Both the electrical conductivity and Seebeck coeffiecient (Figure 6.1b) were improved after the annealing process. The electrical conductivity trippled from 598 S cm^{-1} to 1878 S cm^{-1}, and Seeback coefficient increased from 34 μV K^{-1} to 43 μV K^{-1}. This is attributed to the successful removal of the amorphous carbon by annealing process. With the further step of acid washing, both the electrical conductivity and Seeback

coefficient were further increased to 2315 S cm^{-1} and 65 μV K^{-1}, respectively. This is attributed to the successful removal of also metal catalyst. Ferrum (Fe) catalyst used as a seed in the synthesis of CNT can act as an n-dopant and introduce some metallic behaviour. After acid treatment, the Fe content in the purified CNT veil reduced from 11.5 wt.% to 2.3 wt.%, as suggested by TGA analysis (Figure 6.1c), and its Seebeck coefficient increase from 37 μV K^{-1} to 65 μV K^{-1}. With these thermopower and electrical conductivity after purification process, a significantly enhanced power factors of 1050 μW $m^{-1}K^{-2}$ was achieved compared to only 70 μW $m^{-1}K^{-2}$ of the as-grown CNT veils.

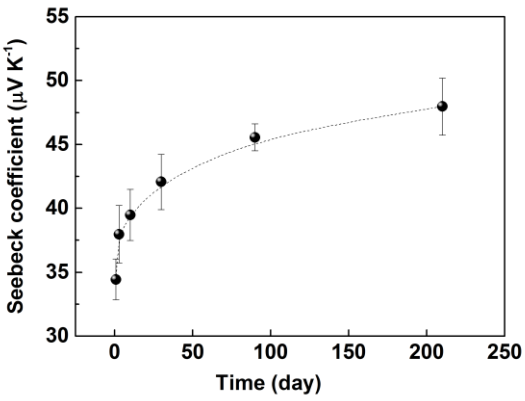

Figure 6.2 *The exposture time influence to Seebeck coefficient of CNT veils. Seebeck coefficient of the as-grown CNT veils changes with the function of time exposure in air at ambient conditions (1 atm, 25–27 °C and relative humidity of 65%). Error bars represent the standard deviations of 5 specimens for 20 measurements each.*

It is well acknowledged that CNT veils can absorb oxygen from the environment, resulting in an increasing p-type doping after several days of exposure to the environment (**Figure 6.2**), due to the formation of hole-like carriers. It is also worth noting that the immersing of the CNT veils in the solution might also reduce their oxygen contents, hence affecting the measured results. Therefore, for a fair

comparison, the Seebeck coefficient values shown in Figure 6.1b were all measured on the third day after treatment to ensure a consistent and reliable results.

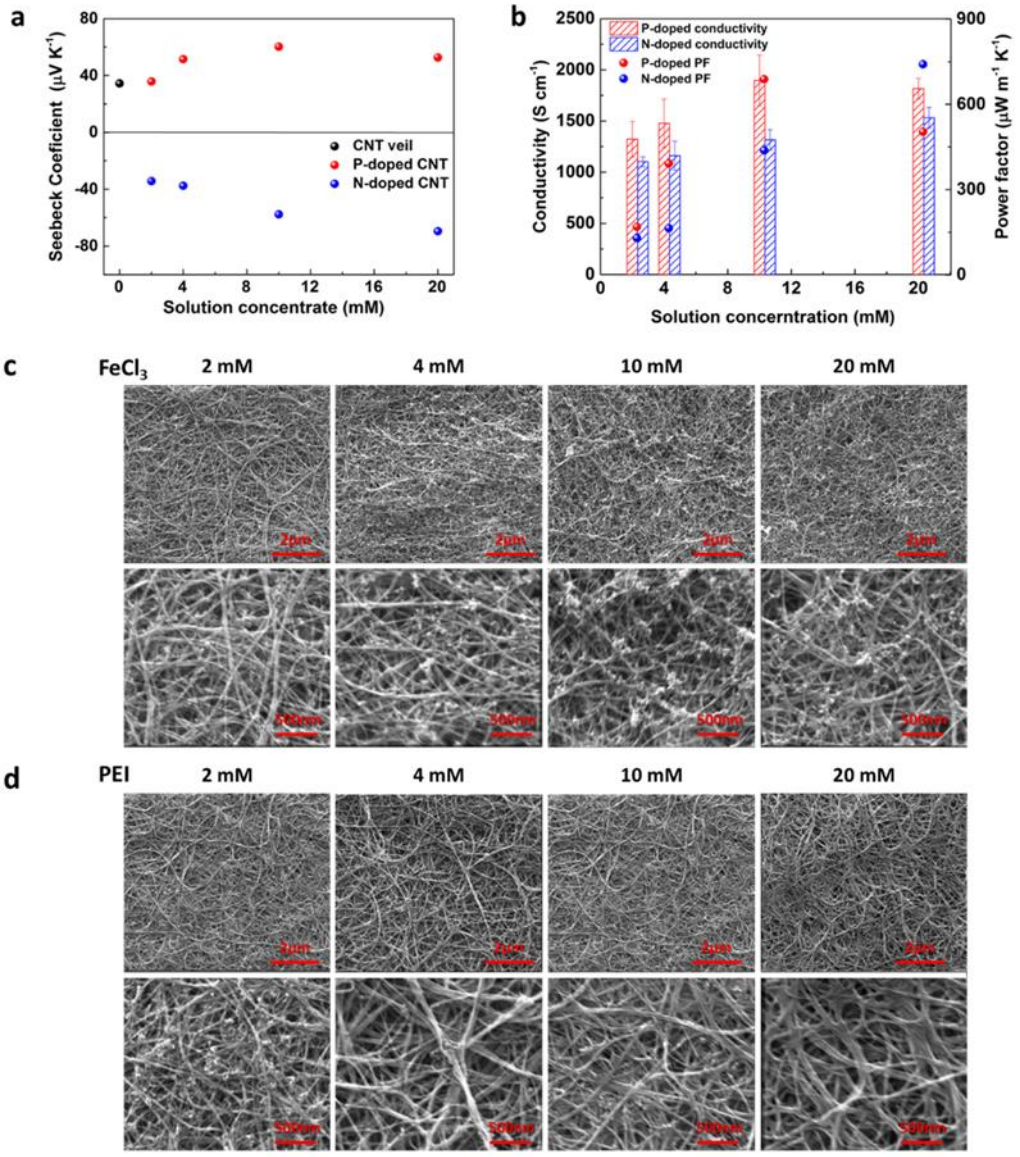

Figure 6.3 *Thermoelectric properties and morphologies of doped CNT veils. (a) The electrical conductivities, (b) Seebeck coefficients and power factor of the annealed and doped CNT veils at room temperature. SEM figures of (c) $FeCl_3$ doped (p-type) and (d) PEI doped (n-type) CNT veils. The dopant is a solution of PEI and $FeCl_3$ in ethanol, with concentrations ranging from 2 mM to 20 mM.*

For the practical application of CNT veil as TE, p and n type have been obtained by doping with $FeCl_3$ and PEI, respectively. Ethanol was used as solvent to promote the

dopant infiltration into the hydrophobic CNT network. However, it was found that the highly condensed nature of these purified CNT veils (Figure 6.1d) has significantly hindered the infiltration process of dopants, resulting in the residual positive Seebeck value (~ 20 μ K^{-1}) even after the veils was immersed in the PEI ethanol solution overnight. In a more detailed study, different concentrations of 50 μl of dopant solution, ranging from 2mM to 20 mM, onto 225 mm^2 square CNT veils.

$FeCl_3$ was used for p-doping, as the charge transfer from CNT valence band to the $FeCl_3$, increasing hole concentration, without disrupting the intrinsic CNT structure (Figure 6.3c). At low dopant concerntration (2mM), the effect of $FeCl_3$ doping was inferior to the O_2 de-doping, causing a reduction in the positive Seebeck (Figure 6.3a). With increase in concentration, the $FeCl_3$ dopant effect surpassed the oxygen doping, leading to an increase in both electrical conductivity (to 1897 S cm^{-1}) and Seebeck coefficient (to 60 μV K^{-1}). For the concetration above 10 mM, a saturation was observed with no further increase in Seebeck coefficient (Figure 6.3a&b). It is worth noting that the p-type doping process has also increased the air stability of the CNTs, with the Seebeck coefficient changing less than 2 μV K^{-1} after exposure to air for 7 months as opposed to the neat sample (Figure 6.4a). This is attributed the saturation of $FeCl_3$ doping and hence a limited number of free electrons available within the CNT veils, eliminating the possibility of oxygen doping from the environments to introduce more holes. The 10 mM $FeCl_3$ doped p-type CNT veil with power factor of 688 μW $m^{-1}K^{-2}$ was selected for following researches.

Amine-rich PEI molecules act as highly effective electron donors that adsorb on the surface of the CNT without disrupting the intrinsic CNT structure. However, a thickening of the CNT bundles was observed with increase in PEI concentration (Figure 6.3d). By the surface charge transfer mechanism, electrons transfer from PEI

to CNTs and reduce the hole concentration until electrons act as main charge carriers, turning the CNT into n-type (-35 μV K^{-1} with 2 mM PEI). With the PEI concentration increasing, both the electrical conductivity and negative Seebeck coefficient increase (Figure 6.3a&b), resulting from more electron injection, which is consistent with previously reported experimental results [71, 86]. The optimumized TE property for n-type CNT veil is obtained at the highest concentration (20 mM), reaching an electrical conductivity of 1532 S cm^{-1} and a Seebeck value of -70 μV K^{-1}. The power factor is 741 μW $m^{-1}K^{-2}$, which is higher than the most reported n-type CNT samples at room temperature [35, 236]. Good stability was also achieved with n-type doped CNT veils, with only 1 μV K^{-1} decrease after 7 months (**Figure 6.4**a). This is because the uniform PEI coating layer acts as an encapsulation and protect it from doping by oxygen in the air and keeping the n-type character.

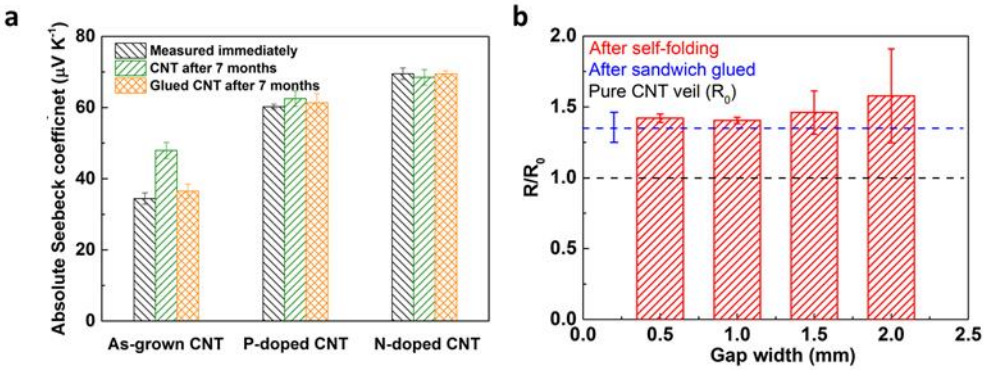

Figure 6.4 *The effect of exposure time, presence of cyanoacrylate glue and folding to thermoelectric properties of CNT veils. (a) Effect of time (7 months) and glue on Seebeck coefficients of pristine, p and n doped CNT veils. (b) Effect of glue and folding to the electrical resistance of the CNT veils. Error bars represent the standard deviations of 5 specimens for 20 measurements each.*

To ensure a consistent and reliable TE performance of the CNT veils, after subsequent fabrication and deformation processes into structural composites, the effect of deformation (folding) and adhesive employed in the subsequent processes have also

been examined. The addition of a cyanoacrylate glue, increased the electrical resistance of the CNT composites by about 30%, compared to a pristine CNT veil with same dimensions (Figure 6.4b), but did not affect the Seebeck coefficient (Figure 6.4a). Interestingly, cyanoacrylate acted as a sort of encapsulation materials, protecting the CNT veils from oxygen absorption. The Seebeck coefficient of the 'encapsulated' undoped CNT veil only increased by 2 $\mu V\ K^{-1}$ after 7 months, less than half of that for pristine CNTs. The 'encapsulation' also helped the doped CNT veils, as demonstrated by a Seebeck coefficient invariant for at least 7 months.

The deformation, from 0° to 150° - 180° induced by the folding process resulted in an increase in electrical resistance. In particular, the resistance increased by 7% to 23%, *i.e.*, 1.4 ~ 1.7 fold of the pristine resistance of the annealed CNT veils (Figure 6.4b), depending on the levels of deformation typical of our folding processes.

6.2.2 Temperature induced self-folding for a honeycomb structure

Honeycomb structures are common core layers for sandwich structural applications and can be manufactured in different ways. However, the direct folding 2D flat CNT veils into 3D honeycomb modules, with accurately connected and alternating p-n legs remains a complex and challenging task. A Kirigami inspired self-folding process is utilised herein to achieve a honeycomb thermoelectric module, which can harvest the thermal energy in out-of-plate direction, with a series of p-n legs connected in series.

The self-folding principle is similar to the bending of bi-metal strips bending [237]. In this work, a b-PS film was used as an active layer with capability to shrink upon heating (negative coefficient of thermal expansion), with a polycarbonate (PC) layer adhered on top acting as substrates and hinges restrict the thermal shrinkage and hence inducing folding (acting like a hinge) at the boundary between PC-restricted and b-PS

only sections. Two thin layers of CNT veils (3-5μm thickness individually) were used to sandwich the shrinkable b-PS layer with the PC layer adhered at the outside (either top or bottom) of CNT/b-PS/CNT structures. By changing the location and patterns of PC layer, various shapes and dimensions can be programmed and achieved by the temperature induced self-folding processes.

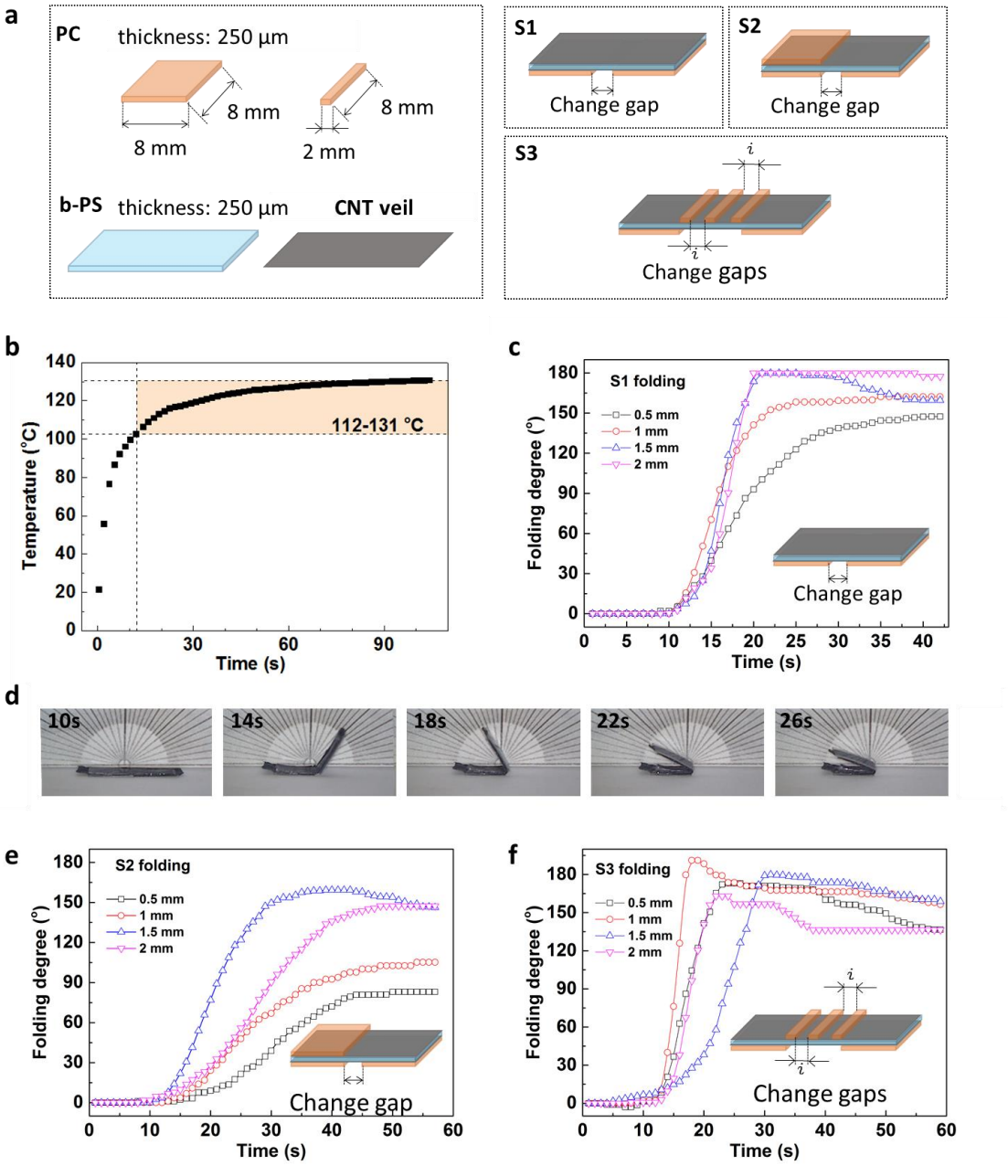

Figure 6.5 *The three structures of self-folding. (a) Constituent materials (CNT veils, b-PS and PC) and three main structures (S1, S2 and S3) utilised for the self-folded*

honeycomb. (b) The actual samples temperature, recorded by an IR camera, as function of time, when the sample is placed in an oven at 130 °C; the self-folding starts at 112 °C. (c) Change of the folding angles with time for S1 samples, with various gaps. (d) Images of the self-folding procedure for a representative sample (S1, gap width of 1mm), showing the folding angles as a function of time, at 130 °C. (e,f) The folding angles change with time and gaps' width, for (e) S2 and (f) S3 structures.

To understand better the self-folding mechanism hence utilising this method to turn 1D CNT veils into 3D honeycomb structure with accurate p-n leg connections, different designs have been examined (S1, S2 and S3 in Figure 6.5a). To establish the folding profile and relationship between folding angles with time and temperature, a simple design (S1) has been employed (Figure 6.5c&d). Two passive PC layers are glued on one side of b-PS, at a distance of 0.5 mm to 2 mm (the 'hinge' gap). After placing the D1 specimen into the oven preheated to 130°C, the sample started folding at t ~ 12s, which corresponds to the sample temperature reaching the glass transition temperature of b-PS of 110 °C (Figure 6.5b). The intact PC layers have constrained the shrinkage of PS layer and created the torque on the hinges, generating the bending moment for the folding process. Very short response time (between 10 and 30s) was required for this temperature induced self-folding process, with great programmability in both folding angles (ranging from 150° - 180°) and folding speed by tuning the gap width between intact layers (Figure 6.5c).

After optimising the gap width and designs with the aim of achieving the correct angles required for honeycomb structures (Figure 6.5e&f), **S**2 with a gap width of 0.5 mm and S3 with a gap width of 1 mm were employed to create the folding angle of 60° and 180°, respectively.

As shown in Figure 6.6a, the p and n doping has been employed prior to the folding process, with the patterns designed for the honeycomb shape, in which p-n legs are

connected autonomously for thermoelectric energy harvesting. According to this pattern, the p and n doped legs are connected in series electrically and in parallel thermally (Figure 6.6a). For fabrication of the self-foldable one-cell honeycomb TE device, a small rectangular hole was cut from the b-PS. PC films were added to both sides of b-PS, recreating the design of S2 and S3 structures, with doped CNT veils in between. Therefore, a five layers sample was fabricated, *i.e.*, PC/doped CNT/b-PS/doped CNT/PC and put into an oven at 130 ^{o}C for self-folding. The single modular honeycomb structure consists of one-unit cell can be self-folded at 130 ^{o}C within 45 seconds, with the sequential folding of S3 followed by S2 as demonstrated in Figure 6.6a. This is in accordance with previous tests of S2, S3 folding, which showed that a 180^{o} folding was completed in 17 seconds (Figure 6.5f), much faster than S2 folding, which is finished after ~ 45 seconds (Figure 6.5e).

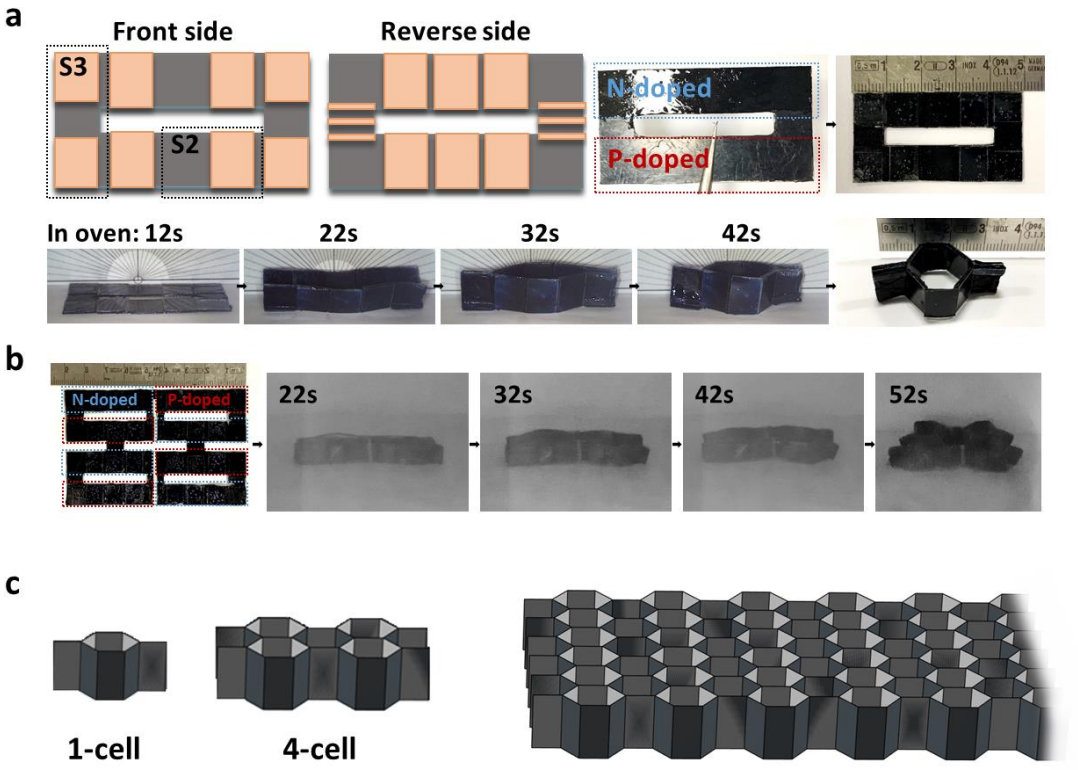

Figure 6.6 *Honeycomb structure via temperature induced self-folding. (a) The schematic illustrations of the design and patterns for the fabrication of modular one*

unit cell honeycomb structure TE module, with circled areas of S2 and S3, and the images of its fabrication procedures of the TE module with 1 cell honeycomb structure. (b) Images of the fabrication procedures of the TE module with 4-cell honeycomb structure via self-folding processes. (c) The schematic illustration of the self-folded one-cell, four-cell and multi-cell honeycomb structured TE modules.

To demonstrate the feasibility of utilising this self-folding process for high TE energy density, a honeycomb structure consisting of four cells of alternating p-n legs has been fabricated (Figure 6.6b). Benefitting from the formation of 4 pairs of p-n legs on each side of the b-PS, 8 thermocouples have been achieved in this self-folded 4-cells honeycomb TE module. Similar to the doping pattern of single module, the undoped regions were folded to the top and bottom side of the module and acted as connecting electrodes, to minimize the internal resistance of the fabricated TE module. By repeating the same pattern in an increased area, a multi-cell honeycomb structured TE module (Figure 6.6c) based on the doped CNT veil can be easily obtained via the self-folding process induced by temperature. Clearly, the vertical alignment of alternating p-n CNT legs in these fabricated TE modules could enable energy harvesting from out-of-plane thermal gradients, opening up a much wider field of practical applications.

6.2.3 Thermoelectric performance of self-folded CNT honeycomb

To evaluate the thermoelectric performance and power output, the fabricated single-cell modular CNT honeycomb, with one pair of p-n legs, was examined under various temperature difference in the out-of-plane direction. Under a $\Delta T \sim 20\ ^{o}C$, a single pair of the p-n legs generated a voltage of 2.5mV with a peak power output up to 115 nW (Figure 6.7a), which is higher than most of the values from CNT-based TE modules in literature [229, 238]. Theoretically, an increasing number of the p-n pairs (n) can increase both the voltage output *U* and the maximum power output P_{max}. Therefore, the energy harvesting performance of the 4-cell TE module has also been examined

(Figure 6.7b) to demonstrate the potential of further enhancing the output power by increasing the number of p–n pairs in series. The maxium power output should be obtained when the external load resistance is equal to the sum of internal resistance (R_i) of the TE module and the contact resistance (R_c), and can be estimated via the following equations:

$$U = n(\alpha_p + \alpha_n)\Delta T \qquad \textbf{\textit{Equation 6.1}}$$

$$P_{max} = \frac{U^2}{4(R_i+R_c)} \qquad \textbf{\textit{Equation 6.2}}$$

where α_p and α_n refer to the absolute values of Seebeck coefficient of the p and n doped CNT veils, which are 60 μV K^{-1} and 69 μV K^{-1}, respectively. Therefore, under a certain temperature difference (ΔT)), U is proportional to n. Meanwhile, the internal resistance is also increasing linearly with the number of p-n pairs due to the increased amount of series connected CNT legs. Thus, for a TE module with a large number of the p-n pairs, R_i should be much higher than R_c and increases linearly with the number of p-n pairs since the average resistance per p-n pair is nearly constant. Therfore, P_{max} should be proportional to n. The measured power output in Figure 6.7b are in good agreement with this relationship. The highest voltage generated by the four cells honeycomb structure with eight elements (thermocouples) was around 21 mV, together with a maximum power output of 812 nW at 17 ^{o}C. These values are around 8 times of the energy harvesting capability of single unit cell element can generate under the same temperature difference. Obviously, both the voltage output and power output can be further increased with increasing numbers of unit cells in current honeycomb structured TE module. Based on the current relationship between numbers of connected p-n leg unit element and obtained power output, 10 μW could be achieved in honeycomb TE module consisting of 50 unit cell elements (100 effective

p-n pairs) at a temperature difference of only 17 °C, fulfilling the practical requirements of many electronics and devices.

Additionally, the existence of plenty of cavities within the honeycomb structure also brings benefits of a low thermal diffusion coefficient at out-of-plane direction, maintaining a stable temperature difference without the needs of an external cooling system. As shown in Figure 6.7c, the temperature gradients across the 4-cell honeycomb TE module were very stable, regardless of a cooling system on the opposite surface. After reaching the thermal equilibrium of the TE module with a bottom heating pad set at 90 °C, the temperature of the cold side was 47 °C without the cooler, translating to a ΔT ~ 43 °C across the TE module. Compared to the system with cooling system set at the top (ΔT ~ 50 °C), only 14% temperature loss was observed, thanks to the empty spaces within these honeycomb structures.

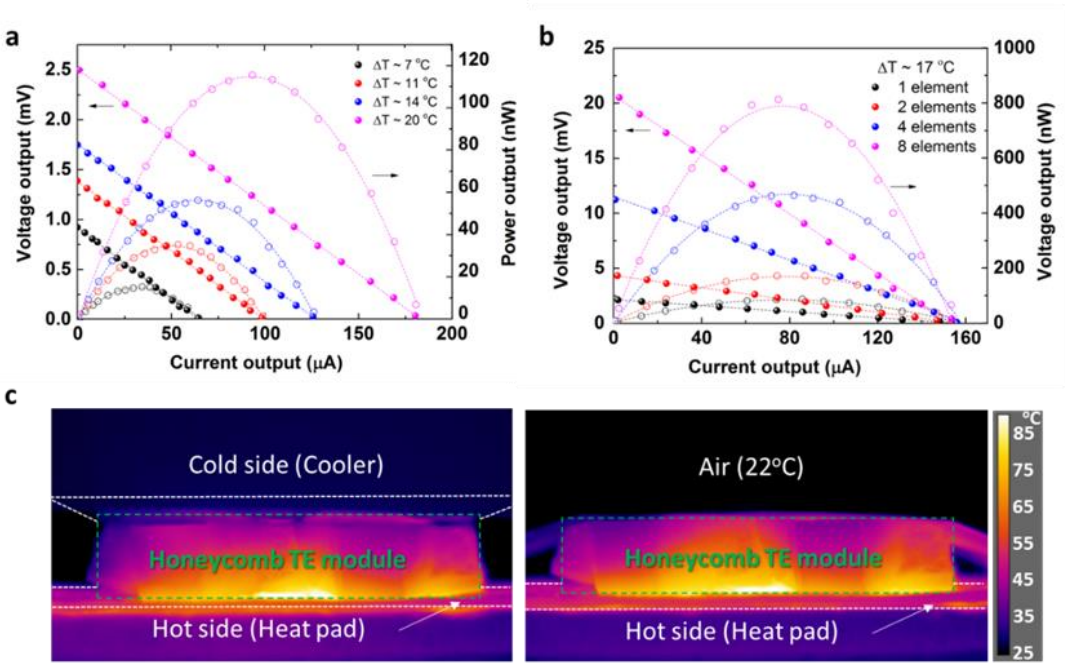

Figure 6.7 *TE performance of honeycomb structure TE module. (a) The voltage and power output from one-cell honeycomb TE module consisting of a single thermal couple at various temperature differences. (b) The voltage and power output from*

different numbers of elements, i.e., thermocouples, within the fabricated 4-cell honeycomb TE module when $\Delta T \sim 17^{o}C$. (c) Thermal images at cross-sectional views of the four-cell honeycomb TE module with a $90^{o}C$ heat pad attached on bottom (hot) side, confirming a stable thermal gradient regardless of a cooler at the cold side.

6.2.4 Self-powered sensing in structural composites

The fabricated honeycomb TE modules can be integrated into composite laminates, adding multifunctionalities such as *in-situ* sensing to the components in two different ways: either as a self-powered sensor by harvesting thermal energy to detect deformations or damages, or as a temperature sensor to monitor the external temperature variations by measuring the variations in power output generated.

The fabricated four-cells CNT honeycomb TE module was integrated into a nano-engineered hierarchical glass fibre reinforced plastics (GFRPs) as illustrated in Figure 6.8a, in order to examine its function of self-powered sensing. The honeycomb TE module plays the role of a power supplier, when it is placed within a temperature gradient created by position a heat pad on the top side only.

Since the electrical sensing method is utilised for deformation and damage monitoring in multifunctional composites, prior to examining the self-powered sensing capabilities based on the honeycomb TE module, the electrical sensing performance with an external power supply has been evaluated first with the current system. The nano-engineered hierarchical composites consist of glass fibre reinforced plastics (GFRPs) with a thin layer of percolated CNT sensory network spray coated at the top ply as the sensing layer, with the resistance measured throughout the test as the sensing signals.

During the three-point bending test (Figure 6.8b), the CNT network is on the bottom side of the GFRC laminate and the resistance (R_0=6kΩ) increased with deformation.

This resistance change originates from the partial disconnection of the nanotubes in the CNT network.

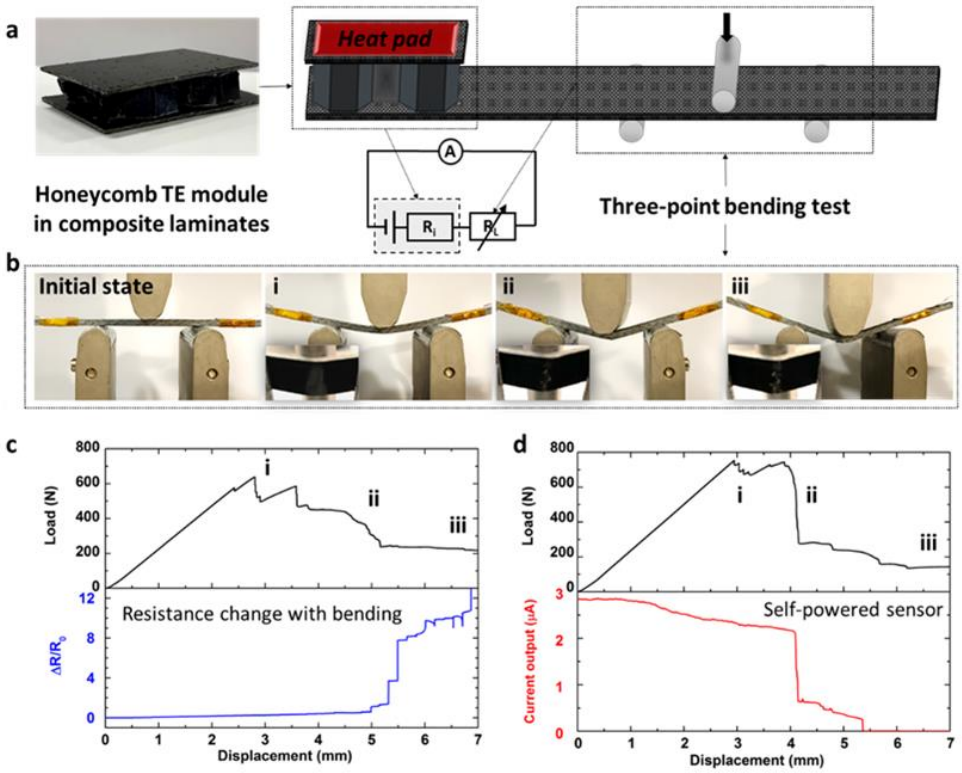

Figure 6.8 *In-situ sensing performance of the composite laminates under flexural loadings. (a) Schematic of the honeycomb structured TE modules applied as a self-powered sensor. TE modules are assembled between GFRCs with a heat pad on the top to provide temperature gradient. The composites laminates are deformed under three-point bending. Its equivalent circuit are inserted, where the grey rectangle refers to the TE modules (a generator with inner resistance, R_i), the R_L is the resistance change of the composites laminates, and a current meter in connected in series. (b) Images of the three-point bending part at different stages (from i to iii) indicated in both (c) and (d), with their bottom view focus on the failure part in inset. In-situ measurement of the (c) resistance change of the composite laminates with an external power supply, and (b) current output variation with bending when self-powered by TE modules with $\Delta T \sim 17\ ^oC$.*

As shown in Figure 6.8c, although matrix cracking and interfacial debonding can be expected at relatively low strains upon loading, the electrical sensing signals remained

almost unchanged at the beginning of the test, due to limited deformation and damage of the sensing layers at the outer layer (under tensile loading) of the laminates. With the damages accumulating within the laminates and propagating to delamination and fibre breakages, obvious changes in the load curve can be found with clear load drops (annotated i within Figure 6.8c), indicating an irreversible damage within the specimen. However, due to the relatively high amount of CNTs employed in the sensing layer, no obvious electrical sensing signals can be observed until the cracks have progressed with obvious damage at the outer sensing layer (annotated ii in Figure 6.8c), showing obvious jumps in electrical sensing signals. Clear sensing signals can be found with the damage propagating within the sensing layers, with reduced loading levels observed from the load-displacement curve.

Instead of relying on external power supply, the current output generated via thermal energy harvesting can be also utilised to develop a self-powered sensing system. Under a constant temperature difference, the voltage output generated from the TE module will remain constant. Therefore, any change in electrical resistance from the sensing layer will lead to a change in the current output, which can be utilised as a sensing signal to detect deformation and damage in composite structures.

For the current self-powered sensing method, a stable current output of around 2.9 μA was achieved with a 17 ^{o}C of temperature difference (Figure 4b). Upon flexural loading, the electrical sensing signals remained stable at the very beginning then started to decrease slightly from relatively early stage of the test (around only 1 mm displacement). A gradual decrease in sensing signal can be found, correlating with increased load and deformation of the specimen. With the load continuously increasing, delamination and fibre breakage can be expected with clear load drop from the load-displacement curve (annotated i in Figure 6.8d). A further decrease in sensing

signals can be found at this stage, regardless of the sensing layer only presented at the outer layer. When the crack propagated and reached outer sensing layer (annotated ii in Figure 6.8d), a very large drop in sensing signals can be found due to the significant change in system resistance value hence the current output. No power supply is required for the honeycomb TE module, while the deformation and health conditions with internal damage propagations can be monitored in real time-based thermal energy harvested self-powered sensing method.

6.3 Conclusions

Self-powered sensing based on thermal energy harvesting has been successfully integrated into a high-performance composite via a temperature induced self-folding process, with capability to detect deformation and damage in composite laminates without external power supply. Two long lasting issues of using thermal electricity in advanced functional composites have been solved simultaneously, namely (i) harvesting thermal gradient at out-of-plane direction and (ii) generating high power output with limited temperature difference. High peak outputs of 21mV and 812nW at temperature difference of only 17 ^{o}C have been achieved with a CNT honeycomb structure consisting of accurately connected four pairs of alternating p-n legs, opening up new routes for self-powered structural health monitoring and thermal energy harvesting in high performance composite applications.

A temperature induced self-folding process has been utilised in this work, turning 1D continues CNT veils into 3D honeycomb structures autonomously upon heating. Various designs have been developed and fabricated to achieve both the modular unit of CNT hexagonal structure as well as the engineered CNT honeycomb structure with accurately connected p-n legs. The thermoelectric properties of continuous CNT veils have been systematically examined and tuned for optimised energy output, with

limited effects observed from the self-folding process. A linear relationship between the power output and numbers of TE legs under a constant temperature gradient has been validated with the fabricated CNT honeycomb structures, indicating that the power output could reach 10μW with 50 unit cell elements at a temperature of 17 ^{o}C only, which can fulfil the practical requirements of various electronics and devices. The generated cavity within the honeycomb structure also enabled low thermal diffusion hence facilitated the stable temperature gradient across the specimen without the needs of any active cooling system.

Self-powered strain and damage sensing based on thermal electric effects has been successfully achieved in a structural composite laminate, with energy harvested from out-of-plane direction without affecting original performance of the composite laminates. Both elastic deformation and the damage propagation have been monitored in real time, with sensing signals clearly correlated with various stages of damage upon loading, confirming its great potential to be used as self-powered structural health monitoring system at remote and/or hard to access locations for advanced composite applications.

Chapter 7 Conclusions and future work

7.1 Conclusions

In this thesis, three types of OTE materials have been explored: PEDOT:PSS, Poly(M-ett) and Carbon nanotubes (CNTs), representing an n-type coordination material, a p-type conjugated polymer and a carbon-based nanocomposites, respectively. They have been evaluated with a particular focus on multi-functional self-powered sensors.

The brittle n-type $Na_x(Ni\text{-}ett)_n$ was compounded within a PU (Lycra®) matrix to create a stretchable TE composite material, named NL (**Chapter 4**). The solution-cast composite film with 50 wt % $Na_x(Ni\text{-}ett)_n$, exhibits an outstanding strain-at-break (~ 510 %), an n-type Seebeck coefficient (-40 $\mu V\ K^{-1}$) and electrical conductivity of 0.01 $S\ cm^{-1}$. This novel material can be easily produced at large scale with continuous processes. When subjected to a small temperature difference (< 20 ^oC), the material generated sufficient thermoelectric power to be used for sensing strain (*Gauge Factor* ~ 20) and a visible light sensor with a *Sensitivity Factor* of ~ 36% $(kW\ m^{-2})^{-1}$ which is independent of humidity (*Sensitivity Factor* ~ 0.1 $(\%RH)^{-1}$) is obtained.

To overcome the typical shortfalls of traditional π-shaped TE devices, such as brittleness and hardly scalable manufacturing, two prototypes have been designed. i) A metal-free, stretchable OTE device was fabricated by connecting n-type legs ($Na_x(Ni\text{-}ett)_n$/Lycra®) and p-type legs (PEDOT:PSS/Lycra®) in series via hot pressing. These legs were separated by a stretchable and insulating PU film before folding into zig-zag structure. ii) An origami inspired and 3D conformable "magic-ball" TE device was also demonstrated, which can be conformable to different 3D shapes. This has been fabricated by brush painting a $Na_x(Ni\text{-}ett)_n$/DMSO solution (n-type) and commercial PEDOT:PSS water suspension (p-type) patterns onto a paper.

To further improve the sensitivity, elastic response and power output, a novel PEDOT:PSS coated conductive yarn for self-powered ultrasensitive sensor was fabricated (**Chapter 5**). Ultrahigh sensitivities (gauge factor ~ 3.6×10^5 at a strain of 10%-20%) together with a very high strain-at-break (~ 1000%) were obtained, with a stable thermoelectric behaviour (Seebeck coefficient of 15 $\mu V\ K^{-1}$). The sensitivity could be tuned (from PF of 8 to 302 at 3% strain) by controlling the crack induced patterns in the conductive coating. This combination of desirable properties is potentially useful in multi-functional self-powered sensors, which are sensitive to temperature, strain and body movements, opening up great potential in many fields like wearable electronics and self-powered sensors at remote locations.

The third TE material selected was CNT veil, which could be turned in a p-type or n-type by a suitable doping. The high flexibility of the CNT veil, combined with the high intrinsic mechanical properties, allowed a Kirigami-inspired shape programming of the 2D veil directly into a 3D TE device (**Chapter 6**). A Kirigami approach was utilised to obtain the 3D structure: a hexagonal cell honeycomb. In particular, the honeycomb TE device structure was achieved via a temperature induced self-folding process. The optimised parameters for purification and p- and n-doping of the CNT veil have been investigated. The annealed CNT veil doped by 10mM $FeCl_3$ and 20mM PEI show the best power factor of 688 $\mu W\ m^{-1}K^{-2}$ and 741 $\mu W\ m^{-1}K^{-2}$, respectively, and a great air-stability. The self-folded procedure at 130 ^oC could be controlled by the patterns of the b-PS and PC films patches. The metal-free self-folded honeycomb structure lowered the thermal conduction and maintained the temperature difference without any cooling system. Under a small temperature difference (~ 17 ^oC), the fabricated 4-cell honeycomb TE module could output 21mV voltage and a maximum power of 812 nW. This was sufficient to *in-situ* detect the deformation and damage of

a structural glass fibre composites, hence working as an embedded self-powered heath monitoring unit.

Overall, different types of OTE materials have been investigated, which can be utilized as multi-functional self-powered sensors. This PhD research explored the potential applications of OTE device in the various fields.

7.2 Future works

The field of organic TE is relatively young and more work is required in the future both, from a fundamental viewpoint, to understand the underlying physical mechanics and, from an engineering viewpoint, to explore and commercialise practical applications. Several ideas were generated during the course of this PhD which are not included in the main body of this thesis, but that might be of use for the reader. Herein we present few preliminary studies which might be considered for further investigation in the future.

7.2.1 The graphene oxide effect

An initial study was performed related to nanocomposites containing Graphene Oxide (GO). GO was used as nano filler in both p-type PEDOT:PSS and n-type Ni-ett semi-conductors.

7.2.1.1 PEDOT:PSS/GO

Upon mixing the GO with PEDOT:PSS via solution casting, the electrical conductivity of the as-fabricated composite increased (Figure 7.1**Figure 7.1** The conductivity and Seebeck results of PEDOT:PSS mixed with/without DMSO and GO, before and after the HI treatment.), despite the electrical insulation property of GO. It can be speculated that some of the functional groups in GO nano sheets (such as –COOH, –OH) might interact via secondary bonds with PEDOT, weakening the coulombic attraction

between PEDOT and PSS, which, in turn, may reduce the percolation threshold of the conductive network. Specifically, 0.02 wt.% GO was mixed with the commercial PEDOT: PSS aqueous solution for the preparation of PEDOT/GO. 5 wt.% DMSO was then added into both pure PEDOT: PSS and PEDOT/GO aqueous solution, which was stirred overnight. The resulting drop casted films are named PEDOT/GO, PEDOT/DMSO, PEDOT/GO/DMSO, respectively.

Afterward, all the films were emerged in 15% HI at 80 ^{o}C for 2 hours to reduce GO. The reduced GO increased the electrical conductivity of PEDOT:PSS above 100 S cm^{-1}. When DMSO was added the conductivity of both hybrid films increased dramatically, and the highest value around 650 S cm^{-1} was obtained in a ternary film containing PEDOT, GO and DMSO. DMSO attract PEDOT while PSS chains are surrounded by water leading to separation of PSS and PEDOT chains. The coulombic repulsions among the PEDOT (PSS) chains making a liner conformation and limited the overlap of PEDOT chains, and thus, form more conductive pathways. The GO in the PEDOT: PSS can deplete the insulating PSS and generate larger contact areas between oriented PEDOT-rich grains, which add more conductive pathways for carriers to improve conductivity of the film. After GO being reduced, the electrical conductivity greatly increased except for the PEDOT: PSS/GO/DMSO ternary film, which decreased to the same level as the others. Reduced-GO can offer more conductive pathways, and the proton from hydroiodic acid is able to combine with PSS chains to form PSSH, which is easily rinsed in water. This theory can explain why conductivity increased of the films made from pure PEDOT: PSS, PEDOT: PSS/DMSO and PEDOT: GO. But for the ternary film, it is unclear why the electrical conductivity decreases. Possible explanation is because the removed functional group on the GO free PEDOT chains so that formed a less liner conformation.

For the Seebeck efficient, both the GO and DMSO have negative effect on PEDOT: PSS, which may because of the trade-off between the electrical conductivity and the Seebeck coefficient in most materials. Reduction makes the Seebeck value of all samples more uniform. Among all of these, the best one is the 5 % DMSO doped PEDOT: PSS mixed with GO, with the highest PF of 17 μW $m^{-1}K^{-2}$.

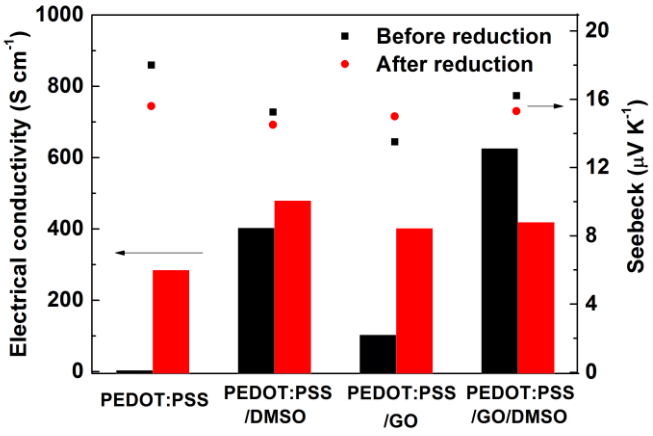

Figure 7.1 *The conductivity and Seebeck results of PEDOT:PSS mixed with/without DMSO and GO, before and after the HI treatment.*

7.2.1.2 $Na_x(Ni\text{-}ett)_n$/GO

The addition of GO into $Na_x(Ni\text{-}ett)_n$ /Lycra composites also increases the electrical conductivity. A systematic experiment has been performed. Different amount of GO were added into the $Na_x(Ni\text{-}ett)_n$ /Lycra solution used for preparing 50% NL of **Chapter 4**. 2 wt.% GO in NL films generates the highest conductivity, which is 5 times higher than pristine NL films (Figure 7.2a). It is assumed that GO helps to bond $Na_x(Ni\text{-}ett)_n$ together and increases the conductive pathways. Similar to the GO effect in PEDOT:PSS, the Seeebeck coefficient of $Na_x(Ni\text{-}ett)_n$ were not influenced by GO.

It is very intriguing that after 1 hour after casting, the electrical conductivity of NL films with GO are all increased (Figure 7.2b). It is assumed that GO in the composites

slows down the solvent evaporation and that the residual solvent is removed further in time. Another intriguing result was found when measuring the electrical conductivity after storage in air for different durations. Although, $Na_x(Ni\text{-}ett)_n$ reported as an air-stable TE material [63], the $Na_x(Ni\text{-}ett)_n$/Lycra composites show a degradation in electrical conductivity and the conductivity dropped to lower than 0.003 S cm^{-1} after 3 months (Figure 7.2b). The possible reason for this phenomenon could a morphology change in time. The GO is potentially protecting the composite films from degradation to some extent because the electrical conductivity decrease is reduced with a higher GO content in the film.

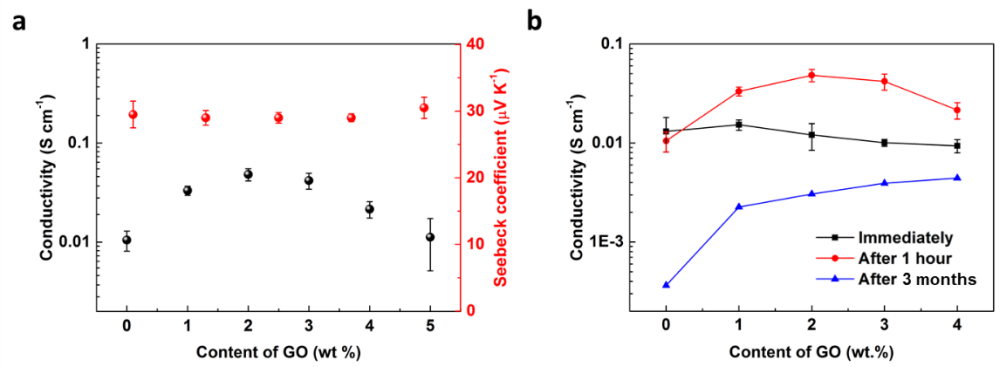

Figure 7.2 *TE properties change with GO content. (a) The electrical conductivity and Seebeck coefficient of 50%NL films correlated with different GO contents. (b) The electrical conductivity of different GO contented 50%NL films measured at different times from been casted. Error bars represent for the standard deviations, which are calculated from 5 measurements at each specimen and at least 5 specimens for each content percentage.*

An initial results are shown as Figure 7.3 for understanding the electrical conductivity change with time at different temperatures. It is obvious that the GO retards the degradation. It is also amazing to observe a slight increase in conductivity of NL-2GO film after exposure for 20 days at room temperature, 12 days at 80 ^oC and 3 days under 120^oC.

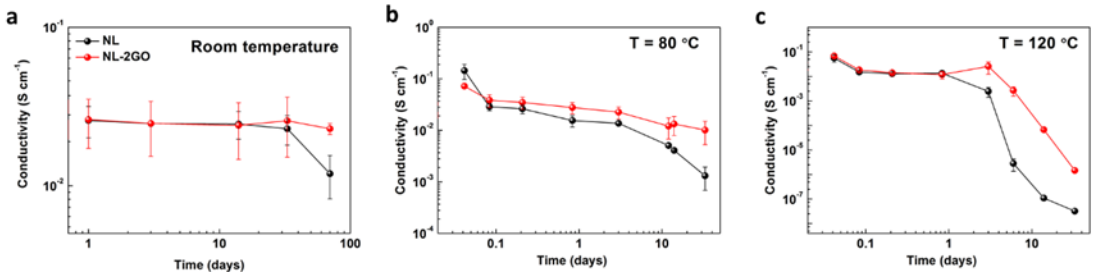

Figure 7.3 *Electrical conductivity of NL films change with time under different temperatures. The electrical conductivity of 50%NL film (black) and 50%NL film with 2wt % GO (namely NL-2GO, red) change with days after exposure in air at (a) room temperature (b) 80 °C and 120 °C. Error bars represent for the standard deviations, which are calculated from 5 measurements at each specimen and at least 5 specimens for each content percentage.*

It is necessary to generate further fundamental understanding of the electrical conductivity change by the GO, time and temperature. A morphological study in combination with chemical element analysis of these films is recommended for the future research on this topic.

7.2.2 The orientation of conducting polymer molecules

As mentioned in **Chapter 2**, enhancing the orientation of the molecules of conductive polymers improves both Seebeck coefficient and conductivity because the charge carriers' mobility increases. Except the addition of nano-sheet materials can orient the polymer chains, there are plenty of technique in the field of polymer engineering can be employed. Take the PEDOT:PSS for example, some strategies have been tried to increase the orientation of PEDOT:PSS chains.

7.2.2.1 Orientated PEDOT: PSS aerogels

The purchased 1.6 wt% PEDOT: PSS aqueous solution in a glass tube (12 mm diameter × 50 mm height) was slowly dipped (5 mm min^{-1}) [239] into liquid nitrogen, and followed by freeze-drying for achieving oriented structures. The orientation is

alongside the dipping direction. Comparing the morphology of a reference sample (Figure 7.4 a), which was fabricated by quickly dipping in liquid nitrogen within 2 seconds, more ordered structures can be find in slow-dipped samples (Figure 7.4 b). With the help of PVA, (25wt.% PVA aqueous solution was mixed with PEDOT: PSS), the order structure seems more stable and shown via SEM (Figure 7.4 c,d). It is worth to mention that different molecular weight of PVA also can influence the orientation structure, and the single molecular weight (M_w) of 9,000 g mol^{-1} can build up the most ordered PEDOT:PSS aerogel (Figure 7.4 d).

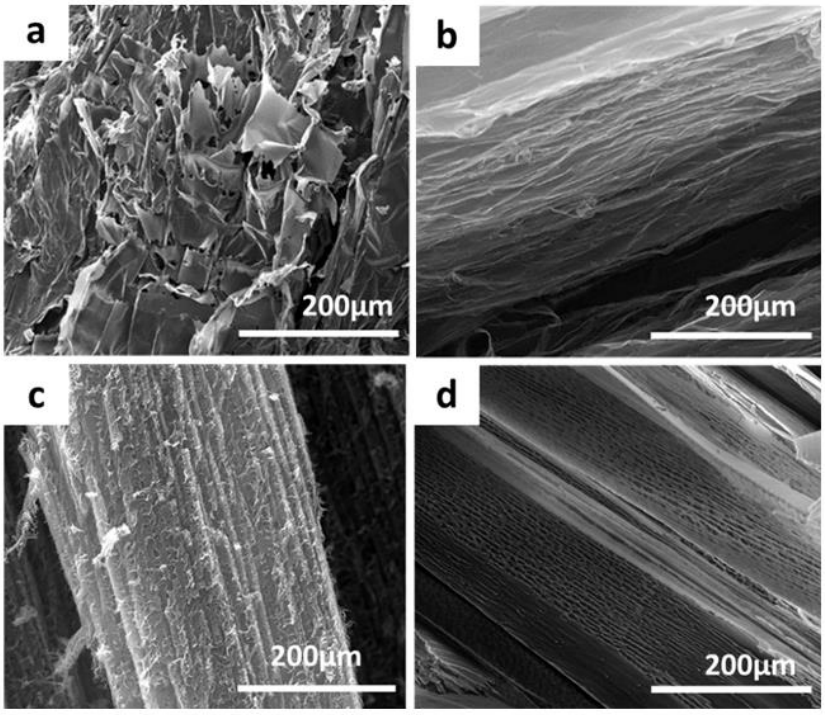

Figure 7.4 *The morphology of the PEDOT: PSS aerogels. SEM images of PEDOT:PSS aerogels fabricated by (a) quickly and (b) slowly (5 mm min^{-1}) dipping. (c, d) SEM images of PEDOT:PSS/PVA aerogels fabricated by slowly (5 mm min^{-1}) dipping. The molecular weight of PVA is Mw =85000-124000 g mol^{-1} for (c) and Mw =9,000 g mol^{-1} for (d).*

The as-fabricated aerogels were cut into small pieces (3mm×5mm×10mm) and cold pressed (2 tons for 1 min) both along with the orientation and perpendicular to the

orientation. By measuring the Seebeck of these thick films processed from the aerogels, it was found that when the temperature difference is provided along the orientation, the Seebeck value is slightly higher (~ 20 μV K^{-1}) than the temperature gradient across the orientation (~ 15 μV K^{-1}). However, for the PEDOT:PSS/PVA aerogels, the Seebeck coefficient is non-detectable by the MMR system due to the high resistances.

These preliminary results point out the route to enhancing the TE property via oriental freeze-drying method. However, several parameters should be further optimized to gain the highest results, including the ratios of PVA to PEDOT:PSS, the post-treatment to the aerogels and the freezing speed.

7.2.2.2 Thermal stretched PEDOT: PSS/PVA films

Solid state drawing is another way widely used for processing polymers to obtain oriented molecular chains along the stretching direction. PEDOT:PSS/PVA composite films have been stretched 10 mm min^{-1}at an 80 ^{o}C oven. The sample with the solid ratio is 90% PVA to 10% PEDOT:PSS was stretched to 400% before it breaks. The Seebeck value of the stretched sample along the stretched direction is 44μV K^{-1} without any other treatments, while the un-stretched PEDOT:PSS/PVA film in same concentration shows a Seebeck coefficient of 30μV K^{-1}.

These interesting results are worth to be further investigated. First, different matrix polymer can be tried. For instance, PVDF which can be stretched for more than 500%, and has unique ferroelectric properties may bring new functions to the TE property and its composite with PEDOT:PSS. One of the challenges is to solve the compatibility issues between PVDF and PEDOT:PSS. Secondly, the understanding of the improved Seebeck coefficient by PVA before stretching is also interesting. Thirdly,

the drawing parameters need to be systematically investigated to optimize for the highest *PF*.

7.2.2.3 Other technique for conducting polymers

Fabricating PEDOT:PSS film under an extremely high magnetic field or electrical field are also fascinating for achieving PEDOT chains orientation. Also, hot-pressing, or cold pressing procedures can introduce an in-plane orientation. These anisotropic samples can help researchers to gain a better understanding of the TE properties' of conducting polymers.

7.2.3 Increasing the legs of OTE device

The relative low power output is a ubiquitous problem of the polymer-based thermoelectric materials. With lots of physics and chemists working on design and synthesis a new generation polymers with high power factor along with processable and air-stable, it is still worth to investigating a new strategy to fabricate a large scale device with more p-n legs connected, especially lowered the contact resistance between legs when connected in series. For example, to the results in **Chapter 5**, n-type counterparts can be fabricated to connect with this p-type yarns to add up the output voltage and form a whole yarn based thermoelectric device. Besides, different sewing or weaving geography should be investigated for fabricating e-textile for real applications. Also, it is also very demanding to develop a TE materials suitable for large-scale processing methods, for example, wet-spun, melt processing and robot casting techniques.

7.2.4 The stability of OTE devices

The stability of the OTEs under different temperatures is always overlooked. Different from the inorganic TE materials, organic-based materials have very limited operation

temperature windows (normally around 0-200 ^{o}C). Besides, various parameters, including the glass transition temperature and soft/melting point, can significantly affect their TE properties. Therefore, the service life of the OTEs under a certain temperature should be investigated in order to satisfied real applications. When applying OTEs as self-powered sensors, it is also important to understand how the gauge factor changes with temperature. It is also important to obtain a reference curve in order to decode the signals. For flexible, especially stretchable OTE devices, the characterization of their deformation life also needs to be completed. Consideing the application of wearable electronics, their washability and robustness to body movements need to be considered.

List of publications

Published Papers

1. **Wan, K.**; Taroni, P. J.; Liu, Z.; Liu, Y.; Tu, Y.; Santagiuliana, G.; Hsia, I. C.; Zhang, H.; Fenwick, O.; Krause, S.; Baxendale, M.; Schroeder,B.C.; Bilotti, E., Flexible and Stretchable Self-Powered Multi-Sensors Based on the N-Type Thermoelectric Response of Polyurethane/Nax (Ni-ett) n Composites. *Adv. Electron. Mater.* **2019,** *5* (12), 1900582. (Chapter 4 of this thesis)
2. Kernin, A.[1]; **Wan, K.[1]**; Liu, Y.; Shi, X.; Kong, J.; Bilotti, E.; Peijs, T.; Zhang, H., The effect of graphene network formation on the electrical, mechanical, and multifunctional properties of graphene/epoxy nanocomposites. *Composites Science and Technology* **2019,** *169*, 224-231. ([1]Equal contribution)
3. Tao, X.; **Wan, K.**; Deru, J.; Bilotti, E.; Assender, H. E., Thermoelectric behaviour of Bi-Te films on polymer substrates DC-sputtered at room-temperature in moving web deposition. *Surf. Coat. Technol.* **2020,** *385*, 125393.
4. Tang, W.; Zhang, J.; Ratnasingham, S.; Liscio, F.; Chen, K.; Liu, T.; **Wan, K.**; Galindez, E. S.; Bilotti, E.; Reece, M.; Baxendale, M.; Milita, S.; McLachlan, M. A.; Su, L.; Fenwick, O., Substitutional doping of hybrid organic–inorganic perovskite crystals for thermoelectrics. *Journal of Materials Chemistry A* **2020,** *8* (27), 13594-13599.
5. Paleo, A.; Vieira, E.; **Wan, K.**; Bondarchuk, O.; Cerqueira, M.; Goncalves, L.; Bilotti, E.; Alpuim, P.; Rocha, A., Negative thermoelectric power of melt mixed vapor grown carbon nanofiber polypropylene composites. *Carbon* **2019,** *150*, 408-416.

6. Liu, Y.; Zhang, H.; Porwal, H.; Tu, W.; **Wan, K.**; Evans, J.; Newton, M.; Busfield, J. J.; Peijs, T.; Bilotti, E., Tailored pyroresistive performance and flexibility by introducing a secondary thermoplastic elastomeric phase into graphene nanoplatelet (GNP) filled polymer composites for self-regulating heating devices. *Journal of Materials Chemistry C* **2018,** *6* (11), 2760-2768.
7. Taroni, P. J.; Santagiuliana, G.; **Wan, K.**; Calado, P.; Qiu, M.; Zhang, H.; Pugno, N. M.; Palma, M.; Fenwick, O.; Baxendale, M.; Bilotti, E., Stingelin-Stutzman, N.; Heeney, M., Toward stretchable self-powered sensors based on the thermoelectric response of PEDOT: PSS/polyurethane blends. *Adv. Funct. Mater.* **2018,** *28* (15), 1704285.
8. Bilotti, E.; Iliffe, S.; Taroni, P. J.; **Wan, K.**; Tuley, R., Thermoelectric module, GB2570669.

Papers in preparation

9. **Wan, K.**; *et al*., Self-powered ultrasensitive and highly stretchable temperature-strain sensors. (Chapter 5 of this thesis)
10. **Wan, K.**; *et al*., Towards self-powered sensing and thermal energy harvesting in high performance composites via self-folded CNT honeycomb structures. (Chapter 6 of this thesis)
11. **Wan, K.**; *et al*., Highly deformable thermoelectric materials and devices: A review. (Part of Chapter 2 of this thesis)

References

1. Kim, H.S., et al., *Relationship between thermoelectric figure of merit and energy conversion efficiency.* Proceedings of the National Academy of Sciences, 2015. **112**(27): p. 8205-8210.
2. Wu, H.J., et al., *Broad temperature plateau for thermoelectric figure of merit ZT>2 in phase-separated PbTe0.7S0.3.* Nature Communications, 2014. **5**: p. 4515.
3. Rull-Bravo, M., et al., *Skutterudites as thermoelectric materials: revisited.* Rsc Advances, 2015. **5**(52): p. 41653-41667.
4. Heremans, J.P., et al., *Enhancement of Thermoelectric Efficiency in PbTe by Distortion of the Electronic Density of States.* Science, 2008. **321**(5888): p. 554-557.
5. Bubnova, O. and X. Crispin, *Towards polymer-based organic thermoelectric generators.* Energy & Environmental Science, 2012. **5**(11): p. 9345-9362.
6. Nolas, G. and H. Goldsmid, *Thermal conductivity of semiconductors*, in *Thermal Conductivity*. 2004, Springer. p. 105-121.
7. Tritt, T.M., *Thermal conductivity: theory, properties, and applications*. 2005: Springer Science & Business Media.
8. Snyder, G.J. and E.S. Toberer, *Complex thermoelectric materials.* Nature materials, 2008. **7**(2): p. 105-114.
9. Kim, W., *Strategies for engineering phonon transport in thermoelectrics.* Journal of Materials Chemistry C, 2015. **3**(40): p. 10336-10348.
10. Nolas, G.S., J. Sharp, and H.J. Goldsmid, *The Phonon—Glass Electron-Crystal Approach to Thermoelectric Materials Research*, in *Thermoelectrics: Basic Principles and New Materials Developments*. 2001, Springer Berlin Heidelberg: Berlin, Heidelberg. p. 177-207.
11. Chen, Y., Y. Zhao, and Z. Liang, *Solution processed organic thermoelectrics: towards flexible thermoelectric modules.* Energy & Environmental Science, 2015. **8**(2): p. 401-422.
12. Vineis, C.J., et al., *Nanostructured thermoelectrics: big efficiency gains from small features.* Adv Mater, 2010. **22**(36): p. 3970-80.
13. Weathers, A., et al., *Significant Electronic Thermal Transport in the Conducting Polymer Poly (3, 4 - ethylenedioxythiophene).* Advanced Materials, 2015. **27**(12): p. 2101-2106.
14. Tian, R., et al., *A solution-processed TiS 2/organic hybrid superlattice film towards flexible thermoelectric devices.* Journal of Materials Chemistry A, 2017. **5**(2): p. 564-570.
15. Beretta, D., et al., *Organic flexible thermoelectric generators: from modeling, a roadmap towards applications.* Sustainable Energy & Fuels, 2017. **1**(1): p. 174-190.
16. Russ, B., et al., *Organic thermoelectric materials for energy harvesting and temperature control.* Nature Reviews Materials, 2016. **1**(10): p. 16050.
17. Friedman, L., *Transport properties of organic semiconductors.* Physical Review, 1964. **133**(6A): p. A1668.
18. Wang, D., et al., *First-principles investigation of organic semiconductors for thermoelectric applications.* The Journal of Chemical Physics, 2009. **131**(22): p. 224704.

19. Chen, J., D. Wang, and Z. Shuai, *First-Principles Predictions of Thermoelectric Figure of Merit for Organic Materials: Deformation Potential Approximation.* Journal of Chemical Theory and Computation, 2012. **8**(9): p. 3338-3347.
20. Wang, S., et al., *Hopping transport and the Hall effect near the insulator–metal transition in electrochemically gated poly (3-hexylthiophene) transistors.* Nature communications, 2012. **3**(1): p. 1-7.
21. Noriega, R., et al., *A general relationship between disorder, aggregation and charge transport in conjugated polymers.* Nature materials, 2013. **12**(11): p. 1038-1044.
22. Tripathi, B.P. and V.K. Shahi, *Organic–inorganic nanocomposite polymer electrolyte membranes for fuel cell applications.* Progress in Polymer Science, 2011. **36**(7): p. 945-979.
23. Anthopoulos, T.D., et al., *Air-stable ambipolar organic transistors.* Applied Physics Letters, 2007. **90**(12): p. 122105.
24. Shi, K., et al., *Toward High Performance n-Type Thermoelectric Materials by Rational Modification of BDPPV Backbones.* Journal of the American Chemical Society, 2015. **137**(22): p. 6979-6982.
25. Schlitz, R.A., et al., *Solubility-Limited Extrinsic n-Type Doping of a High Electron Mobility Polymer for Thermoelectric Applications.* Advanced Materials, 2014. **26**(18): p. 2825-2830.
26. Hicks, L.D. and M.S. Dresselhaus, *Thermoelectric figure of merit of a one-dimensional conductor.* Physical Review B, 1993. **47**(24): p. 16631-16634.
27. Wang, Y., J. Zhou, and R. Yang, *Thermoelectric Properties of Molecular Nanowires.* The Journal of Physical Chemistry C, 2011. **115**(49): p. 24418-24428.
28. Zhang, B., et al., *Promising thermoelectric properties of commercial PEDOT: PSS materials and their Bi2Te3 powder composites.* ACS applied materials & interfaces, 2010. **2**(11): p. 3170-3178.
29. Kim, D., et al., *Improved thermoelectric behavior of nanotube-filled polymer composites with poly (3, 4-ethylenedioxythiophene) poly (styrenesulfonate).* ACS nano, 2009. **4**(1): p. 513-523.
30. Yao, Q., et al., *Enhanced Thermoelectric Performance of Single-Walled Carbon Nanotubes/Polyaniline Hybrid Nanocomposites.* ACS Nano, 2010. **4**(4): p. 2445-2451.
31. Meng, C., C. Liu, and S. Fan, *A Promising Approach to Enhanced Thermoelectric Properties Using Carbon Nanotube Networks.* Advanced Materials, 2010. **22**(4): p. 535-539.
32. Yu, C., et al., *Light-weight flexible carbon nanotube based organic composites with large thermoelectric power factors.* ACS nano, 2011. **5**(10): p. 7885-7892.
33. Zhao, Y., et al., *The effect of graphite oxide on the thermoelectric properties of polyaniline.* Carbon, 2012. **50**(8): p. 3064-3073.
34. Cho, C., et al., *Outstanding Low Temperature Thermoelectric Power Factor from Completely Organic Thin Films Enabled by Multidimensional Conjugated Nanomaterials.* Advanced Energy Materials, 2016. **6**(7).
35. Cho, C., et al., *Stable n-type thermoelectric multilayer thin films with high power factor from carbonaceous nanofillers.* Nano Energy, 2016. **28**: p. 426-432.

36. Cho, C., et al., *Completely organic multilayer thin film with thermoelectric power factor rivaling inorganic tellurides.* Adv Mater, 2015. **27**(19): p. 2996-3001.
37. Wang, H., et al., *Ionic Seebeck Effect in Conducting Polymers.* Advanced Energy Materials, 2015. **5**(11): p. 1500044.
38. Jiao, F., et al., *Ionic thermoelectric paper.* J. Mater. Chem. A, 2017. **5**(32): p. 16883-16888.
39. Zhao, D., et al., *Ionic thermoelectric supercapacitors.* Energy Environ. Sci., 2016. **9**(4): p. 1450-1457.
40. Zhao, D., et al., *Ionic thermoelectric gating organic transistors.* Nat Commun, 2017. **8**: p. 14214.
41. Ou, C., et al., *Compositionally Graded Organic–Inorganic Nanocomposites for Enhanced Thermoelectric Performance.* Advanced Electronic Materials, 2020. **6**(1): p. 1900720.
42. Culebras, M., K. Choi, and C. Cho, *Recent progress in flexible organic thermoelectrics.* Micromachines, 2018. **9**(12): p. 638.
43. Rivnay, J., et al., *Structural control of mixed ionic and electronic transport in conducting polymers.* Nature Communications, 2016. **7**(1): p. 11287.
44. Ouyang, J., et al., *On the mechanism of conductivity enhancement in poly(3,4-ethylenedioxythiophene):poly(styrene sulfonate) film through solvent treatment.* Polymer, 2004. **45**(25): p. 8443-8450.
45. Luo, J.J., et al., *Chemical post-treatment and thermoelectric properties of poly(3,4-ethylenedioxylthiophene):poly(styrenesulfonate) thin films.* Journal of Applied Physics, 2014. **115**(5).
46. Kim, G.H., et al., *Engineered doping of organic semiconductors for enhanced thermoelectric efficiency.* Nat Mater, 2013. **12**(8): p. 719-723.
47. Kim, N., et al., *Highly conductive PEDOT:PSS nanofibrils induced by solution-processed crystallization.* Adv Mater, 2014. **26**(14): p. 2268-72, 2109.
48. Wang, J., K. Cai, and S. Shen, *Enhanced thermoelectric properties of poly (3, 4-ethylenedioxythiophene) thin films treated with H2SO4.* Organic Electronics, 2014. **15**(11): p. 3087-3095.
49. Fan, Z., et al., *Significantly Enhanced Thermoelectric Properties of PEDOT:PSS Films through Sequential Post-Treatments with Common Acids and Bases.* Advanced Energy Materials, 2017. **7**(8): p. 1602116-n/a.
50. Bubnova, O., M. Berggren, and X. Crispin, *Tuning the Thermoelectric Properties of Conducting Polymers in an Electrochemical Transistor.* Journal of the American Chemical Society, 2012. **134**(40): p. 16456-16459.
51. Park, T., et al., *Flexible PEDOT electrodes with large thermoelectric power factors to generate electricity by the touch of fingertips.* Energy & Environmental Science, 2013. **6**(3): p. 788-792.
52. Yan, H., et al., *A high-mobility electron-transporting polymer for printed transistors.* Nature, 2009. **457**(7230): p. 679-686.
53. Wang, S., et al., *A Chemically Doped Naphthalenediimide-Bithiazole Polymer for n-Type Organic Thermoelectrics.* Advanced Materials, 2018. **30**(31): p. 1801898.
54. Sun, Y., et al., *Advances in n-Type Organic Thermoelectric Materials and Devices.* Advanced Electronic Materials, 2019. **5**(11): p. 1800825.
55. Itahara, H., et al., *Thermoelectric properties of organic charge-transfer compounds.* Journal of electronic materials, 2009. **38**(7): p. 1171-1175.

56. Kojima, H., et al., *Universality of the giant Seebeck effect in organic small molecules.* Materials Chemistry Frontiers, 2018. **2**(7): p. 1276-1283.
57. Sun, Y., et al., *Organic Thermoelectric Materials and Devices Based on p- and n-Type Poly(metal 1,1,2,2-ethenetetrathiolate)s.* Advanced Materials, 2012. **24**(7): p. 932-937.
58. Sun, Y., et al., *Flexible n-Type High-Performance Thermoelectric Thin Films of Poly(nickel-ethylenetetrathiolate) Prepared by an Electrochemical Method.* Advanced Materials, 2016. **28**(17): p. 3351-3358.
59. Menon, A.K., et al., *Metallo-organic n-type thermoelectrics: Emphasizing advances in nickel-ethenetetrathiolates.* Journal of Applied Polymer Science, 2017. **134**(3): p. n/a-n/a.
60. Sheng, P., et al., *Optimization of the thermoelectric properties of poly[Cux(Cu-ethylenetetrathiolate)].* Synthetic Metals, 2014. **188**: p. 111-115.
61. Jiao, F., et al., *Inkjet-printed flexible organic thin-film thermoelectric devices based on p- and n-type poly(metal 1,1,2,2-ethenetetrathiolate)s/polymer composites through ball-milling.* Philosophical transactions. Series A, Mathematical, physical, and engineering sciences, 2014. **372**(2013): p. 20130008-20130008.
62. Menon, A.K., et al., *Systematic Power Factor Enhancement in n-Type NiETT/PVDF Composite Films.* Advanced Functional Materials, 2018. **28**(29): p. 1801620.
63. Wolfe, R.M.W., et al., *Simultaneous Enhancement in Electrical Conductivity and Thermopower of n-Type NiETT/PVDF Composite Films by Annealing.* Advanced Functional Materials, 2018. **28**(37): p. 1803275.
64. Zhang, B., et al., *Promising Thermoelectric Properties of Commercial PEDOT:PSS Materials and Their Bi2Te3 Powder Composites.* ACS Applied Materials & Interfaces, 2010. **2**(11): p. 3170-3178.
65. Kim, D., et al., *Improved Thermoelectric Behavior of Nanotube-Filled Polymer Composites with Poly(3,4-ethylenedioxythiophene) Poly(styrenesulfonate).* ACS Nano, 2010. **4**(1): p. 513-523.
66. Wang, H., et al., *Simultaneously Improving Electrical Conductivity and Thermopower of Polyaniline Composites by Utilizing Carbon Nanotubes as High Mobility Conduits.* ACS Applied Materials & Interfaces, 2015. **7**(18): p. 9589-9597.
67. Hung, N.T., et al., *Diameter dependence of thermoelectric power of semiconducting carbon nanotubes.* Physical Review B, 2015. **92**(16): p. 165426.
68. Nonoguchi, Y., et al., *Enhanced thermoelectric properties of semiconducting carbon nanotube films by UV/ozone treatment.* Journal of Applied Physics, 2019. **126**(13): p. 135108.
69. Zhao, W., et al., *Flexible carbon nanotube papers with improved thermoelectric properties.* Energy & Environmental Science, 2012. **5**(1): p. 5364-5369.
70. Liu, Y., et al., *Ammonia Plasma-Induced n-Type Doping of Semiconducting Carbon Nanotube Films: Thermoelectric Properties and Ambient Effects.* ACS Applied Materials & Interfaces, 2019. **11**(24): p. 21807-21814.
71. Zhou, W., et al., *High-performance and compact-designed flexible thermoelectric modules enabled by a reticulate carbon nanotube architecture.* Nature Communications, 2017. **8**(1): p. 14886.

72. Yu, C., et al., *Air-stable fabric thermoelectric modules made of N- and P-type carbon nanotubes.* Energy & Environmental Science, 2012. **5**(11): p. 9481-9486.
73. Ryu, Y., D. Freeman, and C. Yu, *High electrical conductivity and n-type thermopower from double-/single-wall carbon nanotubes by manipulating charge interactions between nanotubes and organic/inorganic nanomaterials.* Carbon, 2011. **49**(14): p. 4745-4751.
74. Freeman, D.D., K. Choi, and C. Yu, *N-Type Thermoelectric Performance of Functionalized Carbon Nanotube-Filled Polymer Composites.* PLOS ONE, 2012. **7**(11): p. e47822.
75. Moriarty, G.P., et al., *Thermoelectric behavior of organic thin film nanocomposites.* Journal of Polymer Science Part B: Polymer Physics, 2013. **51**(2): p. 119-123.
76. Moriarty, G.P., et al., *Fully Organic Nanocomposites with High Thermoelectric Power Factors by using a Dual-Stabilizer Preparation.* Energy Technology, 2013. **1**(4): p. 265-272.
77. Bounioux, C., et al., *Thermoelectric composites of poly(3-hexylthiophene) and carbon nanotubes with a large power factor.* Energy & Environmental Science, 2013. **6**(3): p. 918-925.
78. Wang, J., et al., *Preparation and thermoelectric properties of multi-walled carbon nanotubes/polypyrrole composites.* Synthetic Metals, 2014. **195**: p. 132-136.
79. Liu, J., J. Sun, and L. Gao, *Flexible single-walled carbon nanotubes/polyaniline composite films and their enhanced thermoelectric properties.* Nanoscale, 2011. **3**(9): p. 3616-3619.
80. Yao, Q., et al., *The synergic regulation of conductivity and Seebeck coefficient in pure polyaniline by chemically changing the ordered degree of molecular chains.* Journal of Materials Chemistry A, 2014. **2**(8): p. 2634-2640.
81. Yao, Q., et al., *Abnormally enhanced thermoelectric transport properties of SWNT/PANI hybrid films by the strengthened PANI molecular ordering.* Energy & Environmental Science, 2014. **7**(11): p. 3801-3807.
82. Wang, L., et al., *Engineered Molecular Chain Ordering in Single-Walled Carbon Nanotubes/Polyaniline Composite Films for High-Performance Organic Thermoelectric Materials.* Chemistry – An Asian Journal, 2016. **11**(12): p. 1804-1810.
83. Rivadulla, F., C. Mateo-Mateo, and M.A. Correa-Duarte, *Layer-by-Layer Polymer Coating of Carbon Nanotubes: Tuning of Electrical Conductivity in Random Networks.* Journal of the American Chemical Society, 2010. **132**(11): p. 3751-3755.
84. Cho, C., et al., *Completely Organic Multilayer Thin Film with Thermoelectric Power Factor Rivaling Inorganic Tellurides.* Advanced Materials, 2015. **27**(19): p. 2996-3001.
85. Cho, C. and J. Son, *Organic Thermoelectric Multilayers with High Stretchiness.* Nanomaterials, 2020. **10**(1): p. 41.
86. Choi, J., et al., *Flexible and Robust Thermoelectric Generators Based on All-Carbon Nanotube Yarn without Metal Electrodes.* ACS Nano, 2017. **11**(8): p. 7608-7614.
87. L., B.J., et al., *Carbon‐Nanotube‐Based Thermoelectric Materials and Devices.* Advanced Materials, 2018. **30**(11): p. 1704386.

88. Zhou, W., et al., *Ultrahigh-Power-Factor Carbon Nanotubes and an Ingenious Strategy for Thermoelectric Performance Evaluation.* Small, 2016. **12**(25): p. 3407-14.
89. An, C.J., et al., *Foldable Thermoelectric Materials: Improvement of the Thermoelectric Performance of Directly Spun CNT Webs by Individual Control of Electrical and Thermal Conductivity.* ACS Applied Materials & Interfaces, 2016. **8**(34): p. 22142-22150.
90. An, C.J., et al., *High-performance flexible thermoelectric generator by control of electronic structure of directly spun carbon nanotube webs with various molecular dopants.* Journal of Materials Chemistry A, 2017. **5**(30): p. 15631-15639.
91. Liang, L., et al., *Large-area, stretchable, super flexible and mechanically stable thermoelectric films of polymer/carbon nanotube composites.* Journal of Materials Chemistry C, 2016. **4**(3): p. 526-532.
92. Xiao, C., et al., *Polymer composites with lychee-like core covered by segregated conducting and flexible networks: unique morphology, high flexibility, stretchability and thermoelectric performance.* Composites Science and Technology, 2018. **161**: p. 16-21.
93. Oh, J.Y., et al., *Chemically exfoliated transition metal dichalcogenide nanosheet-based wearable thermoelectric generators.* Energy & Environmental Science, 2016. **9**(5): p. 1696-1705.
94. Kim, J.Y., J.Y. Oh, and T.I. Lee, *Multi-dimensional nanocomposites for stretchable thermoelectric applications.* Applied Physics Letters, 2019. **114**(4): p. 043902.
95. Teng, C., et al., *Polymer in situ embedding for highly flexible, stretchable and water stable PEDOT:PSS composite conductors.* RSC Advances, 2013. **3**(20): p. 7219-7223.
96. Hansen, T.S., et al., *Highly Stretchable and Conductive Polymer Material Made from Poly(3,4-ethylenedioxythiophene) and Polyurethane Elastomers.* Advanced Functional Materials, 2007. **17**(16): p. 3069-3073.
97. Kim, N., et al., *Elastic conducting polymer composites in thermoelectric modules.* Nature Communications, 2020. **11**(1): p. 1424.
98. Kee, S., et al., *Highly Stretchable and Air-Stable PEDOT:PSS/Ionic Liquid Composites for Efficient Organic Thermoelectrics.* Chemistry of Materials, 2019. **31**(9): p. 3519-3526.
99. Jo, J., et al., *Highly stretchable organic thermoelectrics with an enhanced power factor due to extended localization length.* Organic Electronics, 2017. **50**: p. 367-375.
100. Kee, S., et al., *Self-Healing and Stretchable 3D-Printed Organic Thermoelectrics.* Advanced Functional Materials, 2019. **29**(51): p. 1905426.
101. Rowe, D.M., *CRC handbook of thermoelectrics*. 1995: CRC press.
102. Vining, C.B., *An inconvenient truth about thermoelectrics.* Nat Mater, 2009. **8**(2): p. 83-85.
103. Bubnova, O., et al., *Optimization of the thermoelectric figure of merit in the conducting polymer poly(3,4-ethylenedioxythiophene).* Nat Mater, 2011. **10**(6): p. 429-33.
104. Søndergaard, R.R., et al., *Practical evaluation of organic polymer thermoelectrics by large‐area R2R processing on flexible substrates.* Energy Science & Engineering, 2013. **1**(2): p. 81-88.

105. LeBlanc, S., *Thermoelectric generators: Linking material properties and systems engineering for waste heat recovery applications.* Sustainable Materials and Technologies, 2014. **1-2**: p. 26-35.
106. Sheng, P., et al., *A novel cuprous ethylenetetrathiolate coordination polymer: Structure characterization, thermoelectric property optimization and a bulk thermogenerator demonstration.* Synthetic Metals, 2014. **193**: p. 1-7.
107. Ou, C., et al., *Fully Printed Organic–Inorganic Nanocomposites for Flexible Thermoelectric Applications.* ACS Applied Materials & Interfaces, 2018. **10**(23): p. 19580-19587.
108. Ou, C., et al., *Enhanced thermoelectric properties of flexible aerosol-jet printed carbon nanotube-based nanocomposites.* APL Materials, 2018. **6**(9): p. 096101.
109. Wei, Q., et al., *Polymer thermoelectric modules screen-printed on paper.* RSC Advances, 2014. **4**(54): p. 28802-28806.
110. Mukaida, M., Q. Wei, and T. Ishida, *Polymer thermoelectric devices prepared by thermal lamination.* Synthetic Metals, 2016. **225**.
111. Kim, D., D. Ju, and K. Cho, *Heat-Sink-Free Flexible Organic Thermoelectric Generator Vertically Operating with Chevron Structure.* Advanced Materials Technologies, 2018. **3**(4): p. 1700335.
112. Park, S.H., et al., *High-performance shape-engineerable thermoelectric painting.* Nature communications, 2016. **7**: p. 13403.
113. Menon, A.K., et al., *Radial thermoelectric generator fabricated from n- and p-type conducting polymers.* Journal of Applied Polymer Science, 2017. **134**(3).
114. Menon, A.K. and S.K. Yee, *Design of a polymer thermoelectric generator using radial architecture.* Journal of Applied Physics, 2016. **119**(5): p. 055501.
115. Liu, L., et al., *Flexible unipolar thermoelectric devices based on patterned poly[Kx(Ni-ethylenetetrathiolate)] thin films.* Materials Chemistry Frontiers, 2017. **1**(10): p. 2111-2116.
116. Ryan, J.D., et al., *Machine-Washable PEDOT:PSS Dyed Silk Yarns for Electronic Textiles.* ACS Applied Materials & Interfaces, 2017. **9**(10): p. 9045-9050.
117. Ryan, J.D., et al., *All-organic textile thermoelectrics with carbon-nanotube-coated n-type yarns.* ACS applied energy materials, 2018. **1**(6): p. 2934-2941.
118. Du, Y., et al., *Thermoelectric Fabrics: Toward Power Generating Clothing.* Scientific Reports, 2015. **5**(1): p. 6411.
119. Yang, Y., et al., *Nanowire-composite based flexible thermoelectric nanogenerators and self-powered temperature sensors.* Nano Research, 2012. **5**(12): p. 888-895.
120. Li, Z., et al., *A Free-Standing High-Output Power Density Thermoelectric Device Based on Structure-Ordered PEDOT:PSS.* Advanced Electronic Materials, 2018. **4**(2): p. 1700496.
121. Song, H. and K. Cai, *Preparation and properties of PEDOT:PSS/Te nanorod composite films for flexible thermoelectric power generator.* Energy, 2017. **125**: p. 519-525.
122. Hewitt, C.A., et al., *Improved thermoelectric power output from multilayered polyethylenimine doped carbon nanotube based organic composites.* Journal of Applied Physics, 2014. **115**(18): p. 184502.
123. Rojas, J.P., et al., *Paper-based origami flexible and foldable thermoelectric nanogenerator.* Nano Energy, 2017. **31**: p. 296-301.

124. Rojas, J.P., et al., *Stretchable helical architecture inorganic-organic hetero thermoelectric generator.* Nano Energy, 2016. **30**: p. 691-699.
125. Prieto Rojas, J., et al., *Folding and stretching a thermoelectric generator*. SPIE Defense + Security. Vol. 10639. 2018: SPIE.
126. Fukuie, K., Y. Iwata, and E. Iwase, *Design of Substrate Stretchability Using Origami-Like Folding Deformation for Flexible Thermoelectric Generator.* Micromachines, 2018. **9**(7): p. 315.
127. Akuto, M., K. Fukuie, and E. Iwase. *Origami Heat Radiation Fin for Stretchable Thermoelectric Generator*. in *2019 19th International Conference on Micro and Nanotechnology for Power Generation and Energy Conversion Applications (PowerMEMS)*. 2019.
128. Nan, K., et al., *Compliant and stretchable thermoelectric coils for energy harvesting in miniature flexible devices.* Science Advances, 2018. **4**(11): p. eaau5849.
129. Xu, X., et al., *Three-dimensional helical inorganic thermoelectric generators and photodetectors for stretchable and wearable electronic devices.* Journal of Materials Chemistry C, 2018. **6**(18): p. 4866-4872.
130. Guan, Y.-S., et al., *Kirigami-Inspired Conducting Polymer Thermoelectrics from Electrostatic Recognition Driven Assembly.* ACS Nano, 2018. **12**(8): p. 7967-7973.
131. Jeong, S.H., et al., *Stretchable Thermoelectric Generators Metallized with Liquid Alloy.* ACS Applied Materials & Interfaces, 2017. **9**(18): p. 15791-15797.
132. Suarez, F., et al., *Flexible thermoelectric generator using bulk legs and liquid metal interconnects for wearable electronics.* Applied Energy, 2017. **202**: p. 736-745.
133. Han, M.-W. and S.-H. Ahn, *Blooming Knit Flowers: Loop-Linked Soft Morphing Structures for Soft Robotics.* Advanced Materials, 2017. **29**(13): p. 1606580.
134. Jung, M., S. Jeon, and J. Bae, *Scalable and facile synthesis of stretchable thermoelectric fabric for wearable self-powered temperature sensors.* RSC Advances, 2018. **8**(70): p. 39992-39999.
135. Sun, T., et al., *Stretchable fabric generates electric power from woven thermoelectric fibers.* Nature Communications, 2020. **11**(1): p. 572.
136. Starner, T.E. and J. Paradiso, *Human-generated power for mobile electronics*. 2004. p. 45-1.
137. Leonov, V. and R.J.M. Vullers. *Wearable electronics self-powered by using human body heat: The state of the art and the perspective*. 2009.
138. Bahk, J.-H., et al., *Flexible thermoelectric materials and device optimization for wearable energy harvesting.* Journal of Materials Chemistry C, 2015. **3**(40): p. 10362-10374.
139. We, J.H., S.J. Kim, and B.J. Cho, *Hybrid composite of screen-printed inorganic thermoelectric film and organic conducting polymer for flexible thermoelectric power generator.* Energy, 2014. **73**: p. 506-512.
140. Jin Bae, E., et al., *Enhancement of Thermoelectric Properties of PEDOT:PSS and Tellurium-PEDOT:PSS Hybrid Composites by Simple Chemical Treatment.* Scientific Reports, 2016. **6**(1): p. 18805.
141. Stark, I., *Converting body heat into reliable energy for powering physiological wireless sensors*, in *Proceedings of the 2nd Conference on Wireless Health*.

2011, Association for Computing Machinery: San Diego, California. p. Article 31.
142. Glynne-Jones, P. and N.M. White, *Self-powered systems: a review of energy sources.* Sensor review, 2001. **21**(2): p. 91-98.
143. Han, S., et al., *Thermoelectric Polymer Aerogels for Pressure–Temperature Sensing Applications.* Advanced Functional Materials, 2017. **27**(44): p. 1703549.
144. Cheng, H., et al., *Flexible cellulose-based thermoelectric sponge towards wearable pressure sensor and energy harvesting.* Chemical Engineering Journal, 2018. **338**: p. 1-7.
145. Oh, J., et al., *Coaxial struts and microfractured structures of compressible thermoelectric foams for self-powered pressure sensors.* Nanoscale, 2018. **10**(38): p. 18370-18377.
146. Zhang, D., et al., *Thermoelectric effect induced electricity in stretchable graphene-polymer nanocomposites for ultrasensitive self-powered strain sensor system.* Nano Energy, 2019. **56**: p. 25-32.
147. Taroni, P.J., et al., *Toward Stretchable Self-Powered Sensors Based on the Thermoelectric Response of PEDOT:PSS/Polyurethane Blends.* Advanced Functional Materials, 2018. **28**(15): p. 1704285.
148. Tauc, J., *Optical properties and electronic structure of amorphous Ge and Si.* Materials Research Bulletin, 1968. **3**(1): p. 37-46.
149. Menon, A.K., et al., *Radial thermoelectric generator fabricated from n‐and p‐type conducting polymers.* Journal of Applied Polymer Science, 2017. **134**(3).
150. Xie, Y., et al., *Flexible thermoelectric nanogenerator based on the MoS2/graphene nanocomposite and its application for a self-powered temperature sensor.* Semiconductor Science and Technology, 2017. **32**(4): p. 044003.
151. Jao, Y.-T., et al., *A Self-Powered Temperature Sensor Based on Silver Telluride Nanowires.* ECS Journal of Solid State Science and Technology, 2017. **6**(3): p. N3055-N3057.
152. Zhang, F., et al., *Flexible and self-powered temperature–pressure dual-parameter sensors using microstructure-frame-supported organic thermoelectric materials.* Nature communications, 2015. **6**: p. 8356.
153. Slobodian, P., et al., *Analysis of sensing properties of thermoelectric vapor sensor made of carbon nanotubes/ethylene-octene copolymer composites.* Carbon, 2016. **110**: p. 257-266.
154. Sun, Y., et al., *Organic Thermoelectric Materials and Devices Based on p‐and n‐Type Poly (metal 1, 1, 2, 2‐ethenetetrathiolate) s.* Advanced Materials, 2012. **24**(7): p. 932-937.
155. Menon, A.K., et al., *Metallo‐organic n‐type thermoelectrics: Emphasizing advances in nickel‐ethenetetrathiolates.* Journal of Applied Polymer Science, 2017. **134**(3).
156. Gupta, R.K., E. Kennel, and K.-J. Kim, *Polymer nanocomposites handbook*. 2009: CRC press.
157. Stauffer, D. and A. Aharony, *Introduction to percolation theory: revised second edition*. 2014: CRC press.
158. Fan, W., C.-Y. Guo, and G. Chen, *Flexible films of poly(3,4-ethylenedioxythiophene)/carbon nanotube thermoelectric composites*

prepared by dynamic 3-phase interfacial electropolymerization and subsequent physical mixing. Journal of Materials Chemistry A, 2018. **6**(26): p. 12275-12280.
159. Toshima, N., *Recent progress of organic and hybrid thermoelectric materials.* Synthetic Metals, 2017. **225**: p. 3-21.
160. Petsagkourakis, I., et al., *Correlating the Seebeck coefficient of thermoelectric polymer thin films to their charge transport mechanism.* Organic Electronics, 2018. **52**: p. 335-341.
161. Han, Z. and A. Fina, *Thermal conductivity of carbon nanotubes and their polymer nanocomposites: A review.* Progress in Polymer Science, 2011. **36**(7): p. 914-944.
162. Sun, Y., et al., *Optimization of the thermoelectric properties of poly(nickel-ethylenetetrathiolate) synthesized via potentiostatic deposition.* Science China Chemistry, 2016. **59**(10): p. 1323-1329.
163. Jiao, F., et al., *Inkjet-printed flexible organic thin-film thermoelectric devices based on p-and n-type poly (metal 1, 1, 2, 2-ethenetetrathiolate) s/polymer composites through ball-milling.* Philosophical Transactions of the Royal Society A: Mathematical, Physical and Engineering Sciences, 2014. **372**(2013): p. 20130008.
164. Pang, C., et al., *A flexible and highly sensitive strain-gauge sensor using reversible interlocking of nanofibres.* Nature materials, 2012. **11**(9): p. 795.
165. Window, A.L., *Strain gauge technology*. 1992: Springer.
166. Amjadi, M., Y.J. Yoon, and I. Park, *Ultra-stretchable and skin-mountable strain sensors using carbon nanotubes–Ecoflex nanocomposites.* Nanotechnology, 2015. **26**(37): p. 375501.
167. Gong, S., et al., *Highly Stretchy Black Gold E-Skin Nanopatches as Highly Sensitive Wearable Biomedical Sensors.* Advanced Electronic Materials, 2015. **1**(4): p. 1400063.
168. Boland, C.S., et al., *Sensitive, High-Strain, High-Rate Bodily Motion Sensors Based on Graphene–Rubber Composites.* ACS Nano, 2014. **8**(9): p. 8819-8830.
169. Fawcett, A.H. and T.M. McNally, *A dynamic mechanical and thermal study of various rubber–bitumen blends.* Journal of Applied Polymer Science, 2000. **77**(3): p. 586-601.
170. Bhat, G., S. Chand, and S. Yakopson, *Thermal properties of elastic fibers.* Thermochimica Acta, 2001. **367-368**: p. 161-164.
171. Wang, H., et al., *Ionic Seebeck effect in conducting polymers.* Advanced Energy Materials, 2015. **5**(11).
172. Zou, Z., et al., *Radio frequency identification enabled wireless sensing for intelligent food logistics.* Philosophical Transactions of the Royal Society A: Mathematical, Physical and Engineering Sciences, 2014. **372**(2017): p. 20130313.
173. Liu, X. and E. Sánchez-Sinencio, *An 86% efficiency 12 μW self-sustaining PV energy harvesting system with hysteresis regulation and time-domain MPPT for IOT smart nodes.* IEEE Journal of Solid-State Circuits, 2015. **50**(6): p. 1424-1437.
174. Zhang, X., et al. *A 2.89-μW clockless wireless dry-electrode ECG SoC for wearable sensors*. in *2015 IEEE Asian Solid-State Circuits Conference (A-SSCC)*. 2015. IEEE.

175. Lee, D., et al. *Fabrication of origami wheel using pattern embedded fabric and its application to a deformable mobile robot*. in *2014 IEEE International Conference on Robotics and Automation (ICRA)*. 2014.
176. Chen, Y., et al., *Symmetric waterbomb origami.* Proceedings of the Royal Society A: Mathematical, Physical and Engineering Sciences, 2016. **472**(2190): p. 20150846.
177. Le, P.H., Z. Wang, and S. Hirai. *Origami structure toward floating aerial robot*. in *2015 IEEE International Conference on Advanced Intelligent Mechatronics (AIM)*. 2015.
178. Wang, C., et al., *Advanced Carbon for Flexible and Wearable Electronics.* Advanced Materials, 2019. **31**(9): p. 1801072.
179. Lee, J.A., et al., *Woven‐Yarn Thermoelectric Textiles.* Advanced Materials, 2016. **28**(25): p. 5038-5044.
180. Park, S.-J., et al., *Highly Flexible Wrinkled Carbon Nanotube Thin Film Strain Sensor to Monitor Human Movement.* Advanced Materials Technologies, 2016. **1**(5): p. 1600053.
181. Khan, Y., et al., *Monitoring of Vital Signs with Flexible and Wearable Medical Devices.* Advanced Materials, 2016. **28**(22): p. 4373-4395.
182. Randeniya, L.K., et al., *Ammonia sensing characteristics of carbon-nanotube yarns decorated with nanocrystalline gold.* Carbon, 2011. **49**(15): p. 5265-5270.
183. Jia, T.J., et al., *Moisture Sensitive Smart Yarns and Textiles from Self-Balanced Silk Fiber Muscles.* Advanced Functional Materials, 2019. **29**(18).
184. He, W., et al., *Integrated textile sensor patch for real-time and multiplex sweat analysis.* Science Advances, 2019. **5**(11): p. eaax0649.
185. Li, W., et al., *A novel flexible humidity switch material based on multi-walled carbon nanotube/polyvinyl alcohol composite yarn.* Sensors and Actuators B-Chemical, 2016. **230**: p. 528-535.
186. Wang, Y., et al., *Flexible electrically resistive-type strain sensors based on reduced graphene oxide-decorated electrospun polymer fibrous mats for human motion monitoring.* Carbon, 2018. **126**: p. 360-371.
187. Park, B., et al., *Dramatically Enhanced Mechanosensitivity and Signal-to-Noise Ratio of Nanoscale Crack-Based Sensors: Effect of Crack Depth.* Advanced Materials, 2016. **28**(37): p. 8130-8137.
188. Yamada, T., et al., *A stretchable carbon nanotube strain sensor for human-motion detection.* Nature Nanotechnology, 2011. **6**(5): p. 296-301.
189. Zheng, Y., et al., *A highly stretchable and stable strain sensor based on hybrid carbon nanofillers/polydimethylsiloxane conductive composites for large human motions monitoring.* Composites Science and Technology, 2018. **156**: p. 276-286.
190. Kasimatis, M., et al., *Monolithic Solder-On Nanoporous Si-Cu Contacts for Stretchable Silicone Composite Sensors.* ACS Applied Materials & Interfaces, 2019. **11**(50): p. 47577-47586.
191. Jiang, Y., et al., *Auxetic Mechanical Metamaterials to Enhance Sensitivity of Stretchable Strain Sensors.* Advanced Materials, 2018. **30**(12): p. 1706589.
192. Liao, X., et al., *Ultrasensitive and stretchable resistive strain sensors designed for wearable electronics.* Materials Horizons, 2017. **4**(3): p. 502-510.
193. Weng, W., et al., *Smart Electronic Textiles.* Angewandte Chemie International Edition, 2016. **55**(21): p. 6140-6169.

194. Chen, J., et al., *Micro-cable structured textile for simultaneously harvesting solar and mechanical energy.* Nature Energy, 2016. **1**(10): p. 16138.
195. Zhang, N., et al., *A Wearable All-Solid Photovoltaic Textile.* Advanced Materials, 2016. **28**(2): p. 263-269.
196. Soin, N., et al., *Novel "3-D spacer" all fibre piezoelectric textiles for energy harvesting applications.* Energy & Environmental Science, 2014. **7**(5): p. 1670-1679.
197. Guo, H., et al., *A highly sensitive, self-powered triboelectric auditory sensor for social robotics and hearing aids.* Science Robotics, 2018. **3**(20): p. eaat2516.
198. Pu, X., et al., *Eye motion triggered self-powered mechnosensational communication system using triboelectric nanogenerator.* Science Advances, 2017. **3**(7): p. e1700694.
199. Kim, S.J., J.H. We, and B.J. Cho, *A wearable thermoelectric generator fabricated on a glass fabric.* Energy & Environmental Science, 2014. **7**(6): p. 1959-1965.
200. Fan, W., et al., *Machine-knitted washable sensor array textile for precise epidermal physiological signal monitoring.* Science Advances, 2020. **6**(11): p. eaay2840.
201. Sun, H., et al., *A Highly Sensitive and Stretchable Yarn Strain Sensor for Human Motion Tracking Utilizing a Wrinkle-Assisted Crack Structure.* ACS Applied Materials & Interfaces, 2019. **11**(39): p. 36052-36062.
202. Montazerian, H., et al., *Graphene-Coated Spandex Sensors Embedded into Silicone Sheath for Composites Health Monitoring and Wearable Applications.* Small, 2019. **15**(17): p. 12.
203. Wu, S.H., et al., *Flexible and conductive nanofiber-structured single yarn sensor for smart wearable devices.* Sensors and Actuators B-Chemical, 2017. **252**: p. 697-705.
204. Wen, Z., et al., *Self-powered textile for wearable electronics by hybridizing fiber-shaped nanogenerators, solar cells, and supercapacitors.* Science Advances, 2016. **2**(10): p. e1600097.
205. Zamarayeva, A.M., et al., *Flexible and stretchable power sources for wearable electronics.* Science Advances, 2017. **3**(6): p. e1602051.
206. Zhandarov, S.F. and E.V. Pisanova, *Two interfacial shear strength calculations based on the single fiber composite test.* Mechanics of Composite Materials, 1996. **31**(4): p. 325-336.
207. Ohsawa, T., et al., *Temperature dependence of critical fiber length for glass fiber-reinforced thermosetting resins.* Journal of Applied Polymer Science, 1978. **22**(11): p. 3203-3212.
208. Lang, U., N. Naujoks, and J. Dual, *Mechanical characterization of PEDOT:PSS thin films.* Synthetic Metals, 2009. **159**(5): p. 473-479.
209. Zhang, S., *Biological and Biomedical Coatings Handbook: Applications*. 2016: CRC Press.
210. Kim, J.Y., et al., *Enhancement of electrical conductivity of poly(3,4-ethylenedioxythiophene)/poly(4-styrenesulfonate) by a change of solvents.* Synthetic Metals, 2002. **126**(2): p. 311-316.
211. Lang, U., N. Naujoks, and J. Dual, *Mechanical characterization of PEDOT: PSS thin films.* Synthetic Metals, 2009. **159**(5-6): p. 473-479.

212. Ge, Z.-H., et al., *Improved thermoelectric properties of PEDOT: PSS polymer bulk prepared using spark plasma sintering.* Chemical communications, 2018. **54**(19): p. 2429-2431.
213. Zhang, F., et al., *Flexible and self-powered temperature–pressure dual-parameter sensors using microstructure-frame-supported organic thermoelectric materials.* Nature Communications, 2015. **6**(1): p. 8356.
214. Wan, K., et al., *Flexible and Stretchable Self‐Powered Multi‐Sensors Based on the N‐Type Thermoelectric Response of Polyurethane/Nax (Ni‐ett) n Composites.* Advanced Electronic Materials, 2019. **5**(12): p. 1900582.
215. Gong, S., et al., *Tattoolike Polyaniline Microparticle-Doped Gold Nanowire Patches as Highly Durable Wearable Sensors.* ACS Applied Materials & Interfaces, 2015. **7**(35): p. 19700-19708.
216. Xiao, X., et al., *High-Strain Sensors Based on ZnO Nanowire/Polystyrene Hybridized Flexible Films.* Advanced Materials, 2011. **23**(45): p. 5440-5444.
217. Kang, D., et al., *Ultrasensitive mechanical crack-based sensor inspired by the spider sensory system.* Nature, 2014. **516**(7530): p. 222-226.
218. Lu, N., et al., *Highly Sensitive Skin-Mountable Strain Gauges Based Entirely on Elastomers.* Advanced Functional Materials, 2012. **22**(19): p. 4044-4050.
219. Roh, E., et al., *Stretchable, Transparent, Ultrasensitive, and Patchable Strain Sensor for Human–Machine Interfaces Comprising a Nanohybrid of Carbon Nanotubes and Conductive Elastomers.* ACS Nano, 2015. **9**(6): p. 6252-6261.
220. Jeong, Y.R., et al., *Highly Stretchable and Sensitive Strain Sensors Using Fragmentized Graphene Foam.* Advanced Functional Materials, 2015. **25**(27): p. 4228-4236.
221. Mattmann, C., F. Clemens, and G. Tröster, *Sensor for measuring strain in textile.* Sensors, 2008. **8**(6): p. 3719-3732.
222. Muth, J.T., et al., *Embedded 3D Printing of Strain Sensors within Highly Stretchable Elastomers.* Advanced Materials, 2014. **26**(36): p. 6307-6312.
223. Kong, J.-H., et al., *Simple and rapid micropatterning of conductive carbon composites and its application to elastic strain sensors.* Carbon, 2014. **77**: p. 199-207.
224. Hwang, B.-U., et al., *Transparent Stretchable Self-Powered Patchable Sensor Platform with Ultrasensitive Recognition of Human Activities.* ACS Nano, 2015. **9**(9): p. 8801-8810.
225. Amjadi, M., et al., *Highly Stretchable and Sensitive Strain Sensor Based on Silver Nanowire–Elastomer Nanocomposite.* ACS Nano, 2014. **8**(5): p. 5154-5163.
226. Amjadi, M., et al., *Stretchable, Skin-Mountable, and Wearable Strain Sensors and Their Potential Applications: A Review.* Advanced Functional Materials, 2016. **26**(11): p. 1678-1698.
227. Fernández-Toribio, J.C., et al., *A Composite Fabrication Sensor Based on Electrochemical Doping of Carbon Nanotube Yarns.* Advanced Functional Materials, 2016. **26**(39): p. 7139-7147.
228. Iglesias, D., et al., *Gas-Phase Functionalization of Macroscopic Carbon Nanotube Fiber Assemblies: Reaction Control, Electrochemical Properties, and Use for Flexible Supercapacitors.* ACS Applied Materials & Interfaces, 2018. **10**(6): p. 5760-5770.
229. Blackburn, J.L., et al., *Carbon-Nanotube-Based Thermoelectric Materials and Devices.* Advanced Materials, 2018. **30**(11): p. 1704386.

230. Choi, J., et al., *High-Performance, Wearable Thermoelectric Generator Based on a Highly Aligned Carbon Nanotube Sheet.* ACS Applied Energy Materials, 2020. **3**(1): p. 1199-1206.
231. Karalis, G., et al., *A carbon fiber thermoelectric generator integrated as a lamina within an 8-ply laminate epoxy composite: Efficient thermal energy harvesting by advanced structural materials.* Applied Energy, 2019. **253**: p. 113512.
232. Xu, H., et al., *Mechanical and electrical properties of laminated composites containing continuous carbon nanotube film interleaves.* Composites Science and Technology, 2016. **127**: p. 113-118.
233. Xu, X., et al., *In-situ curing of glass fiber reinforced polymer composites via resistive heating of carbon nanotube films.* Composites Science and Technology, 2017. **149**: p. 20-27.
234. Xu, D., et al., *Fabrication of free-standing hierarchical carbon nanofiber/graphene oxide/polyaniline films for supercapacitors.* ACS Appl Mater Interfaces, 2014. **6**(1): p. 200-209.
235. Tai, Z., et al., *Enhancement of capacitance performance of flexible carbon nanofiber paper by adding graphene nanosheets.* Journal of Power Sources, 2012. **199**: p. 373-378.
236. Wu, G., et al., *Exploring High-Performance n-Type Thermoelectric Composites Using Amino-Substituted Rylene Dimides and Carbon Nanotubes.* ACS Nano, 2017. **11**(6): p. 5746-5752.
237. Timoshenko, S., *Analysis of bi-metal thermostats.* Josa, 1925. **11**(3): p. 233-255.
238. Zhang, Y., et al., *Recent advances in organic thermoelectric materials: Principle mechanisms and emerging carbon-based green energy materials.* Polymers, 2019. **11**(1): p. 167.
239. Zhang, H., et al., *Aligned two- and three-dimensional structures by directional freezing of polymers and nanoparticles.* Nat Mater, 2005. **4**(10): p. 787-793.